UNIVERSITÀ DI PARMA

DOTTORATO DI RICERCA IN SCIENZE DELLA TERRA

CICLO XXXV

Turbidites dominated by supercritical flows and hydraulic jumps in relation to morphologic variations in tectonically controlled basins

Coordinatore:

Chiar.mo Prof. Roveri Marco

Tutors:

Chiar.mo Prof. Tinterri Roberto

Chiar.mo Prof. Gamberi Fabiano

Candidata:

Elena Scacchia

UNIVERSITY OF PARMA

Department of Chemistry, Life Sciences and Environmental Sustainability

PhD degree in Earth Sciences

XXXV cycle

Turbidites dominated by supercritical flows and hydraulic jumps in relation to morphologic variations in tectonically controlled basins

Coordinator:

Prof. Roveri Marco

Tutors:

Prof. Tinterri Roberto

Prof. Gamberi Fabiano

Candidate:

Elena Scacchia

Contents

Chapter 1: Introduction

Chapter 2: "The influence of channel planform and slope topography on turbidity current overbank processes: the example of the Acquarone Fan (Southeastern Tyrrhenian Sea)"

Chapter 3: "Supercritical bedforms and related downslope evolution in a confined lobe, Amantea Fan, Paola Basin (Southeastern Tyrrhenian Sea)"

Chapter 4: "Small-scale facies change in relation to the articulate seafloor topography in two lobes of the Paretaio Turbidite System (Marnoso-arenacea Formation, Northern Apennines)"

Chapter 1

Introduction

1. Why is still important to study turbidity currents?

The depositional systems on the ocean floor are by far the largest on the planet and serve as the sink for a large part of the sediment that is transported to the coastal domain. The sediment is principally transported from proximal to distal submarine environments by gravity-driven sediment flows called turbidity currents.

A single turbidity current can last from minutes to hours (Hughes Clarke, 2016) up to weeks (Azpiroz-Zabala et al., 2017) and turbidity currents can redistribute more sediment across the surface of the Earth than any other sediment flow process (Talling et al., 2015) and, therefore, they are one of the most important processes characterizing source-to-sink sedimentary systems.

Monitoring of turbidity currents revealed that they can flow through channels with velocities of 1 – 7 m/s (Azpiroz-Zabala et al., 2017). Largescale sediment remobilizations triggered by a catastrophic event like an earthquake may even result in flow velocities of up to ~18 m/s (~70 km/h) and travel distances of 1000s of kilometres, as documented for the Grand Banks turbidity current in 1929 (Kuenen 1952; Hughes Clarke et al., 1990).

Due to their destructive nature, turbidity currents also represent a significant factor for equipment placed on the ocean floor. This involves oil and gas pipelines, and also communication cables which nowadays host > 95% of the worldwide internet traffic (Carter et al., 2009).

Downstream of the terminations of channels, sediment is deposited as lobate sediment bodies composing deep-sea fans, representing the biggest sediment accumulations on Earth (e.g., Normark, 1970; Mutti et al., 2009; Mutti & Normark, 1987; Prélat et al., 2009). Deep-sea fans are the subject of many studies because they represent potential reservoirs for natural resources such as hydrocarbons (e.g., Pettingill, 2004), mineral ores, and rare-earth elements (e.g., Kato et al., 2011). In addition, deep-sea fans accumulate large quantities of organic matter (Azpiroz-Zabala et al., 2017) and man-made materials such as microplastics (Pohl et al., 2020; Zhong & Peng, 2021).

Understanding the transportation and deposition mechanisms of turbidity currents is of key interest to predicting the distribution of turbiditic sediment and any other material on the ocean floor.

Modern technology and measurement techniques allow monitoring turbidity currents in canyons and channels, revealing astonishing new insights into the dynamics and the nature of turbidity currents (Azpiroz-Zabala et al., 2017; Dorrell et al., 2016; Hage et al., 2018; Heijnen et al., 2020; Hughes Clarke, 2016). Anyway direct measurements from turbidity currents are remarkably few and so laboratory experiments are increasingly used to mimic the turbidity current behaviour and relative deposits in different and simplified geological settings (Amy et al., 2004; Cartigny et al., 2014; de Leeuw et al., 2018; Kneller, 1995; Kneller et al., 1991; Ono et al., 2021; Patacci et al., 2015; Soutter et al., 2021).

Nevertheless, it can be said that these studies have focused on specific and local aspects of turbidite sedimentation often not considering their stratigraphic and depositional context. Basin morphology and changes in slope topography can influence flow transformations and relative facies types (e.g., Amy et al., 2004; Tinterri et al., 2016; Tinterri & Muzzi Magalhaes, 2011; Tinterri & Piazza, 2019; Tinterri & Tagliaferri, 2015). The great complexity behind the way turbidity currents interact with the ocean floor topography makes its knowledge elusive.

Tank experiments and numerical modelling are useful and fascinating tools to directly observe the flowing and deposition from a turbidity current in relation to a more or less complex floor topography. In fact, the studies applying the aforementioned methodologies are increasingly replacing those carried out with “old”-style field-based approach. Anyway, to understand the validity of those experiments is important to compare the result obtained with natural examples. The study of modern and ancient turbiditic systems should go hand-in-hand with increasing interest in the laboratory-based approach since those methodologies are strictly related and gain advantages from each other.

2. Turbidity currents historical perspectives

Turbidity currents have been firstly defined by Kuenen and Migliorini (1950) as “a current flowing in consequence of the load of sediment it is carrying, and which gives it excess density. This leaves the controversial mode of suspension out of account (turbulence, impact, inertia flow, etc.)” (Kuenen in Sanders, 1965). This concept was successively worked out in detail by Kuenen’s student Arnold Bouma who elaborated the first and most famous turbidite depositional model: the Bouma

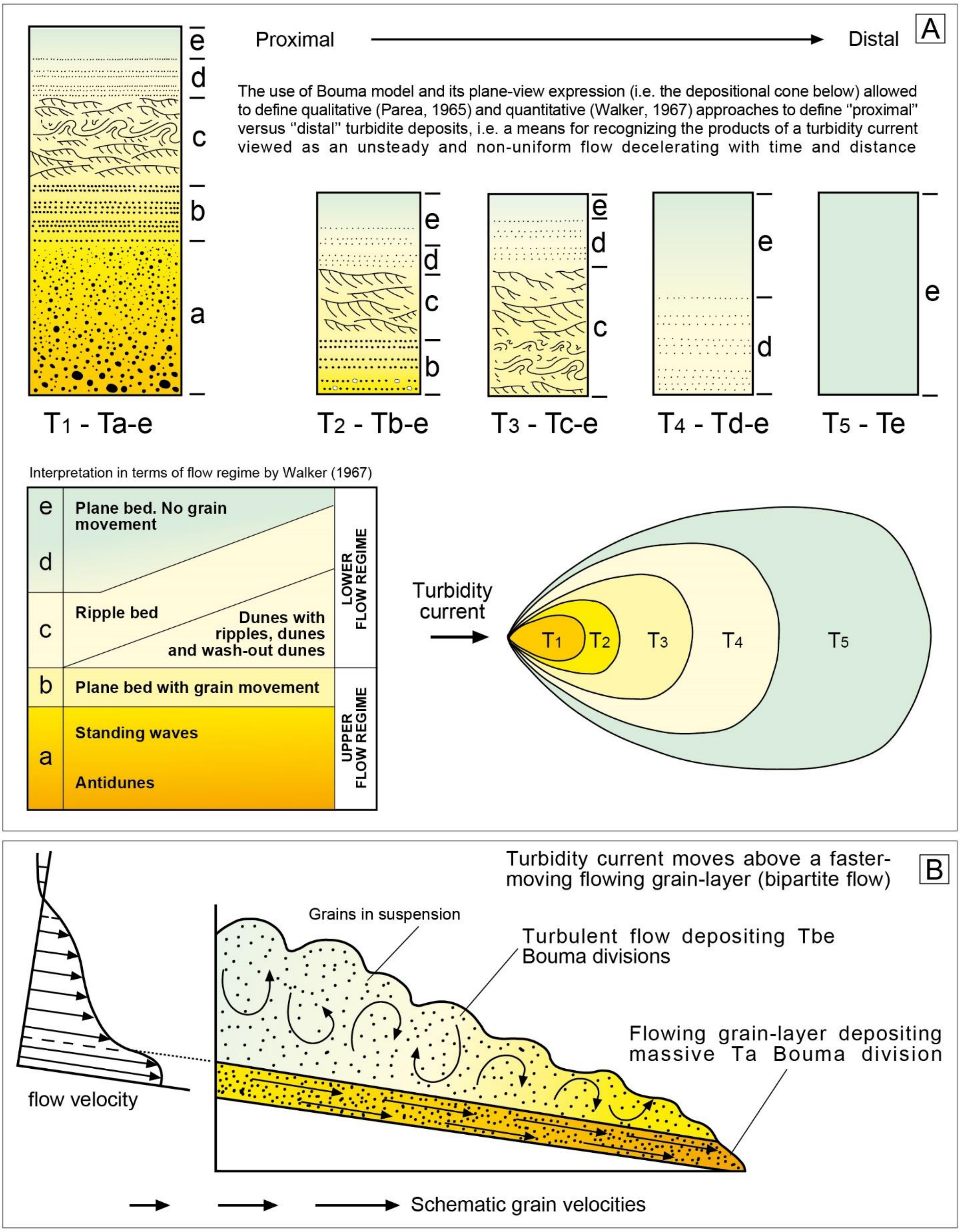

Figure 1 *(A) The Bouma sequence and its 'depositional cone'. The interpretation of the Bouma sequence in terms of flow regime by Walker (1967) is also shown. (B) Velocity profile of a turbidity current consisting of a basal, faster moving, flowing grain layer overlain by a turbulent flow. From Tinterri et al. (2020) (A) modified from Bouma (1962), (B) modified from Sanders (1965).*

sequence. His "Ta-e" sequence represents the time-space evolution of an ideal wining and depletive turbidite current resulting in a normally graded deposit (Bouma, 1962) (Figure 1a). Later on, Bagnold's (1954) experiments showed that at volumetric sediment concentration above 9%, grains are supported by collisions between grains instead of fluid turbulence, highlighting that turbulence couldn't be the only support mechanism inside turbidity currents. In this context the pioneering insight comes from Sanders (1965), who proposed, for the first time, a bipartite turbidity current model; this model provides for an inertial laminar basal flow depositing the lower massive Ta interval and overlaid by an upper turbulent flow depositing the upper Tb-e divisions through traction plus fallout processes (Figure 1b). According to this model, only the upper Tb-e division is deposited by a turbidite current (*sensu strictu*). Insights about the origin of turbidite currents came also from the laboratory experiments by Hampton (1972), who proved that they could derive also from head transformation of debris flows. From the seventies onwards, turbidite facies schemes developed following two parallel ways: a descriptive one based on the geometric features of the structures and a genetic one, which linked structures to processes. The latter has always focussed on the genetic link between the several facies deposited by the same turbidite current. This concept is expressed by the *facies tract*, which represents the suit of facies deposited by the same gravity flow that, in turn, can be seen as the downcurrent evolution of the flow itself. The facies tract concept was developed by Lowe (1982), who based his scheme on three dynamic grain populations, each of which is deposited by a specific dynamic process (Figure 2a): 1) pebble to coarse sand, 2) coarse to medium sand, 3) fine sand to mud. The first would be deposited by cohesive debris flow and gravelly-high density turbidite currents, the second by sandy-high density turbidite currents, and the third by low-density turbidity currents. Lowe also explains the three main depositional phases of high-density turbidity currents caused by the progressive flow deceleration and related increase in fallout rate: 1) traction (S1), 2) traction carpets (S2) and 3) suspension sedimentation (S3). All these concepts are encompassed in a facies tract and represent the downcurrent evolution gravity flows that, from a cohesive state, progressively transform into high-density and low-density turbidity currents. Following Lowe's model, Mutti (1992) created a scheme (Figure 2b) based on four dynamic grain populations and introduced the concept of hyperconcentrated flows (facies F2), which represent an intermediate state between cohesive debris flow (facies F1) and more diluted turbidite currents. The latter can be divided into gravelly (facies F4 and F5) and sandy high-density turbidite current (F6, F7, F8) followed by low density ones (facies F9a, b). Mutti's scheme also stresses bypass facies, expressed by residual orthoconglomerate (facies F3) and sandy megaripple

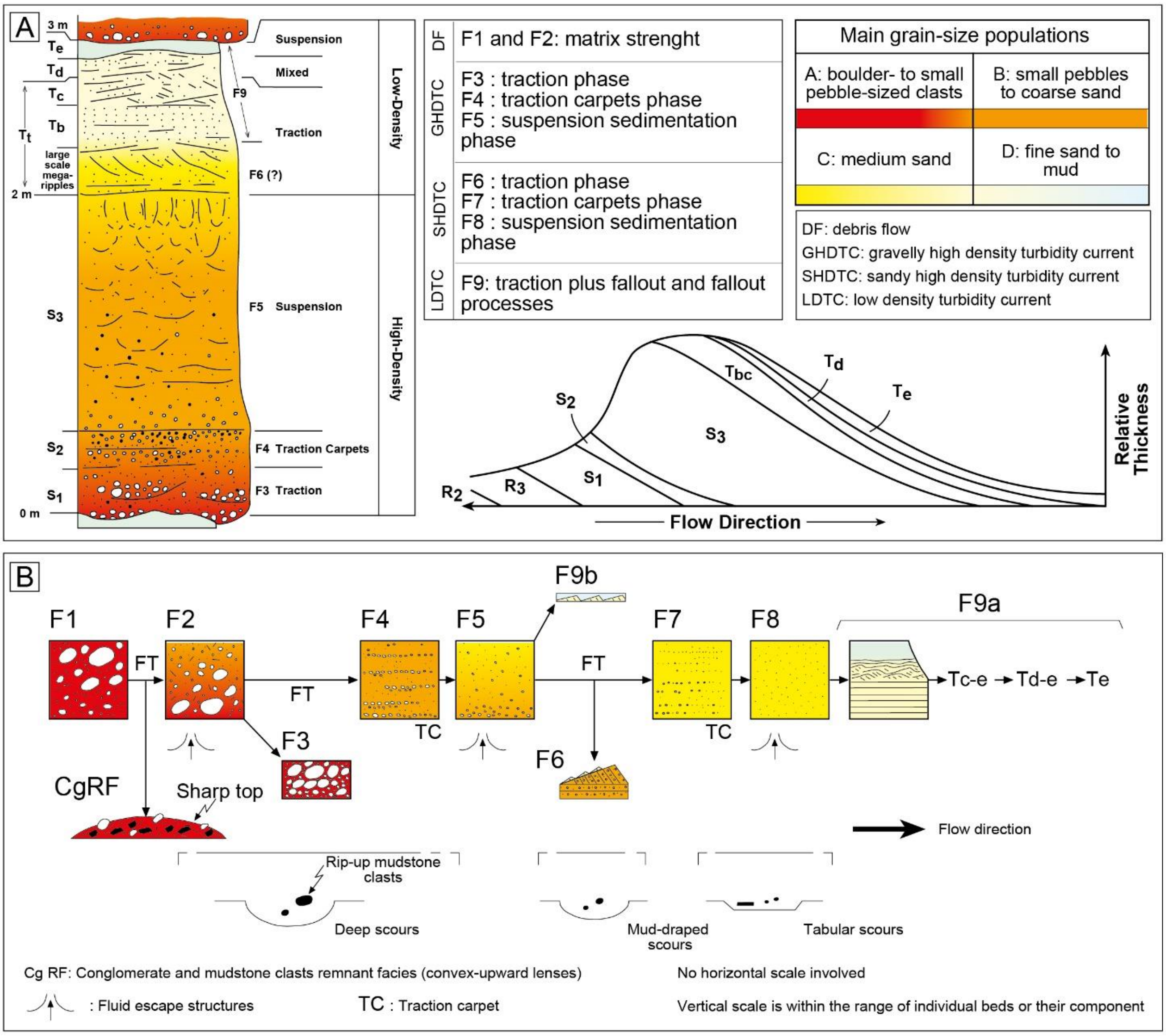

Figure 2 *(A) On the left, ideal deposit of a sandy high-density turbidity current from Lowe (1982), showing both high density (S1-3) and late-stage low-density (Tt, Td-e) divisions; on the right, generalized diagram showing downslope changes in turbidite organization. The horizontal line represents the turbidite base. A comparison between the facies by Mutti (1992) and the three depositional phases by Lowe (1982) is also shown; (B) Framework for a predictive classification scheme of turbidite facies (from Mutti 1992, for an updated version, see Mutti et al., 2003). From Tinterri et al. (2020) (A) modified from Lowe (1982), (B) modified from Mutti (1992).*

(facies F6). The schemes by Mutti et al. (2003) are an evolution of the scheme published in 1992 and will be described in detail in the third paragraph of this introduction.

In the early 2000s, after the works by Lowe & Guy (2000) and Baas & Best (2002), it became clear that the amount and the type of mud can be very important for the dynamics of the sediment gravity flows. These studies were important in the interpretation of hybrid sediment gravity flow deposits (or hybrid beds) that were receiving great attention at that time and will have it for the next years

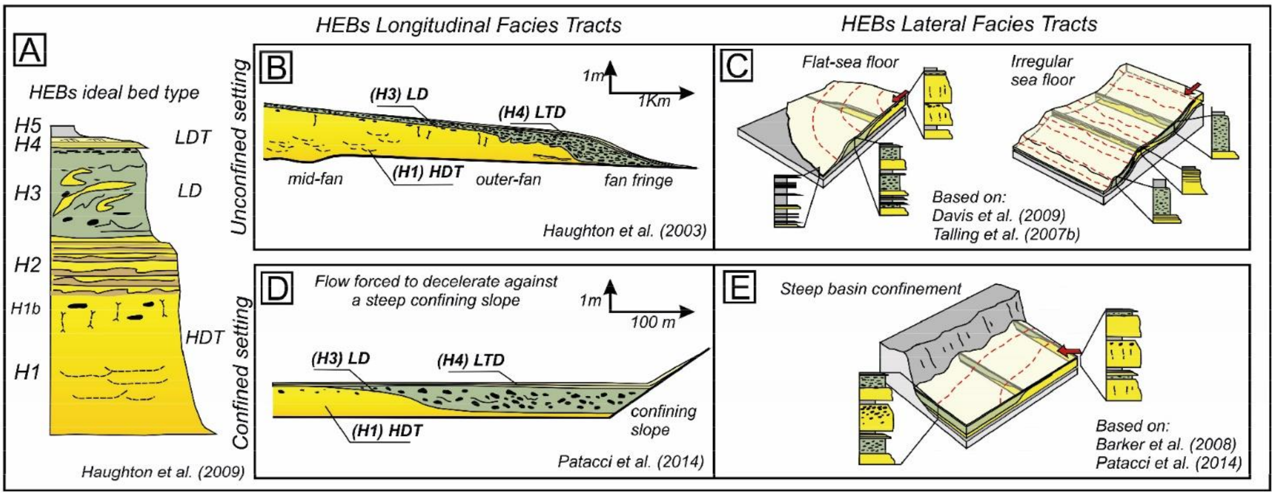

***Figure 3** Hybrid event bed type model and hybrid gravity flow facies tract expression. (A) Idealised organisation of a typical hybrid event bed (H1-H5 sequence) as suggested by Haughton et al. (2009). (B) Longitudinal facies tract expression of an hybrid flow deposit in unconfined setting; (C) hybrid event beds are preferentially distributed in the marginal sectors of unconfined lobes (Davis et al., 2009) and influenced by local changes of gradient which make flatter areas prone to debris flow development and deposition (Talling et al., 2007b). (D) In obliquely confined settings the slope forces the flow to decelerate, rapidly damping turbulence and producing a transformation to cohesive flow which deposits close to the margin. (E) In laterally confined settings, thinner, slope-adjacent flows become less turbulent, becoming hybrid, and depositing hybrid event beds adjacent to the margin (HDT: high-density turbidite; LD: linked-debrite; LTD: low-density turbidite). From Fonnesu et al. (2015).*

(Amy & Talling, 2006; Fonnesu et al., 2015, 2016; Haughton et al., 2003, 2009; Muzzi Magalhaes & Tinterri, 2010; Spychala et al., 2017; Talling et al., 2004, 2012; Tinterri & Piazza, 2019; Tinterri & Tagliaferri, 2015). According to Haughton et al., 2009, these beds are generally characterized by five facies where structureless sandstones, deposited by high-density flows (H1, "a" according to Muzzi Magalhaes & Tinterri (2010) the latter terminology is used in this work), pass into muddy and mud clast-bearing sandstones deposited by cohesive flows (H3 or "b") through banded sandstones deposited by a transitional flow (H2 or "a_2") (Figure 3a). The slurry or debrite unit "b" is capped by a relatively thin, well-structured and graded sand-mud couplet (H4, "c") deposited by residual low-density turbidity current (Figure 3a). The origin of these bed types can essentially be considered related to an interplay between mud content and deceleration rates that can create a near-bed suspension able to produce progressive turbulence damping at the boundary layer. A common general observation is that hybrid event beds become increasingly important in the outer and marginal parts of many systems, like lobe fringes, where they replace beds composed dominantly of clean sand either up-dip and/or axially (Haughton et al., 2003, Figure 3b). Shorter length-scale (km) transitions from turbidite to hybrid event bed are particularly common where flows are forced to decelerate against topography (Muzzi Magalhaes & Tinterri, 2010; Patacci et al., 2014; Tinterri & Tagliaferri, 2015) (Figure 3d-e). Also, subtle basin floor topography can be important in either triggering or delaying linked debrite formation and may contribute to more complex patterns of debrite distribution, including local pods of debrite developed in zones of flow expansion or lower gradient that promote flow transformation (Talling et al., 2007) (Figure 3c). The interest behind this bed type and the spatial changes in bed make-up (i.e., facies tracts) is related to the consequences that their occurrence cause of the reservoir proprieties since much of the sandy part of the event bed is compromised by high mud concentrations.

3. Supercritical flows and hydraulic jump related deposits

In the last decade, supercritical flows and their deposits become an important topic in the comprehension of flow processes in deep-water settings. A paper published in 2015 in the Journal of Sedimentary Research pointed out that the research about supercritical flow dynamics and their related deposits were one of the key future directions for research on turbidity currents (Talling et al., 2015). The importance of the criticality inside turbidity currents was first introduced by Komar (1971) pointing out that turbidity currents could reach the supercritical condition flowing into a canyon, in the same way it occurs in river flow. In fact, a flow is supercritical when its velocity exceeds the velocity of the wave speed at the free surface, this concept is summarized by the densimetric Froude number:

$$Fr' = \frac{U}{\sqrt{hg'}}$$

where *U* is the flow velocity, *h* the flow depth and *g'* is the reduced gravity

where $g' = g\,\frac{\rho-\rho w}{\rho w}$

and where ρ is the density of the flow and ρw the density of the ambient water and *g* the gravity constant. Flow with Fr' exceeding unity (Fr'>1) is said to be supercritical. Flow where Fr< 1 is referred to as subcritical. In synthesis, in turbidity currents, the balance between inertial and gravity forces defines the densimetric Froude number.

The passage from the supercritical to the subcritical condition is marked by the occurrence of a hydraulic jump (Figure 4). The early tank experiment conducted by Garcia & Parker (1989) demonstrated for the first time the formation of a hydraulic jump in turbidity currents flowing over

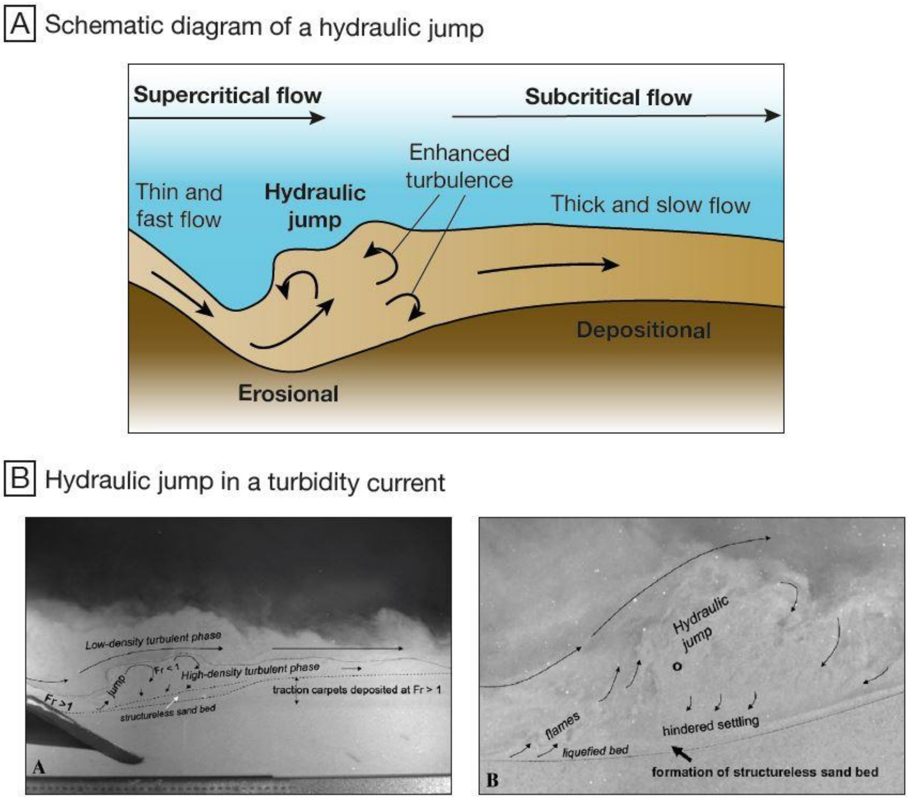

Figure 4 *A) Schematic diagram showing the key features of a hydraulic jump. Modified from Dorrell et al. (2016). (B) Pictures from flume experiments showing a hydraulic jump in a turbidity current and the forming of backsets forcing the hydraulic jump to migrate upstream (Postma et al. 2009).*

a slope break during which the velocity of the flow would be reduced significantly and its thickness markedly increased (Figure 4). A hydraulic jump results in enhanced turbulence that would give the flow an increased erosion potential producing scours (Komar, 1971), while the subcritical flow downstream of the jump is generally highly depositional (Figure 4a). Deposition on the lee side of these jumps progressively backfills them (Figure 4b), whilst the steps move upstream. The magnitude of the hydraulic jump can be classified by flow height expansion downstream of the jump, which is defined by the ratio of the incoming and outgoing flow depth ($\Delta Fr = h_2/h_1$). The height of the jump (ΔFr) results to be related to the Fr' value of the flow before the jump (Komar, 1971).

Bedforms in unidirectional flow are traditionally divided into upper flow-regime and lower flow-regime, depending on Froude number and grain-size. Upper flow-regime bedforms are

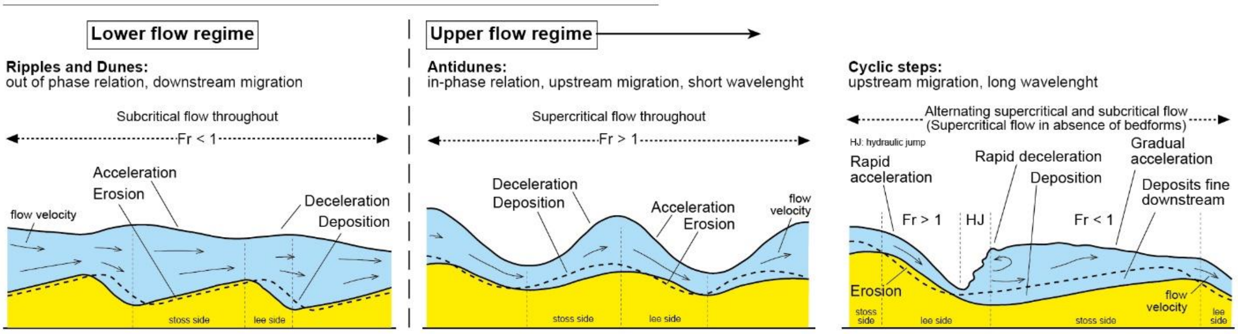

Figure 5 *Diagrams describing bedforms of the lower and upper flow regimes are also indicated (see below). From Tinterri et al. (2020) modified from Cartigny (2012).*

characterized by in-phase relations in which the crest and trough of individual bedforms correspond to the crest and trough of in-phase waves on the free water surface (Figure 5).

Consequently, in general, supercritical bedforms are characterized by lee-face erosion and a stoss-side deposition that cause upstream migration of bedforms (Slootman & Cartigny, 2020). Upper flow-regime bedforms range from antidunes and cyclic steps, spanning a continuum of transitional bedforms that are still poorly understood (Cartigny et al., 2014) (Figure 5). In particular, as the Froude number increases, short-wavelength antidunes deposited under trains of in-phase surface waves gradually transform into longer-wavelength cyclic steps characterized by a series of steps with supercritical flows down the lee side and subcritical flows on the stoss side separated by hydraulic jumps in the intervening trough (Figure 5). The antidunes have been observed to migrate both up and downstream forming at Fr'~1.4 while cyclic steps are associated with Froude numbers Fr'> 1.5–2 and are prevalently upslope migrating (Postma et al., 2009).

The common long wavelength and low amplitude (Cartigny et al., 2014) of supercritical-flow sedimentary structures make their recognition difficult, especially in outcrops of limited size. Anyway, developing turbidite facies is of prime importance for understanding large-scale flow hydraulics (i.e density flow criticality). Not only is the flow's velocity profile very different for super and subcritical flows (Sequeiros, 2012), which has important consequences for the flow's carrying

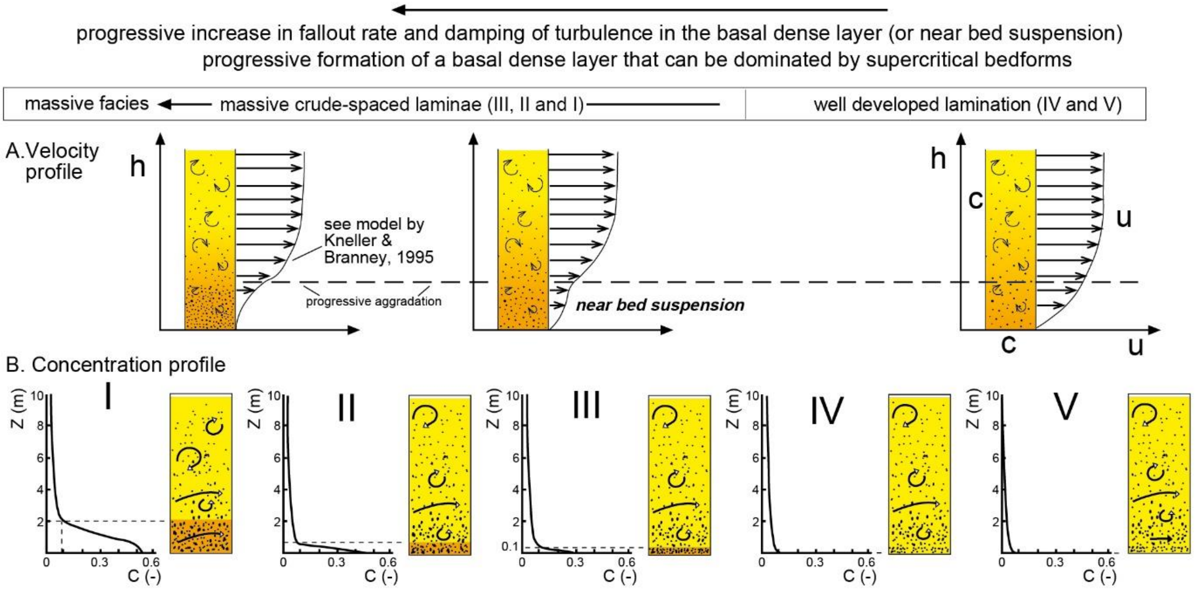

__Figure 6__ Bedform stability diagrams (above) associated with five flow types that, through the increase in fallout rate, show different velocity profiles and concentration profiles related to the progressive formation of a high-density layer. Transitions between subcritical and supercritical flows are Froude-scaled based on the basal layer thickness. From Tinterri et al. (2020) modified from Cartigny and Postma (2014).

capacity (Figure 6), but a supercritical flow passing through a hydraulic jump leaves distinct sedimentary facies (Cartigny et al., 2014; Hage et al., 2018; Postma et al., 2009).

Most of the turbidity currents, due to higher fall-out rate, present higher density and velocity flow nearer the bed producing a stratified flow with a dense, pseudolaminar basal layer and a fully turbulent, low-density upper layer (Figure 6). Such upper-flow regime bedforms are only thought to form in the basal layers of stratified flows (Postma and Cartigny, 2014).

In particular, stratified flows, represented by the 2-phase diagram in Figure 7, are characterized by a basal high-concentration traction carpet, where particles are predominantly suspended by dispersive pressure due to grain interaction, and the less dense overriding suspension. Field and flume evidence indicate that traction carpets can form under both super and sub-critical flows, as long as the required fall-out rate is achieved.

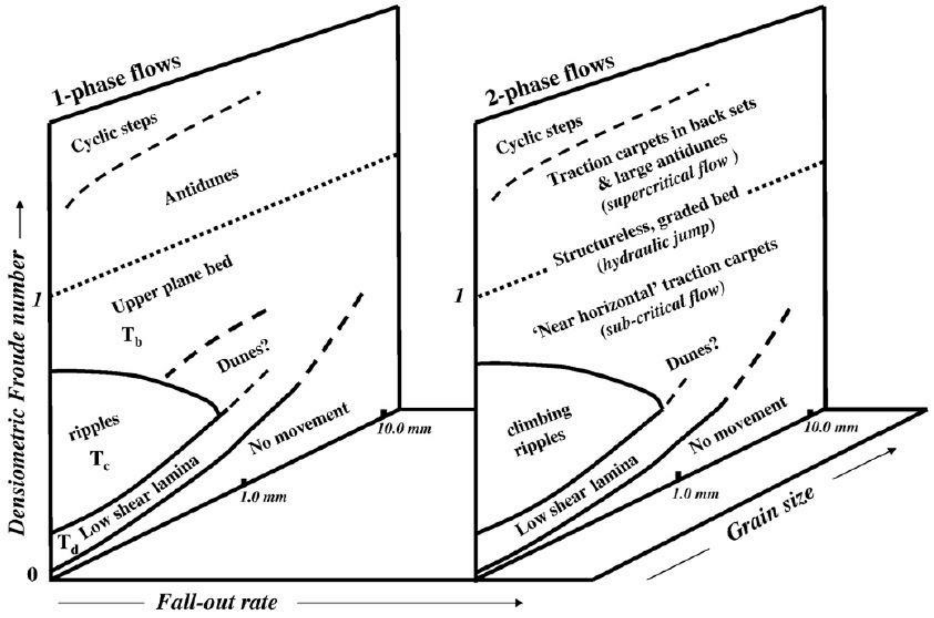

Figure 7 Three-dimensional bedform stability diagram for 1 and 2-phase suspension flows. To illustrate the position of the hydraulic jump, the stability fields of the various bed forms are given relative to critical flow conditions (Fr'=1). Hence, the boundaries of the stability feeds are only approximate. From Postma et al. (2009).

Under supercritical condition the deposition from the basal dense layer produce large back sets of traction carpets as long wave antidunes and large sand and gravel waves (cyclic steps) (Cartigny et al., 2014; Postma et al., 2009) (Fr>1 in Figure 7). Tank experiments highlighted that in antidunes and cyclic steps, the angle of the boundaries between stacked lamine is directly proportional to the preserved set thickness. The structures of very thin or only partially preserved lamina sets resemble plane parallel lamination. In thicker sets, the average upcurrent dip of laminae is distinctly higher and the resulting backset geometry is thus much more evident (Cartigny et al., 2014).

When a flow passes the hydraulic jump, it expanded vigorously. This behaviour resulted in strong, upward disruption of the top of the substrate resulting in the formation of scour; moments later the dense suspension rained down. Facies at the hydraulic jump is thus characterized by soft-sediment deformation (flame structures), due to the rapid drop in velocity that increases the pressure above the bed, and structureless coarse-tail graded sediments deposited during conditions of hindered settling with virtually no horizontal shear (Postma et al., 2009; see also Tinterri et al. 2016) (Fr=1 in Figure 7).

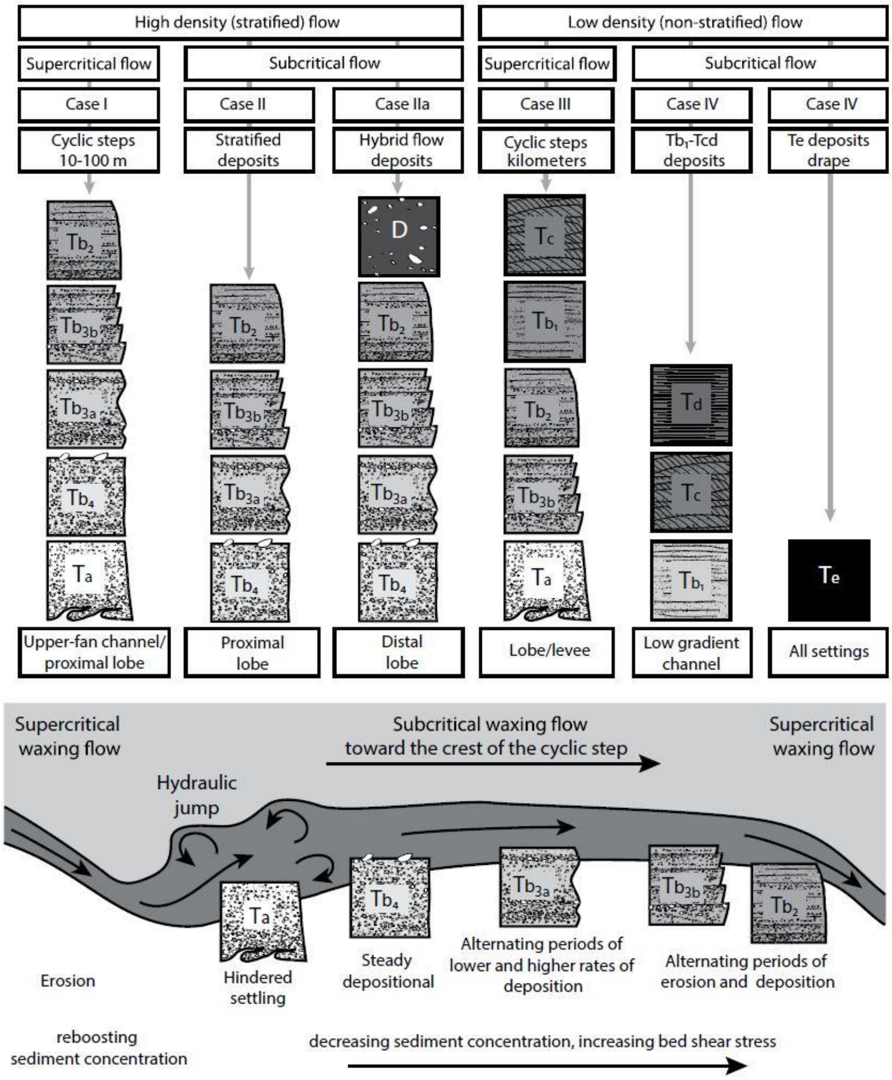

Figure 8 *Facies associations for cyclic step from Postma and Cartigny 2014. Unit legend: Ta = coarse-tail normally graded with flame structures at the base;* Tb_4 *= mainly massive and inversely graded;* Tb_{3a} *= crude stratification;* Tb_{3b} *= spaced stratification;* Tb_2 *= <0.5 cm planar stratification; Tb1= plane bed lamination with parting lineation; Tc = ripples; Td = plane bed of the lower flow regime and Te = hemipelagic fall out; D = debrite. From Postma & Cartigny (2014).*

Under subcritical conditions the fallout rate decrease and flow shear along the bed increases again resulting in increasingly more stratified depositional facies. Sub-critical conditions are initially characterized by straight and tabular traction carpets, the progressive decrease in flow velocity led to the successive deposition of plane bed lamination (Bouma Tb) and climbing ripple sets (Bouma Tc) (Postma et al., 2009) (Fr<1 in Figure 7).

It has been observed that the progressive increase of this basal density (i.e increase in the fallout rate) causes the downward expansion of the supercritical flow domains and a progressive lowering of the stability field of plane beds into zones of lower velocity, where flows with very low or null fallout rate would form dunes and ripples (see also Arnott, 2007). As a consequence, according to the degree of stratification of the flow and the flow regime, different associations of facies are produced. This is exposed in a synthesis of the facies associations related to the combination of different degrees of stratification with sub- or supercritical flow regime (Postma & Cartigny, 2014) (Figure 8). This scheme is mainly based on cyclic steps that, differently from antidunes, are characterized by a series of hydraulic jumps occurring in the troughs of the undulations producing massive sandstone deposition. This scheme also highlights the importance of the bypassing turbulent upper layer, testified by the absence of a fine-grained portion in the deposit of high-density stratified flow (Figure 8).

The importance of the bypass process during the occurrence of hydraulic jump in stratified flow has recently been observed through field investigation of a saline gravity current in the southwest Black Sea (Dorrell et al., 2016). Field observations suggest a newly identified type of hydraulic jump, that is a stratified low Froude number (Fr'= 1.5–2) subaqueous hydraulic jump, with an enhanced ability to transport sediment downstream of the jump (Figure 9c), in comparison to hydraulic jumps in other subaerial and submarine flows (Figure 9a-b). Differently, this type the hydraulic jump occurs in the lowermost component of the flow while there exists an uppermost component of the flow that bypasses above it (Figure 9c). This mechanism of maintained sediment transport capacity is opposed to current models that suggest that downstream of a hydraulic jump flows are strongly depositional (Postma et al., 2009; Symons et al., 2016). The same process was previously theorized by Mutti (1992) that associated the bypass process following the hydraulic jump with a peculiar facies association that will be extensively described in the following chapter.

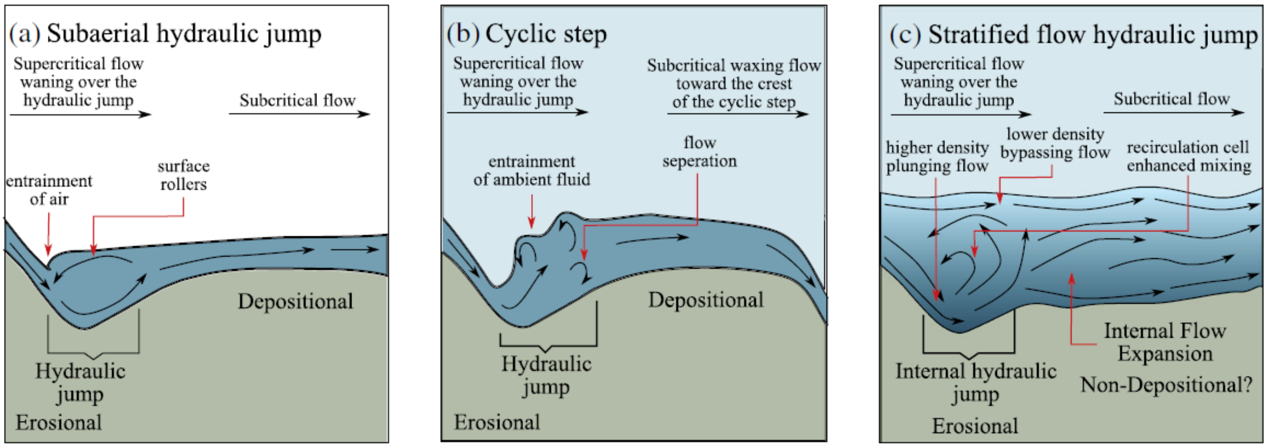

Figure 9 *Sketched behaviour of different types of hydraulic jumps in different environments, including: (A) open channel flow; (B) cyclic steps; (c) stratified subaqueous. From Dorrell et al. (2016).*

4. Reference facies scheme and recent revisitation

The facies analysis of this work is based on the facies scheme of Mutti et al. (2003) (Figure 2b), resulting from the re-elaboration of previous facies schemes (Mutti and Ricci Lucchi, 1972, 1975; Mutti, 1992). This facies scheme is based on the facies tract concept, which represents an ideal genetically-linked suite of facies, deposited by the downcurrent evolution of a unidirectional waning and depletive sediment gravity flow. The scheme classifies the turbidite facies according to their principal grain-size population, deposited by a basal dense flow and its overlying low-density turbulent flow. These grain size populations are:

A) boulders to small pebbles

B) small pebbles to coarse sand

C) medium sand

D) fine sand

The coarser A and B populations are mainly transported by the basal overpressured dense flow, medium sand of the C population can be carried by both basal dense and upper low-density turbulent flow, whereas the finest D population is essentially transported as a suspended load within the overlying turbulent flow. In that way, each population is deposited by a well-defined process affecting a well determined part of the turbidite current. The vertical stacking of facies within the same bed in a specific location is named facies sequence and represents the time evolution of the turbidite current at a given point.

A short overview of each facies will be described below.

Facies F2 is made of an immature, very poorly sorted paraconglomerate, in which larger clasts are dispersed throughout a finer matrix made of gravel, sand and mud. It’s deposited by an hyperconcentrated flow (as meant by Mutti, 1992) or an overpressured dense flow (as meant by Mutti et al., 1999) that results from the downslope transformation of a cohesive debris flow through progressive mixing with ambient fluid.

Facies F3 consists of a relatively well-sorted, sometimes inverse-graded orthoconglomerate, mainly made of the grain-sized population “A”. It represents a residual lag, whose lens-shaped deposits tend to pinch over short distances. Usually, it is overlaid by sharp-based finer facies, testifying bypass processes.

Both facies F2 and F3 can be interpreted as being the head and body deposits of a gravelly dense flow, whose erosive capacity can cause erosion of a great amount of mud clasts during its downcurrent motion; the progressive disintegration of these mud clasts can contribute to the increase fine-grained sediments in the overlying turbulent flow.

Facies F4 represents the first deposit of the gravelly high-density turbidite current; in terms of sedimentary structure, it is made of pebbly traction carpets that can be considered the equivalent of the S2 division of Lowe (1982).

Facies F5 consists of coarse to very coarse, poorly sorted massive to poorly graded sandstones. It represents the deposit of high-density turbidite currents able to bypass more proximal areas characterized by F2 and F3 conglomerate deposition. The sediment in this phase is mainly sustained by overpressure, as testified by common water escape structures (Mutti et al., 1999). The erosive power of the head of the flow is testified by erosive and impact structures associated with rip-up of mudstone clasts. The lateral and downcurrent extension of these facies is quite variable, according to the efficiency degree of the systems.

Facies F6 and F7 facies represent bypass facies between dense and turbulent flows. The former is made of well-sorted, coarse-grained sandstone showing megaripples structures, sharply overlaid by a thin level of fine-grained sandstone (named F9) deposited by the tail of bypassed low-density turbulent flows. In that way, the megaripples within F6 represent the reworking structure of the distal part of the F5 coarse sandstone, whereas the overlying sharp passage to the fine F9 facies represents the bypass surface.

Facies F7 represents the deposition by the near bed suspension, namely the basal part of the turbulent flow in which the high rate of fallout is able to suppress the turbulence and cause the formation of coarse to medium-grained sandstone with traction carpets. In terms of depositional processes, F6 and F7 can be seen as facies representing different deceleration degrees of the turbulent flow (Mutti et al., 2003; Tinterri et al., 2003; Tinterri & Tagliaferri, 2015): higher in the former, lower in the latter. F6 and F7 deposits are here interpreted as the result of sudden deceleration of the dense flow, probably forced by subtle depositional topography and favoured by the characteristics of the dense flow, followed by flow expansion and full turbulent mixing associated with the occurrence of hydraulic jump (Mutti et al., 2003).

Those facies can be overlaid by F8 facies made of massive, well-sorted, medium-grained sandstone, testifying the sedimentation rate increase (suspension phase, according to Lowe, 1982) and representing the Ta of the Bouma sequence.

Finally, facies F9 is the most evolved and finest one in Mutti's scheme and is deposited by the low-density tail of the turbulent flow, able to reach the most distal zones of the depositional basin. It is made of traction plus fallout structures (Tb-e in the Bouma sequence), testifying the depletive and wining nature of the flow in the final part of its path.

Mutti's facies scheme represents the suite of facies deposited by an ideal waning and depletive turbidity current, whose space-time evolution is not affected by topographic control. Most of the turbidite basins are strongly involved in syntectonic deformations able to produce topographic "constraints" that can influence turbidite currents dynamics and, as a consequence, the nature and distribution of turbidite facies. In fact, bed slope, bed roughness, and size of suspended sediment affect Froude number by changing the balance between inertial and gravitational forces (Spinewine et al., 2009) that, as previously illustrated, have a direct effect on the sedimentology of the relative deposits. For this reason, Mutti's facies scheme has recently been implemented by Tinterri (2022, in preparation) (see also Tinterri et al., 2023) with further facies subcategories and interpreting them according to the related flow regime (Figure 10). The result of this interpretation derives from turbidite system in tectonically confined foredeeps, such as the upper part of the Marnoso-arenacea formation or the Annot Sandstones in the Peïra Cava basin (Tinterri et al., 2016; Cunha et al., 2017), and in tectonically confined wedge-top basins, such as the Ranzano Sandstones in the northern Apennines (Tinterri et al., 2017), since they are good candidates to be classified as supercritical fans.

The F4 and F5b facies are considered the result of deposition from high-density and supercritical flow. The F5b facies consists of gravel/sandstone with backset laminations and water escape structures.

While F5 (m,f,d,e) facies are characterized by increasing deceleration rates related to the occurrence of hydraulic jump and manifested through intense erosion of the substrate, mudstone clasts and soft sediment deformation as load and water escape structures (i.e dish or pillar).

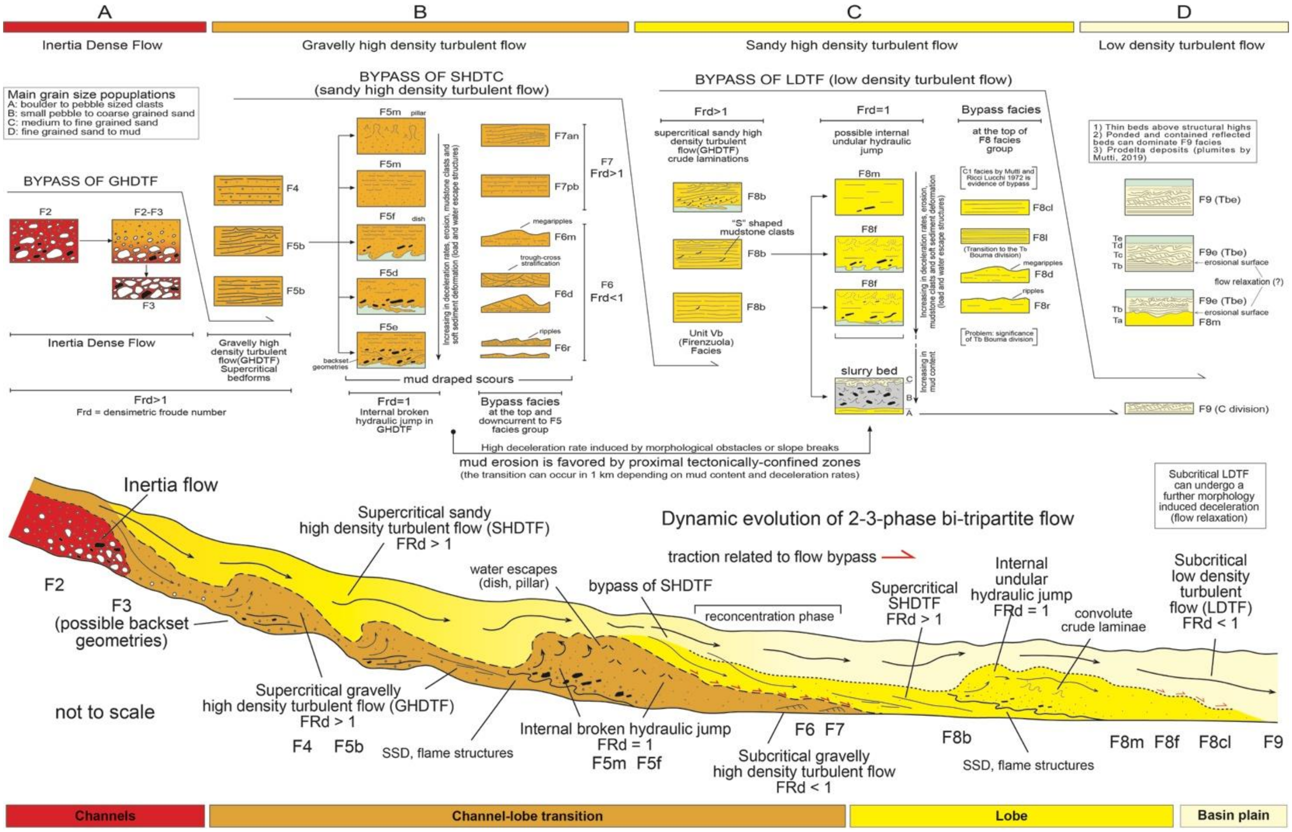

From Tinterri, 2022 (GEOSED-SGI invited presentation, 25 march 2022)

Figure 10 *Framework for a predictive classification scheme of turbidite facies. Each facies is interpreted in term of the relative flow criticality. The main size population (A, B, C and D) are marked with different colours (red, orange, yellow and light yellow). From Tinterri (2022, in preparation; see also Tinterri et al. 2023); the diagrams are inspired from Mutti et al. (2003) and Postma (2011).*

The bypass facies F7 and F6 are found at the top or downcurrent to the F5 facies group. The minor deceleration associated with the deposition of F7 facies results in the deposition of traction carpets (F7pb) and antidunes (F7an) testifying that the flow is still supercritical. Differently, the F6 facies, divided according to their wave-length in dune (F6d), megaripple (F6m) and ripple (F6r), the higher flow deceleration produce traction in the subcritical regime.

Facies F8b presenting crude laminations, backstepping laminations and "S" shaped mudstone clasts are related to the deposition from supercritical sandy high-density turbulent flow. Facies F8 (m,f), characterized by soft sediment deformations, are the equivalent of F5 (m,f,d,e) and represent an increase in deceleration rates that can lead to the occurrence of hydraulic jump.

At the top of the F8 facies group new subcategories consist of piano-parallel (F8cl, F8l) or megaripple (F8d) and ripple (F8r) made of medium sandstone. These facies are devoid of the upper fine F9 facies marking the bypass of the subcritical low-density turbulent flow.

This facies scheme highlights also as hybrid beds may be related to sudden decelerations related to slope changes at different scale that may produce hydraulic jumps (see also Muzzi Magalhaes & Tinterri, 2010 and Tinterri & Piazza 2019).

5. Distribution of supercritical flow deposits and hydraulic jumps in deep-marine sedimentary systems

Although the supercritical flow and the related sedimentary structures had been well known for a long time (Simons et al., 1965; Middleton, 1965; Walker, 1967) and, even though they were generally considered as having low preservation potential, relatively recent works have shown that these structures could be more present in the geological record than we thought to date. In fact, according to Postma et al.(2009), turbidity currents are commonly super critical if they travel on slopes steeper than 0.001 (0.06°). Continental slopes are usually steeper than 0.6° and as high as 4° or more and so turbidity currents in this environment tend to be supercritical. Following the pioneering work of Komar (1971) and Garcia & Parker (1989) the research has tended to focus on the interpretation of supercritical flow deposits in canyons, channels and channel–lobe transitions, where high slope gradients and abrupt morphological transition occur.

Canyons are large and erosional conduits (Shepard, 1981) that initiate sediment transfer from shallow water areas to the deep sea. According to sea-level variations, perturbations in sediment production and redistribution and to variations in accommodation in the shelf (Gamberi, 2020), hyperpycnal flows are funnelled inside canyons located in upper to mid slope settings. Submarine canyons evolve downslope into channels that act as conduits for the transport of sediment to the deeper basin floor (Mutti & Normark, 1987). Slope gradient exerts a crucial control on the densimetric Froude number by changing the balance between inertial and gravitational forces. In general, a steeper slope and thus a higher densimetric Froude number would be favourable for the formation of cyclic steps that effectively are widely recognized in both in canyons (Li et al., 2020; Wynn & Stow, 2002; Zhong et al., 2015) and channel talwegs (Covault et al., 2017; Hage et al., 2018; Spinewine et al., 2009; Symons et al., 2016; Wynn & Stow, 2002) where generally is common to find slope steeper than 0.6°.

Previous authors propose that such upstream-migrating bedforms could play a key role in submarine channel initiation, evolution, and deposit geometries (Covault et al., 2017; Fildani et al., 2006, 2013). Fildani et al. (2006) were the first to interpret a linear series of four giant scour-shaped depressions on the levee back slope outside of the Shepard Meander of the Monterey Channel as net-erosional and net-depositional cyclic steps formed by turbidity currents and to connect their formation to an early phase of channel evolution (Figure 11). In addition, supercritical bedforms inside channel talweg have been connected to the formation and maintenance of upstream migrating knick-points, morphological features that dominate the evolution of a submarine channel. (Heijnen et al., 2020). Recently, has been recognized that the occurrence of instabilities (i.e hydraulic jumps) inside supercritical flows approaching knickpoints could also enhance the amount of overbank flow and so influence the deposition on levees bounding channels (Scacchia et al., 2022).

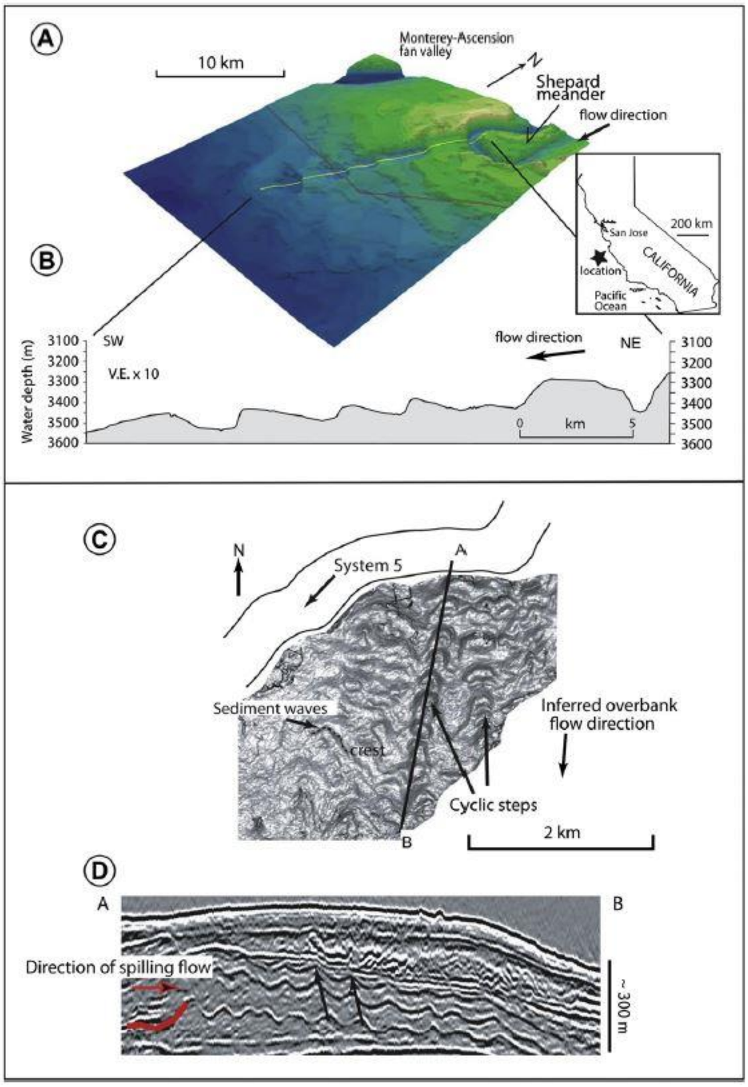

Figure 11 *(A) Shaded relief image of the Monterey East scour-train, associated with overspill on the Shepard Meander. The discontinuous channel floor character of Monterey East is apparent, attributed to cyclic-step erosion. B. Axial bathymetric of the train of scours (C) Surface rendering of cyclic steps obtained from a 3D seismic volume offshore West Africa. (D) Seismic refection profile showing the interpreted cyclic step crests and their up-slope migration. From Fildani et al. (2013).*

The structure of turbidity currents, especially their grain-size and density stratification, is such that in slope environments at least coarse-grained and/or thicker bedded turbidites are largely confined within the negative channel depression, whereas the surrounding overbank regions commonly receive sedimentation from the upper, more dilute portion of the current. For this reason, overbank deposits of submarine channels are typically thin-bedded, fine-grained and predominantly characterized by a series of sedimentary structures interpreted to record a relatively simple history of waning flow (Hansen et al., 2015). Large-scale bedforms adjacent to submarine channels, occurring on levee flanks or depositional terraces, have been documented from seafloor and seismic datasets around the world (Symons et al., 2016). Normark first documents the upslope migration of sediment waves in the six submarine fan system, in particular in the levee environment. The waves presented thicker and coarser beds deposited on the up-current flank of the sediment waves and suggested that upslope migration is enhanced by higher-velocity turbidity currents (Normark et al., 2002). In the following years, an increasing number of examples recognized supercritical bedforms as antidunes (McArthur et al., 2020; Normark et al., 2002; Wynn et al., 2000) or cyclic steps (Cartigny et al., 2011; Kostic, 2014) on levees (Figure 11d).

The transition from the continental slope to the more gently dipping abyssal plain is typically marked by a slope break, i.e. a reduction in slope gradient, which affects the flow dynamics and often results in sediment deposition (Mutti & Normark, 1987). Generally, the slope break coincides with canyon/channel mouths and their downslope transition into depositional lobes. When this transitional area is characterized by abundant erosional features, that may separate sand-rich channel and lobe deposits, it's identified as a channel-lobe transition zone (CLTZ) (Mutti & Normark, 1987). The CLTZ are characterized by large, isolated scours (plunge-pool) or multiple scours, rip-up mud clasts, mud drapes in scours (bypass), coarse-grained supercritical bed forms and attributed them to hydraulic jumps (e.g., Cornard & Pickering, 2019; Fildani et al., 2013; Postma et al., 2021; Wynn et al., 2002).

The CLTZ is continuously evolving in space and time due to the influence of solitary hydraulic jumps at the channel mouth on channel extension and backstepping. Supercritical flows and hydraulic jumps at the channel mouth play an important role in lobe architecture, particularly on avulsion cycles. Three primary phases of the cycle were identified with tank experiment (Hamilton et al., 2015, 2017; Hoyal & Sheets, 2009) and successively recognized in the field (Postma & Kleverlaan, 2018). The initial phase of lobe building is characterized by progradation (green in Figure 12a); 'distal' fan lobe characterized by lobe elements with antidunes and traction carpet deposits (yellow in Figure 12b) is formed by supercritical, high-density (stratified) turbidity currents, deposition ahead of the prograding channel downlaps the prior bathymetry. The second stage consists of lobe aggradation (red in Figure 12a); the distal-fan lobe is truncated by lobe elements of the supra fan. Lobe elements are amalgamated and coarser grained than the distal-fan lobe and characterized by cyclic steps (light brown in Figure 12b), which indicate a higher flow regime compared to the distal

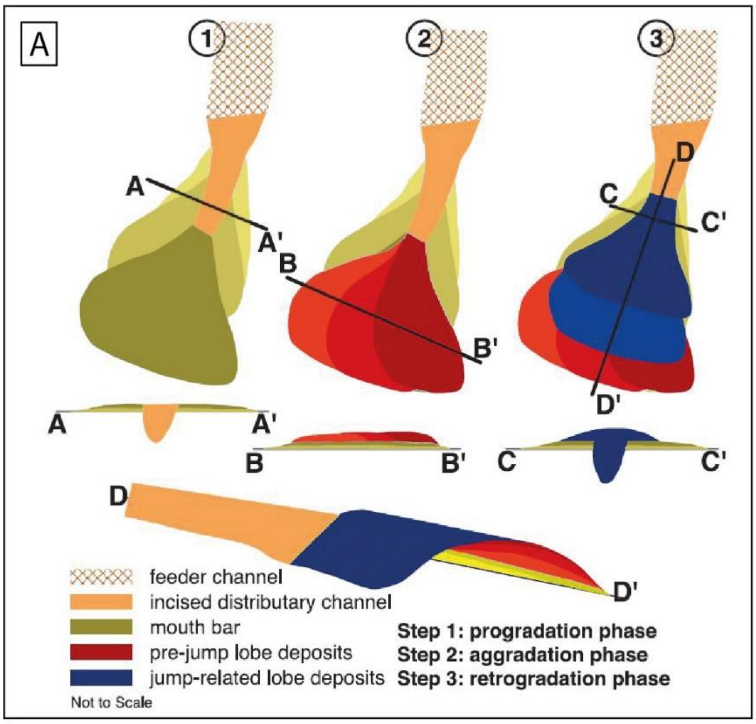

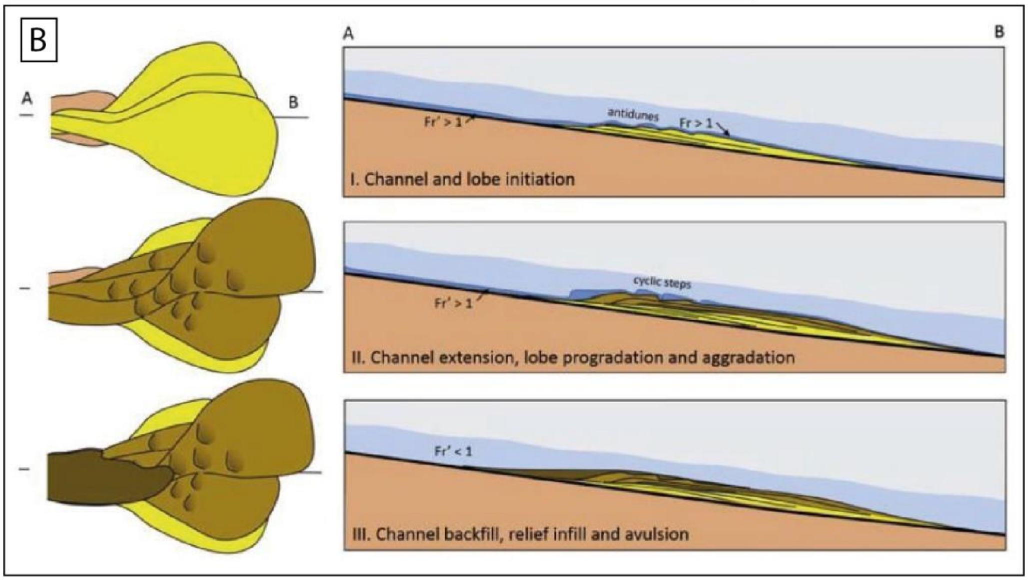

Figure 12 *(A) A schematic of erosion and deposition during a characteristic avulsion cycle composed of three primary phases of the cycle as it applies to the depositional record: (1) progradation, (2) aggradation, and (3) retrogradation. From Hamilton et al. 2017. (B) Sedimentation model from a sand-rich lobe complex. The initial phase of lobe building, characterized by lobe elements with antidunes and traction carpet deposits corresponding to (1). The second stage of lobe building corresponding to the aggradation (2) characterized by cyclic steps. In the third stage, thinning and fining turbidite beds represent the abandonment of the lobe (3). From Postma & Kleverlaan (2018).*

fan lobe deposits. This continues until the bar chokes the approach flow, initiating a hydraulic jump and the transition to the third stage. The third stage creates a retrogradational deposit (blue in Figure 12a) associated with the hydraulic jump. Bedload sediment arriving at the jump from upstream is rapidly deposited in the expanded and decelerated subcritical half of the jump. This process causes the retrogradation of the lobe creating steep backset bedding in the channel. In this stage, the lobe is draped by thinning and fining turbidite beds (dark brown in Figure 12b). This phase terminates with the abandonment of the supra fan lobe due to choking of the channel outlet. According to this model, hydraulic jumps are strictly related to topographic changes of the seafloor, as slope breaks, and consequently to the morphology created by the deposits related to the hydraulic jump occurrence.

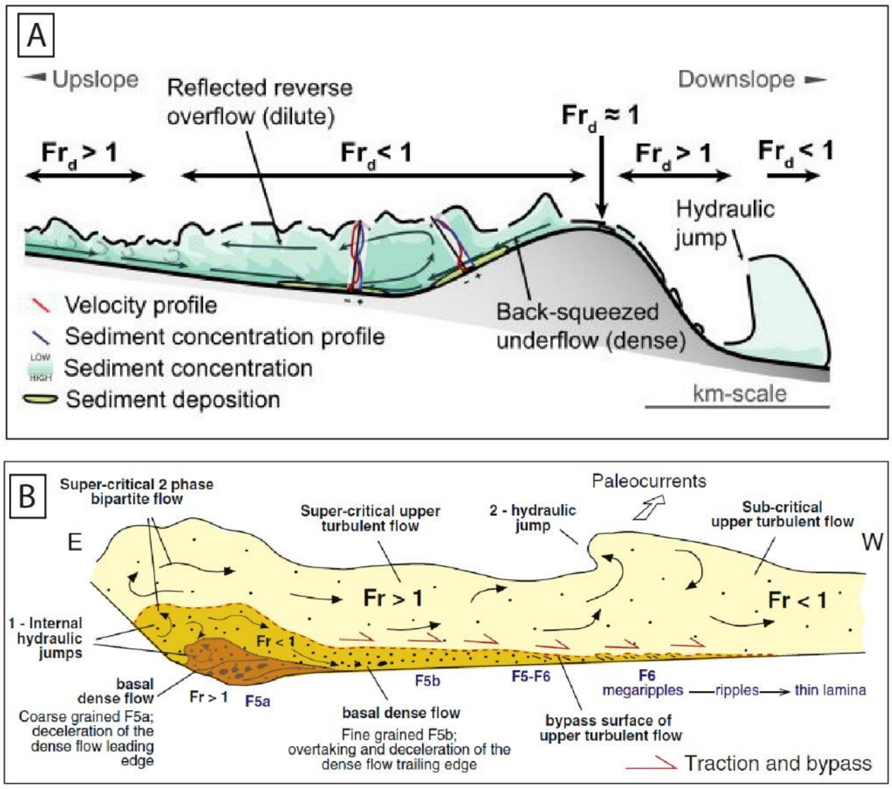

Figure 13 *(A) Schematic longitudinal cross-section summarizing the flow response to a frontal obstacle and related pattern of sediment deposition. Note the hydraulic jump at the fold forelimb. From Howlett et al. 2019 (see also Tinterri et al. 2022). (B) Scheme illustrating processes related to the deceleration of bipartite flows against a lateral obstacle, in which two hydraulic jumps characterizing the dense flow and upper bypassing turbulent flow can be observed. From Tinterri et al. (2017).*

Anyway, topographic changes are not restricted to the area proximal to the slope. Variations in seafloor topography occur also further away from the slope where the lobes expand, in relation to more or less important tectonic features. Nevertheless, very few studies concerning supercritical flow deposits have been carried out in submarine lobe and related environments (Cornard & Pickering, 2020; Piazza and Tinterri, 2020). Although Hamilton et al. (2015, 2017) and Postma and Kleverlaan (2018) showed that supercritical flows and hydraulic jumps play an important role in lobe architecture, relatively little research has considered the hydrodynamic processes in the more distal fan areas. Tank experiment (Soutter et al., 2021) simulated turbidity currents with frontal, oblique and lateral confinement and recognized the occurrence of two styles of topographically-forced transition between supercritical and subcritical flow and a consequent hydraulic jump. Upstream jumps are formed when flows rapidly decelerate upstream of slope topography, resulting in the deposition of thick massive sandstones up-dip of topography. Downstream jumps are formed downstream of topography and are caused by rapid deceleration of flows at the foot of the barrier, with slope erosion occurring at the foot of the barrier as the flow impacts the slope. The prevalence of these jump styles will be greater in deep-water environments capable of producing local and steep slopes e.g., fold and thrust belts and salt-influenced basins (Soutter et al., 2021; Tinterri et al., 2022). This phenomenon has been recognized also through numerical modelling (Howlett et al.,

2019) and in laterally-confined setting related to a peculiar facies tract representing the deceleration of bipartite flows against the margin (Tinterri et al., 2017). Changing the orientation of confining basin topography affects the flow dynamic and so the spatial distribution of the relative deposits. For this reason, investigating submarine lobe environments near tectonic structures could represent a good starting point to fill the knowledge gap about supercritical flow deposits in this environment.

6. Overview of this thesis

In this thesis, a range of different approaches are used in order to accomplish the research objectives consisting in the analysis of the deposits of supercritical turbidity currents and identifying the effects of hydraulic jump occurring in relation to morphological variations of the seafloor. Supercritical turbidity currents are sensitive to morphological variations of the seafloor that are extremely common in areas shaped by active tectonic. Our general aim is to increase the knowledge on this particular type of deposit since still numerous question marks characterize this argument that, nowadays, is principally approached by carrying out tank experiments or numerical modelling. Differently, this thesis approaches three geological cases of study concerning two modern submarine fans and one ancient turbiditic system. The thesis is organized into three principal chapters reporting one case study each. The two modern submarine fans are localized on articulate continental margins, the Acquarone Fan (Chapter 2) and the Amantea Fan (Chapter 3). The study of those modern marine systems have been carried out through the analysis of high-resolution morphobathymetries, subsurface profiles (subbottom chirp) and, in one case (Amantea Fan) sediment gravity cores. While the third case study is an outcrop study on the ancient Paretaio turbidite system (Northern Apennines, Italy), which is presented in Chapter 4.

The first case study (**Chapter 2**) concerns the Acquarone Fan, localized in the Gioia Basin (Southern Tyrrhenian Sea), whose topography is mainly controlled by the presence of the Acquarone structural ridge, which results in the lateral confinement of the left south-west side of the channel-levee system. Seven depositional units (Units I-VII) record the recent depositional history of the fan; their thickness has been mapped and their parent flow types have been interpreted through their seismic response. According to unit thickness maps, two main patterns of deposition are recognized in the overbank area. Their depocenters coincide with different extensive sediment wave fields developed in specific tracts of the right levee and in the frontal splay area. We show that the location of the depocenters varies in time according to the prevalent flow-type and by its interaction with the surrounding seafloor topography and channel planform. We interpret that the lateral confinement of the channel by the structural high generates episodic rebound of the overspilling flow and the inversion of the channel asymmetry. The vertical stratification of the flow strongly influences the overbank deposition where the channel planform has a non-linear shape such as bends and knick-points. In particular, the vertical stratification influences the hydraulic jump size that conditions the amount of overspill and thus the location of overbank depocenters. This study highlights that variations in the sediment distribution and composition on the overbank can be related to the way different flows interact with the tectonic setting.

In **Chapter 3** is reported the study about a lobe belonging to the Amantea Fan, localized in the Paola Basin (Southeastern Tyrrhenian Sea) an example of ponded basin frontally-confined by the Paola Ridge. The interpretation of seismic profiles highlighted that the lobe, generally presenting a high-reflectivity, is characterized by different seismic facies changing in relation to the seafloor topography. In particular, the lobe resulted to be composed of erosive and depositional bedforms in the steep upper basin floor, tabular beds in the flat basin floor while decrease in thickness and gradually pinches out above the Paola Ridge. Great attention have been given to the bedforms area where erosive scours and upslope migrating bedforms occur. Gravity cores sampled in the through of one of the scours revealed the presence of sedimentological facies associated with the action of supercritical flow (coarse-grained traction carpets) and hydraulic jump (such as massive and amalgamed sandstone with flames structures), being thus been interpreted as erosional cyclic steps. While the sample acquired on stoss side of one of those bedforms present prevalently facies associated to the action of subcritical flow (top-cut-out fine-grained sandstone with tractive structures), generally associated to the subcritical phase after the jump occurring in cyclic steps. At the toe of the Paola Ridge, tabular beds have been sampled, and resulted to be composed of medium-grained massive sandstone with soft sediment deformation possibly associated with the occurrence of a hydraulic jump induced by the decelerating flow impacting of the surface of the ridge. This work highlights the importance of topography for the distribution of different depositional elements and provides the sedimentological characterization of supercritical bedforms in a submarine lobe.

The last case study (**Chapter 4)** focus on the two depositional lobes of the Paretaio Turbidite System in the Marnoso-arenacea Formation (northern Apennines, Italy). This system was laterally confined by an important regional structure NW-SE-oriented, namely the M. Castellaccio thrust-related fold.

This study was carried out by combining a classical fieldwork-based sedimentological approach and a laboratory-based approach performing grain-size analysis on a large number of samples. Field data derive from a high-resolution physical stratigraphy, with bed-by-bed correlations, resulting in a high-resolution correlation panel oriented parallel to the paleocurrents. The stratigraphic cross section highlights that subtle topographical variations, probably related to faults associated with the M. Castellaccio thrust. The bed thickness analysis points out that faults where syndepositional and active tectonics influenced the paleo-topography of the seafloor creating a depression in the central sector. Detailed sedimentological facies analysis reveals that small-scale sedimentological variations occur in relation to these subtle topographic variations. In particular, sedimentological evidences highlight that both hybrid and turbidite beds possibly underwent hydraulic jumps in the transition between the morphologic high and the depocentre. In hybrid beds this phenomenon is revealed by an increase in the depocentre area of the fine-grained fraction in the slurry unit related to the decrease in transport capacity of the flow after the jump. Turbidite beds show characteristic facies previously associated to the action of supercritical flows (coarse-grained traction carpets or backstepping laminations), hydraulic jumps (structureless facies with soft sediment deformations or mud-draped scours) and bypass (medium-grained sandstone with tractive structures) of the upper dilute fraction. Our work shows that, according to the degree of stratification of the flow, turbidity currents respond in a different way to subtle morphological variation as testified by small facies changes occurring over short distances.

Chapter 2

"The influence of channel planform and slope topography on turbidity current overbank processes: the example of the Acquarone Fan (Southeastern Tyrrhenian Sea)"

Published article

Authors: Scacchia E., Tinterri R. and Gamberi F.

Journal: Frontiers in Earth Science

Volume: 9

Published on: 10 January 2022

DOI: https://doi.org/10.3389/feart.2021.785164

1. Introduction

Turbidity currents are one of the primary mechanisms for sediment transport to the deep-marine environment and their deposits represent the fundamental building blocks of submarine fans. During part of their path, turbidity currents flow within submarine channels, the principal conduits for the transport of sediment from the shelf to the basin floor (Mutti & Normark, 1991). When the thickness of the turbidity current is greater than the channel depth, the upper part of the flow can escape the channel's confinement and relatively fine-grained sediment settles beyond the channel banks and built overbank wedges (Piper & Normark, 1983).

The internal architecture and the distribution of lithologies in submarine fans and their control on the distributions of reservoir properties is fundamental information for petroleum exploration and for the advancement of the techniques for Carbon Capture Storage (CCS). As a consequence, the overbank depositional setting has recently become the focus of growing attention, since thin-bedded turbidite layers composing overbank wedges can be extremely laterally continuous (Hansen et al., 2015; Peakall et al., 2000) and contain large sand volume. As an example, a net to gross value >50% has been reported in the Cretaceous San Fernando slope channel system of the Rosario Formation in Mexico (Hansen et al., 2015). In addition, a knowledge of the processes inherent with turbidity current behaviour is fundamental for the study of the fate of pollutants, plastics and microplastics in the marine realm (Zhong & Peng, 2021). Notwithstanding these issues with important applied outcomes, many aspects, related to turbidity current behaviour in overspilling submarine channels, remain one of the least well understood sedimentary processes.

The trends of lateral decay of levee, sand bed thickness and sand percentage transverse to the channel are thought to be predictable, and to follow power law, logarithmic or exponential decay according to the regional slope (Birman et al., 2009; Kane et al., 2010; Nakajima & Kneller, 2013). On the contrary, downslope trends in sediment distribution are less constrained. In general, levee construction involves the progressive downflow loss of fine-grained material that results in the downslope thinning of overbank wedges and increase in their sand content (Hiscott et al., 1997; Posamentier & Kolla, 2003).

However, the seafloor morphology can affect the behaviour of a turbidity current in several ways: it can halt the flow or change its velocity and alter its pathway (Kneller, 1995; Patacci et al., 2015). Those changes leave a footprint in the sedimentation pattern and in the facies and lithology distribution in submarine fans and the predictivity of those simple models can be drastically altered. The response of turbidity currents to slope topography has been investigated through several case studies specifically concentrating on their final depositional sites, corresponding to terminal lobes (Pickering and Hiscott, 1985; Haughton et al, 1994; Amy et al., 2005; Remacha et al., 2005; Gamberi et al., 2008; Tinterri and Muzzi Maghales, 2011; Tinterri and Piazza, 2019) and confirmed by experiments (Kneller et al., 1991; Kneller et al., 1995; Haughton et al., 2004; Amy et al., 2005; Patacci et al., 2015; Howlett et al., 2019). In contrast, few studies so far have linked the development of the overbank area of leveed channels to seafloor topography (Tek et al., 2021).

Information about the variation of sediment distribution over time can be used to reconstruct changes in the flow proprieties. Such reconstructions can be valuable for comparison with the trends expected from the application of existing models. In addition, studies on the modern seafloor, tied to well-known morphological contexts of deposition, can be vital for unravelling the effects of seafloor topography on sedimentation. This approach is used in this study focused on the overbank wedges of the Acquarone Fan, a deep-sea fan located in the continental slope of the Gioia Basin in the southeastern Tyrrhenian Sea. The study area has a complex physiography, mainly controlled by the presence of the Acquarone structural ridge, which confines the south-west side of the channel-levee system.

The objectives of this work are: a) integrate bathymetric and seismic data to characterize seafloor morphology and the stratigraphic architecture of the last 40 m of the sedimentary succession; b) provide a detailed analysis of sediment thickness distribution on a submarine channel overbank area. The final purpose of our study is to investigate the effects of topographic features, resulting from tectonic processes, on overbank deposition. In particular, with the examination of overbank processes in a topographically complex slope, we aim at highlighting the divergence from the established models of overbank sedimentation in simple slope settings.

In general, our results expand our understanding of overbank flow processes and show that, particularly in active continental margin, many factors, mostly extrinsic to the turbidite system, contribute to the final fate of sediment within leveed channels.

2. Geological setting

The Acquarone Fan is located in the southern part of the Calabrian sector of the Gioia Basin, an intraslope basin in the southeastern Tyrrhenian Sea (Figure 1a). The Gioia Basin formed in response to the backarc extension associated with the Ionian-Calabrian subduction zone, which started in the Late Miocene (Fabbri et al., 1980; Gamberi and Marani, 2006). Since then, the Gioia Basin has been affected by major NE–SW, N–S and E–W trending extensional faults (Fabbri et al., 1980; Casas et al., 2016). The Acquarone Fan developed in the depocenter of the Calabrian sector of the Gioia Basin, a semi-graben created by the past action of a NW-SE-trending, NE-dipping extensional fault (Figure 1c). Since the Middle Pleistocene, the physiography of the basin has been mainly controlled by the recent tectonic deformation, associated with high rates of vertical movement, also affecting the Sicilian and Calabrian mainland.

The submarine expression of the high rates of uplift of the basin margin is particularly evident in the Sicilian sector, where seafloor instability resulted in an extensive mass-transport complex (Gamberi and Marani, 2006; Gamberi and Rovere, 2011; Rovere et al., 2014; Gamberi et al., 2019) (Figure 1a). In the Calabrian part of the basin, tectonic unrest is shown by the presence of structural ridges that are also affected by large collapses (Gamberi and Marani, 2006; Casas et al., 2016; Casalbore et al., 2019). The Acquarone Fan is bounded to the south by the Acquarone high, a structural ridge that represents the submarine continuation of the Castanea ridge (Figure 1a) (Gamberi et al., 2011), an uplifting area (1.1 mm/y) on the Peloritani Mountains (Catalano and Di Stefano, 1997; Antonioli et al., 2006). Evidence of the recent tectonic activity is given by the presence of fluid escape features

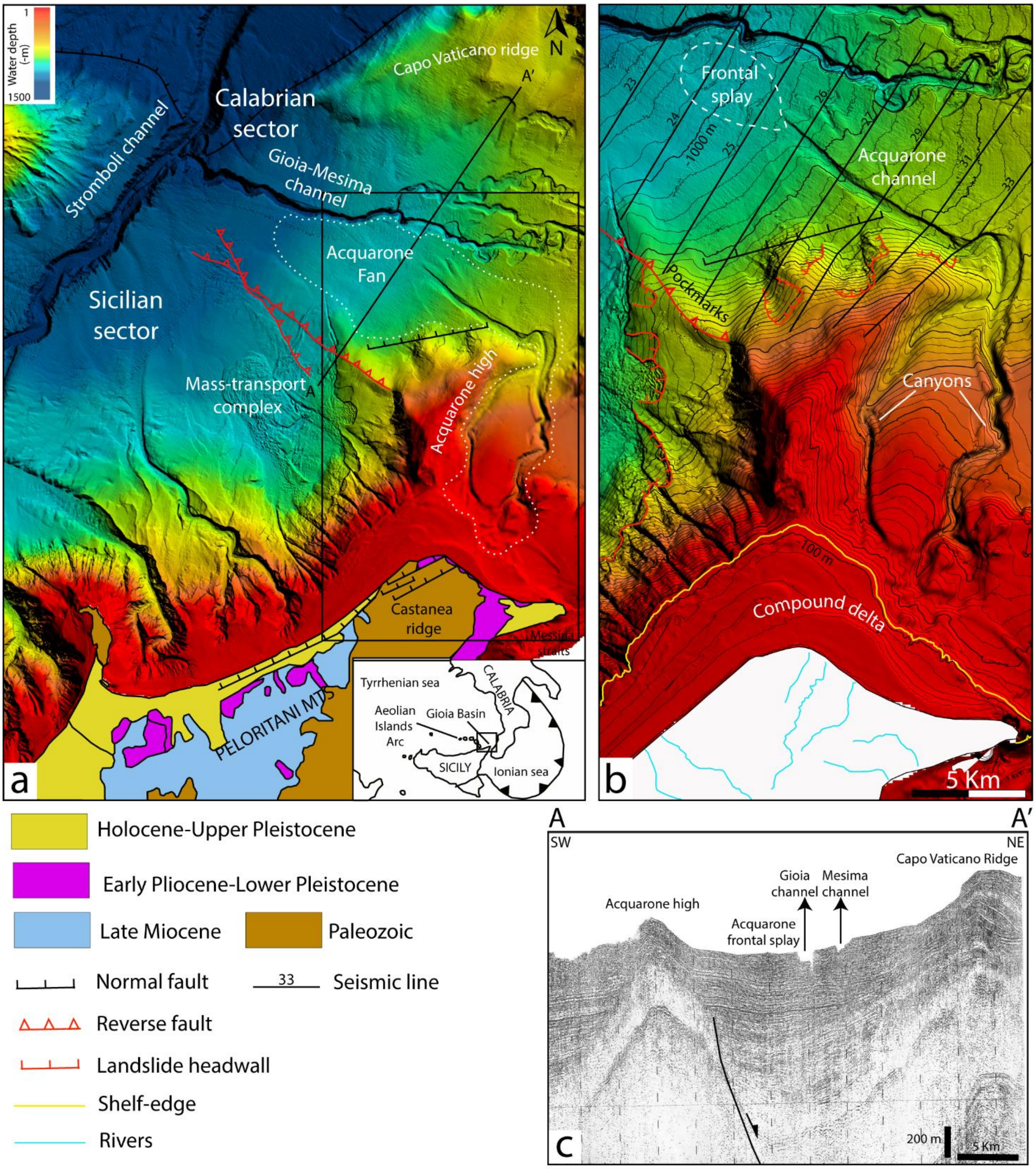

Figure 1 *(A) Shaded relief map from multibeam bathymetric data of the Gioia Basin and geological map of north-eastern Sicily (Gamberi et al., 2011). (B) Zoom of the study area (box in a) over a bathymetric map with 20 m contour and location of the available seismic lines. Two submarine canyons feed the Acquarone leveed channel and its frontal splay (dashed white line). (C) Strike airgun seismic profile (location in A) of the northern part of the Gioia Basin. The Acquarone frontal splay is between the Gioia-Mesima channel system and the Acquarone ridge.*

(pockmarks) at the seafloor in connection with a transpressive fault (Rovere et al. 2014) (Figure 1a). An extensional fault crosses the base of the Acquarone high with a W-E direction in a sector highly affected by mass-wasting processes (Gamberi et al., 2019) (Figure 1a, b). The Acquarone fan develops southward from the Gioia-Mesima channel, a tributary to the Stromboli channel (Figure 1a). The Gioia-Mesima channel has undergone a complex evolution a complex evolution shown by abandoned meanders incised by a straight course due to base level deepening associated with the erosion and deepening of the Stromboli valley (Gamberi and Marani, 2008; Gamberi et al., 2019). The Acquarone Fan develops in the ENE-dipping slope and reaches a water depth of 1000 m. The fan is fed by two submarine canyons (Figure 1b). The eastern canyon-head is at a depth of 90 m on the shelf edge and is 2.8 km off the coast; the western canyon head is at depth of 120 m and 5.3 km off the coast. On land, a small subaerial drainage basin of about 13 km2 in the Paleozoic terrain of the Castanea ridge flanks the canyon head (Figure 1a). In these mountainous, tectonically active and uplifting catchments, rivers are incisional features with high gradient, torrential discharges and high sediment yield (Regione Siciliana, 2006). At present, the sediment load is ultimately deposited on the continental shelf where is interpreted to be resuspended by longshore currents and rearranged into an asymmetric compound delta (Figure 1b). The compound delta, in its apex position, is only 700 m from the shelf edge and is in front of the eastern canyon head.

3. Influence of external factors on the Acquarone Fan

Like the majority of submarine fans in tectonically active continental margins, the Acquarone Fan is a small turbiditic system: from the canyon head to the edge of the frontal splay it is 33 km long and is 8 km wide at the most. Its limited lateral extension is due to the topographic confinement caused by the Acquarone high to the south and the presence of the Gioia-Mesima canyon-channel system to the north.

3.1 Confinement by the Acquarone high

The Acquarone channel is bounded to the south by the Acquarone high, which stands out for about 900 m from the surrounding seafloor. The Acquarone high confines the proximal tract of the channel-levee system to its west preventing the construction of a levee in the left channel side down to a depth of 810 m (Figure 2). Moreover, the presence of the Acquarone high has “forced” the channel to develop a bend that steers the channel pathway from the N–S direction of its proximal sector to the NW–SE pathway of its distal sector (Figure 1b, Figure 2). Further downslope, the confinement gradually decreases resulting in a partially confined area which extends until a water depth of 880 m, where the channel-levee system is no longer confined (Figure 2). The Acquarone high also controls the distribution of mass-transport deposits (MTDs), since, according to the seafloor reflectivity, recent collapses occurred on its flanks (Figure 2) (Gamberi and Marani, 2008). The recent MTDs are localized in the Acquarone channel thalweg, downslope from the meander, and on the surface of the left levee in the partially confined area (Figure 2).

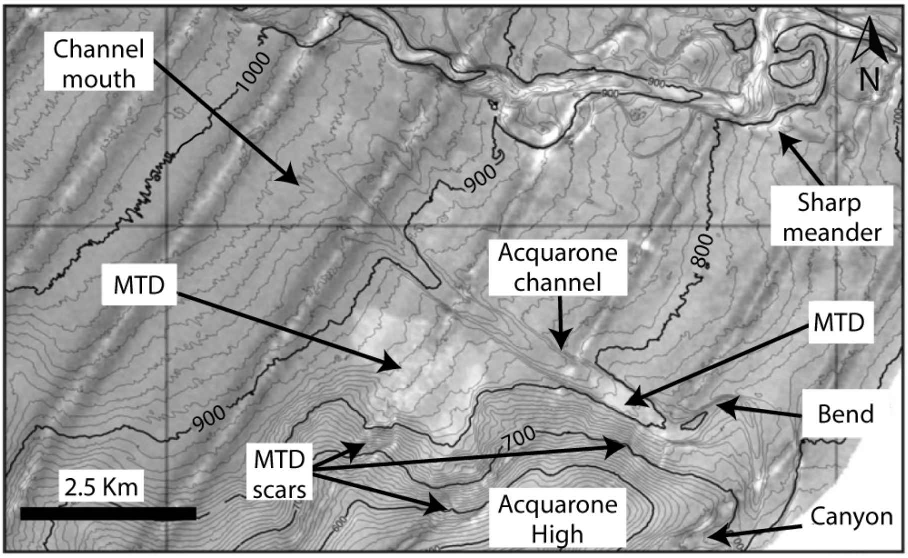

Figure 2 *Sea floor reflectivity image of the Acquarone Fan and of the portion of the Gioia channel to the north, draped over a bathymetric map with 10 m contours. The floor of the Acquarone channel shows mainly a low backscatter, with high backscatter only near a slide deposit (MTD) at the base of a scar on the flank of the Acquarone High. The lobate sea floor mound with high backscatter south of the Acquarone channel represents accumulation of slope-waste deposits derived from the Acquarone High. The Gioia channel floor shows patches of high backscatter, indicating recent activity. (Modified from Gamberi and Marani, 2008).*

3.2 The proximity to the Gioia-Mesima channel

The leveed Gioia-Mesima channel system limits the Acquarone Fan to the north and act as its base level (Figure 1a). Thus, the Acquarone Fan is an example of a transient fan, i.e. those fans that store part of the sediment but are connected to a deeper depositional area (Adeogba et al., 2005; Gamberi and Rovere, 2011). The distance between the Acquarone and the Gioia channels decreases downslope: the Gioia channel is 8 km far from the Acquarone channel bend and 3 km far from the Acquarone channel mouth (Figure 2). The interaction with other channels is one of the possible factors complicating thickness and sand distribution in external levees (Hansen et al., 2015). The Gioia–Mesima channel is principally characterized by erosional processes (Gamberi and Marani, 2008) as shown by an incision of about 80 m. Said incision is consistent with the erosional deepening of the Stromboli Slope Valley that lowered the base level of the Gioia-Mesima channel, which became strongly entrenched and straight (Figure 1a). Moreover, the overspilling clouds, flowing from east to west, preferentially deposit on the right-side of the Gioia-Mesima channel, and therefore the left overbank splay is exclusively alimented by the high-momentum spill-over process near a sharp channel meander (Figure 2) located 7 km far from the Acquarone channel bend

(Gamberi and Marani, 2008). The sediment starvation of the left overbank splay of the Gioia-Mesima channel is confirmed by its low backscatter compared to the channel floor (Figure 2). All these observations suggest that the proximity of the Gioia-Mesima channel does not represents a bias for the quantification of the sedimentary budget on the Acquarone overbank area.

4. Data & Methods

Multibeam bathymetric data and high-resolution seismic data, imaging the Acquarone Fan in its whole length, represent our primary dataset. The major part of the study area is covered by a digital high-resolution terrain model. The latter consists of a mosaic of multibeam data acquired during two surveys carried out in 2013 and 2014 (CAT13 and MARBEEP14 respectively) on board the R/V Urania with the multi-beam system Kongsberg EM710 (frequency 70-100 kHz). In general, given the frequency of the multibeam instruments and the depth range of the study area, the bathymetric data have a vertical resolution less than 0.5 m. The acquired data cover depths between 300 and 1300 m and has been merged with the EMODnet Project bathymetric data available for the shallower areas. High resolution subbottom data consists of Chirp profiles, acquired in 2013 with the Chirp Benthos III technology (frequency 2-7 kHz). Vertical resolution of the seismic profiles is in the order of 0.5 m. The Chirp sections, spaced at about 2 km, cut perpendicularly the Acquarone Fan, from the leveed channel to the fan fringe (Figure 1b). The penetration of the Chirp profiles depends on the type of sediment, being inversely proportional to sediment grain size and compaction. The multibeam bathymetric data was imported and analysed using the Global Mapper® software for the production of contour and slope maps, channel and levee longitudinal profiles and cross-sections of the sediment waves. Sediment wave wavelength is calculated as the distance between two consecutive troughs, whereas wave heights as the distance from the wave crest to a straight line connecting two consecutive troughs (Figure 3). Following Symons et al. (2016), the cross-sectional shape of a sediment wave was defined as upslope asymmetric, when the downslope limbs are longer and shallower (Figure 3). Accordingly, when the downslope and upslope limbs are even, sediment waves are classified as symmetric (Figure 3). The principal overspilling flow direction is assumed perpendicular to the local orientation of the sediment wave crests (Normark et al., 2002). In particular, for crescentic forms the flow direction is assumed to be parallel to the principal plane of curvature of the bedform, whereas for sinuous bedforms the flow direction is assumed to be at 90° from the line connecting to two subsequent inflections in the crest of the sediment wave (Figure 3). The Chirp profiles allowed us to recognize seven units (I-VII) in the last 40 m of the

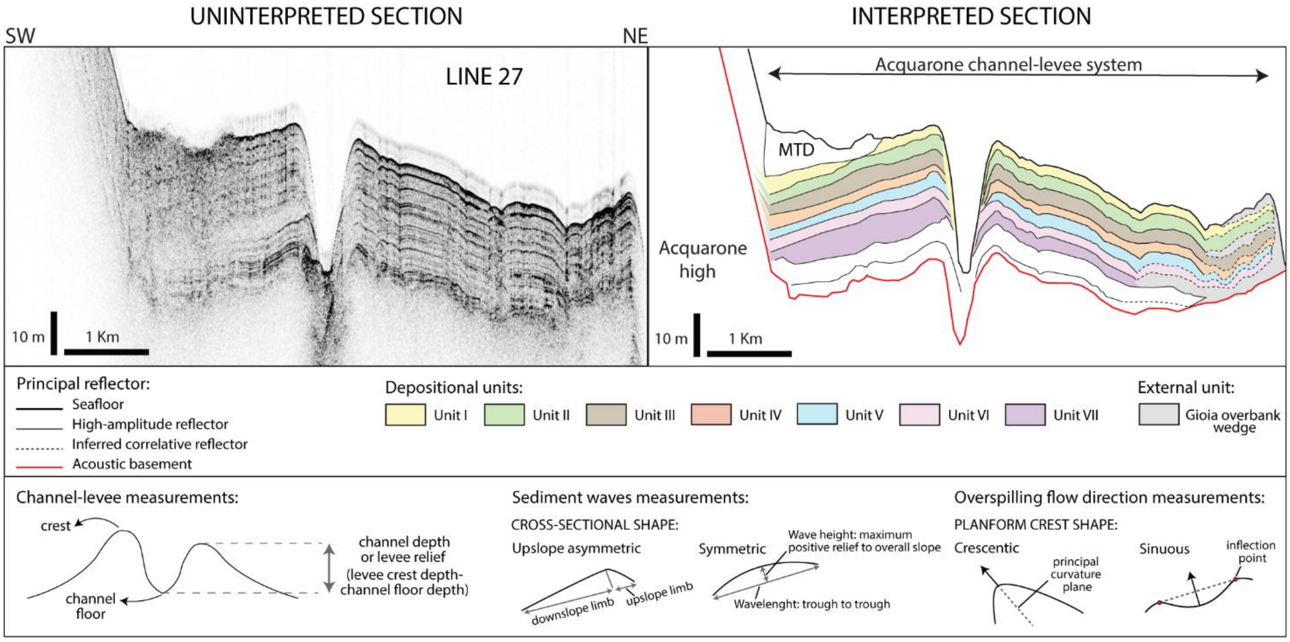

Figure 3 *To the left the uninterpreted seismic section (location on Figure 1B), to the right the interpreted line drawing of the principal reflector that have been traced across the study area and the units comprised between them. At the bottom of the image, sketches about the methodologies applied for the measurements of channel-levee elements, sediment waves morphological parameters and overspilling flow direction.*

sedimentary succession (Figure 3). The boundary of the units correspond to high-amplitude reflectors, which can be followed throughout the study area. Each unit consists therefore of a coherent set of turbidites deposited, during a specific time interval, by successive flows in the different environments of the Acquarone Fan. As such, our units correspond with depositional packages deposited during discrete time interval and have a chronostratigraphic meaning. Owing to the correlatability of the units throughout the study area, spatial variations in sedimentary processes can be observed, through seismic facies and thickness analysis. In particular, the thickness distribution of the units is represented in isopach maps, which are useful to pinpoint and visualize the successive phases of construction of the Acquarone Fan. Moreover, based on the reflection character in the subbottom profiles, we defined five acoustic facies. The spatial-temporal changes in facies distribution, reconstructed from the comparison of the detailed facies maps of the seven units, are the key for interpreting sedimentary processes.

5. Morphology of the Acquarone Fan

Based on interpretation of the multibeam bathymetric data, the morphology of the depositional environments of the fan will be presented.

5.1 Channel

The Acquarone leveed channel has formed at the slope base, at a water depth of about 750 m, at the junction of the two tributary canyons in the upper slope (channel initiation in Figure 4a). The two canyons are confined within a depression that cuts the slope of the Acquarone High. The Acquarone channel exits the depression confinement and makes a wide westward turn taking up a NW course, perpendicular to the slope gradient. The channel has an average gradient of about 1°, but it displays several variations in gradient as shown by its long profile in Figure 4b. Also the channel depth, calculated as the relief of the levee crest with respect to the channel floor for each levee (Figure 3) shows large variations (the red line refers to the right levee and the light blue line to the left levee in Figure 4b). The deepest tract of the channel is in its confined part, where, in the bend, the channel depth increases reaching its maximum of almost 60 m (section 1 in Figure 4b). The channel profile in the confined tract is affected by a recent MTD, whose topographic effect causes a drastic reduction in the channel height (section 2 in Figure 4b). At the beginning of the partially confined area, the channel depth gradually decreases to 30 m (section 3 in Figure 4b). The central tract of the channel profile has two knick-points, named KP1 and KP2, that are, respectively, 7 m and 11 m high (Figure 4b). At KP1 the channel gradient halves abruptly, while the gradient difference in KP2 is less sharp (Figure 4c). Along the flat segments of the knick-points the channel depth increases (section 4-5 in Figure 4b, c). Knick-point initiation has been linked to different processes: channel avulsion (Deptuck et al., 2007), bend cutoff (Sylvester and Covault, 2016), internally generated within channels (Heijnen et al., 2020) or tectonics (Heiniö and Davies, 2007). In the Acquarone channel there is no evidence of channel avulsion and knick-points are located far from the bend. Also the internally generated origin has been excluded since it have been recognized in a prevalently erosional channel where turbidity currents originate knick-point far higher (about 20 m) and steeper (10°-30°) than the knick-points in the Acquarone channel (Heijnen et al., 2020). Accordingly with the interpretation of Gamberi et al. (2019), the origin of the knick-points in the Acquarone channel can most likely be ascribed to the tectonic framework. This thesis is supported by KP1 which represent the prosecution of an extensive fault that cross the base of the Acquarone High (Figure 4a). Moreover, the alternation of ramp and flat segments related to the channel profile is in phase with the gradient variation in the levee crest profiles (Figure 4c). This configuration shows that the topographic displacement is not localized in the knick-points, but it is laterally continuous and, therefore, conceivably connected to allogenic, tectonic processes.

5.2 External levees

The right and left levees are very different in terms of their extension, relief and distribution of sediment waves. The left levee is 6 km long, it begins at a depth of 800 m, downslope from the Acquarone ridge slope and terminates at a depth of 950 m (Figure 4a). On the contrary, the right levee bounds the channel for its whole length, i.e. 14 km (Figure 4a). In its proximal tract, the left levee is about 15 meters higher than the right one (Figure 4b). The difference between the relief of the two levees decreases downslope and, at the end of the confined tract, at a depth of 900 m, the two levees have the same height (Hdx=Hsx, in Figure 4). Beyond this point, the left levee has a lower relief than the right one (Figure 4b).

Extensive sediment wave fields develop in specific tracts of the right levee (Figure 5). According to the classification of Symons et al. (2016), based on wavelength and amplitude, they fall into the group of small-scale sediment waves (<300 m wavelength and <8m wave height) but, at the small scale, the sediment waves have different dimensions and cross-sectional shapes resulting in highly different morphologies. They have been subdivided into different sediment wave fields, according to their wavelength, wave height and spreading direction, occupying different areas (Fig. 5a, b): A) Bend area: the outer side of the bend on the right levee; B) Laterally confined area: a lobe-shaped area on the right-levee; C) Knick-points area: a triangular shaped area with upslope apex on the levee crest laterally to KP1 and termination at the end of the channel.

The Bend area presents sediment waves spreading out from the outer side of the bend (Figure 5a). The crests are parallel to the bend suggesting that they were formed by the spreading of high-momentum spillover flows. In cross-section, they are upslope asymmetric, with amplitude and wavelength that reach a maximum of 3 m and 300 m respectively; they become symmetrical, smaller and more closely spaced downslope, suggesting a rapid loss of momentum (Profile A-A’, Figure 5b). Moreover, the seismic line 33, that cross perpendicularly part of the bedfroms, highlights that the sediment waves in the Bend area show an initial slow up-slope migration followed by a more aggradational phase, with almost no change in trough and crest position (Profile A-A’, Figure 5b).

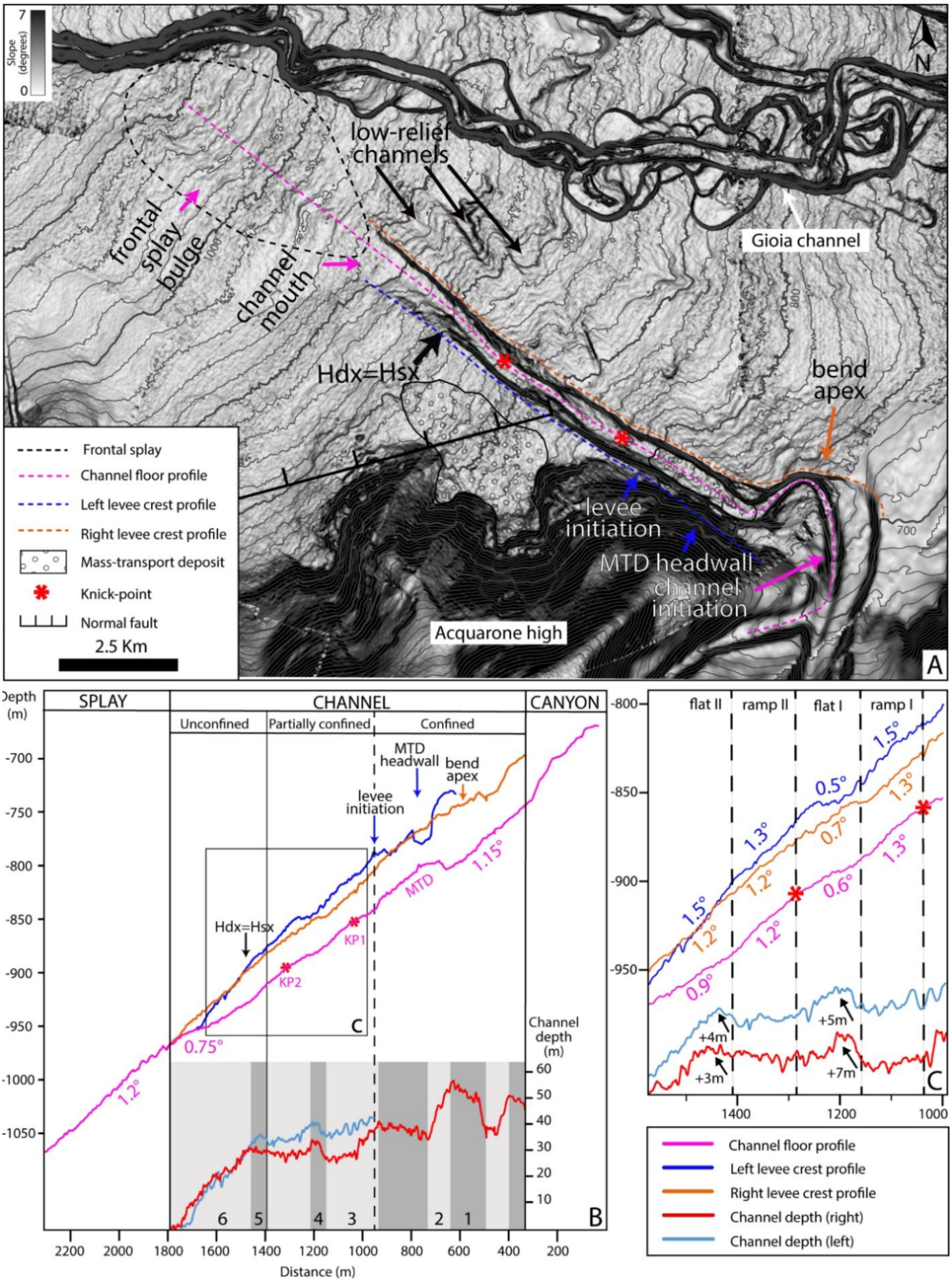

Figure 4 (A) Shaded relief map in BW colours that highlights the principal morphological features of the seafloor marked by arrows. (B) Acquarone channel talweg (pink), right levee (orange) and left levee (blue) longitudinal depth profiles. At the bottom, the channel relief referred to the right levee (red) and to the left levee (light blue), the dark grey sections mark where the channel depth tends to increase, while in light grey where it tends to decrease. (C) Zoom of the channel depth and longitudinal profiles in the central sector of the channel with the related slope values.

Further downslope, in the Laterally confined area, the second sediment wave train develops on the right levee (Figure 5a). The trend of the sediment waves crests indicates that, initially, the overbanking flows are parallel to the course of the channel, but they rapidly become orthogonal to the channel trend and follow the slope direction. They have a symmetrical profile and very low relief with an average wave height of 0.9 m and a wavelength of 140 m (Profile B-B’, Figure 5b).

In the Knick-points area, the third train of sediment waves trends subparallel/oblique to the channel axis (Figure 5a). The waves have a symmetrical cross-section and are regularly spaced with wavelength of 150 m, while their amplitude increases downslope from 0.5 m to a maximum of 2 m (Profile C-C’, Figure 5b). The crests have a sinuous planform; within a bedform row, the landward

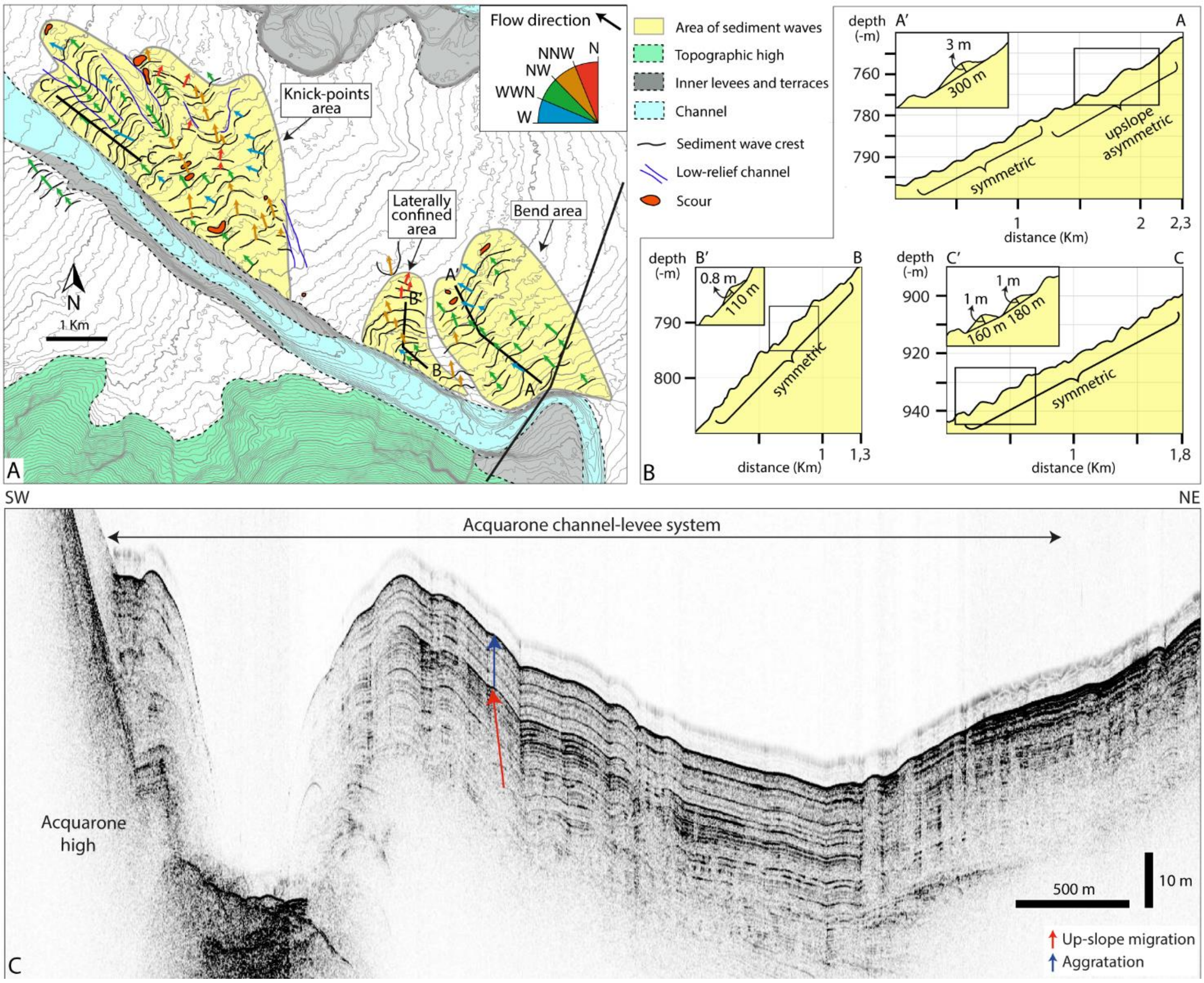

__Figure 5__ (A) Illustration of the three areas of sediment wave fields in the overbank area. For each sediment wave field. Flow direction arrows are coloured to highlight the flow diversions. (B) Bathymetric profiles perpendicular to the crest direction of the waves in the three areas. (C) Chirp line 33 cuts perpendicularly the channel-levee system in correspondence of the meander. In the proximal part of the outer levee it shows the upslope migration of the sediment waves, followed by a more aggradational behaviour.

convex part of single bedforms are in phase and appear to form low-relief, 2-3 km-long channels, with NW-SE direction (Figure 4a).

5.3 Frontal splay

The Acquarone channel dies out in the lower slope forming a frontal splay that has a NW-SE-trending main elongation axis and stretches the slope with a width of 5 km. It has an area of about 28 km2 and laterally and distally passes to a fan fringe area, which occupies most of the remaining slope. The frontal splay has its apex at a depth of 950 m, at the distal end of the channel left levee, and terminates at a depth of 1070 m where the southern flank of the Gioia-Mesima channel is (Figure 4a). The apex of the fan is where the slope gradient increases, from 0.75° in the distal tract of the channel, to 1.20° (Figure 4b). Just beyond the channel mouth, the frontal splay has a convex cross-section (Figure 4a). Further downslope, the fan has a central bulge flanked by two slightly depressed areas (frontal splay bulge in Figure 4a). Another sediment wave field occupies the Frontal splay area, a lobate area that occupies the whole surface of the frontal splay (Figure 6). In the Frontal splay area the sediment waves have an upslope asymmetric cross-section shape with wavelength of about 300 m and maximum height of 4,6 m, which decreases moving away from the channel mouth (Profile D-D', Figure 6). The wave crests have a general NE-SW orientation, and they are aligned roughly parallel with the main flow pathway. The crest directions are not perfectly parallel with each other showing a deflection in their orientation, highlighted by the coloured arrows in Figure 6.

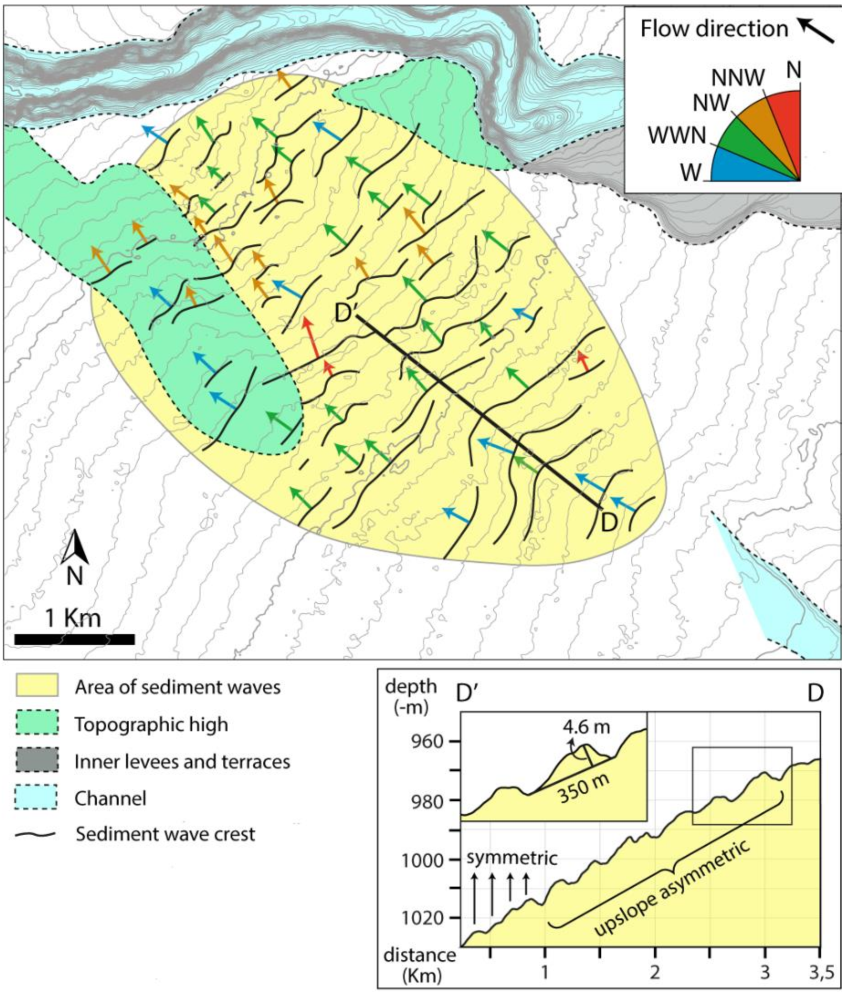

Figure 6 (A) Illustration of the sediment wave field in the frontal splay area. Flow direction arrows are coloured to highlight the flow diversions. (B) Bathymetric profile perpendicular to the crest direction of the waves.

6. Stratigraphy

The interpretation of the subbottom Chirp profiles allowed the recognition of five acoustic facies whose characteristics will be described in the following paragraph. A seismic characterization based on the distribution of the acoustic facies and their lithology interpretation is reported in the second paragraph of this chapter for each depositional environments.

6.1 Acoustic facies

Taking into account the presence or absence of reflections, the relative amplitude of reflections, the geometry of reflectors (parallel, irregular, etc.), five different acoustic facies have been distinguished. A brief description of the acoustic facies, comprehensive of their interpretation in terms of their most likely lithology and depositional environment, is reported in Table 1. The first word of the acoustic facies name describe, when the reflection are present, their geometry (parallel or irregular) while, when the reflections are absent, is labelled as transparent; the second word describe the strength of the acoustic reflection (high or low):

Transparent Low-reflectivity (TL) Intervals lacking coherent reflectors with faint reflectivity

Parallel Low-reflectivity (PL) Parallel to subparallel, continuous to discontinuous, low-amplitude and high-frequency reflections.

Parallel High-reflectivity (PH) Parallel to subparallel, continuous to discontinuous, high-amplitude reflections and high-frequency reflections.

Irregular High-reflectivity (IH) Irregular, discontinuous, variably spaced, high-amplitude reflections.

Transparent High-reflectivity (TH) Intervals lacking coherent reflectors but highly reflective, commonly reducing the penetration of acoustic energy.

6.2 Seismic characterization of the slope elements

6.2.1 Overbank wedge and channel fill

At a large scale, subsurface imaging reveals the typical components of channel-levee systems, with channel floor deposits and overbank wedges. The most part of the channel axis has a transparent, highly-reflective facies, suggestive of coarse-grained channel fill deposits (Figure 7, 8). The only exception occurs at the channel mouth where the coarse-grained sediments of the channel-axis infill are buried under a homogeneous fine-grained deposit (TL) (Figure 8c).

Seismic facies	Brief description	Lithology interpretation	Depositional environment	Figure
TL	Transparent, faintly reflective	Relatively homogeneous fine-grained sediments	Left overbank, Frontal splay and Fan fringe	Figure 8-9
PL	Parallel, low-amplitude reflections	Well stratified fine-grained sediments	Confined and partially confined right overbank – Fan fringe	Figure 7-8-9
PH	Parallel, high-amplitude reflections	Well stratified coarser (respect to PL)-grained sediments	Confined overbank – Inner levee	Figure 7a, 8c
IH	Irregular, discontinuous, high-amplitude reflection	Laterally discontinuous coarse-grained sediments	Frontal splay	Figure 9c
TH	Transparent, highly reflective	Relatively homogeneous coarse-grained sediments	Frontal splay, Channel fill	Figure 7-8-9

Table 1. Seismic facies recognized in the Acquarone Fan

The overbank deposits consist of a thick sedimentary wedge that tapers laterally and longitudinally. The left overbank wedge consists of relatively fine-grained sediments (TL) (Figure 8). At the base of the Acquarone high slope, a recent MTD can be recognized thanks to the rough seabed in the channel floor; according to its transparent, faintly reflective facies, it consists of a fine-grained MTD (Figure 8a, b).

In the right levee, the overbank deposits show a less homogeneous character, with varied acoustic facies. In the Bend area (Figure 7a), most of the units (I, II, III, VI and VII) are composed principally of well stratified fine-grained sediments (PL), while Units IV and V have a major coarse-grained component (PH). In the Laterally confined area (Figure 7b), there is a prevalence of well stratified fine-grained deposition (PL). At the end of the confined tract, in the Knick-points area, the left overbank deposits are composed by homogeneous fine-grained sediments (TL), while the right overbank by well-stratified fine-grained sediments (PL) (Figure 8a, b).

6.2.2 Frontal splay and fan fringe

The seven seismic units recognized in the overbank wedges extend downslope, in the frontal splay and fan fringe elements. The frontal splay and the fan fringe are composed of different acoustic facies that vary longitudinally and laterally. The first 8 meters (Units I, II and III) of the Frontal splay area consist of relatively homogeneous fine-grained sediments (TL) (Figure 9a). This low-amplitude package drapes more reflective deposits interpreted to be composed of relatively coarse-grained sediments (TH) of Units IV and V (Figure 9a). Their high reflectivity strongly attenuates the acoustic signal, making the recognition of the deeper units uncertain, which are thus characterized only on the basis of some minor reflections. In the fan fringe, the downslope continuation of Units IV, V and VII present irregular high-amplitude reflectors interpreted as laterally discontinuous coarse-grained sediments, laterally the reflectors have a parallel configuration and slightly decrease in amplitude (PL) highlighting better organization and an increase in the fine content (Figure 9c).

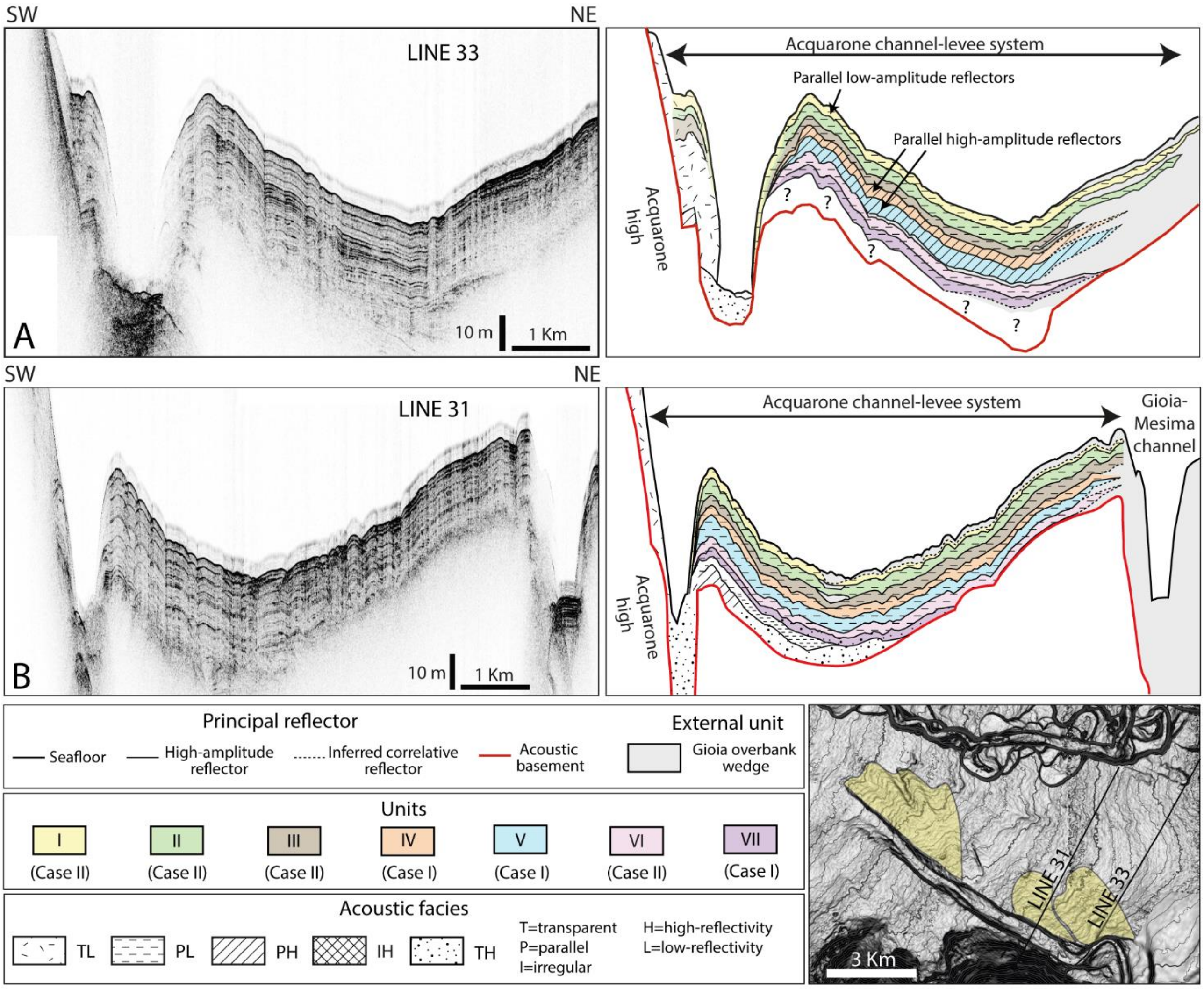

Figure 7 To the left the original subbottom Chirp profiles, to the right the subsurface drawing. The different units are marked with colours while the seismic facies with patterns. The acoustic basement is marked by the red line and the Gioia overbank wedge is grey. The seismic profiles are perpendicular to the channel-levee system where only the right-side overbank wedge is well built. Line 33 (A) cuts the Bend area; Line 31 (B) cuts the Laterally confined area.

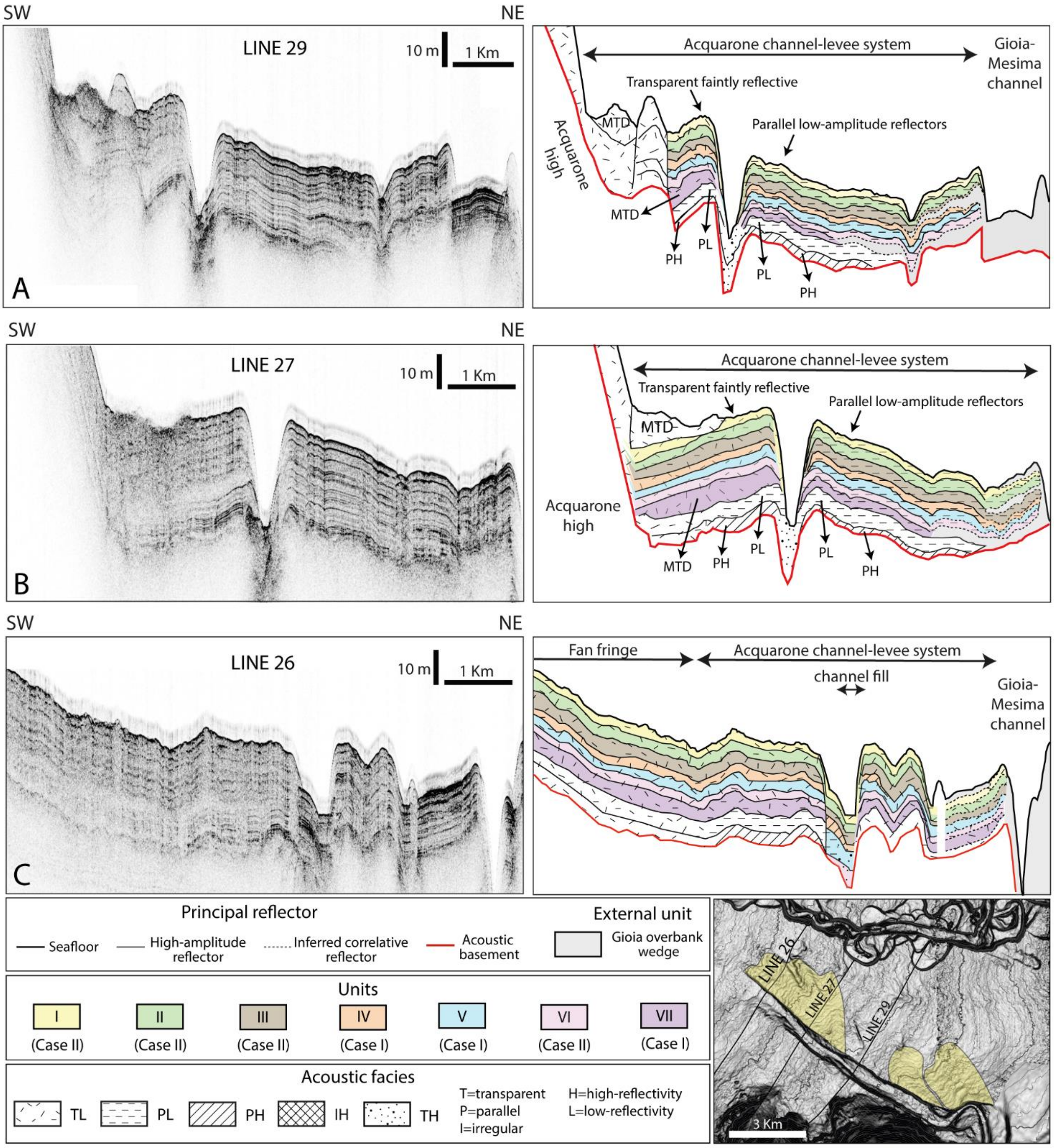

Figure 8 *To the left the original subbottom Chirp profiles, to the right the subsurface drawing. The different units are marked with colours while the seismic facies with patterns. The acoustic basement is marked by the red line and the Gioia overbank wedge is grey. The seismic profiles are perpendicular to the channel-levee system where both the overbank wedges are well constructed. Line 29 (A) cuts the channel-levee in the partially-confined area (Figure 4a); Line 27 (B) and Line 26 (C) cross the Knick-points area.*

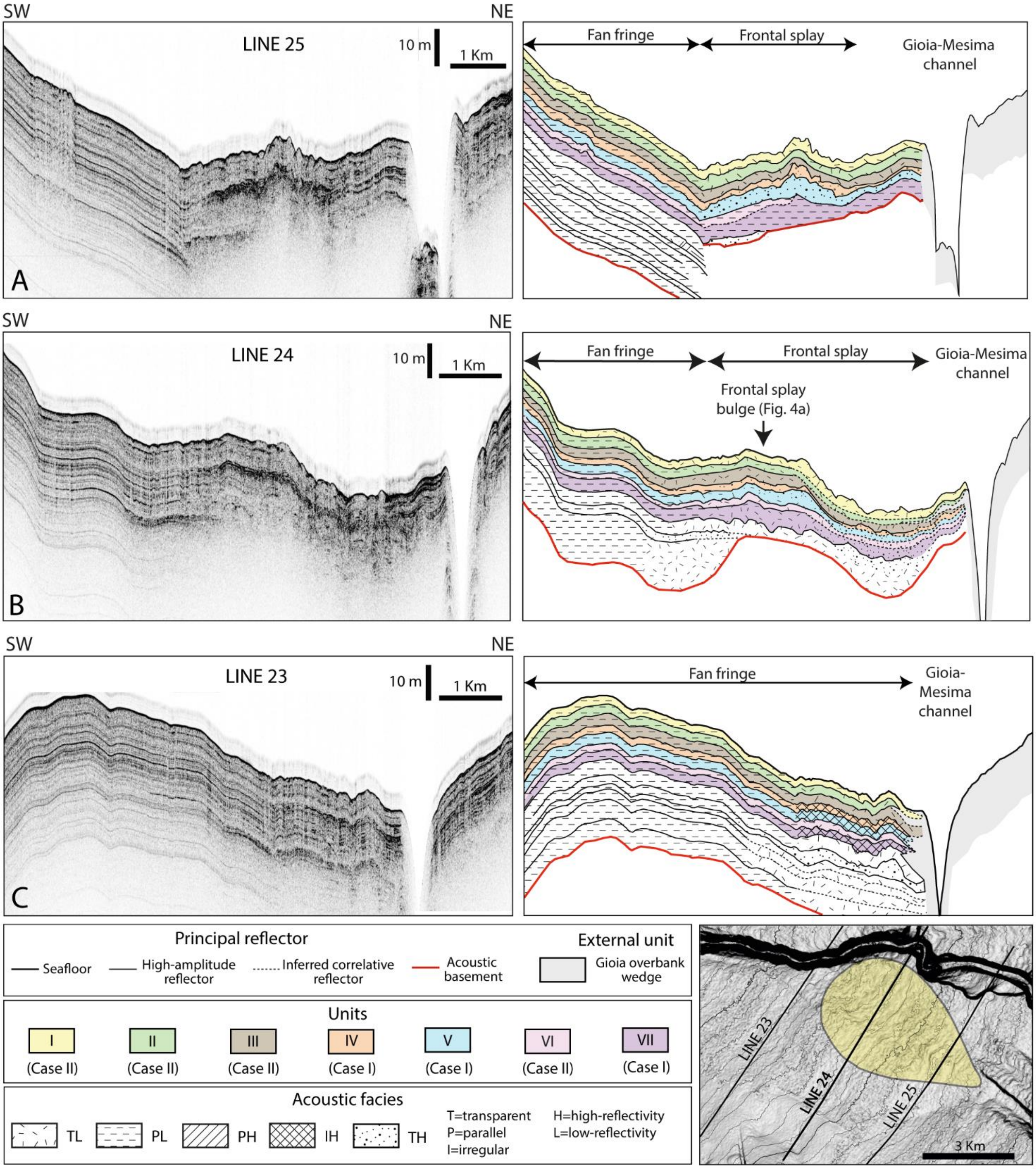

Figure 9 *To the left the original subbottom Chirp profiles, to the right the subsurface drawing. The different units are marked with colours while the seismic facies with patterns. The acoustic basement is marked by the red line and the Gioia overbank wedge is grey. Line 25 (A) and Line 24 (B) cut the Frontal splay area and the lateral fan fringe. Line 23 (C) is perpendicular to the fan fringe.*

7. Pattern of sediment distribution

The isopach maps of the seven units show the sediment distribution within the entire turbidite system (Figure 10). Each unit is characterized by a distinctive distribution of sediments, thus pointing to highly spatial variability of overspilling flow behaviour over time. In particular, the depocenters location and their seismic response are indicative of two main patterns of deposition in the Acquarone Fan. Each unit displays one of the two depositional patterns, named Case I and Case II.

Case I depositional pattern has three depocenters, in the Bend area, Knick-points area and Frontal splay area. This pattern is displayed by Units IV and VII and by Unit V, which, has a depocenter also in the Laterally confined area (Figure 10a). The depocenter in the Bend area has thicker values near the levee crest, where sediment waves are better developed and are upslope asymmetric (Figure 5b). The depocenter in the Knick-points area starts laterally to the flat sector downslope from KP1. The depocenter in the Frontal splay area has a convex shape, with maximum accumulation along the axis, where the sediment waves develop (Figure 6), and decreasing thickness laterally and downslope. In the Frontal splay area units IV and V are composed of homogeneous/laterally discontinuous coarse-grained sediments.

Case II depositional pattern is displayed by Units I, II, III and VI (Figure 10b). The second pattern of deposition is characterized by thickness mostly constant on the overbank, with only slightly increasing values in the Bend area, and a slight decrease in the frontal splay. Units II and III also present a depocenter in the Laterally confined area with maximum values near the levee crest (Figure 10b). At the end of the channel, the units are homogeneously distributed on the slope with a slightly thicker accumulation in the fan fringe than in the frontal splay. Case II units, in the Frontal splay area, show a homogeneous fine-grained composition.

Moreover, the thickness maps show that, concomitantly with the deposition of Units I, III, IV and VII the Acquarone high was affected by multiple landslides, finally deposited on the left overbank. The recurrence of MTD deposits in the same position in different time intervals highlight the reactivation of the landslide headwall resulting in its retrogression (Figure 10).

8. Interpretation

8.1 The Acquarone channel-levee: an atypical overbank pattern in the northern hemisphere

Generally, in the northern hemisphere, the Coriolis force causes more sediment overspill in the right levees, which, therefore, are often higher than the left ones (Mutti and Normark, 1987; Abd El-Gawad et al., 2012; Wells and Cossu, 2013). On the contrary, in the Acquarone channel-levee system, the left levee is in general higher than the right one (Figure 4b). At the beginning of the partially confined area, this difference in relief is partly due to the structural setting, since the left

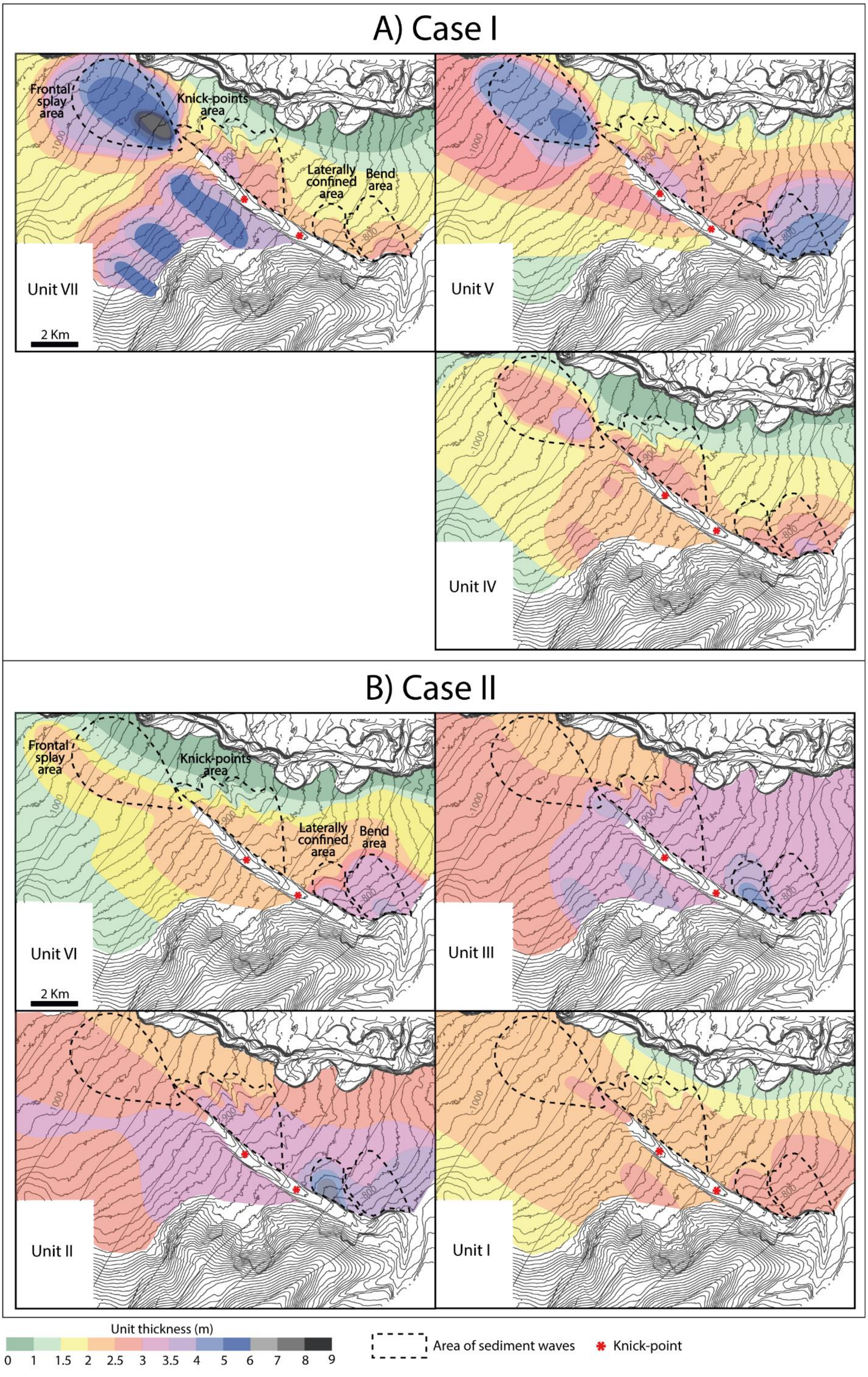
A) Case I
Frontal splay area
Knick-points area
Laterally confined area
Bend area
-1000
-900
-800
Unit VII
2 Km
Unit V
Unit IV
B) Case II
Unit VI
Unit III
Unit II
Unit I
Unit thickness (m)
0
1
1.5
2
2.5
3
3.5
4
5
6
7
8
9
Area of sediment waves
Knick-point

Figure 10 *Thickness maps of the seven (VII-I) units in the Acquarone Fan. The units have been grouped in Case I (Unit VII, V and IV) and Case II (VI, III, II and I) since they present two different sediment distribution patterns. (A) Case I units have depocenters in the Bend area, Knick-points area and Frontal splay area (only Unit V has thick accumulation also in the Laterally confined area). (B) Case II units show more homogeneous sediment distribution on the overbank, with the exception of Units II and III that have a depocenter in the Laterally confined area, and slightly thin in the frontal splay.*

levee grows on a more elevated terrain than the right levee, as highlighted by the relief of the acoustic basement in Line 29 (Figure 8a). Downslope, however, the acoustic basement reveals that the difference in relief is due to the greater aggradation of the left levee, since both the levees had initially the same height (Figure 8b). The left levee relief started to overcome that of the right one from the deposition of Unit VII. The isopach map shows that Unit VII presents an elongate depocenter on the left overbank running parallel to the levee crest (Figure 10a). It has been interpreted that part of this body is composed by an MTD coming from the retrogressive scarp located on the Acquarone high. Figure 8b shows that the volume of the MTD on the left overbank area, enhanced the left levee to overcome the relief of the right one, inverting the characteristic asymmetry of the channel-levee system of the northern hemisphere.

The most important parameters controlling overbank composition are vertical distribution of different grain-sizes in relation to the height of the levee (Straub et al., 2008; Hansen et al., 2015; Jobe et al., 2017). In fact, the relief of the levees, depending on the vertical grain-size, will control the partitioning of different grain-sizes between the in-channel flow and deposits on the levee, directly influencing the composition of the overbank wedges (Pirmez et al., 1997; Peakall et al., 2000; Pirmez and Irman, 2003).

Before the MTD deposition, the difference in relief between the right and left levee appears to have been negligible as they show the same seismic response on each side (Figure 8a, b). In this case, the same grain-sizes reached the right and left levee crest (Figure 11). However, after the deposition of the MTD, the two overbank wedges of the Acquarone fan show markedly different seismic responses. The right overbank is principally characterized by parallel low-amplitude reflector indicative of a relatively well stratified fine-grained sediment, whereas, in the left overbank wedge, the absence of any internal structure and faintly reflective seismic facies could be indicative of homogeneous and structureless fine-grained deposition (Figure 8a, b).

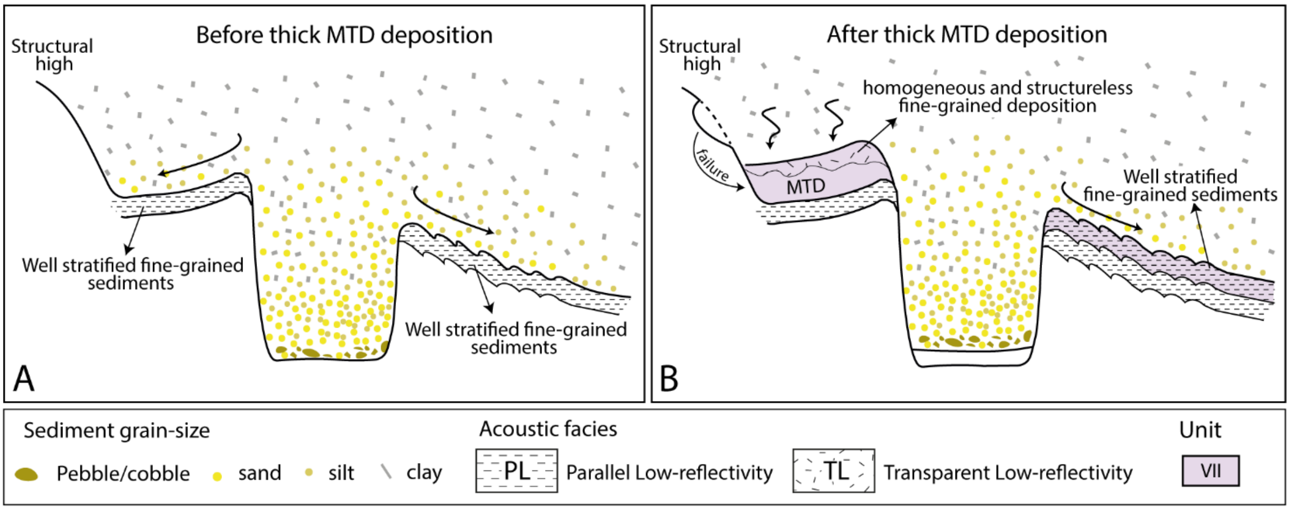

Figure 11 *Schematic diagram of the channel-levee illustrating how the interplay between the levee relief and the vertical distribution of the grain-sizes can affect the deposition on the overbank. (A) Before the MTD deposition the same grain-sizes reached the levees producing analogous deposits on the opposite overbanks, (B) while after the MTD deposition, the increased difference in levee relief led to a different segregation of the flow producing lithologically different deposits on the opposite overbanks.*

Our case study shows that, the geologically-instantaneous emplacement occurrence of an MTD on the left overbank asymmetrically increased the levee relief and so the confinement of the flow towards the side interested by the failure. The stratification of the flow combined with the increase in confinement, led to the preferential overspill of coarser grain-seizes on the less elevated overbank, producing stratified deposits with sand beds (Figure 11). Instead, only fine grain-sizes, are able to reach the surface of the higher levee, creating homogenous mud-dominated deposits (Figure 11). This process led to drastic change in the resulting overbank composition that can have important consequences on facies prediction: the proximity with a structural high can originate overbank deposit with higher sand % respect to the opposite wedge where finer deposition can occur and interrupt the lateral continuity of sand beds.

We conclude that the occurrence of collapses from the Acquarone high and landslide deposition on the left levee caused significant differences in the levee topography and, consequently, in the composition of the overbank wedges. Therefore, the Acquarone fan sheds light on a mechanism, i.e. slope failure, whereby channel-levee systems in topographically complex areas deviate from the characteristic asymmetry connected to the action of the Coriolis force.

8.2 Two types of flows

The two pattern of sediment distribution (Case I and II) and their seismic response, suggest that two types of flows, with distinct dynamics, are responsible for the different distributions of the seven depositional units in the study area. Of the many parameters that characterize turbidity currents, flow density is fundamental in controlling their depositional pattern (Lowe, 1982). We have thus explored the possibility that flows with an initial different density and internal structure may interact differently with the seafloor topography, exploiting distinct overbank points along the channel and following different flow paths in the overbank and frontal splay areas. We follow the definition of the flow type in the classification by Lowe (1982), which distinguishes high and low-density turbidity current depending on their dominant grain-size population.

Low density turbidity currents consist largely of clay, silt and fine- to about medium-grained sand-size particles that can be maintained in the flow by turbulence alone. Conversely, high-density turbidity currents can include particles coarser than about medium-grained sand, which are supported by different mechanisms dependent on concentration effects. We have also taken into account that, in many cases, turbidite flows are bipartite, with a coarser-grained basal part behaving as high-density turbidity current and a finer-grained top behaving like a low-density one (Lowe, 1982; Mutti et al., 2003; Tinterri et al., 2003).

As summarized in Figure 12, in the study area, in Case I (Figure 12a) the bulk of sediments are deposited in the frontal splay with a transparent high-reflectivity acoustic facies indicative of prevalently coarse-grained sediment and producing a positive topography, which we interpret as resulting from high-density turbidity currents. On the contrary, in Case II (Figure 12b) a transparent low-reflectivity acoustic facies prevail and indicate a mud prone frontal splay, associated very likely with low-density turbidity currents even if the presence of mud-rich hybrid beds (sensu Haughton et al., 2009) cannot be completely ruled out.

The reason for privileging the interpretation linked to low density turbidity currents lies in the fact that, theoretically, the difference in acoustic impedance between the lithological internal divisions of hybrid beds should produce a reflection in the seismic profile whereas the frontal splay of the study area is characterized by transparent acoustic facies. Furthermore, the increase of the slope gradient downcurrent to the channel mouth (Figure 4a) would enhance the bypass of hybrid flows away from the frontal splay area rather than their deposition. Indeed, hybrid beds, deposited by transitional flows where the cohesive forces prevail over turbulence, tend to be more common into

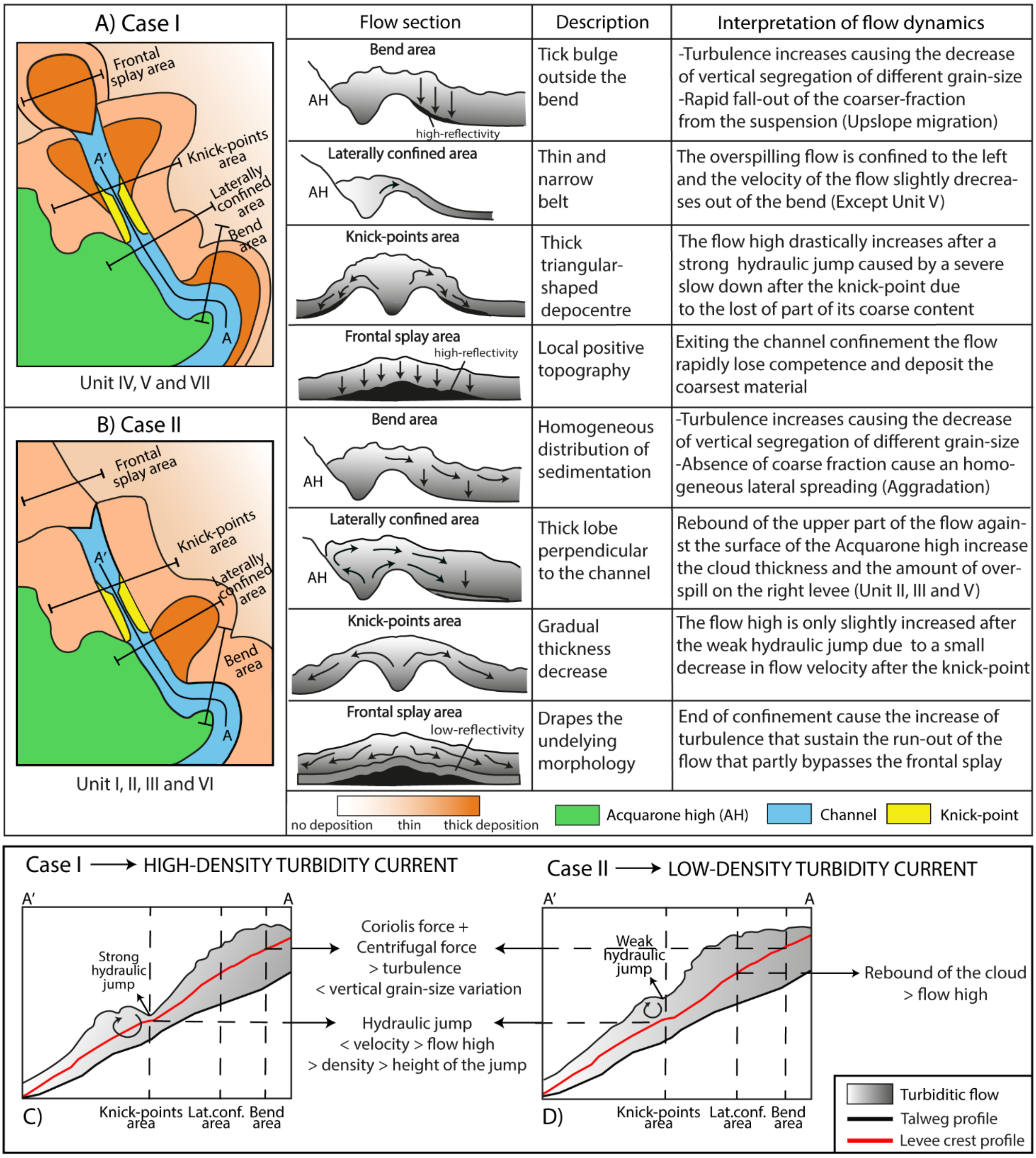

Flow section	Description	Interpretation of flow dynamics
Bend area	Tick bulge outside the bend	-Turbulence increases causing the decrease of vertical segregation of different grain-size -Rapid fall-out of the coarser-fraction from the suspension (Upslope migration)
Laterally confined area	Thin and narrow belt	The overspilling flow is confined to the left and the velocity of the flow slightly drecreases out of the bend (Except Unit V)
Knick-points area	Thick triangular-shaped depocentre	The flow high drastically increases after a strong hydraulic jump caused by a severe slow down after the knick-point due to the lost of part of its coarse content
Frontal splay area	Local positive topography	Exiting the channel confinement the flow rapidly lose competence and deposit the coarsest material
Bend area	Homogeneous distribution of sedimentation	-Turbulence increases causing the decrease of vertical segregation of different grain-size -Absence of coarse fraction cause an homogeneous lateral spreading (Aggradation)
Laterally confined area	Thick lobe perpendicular to the channel	Rebound of the upper part of the flow against the surface of the Acquarone high increase the cloud thickness and the amount of overspill on the right levee (Unit II, III and V)
Knick-points area	Gradual thickness decrease	The flow high is only slightly increased after the weak hydraulic jump due to a small decrease in flow velocity after the knick-point
Frontal splay area	Drapes the underlying morphology	End of confinement cause the increase of turbulence that sustain the run-out of the flow that partly bypasses the frontal splay

***Figure 12** Summary sketch of the two patterns of overbank sediment distribution, Cases I (A) and II (B) and schematic cross-sections of the flow highlighting the relevant flow dynamics. Below, the longitudinal variation in flow thickness, for Cases I (C) and II (D) and inferred variations in flow proprieties connected to the dynamics of the hydraulic jumps around the knick-points.*

lateral and distal lobe fringes and basin plains and, more in general, where reduction in seafloor gradient favors flow deceleration and deposition (Haughton et al., 2009; Tinterri and Muzzi Magalhaes, 2011; Talling et al., 2013; Kane et al., 2016). Our reconstruction show that the two types of flow behaviour characterize specific time intervals and alternate during the construction of the overbank wedge through the deposition from unit VII to I.

8.3 Flow type and sedimentation pattern

8.3.1 Bend area

Bends are crucial morphological elements that affect sediment distribution in the channel and overbank areas. In this case study, the origin of the bend is connected to the presence of the Acquarone high that deviates the channel pathway from a N-S to a NW-SE direction. The lateral confinement imposed by the Acquarone high led to a large amount of sediment discharge outside the bend on the eastern right levee (Figure 10).

The backslopes of channel levees are in general thought as sites of fine-grained turbidity currents and of predominantly mud and silt deposition (Mutti and Normark, 1987; Normark et al., 2002; Wynn and Stow, 2002; Hansen et al., 2015). In a current able to transport various grain sizes, the coarse sediment fraction is concentrated near the base of the current, while finer sediment fractions are more homogenously distributed over the height of the current (Kneller and Buckee, 2000) (Figure 13). Progressive levee construction increases flow confinement and, accordingly, causes reduction in the grain-size of the sediment that can overspill the channel. As a consequence, an overall fining-upward trend generally characterizes the overbank sequence (Hansen et al., 2015).

On the outer side of the bend of the Acquarone channel, despite the high relief of the levee crest (about 60 m), Units IV and V (Case I) are characterized by a high-reflectivity interpreted as deposits with a percentage of coarse-grained sediments (Figure 7a). There is a drastic change of facies

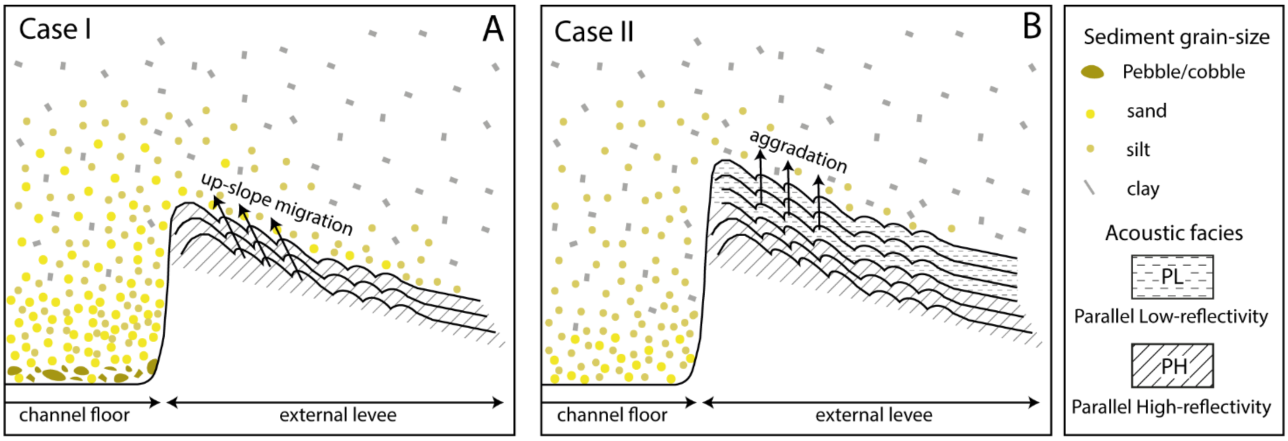

Figure 13 *Schematic diagram of the channel belt and the external levee showing the interaction of (A) High-density turbidity current (Case I) and (B) Low-density turbidity current (Case II) with topography and the different migration direction of the sediment waves created by the two types of flow on the outer levee slope.*

between Unit IV and the overlying units belonging to Case II consisting in 8.5 m of relatively fine-grained deposit, as inferred from the low acoustic reflectivity (Figure 7a). The passage between PH and PL facies is sharp and abrupt, indicating that a sudden change in the proprieties of the flows occurred after the deposition of Unit IV. According to Baas et al. (2005), highly-turbulent flows keep the coarser particles more easily in suspension, owing to an upward directed component of turbulent velocity that overcomes the falling velocity of most particle sizes. This effect would eventually cause a decrease in the vertical segregation of the different grain-sizes compared to flows with weaker turbulence. In the study area, the high gradient of the confined tract (1.15°, Figure 4b) and the centrifugal force at the bend are consistent with an increase in the flow velocity, which can develop high turbulence. So, we suggest that, in Case I, whose parent flows have a high percentage of sand fraction, the increased turbulence enhanced the coarser fraction to reach the upper part of the flows and overspill. Therefore, the overbank deposit created by high-density turbidity currents has a higher sand to mud ratio than the product of low-density turbidity currents, which does not account for a significant coarse-grained fraction to be transported over the levee crest (Figure 13b).

Sediment waves in the Bend area, in their early phase (Case I), are associated with parallel reflector with a high-reflectivity and have slow rates of up-current migration (Figure 5c; Figure 13a). Anyway, later (Case II), the migration rate diminishes, the seismic response becomes less reflective and pure aggradational growth prevails (Figure 5c; Figure 13b). Generally, up-current migrating sediment waves are associated with thicker and more abundant sand beds on their stoss side (Normark et al., 2002; Kostic, 2014). This general observation is consistent with a higher sand content in the overflow connected to Case I, further substantiating that they can be associated with high-density turbidity currents.

8.3.2 Laterally confined area

Generally, in a leveed-channel system, the upper part of turbidity currents continuously over-spills onto the overbank area and the flows within the channel are progressively depleted of fine-grained material (Peakall et al., 2000; Hansen et al., 2015). As a consequence, the thickness of overbank units is expected to decrease in a downstream direction. On the contrary, in the Laterally confined area of the right levee, Units II, III (Case II) and V (Case I) have higher thickness than upslope (Figure 10). This unusual and localized increase in sedimentation can have two different explanations:

1) A localized reduction in the channel depth value enhances the overspill of a thicker part of the flow. Different depositional features may reduce the channel relief, such as nested mounds that

develop on the outside of a specific bend (i.e. the first sharp bend) (Peakall et al., 2000) or MTD coming from the surface of the Acquarone high. However, those feature cannot be recognized, as, if present, they are now buried under the more recent MTD (Figure 2).

2) The flow experienced a reflection on the surface of the structural high.

In the case of the first hypothesis, the overspill of the lower, coarser-grained part of the flows should result in a high-amplitude seismic facies, similar to what observed in the high-density flows of Case II. This is not the case, as shown by Figure 7b, which highlights the low-amplitude parallel reflections of the overbank wedge. Therefore, we prefer the second hypothesis also because it is consistent with the spreading direction of the lobe-shaped depocenter in the Laterally confined area that is almost specular to the channel path at the bend. It can be hypothesized that the confining action of the Acquarone high could impose the thickening and the successive rebound of the upper portion of the flow outgoing from the bend (Figure 12b, d). In fact, a turbidity current can be reflected depending on the geometry of the bounding slope and the angle of incidence of the current (Patacci et al., 2015). This assemblage has commonly been detected in tectonically confined basins (Kneller et al., 1991; Kneller and McCaffrey, 1999; Amy et al., 2004; Tinterri et al., 2016, 2017; Tinterri et al., 2019) resulting in the production of contained-reflected beds (sensu Pickering and Hiscott, 1985). Dalla Valle and Gamberi (2009) and Tek et al. (2021) provide other examples where changes of the overbank architecture are interpreted to be connected to flow reflection processes.

Laboratory experiments (Kneller et al., 1991; Kneller 1995; Haughton 1994; Amy et al., 2004; Patacci et al., 2015) and numerical models (Howlett et al., 2019) have shown that a reverse overflow forms as soon as a turbidity current impacts on a topographic high and a deceleration from supercritical to subcritical condition is accompanied by abrupt flow inflation. However, in order to produce a reflected overflow, the upper part of the flow should have sufficiently high momentum, so when the outbound velocity is too low at the point of incidence with the slope, turbidity-current reflection is not achieved (Patacci et al., 2015). In the case of the Acquarone channel, it is reasonable to argue that turbidity currents that spilled over the left side of the channel experienced complete reflection, being impeded in their travel by the Acquarone High (Figure 12b). However, the sedimentation patterns of Units I, IV, VI and VII do not show this depocenter (Figure 12a). Probably the turbidity currents that generated those units had insufficient velocity due to their strongly depositional behaviour at the bend. In fact, as the current enters the bend and spills over onto the overbank, the in-channel velocity decreases significantly (Abd El-Gawad et al., 2012). Other flow proprieties, such as the volume of the low-density part of the flow and the height of the overspilling flow, could be involved in the occurrence of a reflected overflow, but they cannot be evaluated with the data presently available.

8.3.3 Knick-points area

The relief of levees above the channel floor commonly diminishes in a downslope direction (Hiscott et al., 1997; Posameinter and Kolla, 2003; Hansen et al., 2015). In our case study, along the flat segments (flat I-II, Figure 4c) downslope from knick-points, the relief of the levees crest increase, (respectively about 7 and 3 meters for the right levee and 5 and 4 m for the left one) vs. the upslope levee tract (Figure 4c). This increase in relief could be due to a localized increase in the erosional behaviour of turbiditic flows in the channel floor or to an increase in the growth rate of levee crests. The latter hypothesis is here preferred because the flat I segment on the levee crest profiles coincides with the upslope apex of a depositional field of bedforms (Figure 12a).

In the Knick-points area, the units that fall into Case I show a marked depocenter highlighting increased capability of flows to overtop the levee crest (Figure 12a). A reduction in flow velocity is to be expected when a flow passes through a knick-point (Heijnen et al., 2020). Considering the inverse relationship between flow velocity (U) and flow height (h) marked by the Froude number

$$Fr' = \frac{U}{\sqrt{h(g\frac{\rho - \rho w}{\rho w})}}$$

, where ρ=density of the flow, ρw=density of water and g=acceleration of gravity, flow thickening is connected to flow deceleration.

In the Acquarone channel, slopes are always one order of magnitude above the 0.1° threshold gradient for Froude supercritical flow deposits (Postma et al., 2014). This is why it is reasonable to assume that, irrespective of their nature, all the turbidity currents reached the supercritical conditions and, passing the knick-point, experienced a hydraulic jump. We suggest that in the flat I segment (Figure 4c), where the slope of the channel axis is halved, the turbidity currents rapidly slow down and go through a hydraulic jump, whose consequence is the thickening of the flow and the entrainment of water that reduce the density of the current (Figure 14) (Komar, 1971; Postma et al., 2009).

Recent experiments by Ono et al. (2021) were carried out on a mixture of sediment (including fine-sand to gravel), simulating flows equivalent to the high-density turbidity currents according to the definition of Lowe (1982). The results of Ono el al. (2021) show that after the occurrence of a large hydraulic jump, where the flow depth increased eight time respect the initial value, smaller ones, where the flow was only two times thicker than the initial value, occurs. We have interpreted that the flow behaviour of Case I in the KP1 could thus be connected to a drastic increase in flow thickness. This process can account for a long-lasting overspill and for the formation of the depocenter associated with the Knick-points area (Figure 12a). Anyway, only Unit VII show a depocenter occurring after the KP2. Accordingly with the data of Ono et al. (2021), we interpreted the absence of a depocenter after KP2 for Unit V and IV to be connected to a possibly smaller hydraulic jump whose effect are potentially not related to a long-lasting overspill. The smaller size of the jump can be connected to a slow-down of the velocity of the flow following the first hydraulic jump and to the milder slope difference between the second ramp (1,2°) and the second flat (0,9°) that could have not provided sufficient deceleration to the flow.

Similarly, Case II, interpreted as associated to low-density turbidity currents, does not show any increase in sedimentation in the Knick-points area (Figure 12b). This occurrence is here explained as also resulting from a smaller hydraulic jump. In the crossing of a topographic step, the height of the

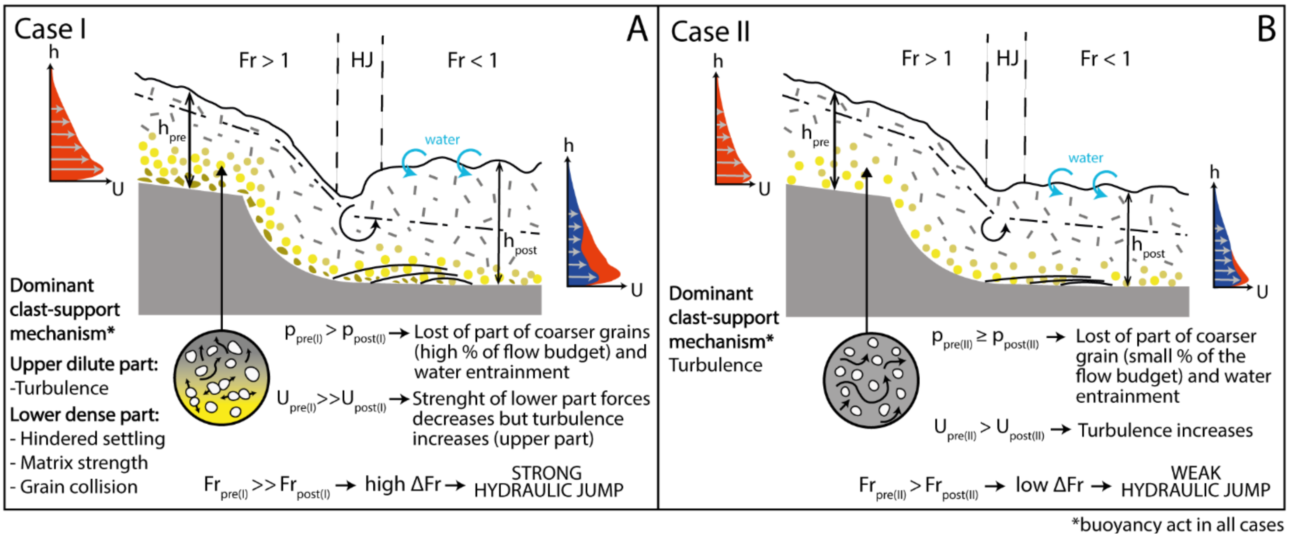

Figure 14 *Schematic diagram of the interpreted flow high transformation of supercritical turbidity currents through a hydraulic jump in the knick-point. (A) Supercritical high-density turbidity current (Case I) is expected to experience strong deceleration after the hydraulic jump because of the loss of part of its coarse-grained particles, which, through clast interactions, creates the principal clast-support mechanism in the lower part of the flow. (B) Supercritical low-density turbidity current (Case II) goes through a milder velocity reduction after the hydraulic jump because its principal clast-support mechanism is maintained and further alimented after the jump.*

jump has been described as the ratio of Froude number before (Fr_{pre} in Figure 14) and after the jump (Fr_{post} in Figure 14). The higher the difference between the Froude number values (ΔFr in Figure 14), before and after the jump, the higher the size of the hydraulic jump (Cartigny et al., 2014).

The lower part of bipartite turbidity currents consist of a relatively dense basal layer sustained by the combined effect of hindered settling, matrix strength and dispersive pressure controlled by sediment concentration (that may exceed 20-30% according to Lowe, 1982). In contrast, a dilute, turbulent low-density turbidity current is primarily sustained by turbulence which is largely independent from particle concentration (Lowe, 1982).

The flow deceleration related to the hydraulic jump, in high-density turbidity currents, causes the en-masse deposition of the coarsest particles of the basal layer (Postma et al., 2014; Postma and Cartigny, 2014; Hage et al., 2018; Slootman and Cartigny, 2020) and the concentration of the basal dense layer is further reduced by the water entrainment effect (Figure 14a). As a consequence, we can expect that high-density turbidity currents experience a drastic slowdown after KP1, due to the marked decrease in sediment concentration, producing a strong hydraulic jump with the consequent increase in sediment deposition on the levee (Figure 14a). While low-density turbidity currents, whose principal transport mechanism is the turbulence of the fine-grained sediments, are expected to experience a milder velocity reduction after KP1 producing a weak hydraulic jump (Figure 14b).

In summary, we suggest that the pattern of sediment distribution created by Case I in the Knick-points area, consisting in a localized increase in the overbank thickness, is the result of high-density turbidity currents experiencing a strong hydraulic jump (Figure 12c); while the sedimentation pattern of Case II does not generate a depocenter in the same area since their former flows (low-density turbidity currents) are interpreted as producing smaller and weaker hydraulic jumps (Figure 12d). We have interpreted the knick-points, inferred by tectonic structures transverse to the channel course whose topography is not completely healed, led to the occurrence of hydraulic jumps whose amplitude, that can be connected to the density stratification of the flow, may or not have a depositional expression on the overbank area.

8.3.4 Frontal splay area

The thickness distribution of the seven units shows that the two different types of flow behave differently also under the rapid flow expansion regime ensuing at the end of the channel confinement. Units falling in Case I present a thick and elongate lobe with very high reflectivity (Figure 12a). This kind of deposition is interpreted as resulting from high-density turbidity currents that, exiting the channel confinement, rapidly lose competence, deposit the coarsest material and create a thick frontal lobe with small-scale coarse grained sediment waves in front of the channel mouth (Figure 6). Moreover, the direction of the crests is indicative of another important behaviour of the lower dense portion of the turbidity current. Where the relief of the bulge in the frontal splay becomes important (Figure 4a, 9b), the sediment wave crests divert by about 30° eastward from their initial WWN-EES orientation (Figure 6). Similar results can also be observed in field studies and flume experiments related to flow deflection against lateral or oblique confining slopes (Amy et al., 2004; Tinterri et al. 2017; Piazza and Tinterri, 2020). The mud portion is completely absent, as shown by the transparent high reflectivity of the frontal splay (Figure 9a), indicating that the upper dilute part of the turbidity currents largely bypassed this area or were eroded by successive flows.

Units belonging to Case II do not present any thick concave upward accumulation, but, rather, deposition on the frontal splay results in a low-reflectivity package, which drapes the underlying morphology (Figure 12b). Sedimentation is higher towards the SW, in the fan fringe, than adjacent to the channel mouth where much of the sediment bypasses and is carried further downslope in the Gioia channel. The loss of confinement at the end of the channel is generally associated with an increase of turbulence in turbidity currents. The increase in turbulence at the mouth of submarine channels has been connected both to the occurrence of hydraulic jump (Mutti and Normark, 1987; Mutti et al., 1991; Mutti et al., 2003; Baas et al., 2004) and to flow relaxation mechanism (Pohl et al., 2019). In turbidity currents with a substantial mud component, as low-density turbidity currents, increase in turbulence, which, preventing sediment deposition, contributes to the flow run-out (Mutti and Normark, 1987; Mutti et al., 1991; Mutti et al., 2003). Moreover, the high value of the slope (1.2°, Figure 4b) and the convergence created by the topography in the frontal splay caused turbidity currents to accelerate in the principal flow direction, while laterally, in the fan fringe, the gentler slope caused a little bypass and a greater amount of fine-grained deposition. In fact, low-density turbidity currents react to the end of confinement and to the morphology of the slope in the same way as the upper dilute part of high-density turbidity currents.

9. Conclusions

A detailed analysis of sediment thickness and facies has been performed to investigate overbank processes in a leveed channel in a slope setting located in the southeastern Tyrrhenian Sea. It reveals considerable complexity in levee facies and thickness, ultimately ensuing from the uneven seafloor topography of the study area, highlighting that, in continental slope settings, where the imprint of tectonic structures is not yet completely healed, sedimentation in overbank areas does not conform to the available, simple predictive models.

In particular, we show that structural highs can confine overbanking turbidity currents, inducing flow deflection, and forming localized depocenters in the levees. Such an interaction between overbanking flows and confining structural highs can eventually lead to reverse channel asymmetry, opposite to what would result from the effect of the Coriolis force alone.

In addition, our research also highlights that planform and gradient variations of slope channels can have a strong influence on the thickness trend in the overbank areas. In particular, we show that overbank depositional patterns change along the channel course depending on the location of bends and knickpoints. This behaviour is recognized in the majority of submarine channels and interpreted as resulting from local perturbations in channel planform and gradient depending on autogenic processes inherent with channel development. Our case study, on the contrary, shows that bends and knick-points can have a tight connection to slope topography, thus further conjoining overbank depositional patterns and allogenic, tectonic shaping of a continental margin.

We have also shown that sediment wave fields coincide with depocenters on the overbank region, indicating that they develop from the principal sediment entry-points. According to their location, the sediment waves have different dimensions and geometries highlighting that the interaction between the overspilling flows and slope topography, influences not only sediment distribution, but also the morphology of the sediment waves. Moreover, our study shows that the direction of migration of sediment waves is connected to the density of the turbidity current: high-density turbidity currents create upslope-migrating coarse-grained sediment waves, whereas low-density turbidity currents are associated with aggrading fine-grained sediment waves.

Finally, our study also shows that patterns of overbank deposition vary over time. We envisage that, upon interacting with gradient variations along the channel course, turbidity currents behave differently, depending on their vertical density profiles. In particular, hydraulic jumps formed by high- and low-density turbidity currents control the amount of sediment that can overspill the channel and the character and location of overbank depocenters. This finding highlights the importance of antecedent conditioning by previous flows in controlling the development of turbidite systems.

Chapter 3

“Supercritical bedforms and related downslope evolution in a confined lobe, Amantea Fan, Paola Basin (Southeastern Tyrrhenian Sea)”

1. Introduction

Deep-sea fans are among the geomorphic features which contribute to the growth of sedimentary successions along continental margins. Submarine fans are composed of packages of turbidites that form during a period of fan activity and are bounded above and below by fine-grained facies produced during phases of fan deactivation (Mutti & Normark, 1987). In submarine fans, sandy depositional lobes commonly accumulate at the termination of a range of submarine feeder conduits, and, where the slope has a simple topography, they freely spread in the basin plain. In contrast, in confined intraslope basins formed as a result of seafloor deformation driven by tectonic activity, the spreading of sediment gravity flows can be obstructed. Structural barriers create morphologic highs and lows in the basin that strongly affect flow behaviour and the distribution of facies and lithology in fan lobe. The effect of seafloor topographic features on sediment gravity flows and relative deposits have been investigated both in modern (Deptuck et al., 2008; Gamberi et al., 2014) and ancient confined basins (Amy et al., 2004; Remacha et al., 2005; Tinterri et al., 2017, 2022; Tinterri & Civa, 2021; Tinterri & Tagliaferri, 2015) and by relative experimental analogs (Amy et al., 2004; Howlett et al., 2019; Patacci et al., 2015; Soutter et al., 2021).

The occurrence of sand-rich high-density turbidity currents, due to the proximity to subaerial drainage system, flowing on steep slopes and basin floors make confined basins particularly prone to the development of supercritical flows and relative upper flow regime bedforms. In fact, the great part of the supercritical bedforms (i.e antidune and cyclic steps as end members) may thus result from rapid-moving high-density stratified flows, as highlighted by Postma et al. (2009). Antidunes are formed by supercritical turbidity currents ($Fr > 1$) while cyclic steps are related to transcritical flows, as each step is bounded at its upstream and downstream ends by a hydraulic jump, which is a short zone over which the flow experiences a rapid transition from shallow and supercritical ($Fr > 1$) to thick and subcritical ($Fr < 1$) (Cartigny et al., 2014; Kostic, 2011). Cyclic steps are generally classified as net-erosional or net-depositional, depending on whether the dominant process across the bed forms is erosion or deposition, respectively (Cartigny et al., 2011, 2014). Net-erosional cyclic steps are manifested as scours, whereas net-depositional cyclic steps take the form of upstream-migrating sediment waves (Cartigny et al., 2011; Fildani et al., 2006; Kostic, 2011; Spinewine et al., 2009). Recognizing supercritical deposits in outcrops is challenging. Nevertheless, the sedimentology of upper flow regime bedforms has been more frequently described through outcrop studies (Cornard & Pickering, 2020, 2020; Gong et al., 2017; Longhitano et al., 2021; Ono et al., 2021; Ono & Plink-björklund, 2018; Postma et al., 2009, 2014, 2016; Postma & Kleverlaan, 2018) than modern marine examples. Sampling those bedforms in submarine fans is not easy due to their possible very coarse grain sizes (Hughes Clarke et al., 1990). To this day, there are very few samples of cyclic steps and they are prevalently located in channel talwegs (Fildani et al., 2006; Hage et al., 2018) but upper flow regime structures are frequent even downslope respect to channel-mouths (i.e most of the previously cited outcrop studies).

Buried below a late quaternary mud drape, analogues of this supercritical erosive and depositional bedforms have been sampled in a sandy submarine lobe (Amantea Fan) located in the Paola basin, one of the intraslope basins of the southeastern Tyrrhenian Sea (Figure 1). This study aimed to describe, from the seismic and sedimentological point of view, these deposits and their relative downslope evolution. High-resolution seismic profiles provide insight into the internal architecture of the lobe also in relation with the presence of a frontally-confining ridge (Paola Ridge) and lateral steep slope. This information is used, combined with gravity cores, to strictly characterize the different depositional and erosional elements that compose the lobe. These data sets thus help to bridge the resolution gap between outcrop studies and morphodynamics studies in modern systems and may help to evaluate the result from recent flume tank experiments.

2. Geological context

The Tyrrhenian Sea is a Neogene back-arc basin formed as a consequence of rifting and back-arc extension of the Alpine/ Apennine suture above the north-westerly subducting Ionian oceanic slab (Kastens & Mascle, 1990) occurred within the overall context of the convergence between the Africa and Eurasia plates. The passive roll-back of the Ionian-Adriatic slab is the most widely accepted mechanism to explain the SE migration of rifting, volcanism, ocean crust emplacement and of the Apennine belt deformation front (Malinverno & Ryan, 1986). Slab roll-back induced the south-eastward drift of the Calabrian terrane, a fragment of a pre-existing Alpine chain located just east of the Corsica/Sardinia continental crustal block before the spreading in the Tyrrhenian Sea (Alvarez et al., 1974).

The onset of the extension in the Tyrrhenian Sea has been dated to the Tortonian (~10 Ma) from ODP drilling results (Kastens & Mascle, 1990). The opening of the Tyrrhenian Sea occurred in two stages: an early (~10-5 Ma) opening of the northern Tyrrhenian Sea and a late (~5-0 Ma) opening of the southern sector. The opening of the southern Tyrrhenian Sea favoured the formation of elongated peripheric basins, the peri-Tyrrhenian basins, the Paola, Gioia, and Cefalù basins, which are characterized by Plio- Quaternary sedimentary infilling up to 5-km-thick (Sartori, 1970).

2.1 The Paola basin geological setting

The Paola Basin is located between the shelf edge and a 60-km-long and NNW-SSE oriented anticline called the Paola Ridge (Figure 1a). According to Gamberi & Rovere (2010), the Paola Ridge has been interpreted as due to a mobile mud belt, connected to a set of extensional faults trending NW-SE to NNW-SSE. The authors also demonstrated that the ridge hosts cold seep structures identified as large fields of pockmarks (Rovere et al., 2014, Figure 1a). The Paola Basin is a large (about 700 km^2) trough that trends NNW-SSE and lies at a depth of around 800 m.

The clastic source area is the Coastal chain, a mountain range located to the east of the basin; it is composed of ophiolitic and crystalline basement unconformably overlapped by Tertiary to Quaternary sedimentary deposits (Figure 1a). The coastal chain is pervasively carved by steep and short subaerial river courses characterized by torrential regimes (locally known as Fiumara stream (Sabato & Tropeano, 2004). Flash floods periodically occur within these short-rivers, often evolving into hyperpycnal flows when they enter the sea and being thus able to transport a large amount of debris into the sea (Casalbore et al., 2011).

The confined Paola Basin is located between the towns of Cetraro and Villaggio del Golfo; the continental shelf to the west of those towns is characterized by an uneven morphology produced by numerous rocky outcrops (Figure 1a). The continental shelf is generally narrow (2 Km), except where rocky outcrops occur and where it widens to 6 Km-thick, and steep (1°-2,5°). These values are generally narrower and steeper compared to other slope values of the Tyrrhenian Sea averages of 13.6 km and 0°39' (Gallignani, 1982). Beyond the shelf break, located at 140-150 m depth, the continental slope is deeply incised by several small canyons that cause the retreat of the shelf break

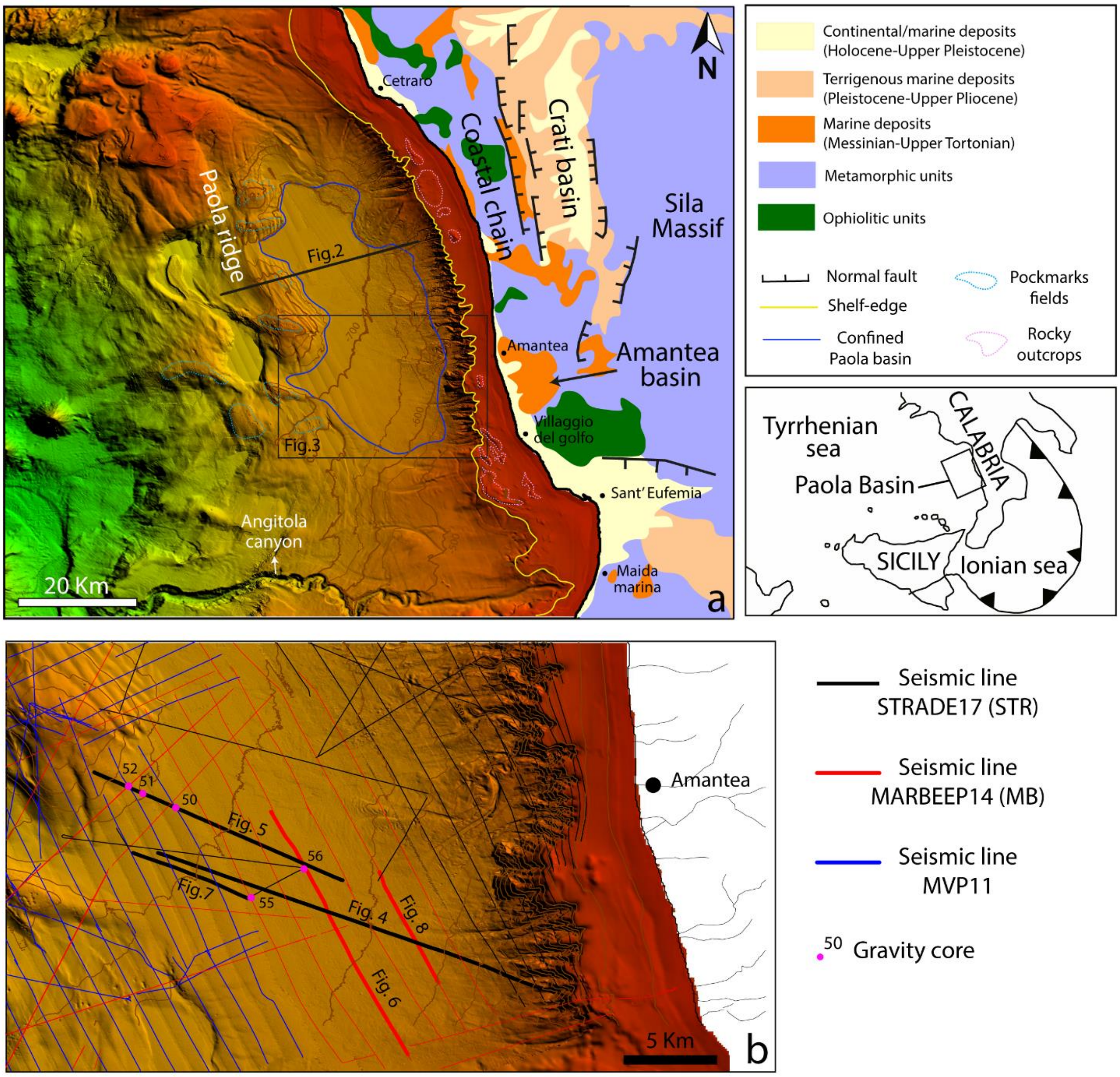

Figure 1 *(A) Shaded relief map of the Paola Basin and geological sketch map of the Northern Calabrian Arc (modified from Corradino et al., 2020).The study area is enclosed in the box. Contour line spacing is 50 m. (B) The location of the seismic profiles and gravity cores in the study area. CHIRP profiles shown in Figs. 4–8 correspond to the bold black lines. The different colors of the CHIRP lines correspond to different acquisition surveys as shown in the upper left legend.*

(Figure 1a). Submarine canyons are typically characterized by straight courses and develop sub-the slope base located at about 650- 700 m of depth. The trough of the confined Paola basin is about 45 Km long (NW-SE direction) deepening and narrowing to the north. The basin floor is about 8 Km wide where it is laterally confined by the counterslope of the Paola ridge (whose base is located at less than 750 m of depth) and widens (reaching about 12 Km of width) to the south where the degree of confinement is minor. This study focuses on the southern sector of the confined Paola Basin (Figure 1a).

2.2 Stratigraphy of the basin fill

The Paola basin fill is composed of a Plio-Quaternary sequence that reaches a maximum thickness of about 5 km, based on the seismic-stratigraphic correlation of the interpreted top of the Messinian (Y horizon in Figure 2a from Trincardi et al., 1995). The main basin fill is likely related to turbidite currents (Trincardi et al., 1995) that pinch-out towards the Paola Ridge which represents a geographical barrier for terrigenous input (Rovere et al., 2014). The Plio-Quaternary deposits are subdivided into three units, L, I, and U established in relation to the tectonic events that produced the slope ridges bordering the Paola basin (Trincardi et al., 1995). The deposition of units L and I are related to the growth of the ridge (Corradino et al., 2020; Trincardi et al., 1995). Whilst the

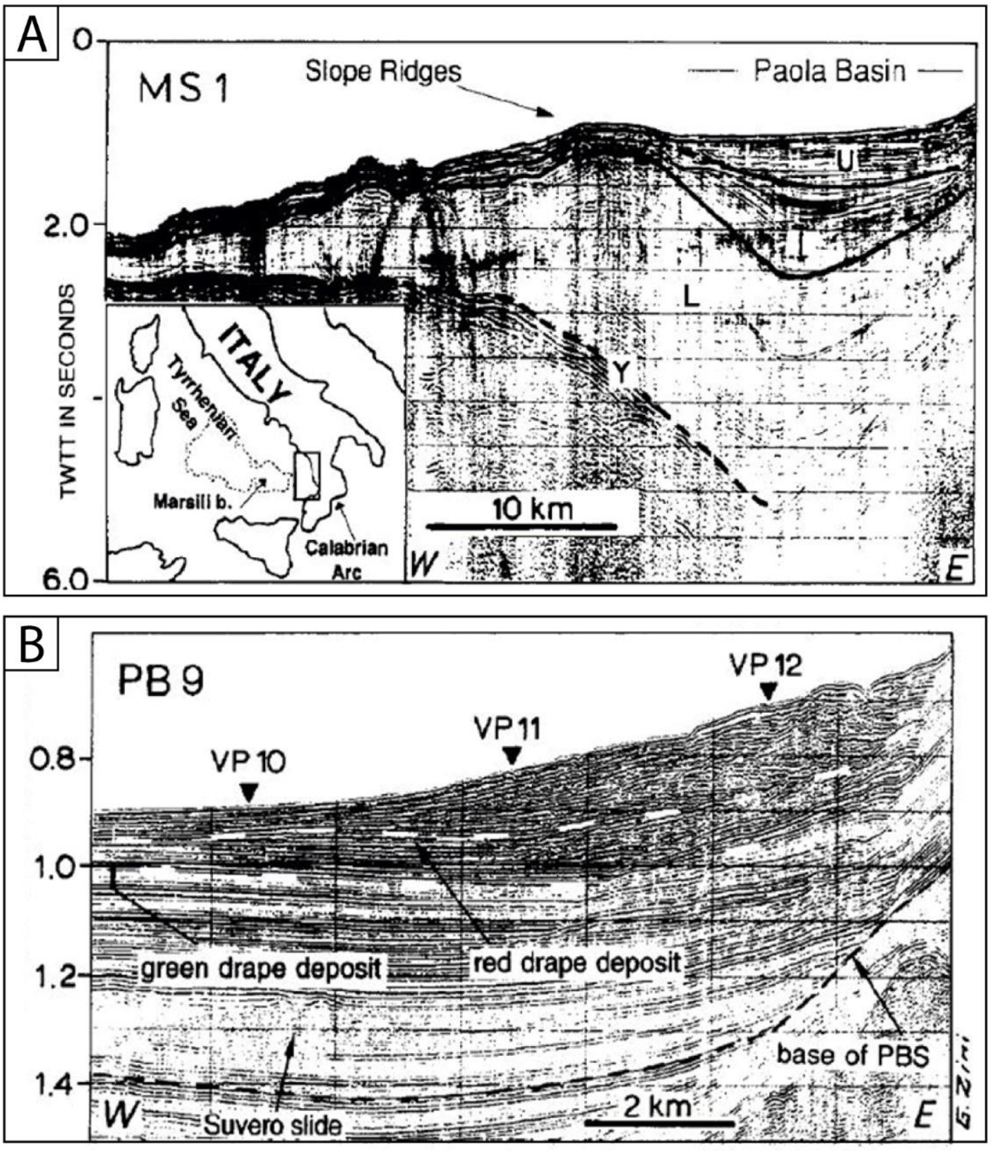

Figure 2 *(A) Multichannel seismic-reflection profile across the Calabrian margin. The uppermost unit, U, represents the Paola Basin System (PBS); underlying units and reflector Y are discussed in text. The location of the profile is reported with black bold line in Figure 1a. (B) Sparker seismic-reflection profile showing the green and red drape (bold dashed line) deposits that correlate throughout Paola Basin. Thin dashed line is the unconformity at the base of PBS. Vertical scale is two-way travel time in seconds.*

subunit U (also named PBS in Trincardi et al., 1995, Figure 2b), whose base is marked by an unconformity, is characterized by parallel and sub-horizontal reflectors and represents the post-tectonic filling of the through (Trincardi et al., 1995). The latter is consequent to the activation of multiple sediment sources along the adjacent Coastal chain (Argnani and Trincardi 1988) that created turbidite complexes in the basin. This stage presents vertically stacked, mounded and channelized deposits indicating the recurrence of turbidites associated to sediment input during low stands separated by draped deposits (green and red drape in Figure 2b) reflecting episodes of quiescence and deactivation of sediment entry points to the basin (Trincardi et al., 1995). The most recent of those drape deposits consists of an acoustically transparent seismic facies connected to the occurrence of mass-transport deposit and hemipelagic sedimentation during the late Quaternary, which correlates with the transgressive and highstand deposits on the shelf (Trincardi et al., 1995).

3. Methods

Multibeam bathymetric data, high-resolution seismic data and submarine cores represent our primary dataset. A major part of the study area is covered by a digital high-resolution terrain model. The latter consists of a mosaic of multibeam data acquired during three oceanographic surveys carried out in 2011, 2014, and 2017 (MVP11, MARBEEP14 and STRADE17 respectively, Figure 1b). The first two cruises were carried out on board the R/V Urania equipped with the multi-beam system Kongsberg EM710 (frequency 70-100 kHz). In general, given the frequency of the multibeam instruments and the depth range of the study area, the bathymetric data have a vertical resolution of less than 0.5 m. During the cruises the bathymetric measurements were carried out between 300 and 1,300 m of depth. The shallower areas, from 700 m to 150 m of depth, were investigated lately during STRADE17 executed with the R/V Minerva UNO presenting on board the multibeam system Seabat7160 (frequency 44 kHz). This equipment provides a higher resolution of 0.1 m. The acquired data has been merged with the EMODnet Project bathymetric data available on the continental shelf. The multibeam bathymetric data were imported and analysed using the Global Mapper® software for the production of contour and slope maps.

High-resolution subbottom data consists of seismic (CHIRP, Compressed High Intensity Radar Pulse) profiles, collected using the Chirp Benthos 179 III technology (frequency 2-7 kHz). This system is able to investigate the first 50 m of the sub-seafloor stratification with a vertical resolution in the order of 0.5 m. Alongside multibeam data, single- channel seismic lines were acquired with an average spacing of 1.5 km with direction parallel and perpendicular to the margin and to the Paola ridge (Figure 1b).

Observations from high-resolution profiles are combined with information derived from 5 gravity core samples to document depositional processes in the surficial sediments (from the seafloor to about 5 m of depth). Three gravity cores have been acquired in the basin floor (STR_GC_56-55-50) and two on the Paola ridge (STR_51-52) (Figure 1b).

4. Results

This section reports the results obtained from the interpretation of the morphological features on the study area derived from an extensive seafloor mapping (4.1). The interpretation of the available seismic profiles leads to the characterization of different units stacking in the first 20 m of sediments and their characterization in terms of acoustic facies (4.2). The last paragraph (4.3) reports the sedimentological characterization of the cores that sampled the upper part of the lobe and the overlying late Quaternary drape.

4.1 Morphological features in the study area

The morphobathymetric data show a complex physiography of the basin in the study area (black square in Figure 1a) where several morphological features occur on the continental margin (Figure 3). To the north, numerous instabilities occurred in recent times on the continental margin as testified by blocky landslide deposits located on the slope until -650 m of depth. Whilst a smoother deposit, interpreted as a finer grained debris avalanche, is more expanded to the north where it reaches -720 m of depth respect to the south. The slope in this sector dips towards the east forcing the landslide deposits to extend in this direction. Three canyon heads (Northern Amantea canyon, Figure 3) are located on the shelf in front of the Amantea town, where the shelf is at its lowest width (2 Km). Occasionally, when high-resolution data are available, gullies are recognized on the shelf behind the head of those canyons suggesting the occurrence of recent erosive processes. Gullies stretching the shelf from the outer shelf to the shelf edge were previously identified in other systems of the Tyrrhenian Sea and were interpreted to be related to flash-flood hyperpycnal flows, favoured by steep drainage basin and torrential regimes (Clementucci et al., 2022). The canyons alimented by gullies on the outer shelf present upslope crescentic bedforms in the talweg (Figure 3). In this location, canyons, previously discussed, are not straight but present more or less tight meanders in the upper slope while they become straight in the lower slope. Here the upper slope

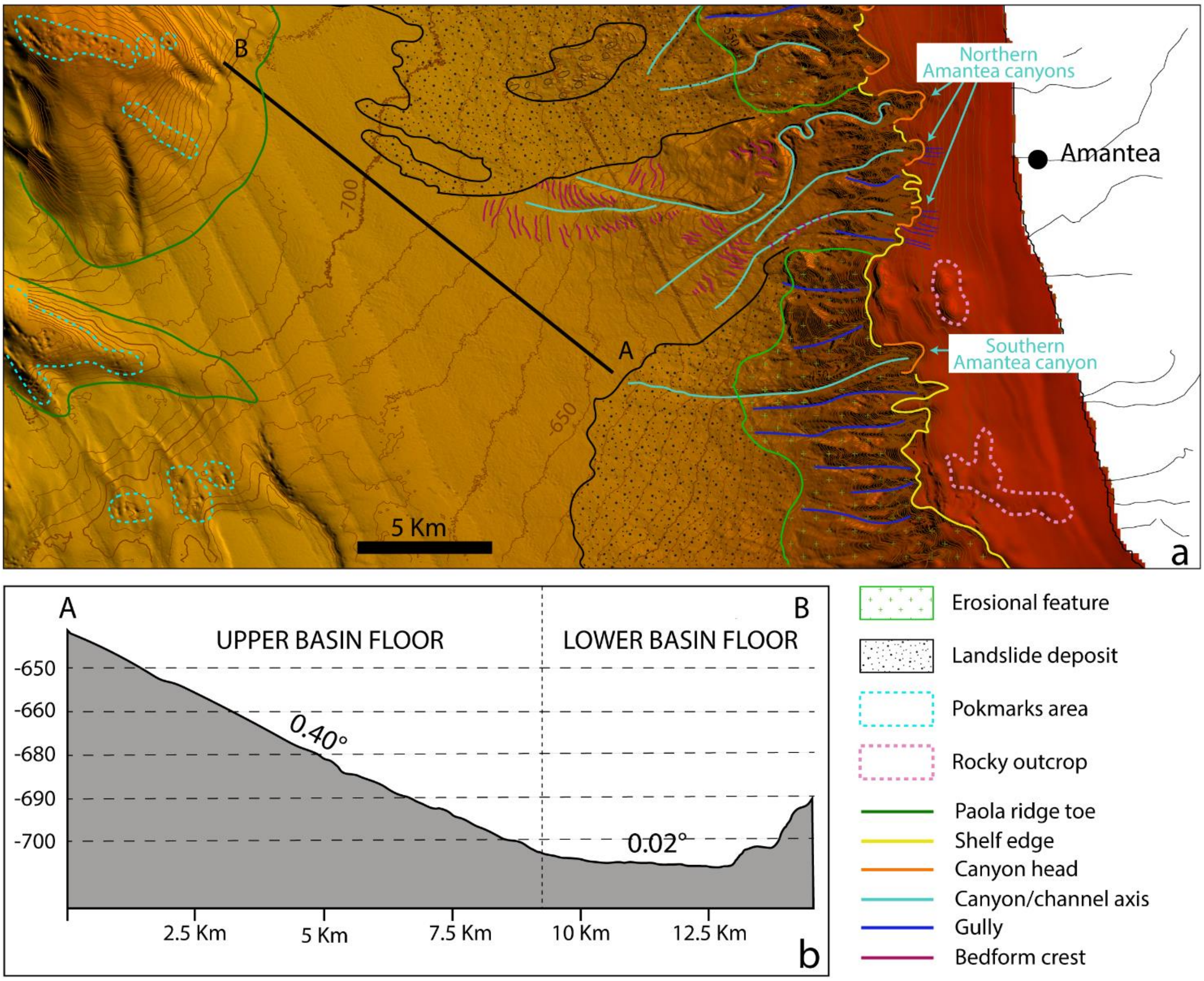

Figure 3 *(A) Geological map of the morphological elements in the study area. The principal linear and areal erosional (gullies, canyon/channel, canyon head, erosional feature) and depositional elements (bedform crest, landslide deposit) are reported, as the principal physiographic element, such as the shelf edge (yellow) and the toe of the Paola ridge (dark green). Contour line spacing is 10 m. (B) Seafloor profile (location in Figure 3a) show the articulate physiography of the basin floor characterized by an upper steep part (0.4°) and a lower almost flat sector.*

has value of about 2-3° while the lower slope is about 1.5°. Outside of a meander bend of the northern canyon, upslope crescentic bedforms are recognized as resembling the cyclic steps formed by turbidity currents outside of the Shepard Meander of the Monterey Channel (Fildani et al., 2013). Other bedforms are identified in the areas surrounding this channel in the lower slope, interpreted to be associated with levee deposits (Figure 3). To the south, where rocky outcrops occur on the shelf that thickens reaching about 4 Km, a straight canyon (Southern Amantea canyon) and gullies develop (Figure 3). Here the upper slope is steeper reaching about 4-5° while the lower slope is about 1.5° steep. The high values of the slope result in a widely incised slope (gullies and canyon) with landslide deposits occurring at its base. In this sector, the slope dips towards northeast. The basin floor, between the base of the slope and the base of the Paola ridge, can be subdivided into two sectors, an upper and lower basin floor, according to the slope value. The upper basin floor occurs from -650 to -700 m of depth, here the floor is on average 0.4° steep while the lower basin floor, starting from -700 m of depth, shows a flat morphology with slope on average 0.02° steep (Figure 3b). From the southern margin of the Paola ridge the basin floor starts to dip toward the southwest creating a corridor that connects the Paola basin to a deeper intraslope basin.

4.2 Seismic stratigraphy

This section reports the interpretation of the subbottom Chirp profiles that resulted in the recognition of six acoustic facies whose characteristics will be described in the following paragraph (4.2.1). The interpretation of the seismic profiles is reported the paragraph 4.2.2.

4.2.1 Acoustic facies

Taking into account the presence or absence of reflections, the relative amplitude of reflections, the geometry of reflectors (parallel, irregular, etc.), six different acoustic facies have been distinguished. The first word of the acoustic facies describes, when the reflections are present, their geometry (parallel or irregular) while, when the reflections are absent, is labelled as transparent; the second word describes the strength of the acoustic reflection (high or low):

Transparent Low-reflectivity (TL) Intervals lacking coherent reflectors with faint reflectivity

Parallel Low-reflectivity (PL) Parallel to subparallel, continuous to discontinuous, low-amplitude and high-frequency reflections.

Parallel High-reflectivity (PH) Parallel to subparallel, continuous to discontinuous, high-amplitude reflections and high-frequency reflections.

Irregular High-reflectivity (IH) Irregular and small-scale convex-shaped high-amplitude reflections.

Convex High-reflectivity (CH) Large-scale convex-shaped high amplitude reflections.

Transparent High-reflectivity (TH) Intervals lacking coherent reflectors but highly reflective, commonly reducing the penetration of acoustic energy.

4.2.2 Seismic profiles interpretation

The first 20 m of subsurface imaging reveals the stacking of five units (Drape 1, MTD 2, Amantea Fan, MTD 3, Drape 2 and Drape 3) characterized by different large-scale acoustic responses. A strongly reflective unit (TH, CH, IH and PH facies) is included between acoustically transparent units

(TL facies) (Figure 4). Since this unit is characterized by high-amplitude reflections, indicative of coarse-grained stratified deposits, it has been interpreted as a submarine fan (Amantea Fan). While the acoustically transparent units (TL facies) are generally associated to homogeneous fine-grained deposits. They have been interpreted as drape deposits (Drape 1-2-3) when their distribution is uniform all through the study area or as mass-transport deposits (MTD 1-2-3) when are areally circumscribed. The Amantea Fan lies above MTD 3 that gradually decreases in thickness and pinches-out towards WNW (Figure 3, 4, 5). The top of the Amantea Fan is capped by other acoustically transparent deposits, that are: 1) MTD 2, whose thickness decreases towards WNW and downlaps on the surface of the fan and 2) a drape deposits (Drape 1) that represents the more recent deposit in the basin (Figure 4, 5, 6, 7). Drape 1 is consistent with the late Quaternary drape deposit identified by Trincardi et al. (1995) and associated with a highstand of sea level.

The Amantea Fan is clearly recognizable in the seismic profiles from the upper basin floor until the surface of the Paola ridge where it gradually thins towards WNW. Parallel to the base of the slope (NW-SE), at about -650 m of depth, the Amantea Fan is characterized by a transparent highly-reflective facies (TH) scoured by 780 m-large concave erosional features (Figure 8). The depression of the channel promotes the higher accumulation of MTD 2 that is thicker in this position. In the upper basin floor, the fan expands towards NW and pinches-out towards SE over the southern margin of the northern Paola Basin (Figure 6). Here the fan is characterized by a 5 m-thick mounded morphology and internally present TH seismic facies. In addition, no erosional elements are identified in this portion, leading to the interpretation that, from this position, the Amantea Fan develops a depositional lobe, the principal object of this study. Parallel to the slope dip direction the proximal part of the lobe is characterized by some small-scale depressions, truncating the surrounding reflectors, these are interpreted as scours eroding the substrate (Figure 4, 6). Downslope, the surface of the lobe develops a wavy trend (Figure 4b). Where the top of the lobe is undulated, the seismic response is characterized by convex high-amplitude reflectors (CH facies), interpreted as depositional bedforms. The internal reflections dip towards SE highlighting the upslope direction of migration of the bedforms (Figure 4, 5, 7). The profile STR_196 crosses perfectly perpendicularly the crest of the bedform that present an upslope asymmetric cross-sectional shape (Figure 4b). Towards NW, where the slope steepens to 0.5° (Figure 4a), the reflectors exhibit an inclined trend (IH facies) and the overall thickness of the Amantea Fan decreases to 2.5 m (Figure 4, 7).

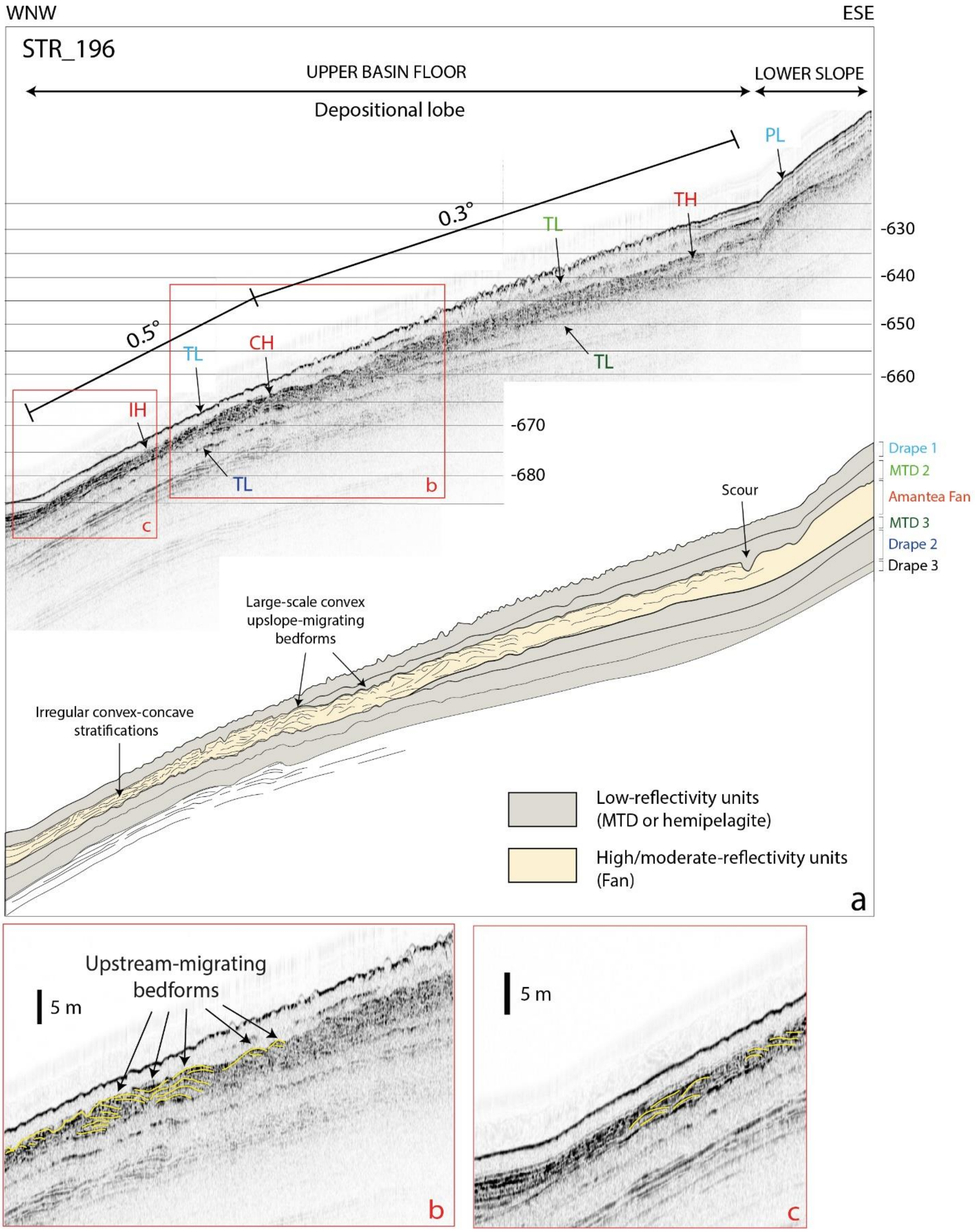

Figure 4 *(A) CHIRP profile STR_196 (profile track is reported in Figure 1a) crossing lower slope and upper basin floor in a WNW-ESE direction, the seismic facies are marked by arrows. Below the interpreted line drawing of the principal reflectors and the units comprised between them. The Amantea Fan (yellow) is enclosed between low-reflectivity units (gray) (B) Detail of the upslope migrating bedforms with upslope asymmetrical profile characterized by CH seismic facies (C) Detail of irregular convex and concave stratifications identified with IH facies.*

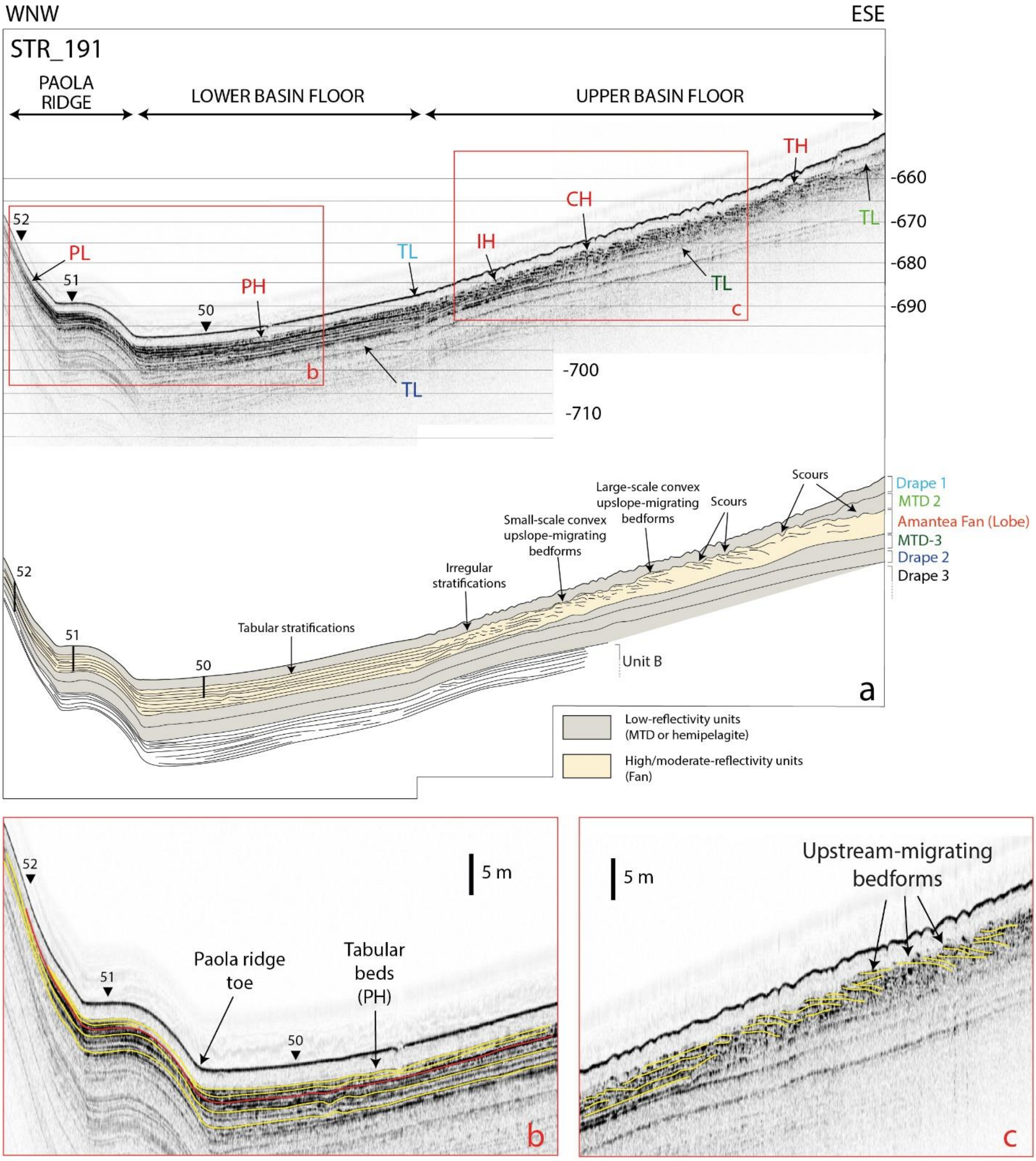

Figure 5 *(A) CHIRP profile STR_191 (profile track is reported in Figure 1a) crossing upper and lower basin floor and the Paola Ridge in a WNW-ESE direction, the seismic facies are marked by arrows. Below the interpreted line drawing of the principal reflectors and the units comprised between them. (B) Detail of the tabular beds in lower basin floor and on the surface of the ridge characterized by PH facies, the exact location of gravity cores (STR_GC_50-51-52) is reported. (C) Detail of the upslope migrating bedforms in the upper basin floor characterized by CH seismic facies.*

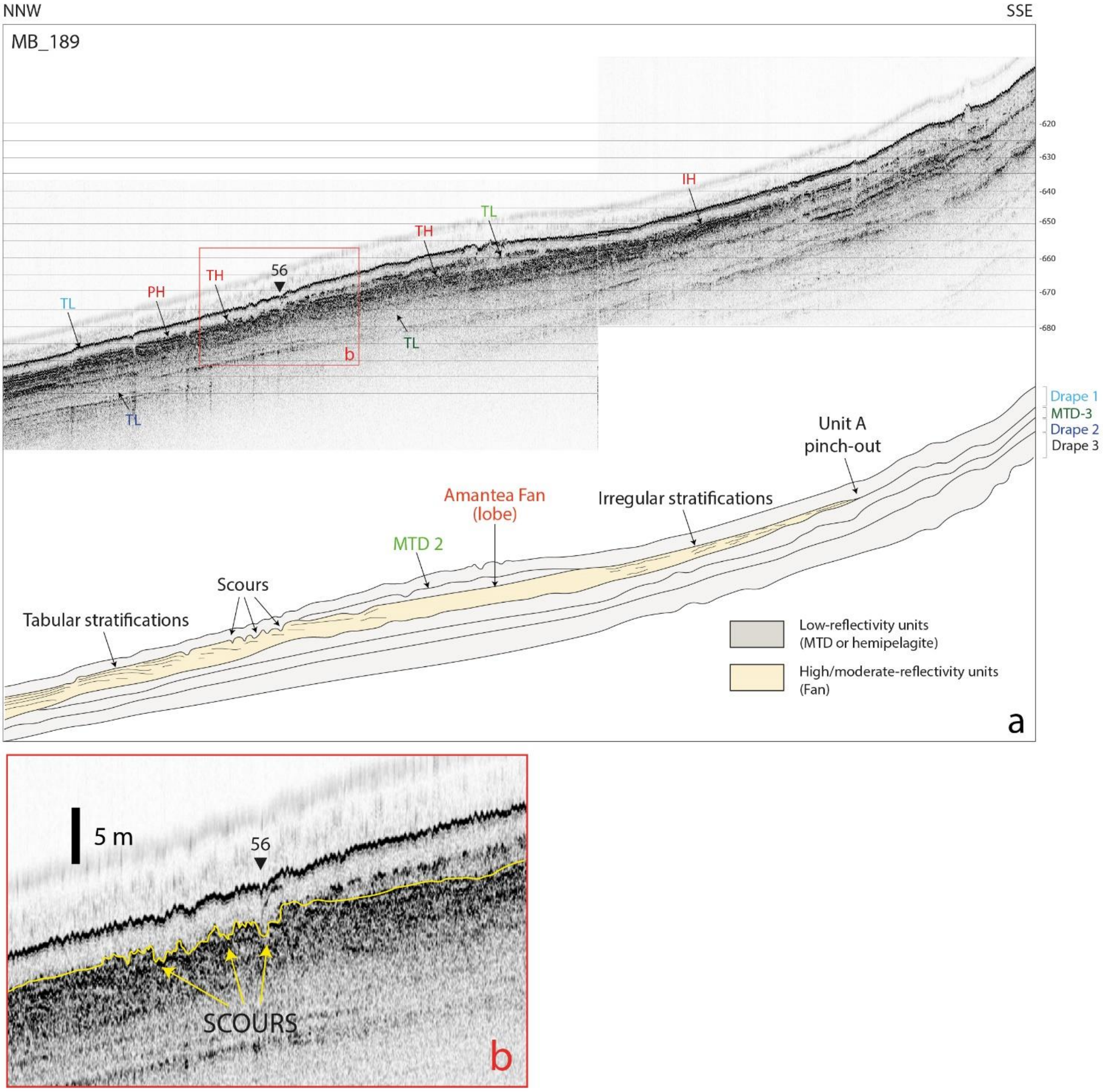

Figure 6 *(A) CHIRP profile MB_189 (profile track is reported in Figure 1a) crossing the upper basin floor in NNW-SSE direction, the seismic facies are marked by arrows. Below the interpreted line drawing of the principal reflectors and the units comprised between them. Note the pinching of the lobe towards SSE and the presence of scours towards NNW. (B) Detail of the scours where a sample (STR_GC_56) have been acquired.*

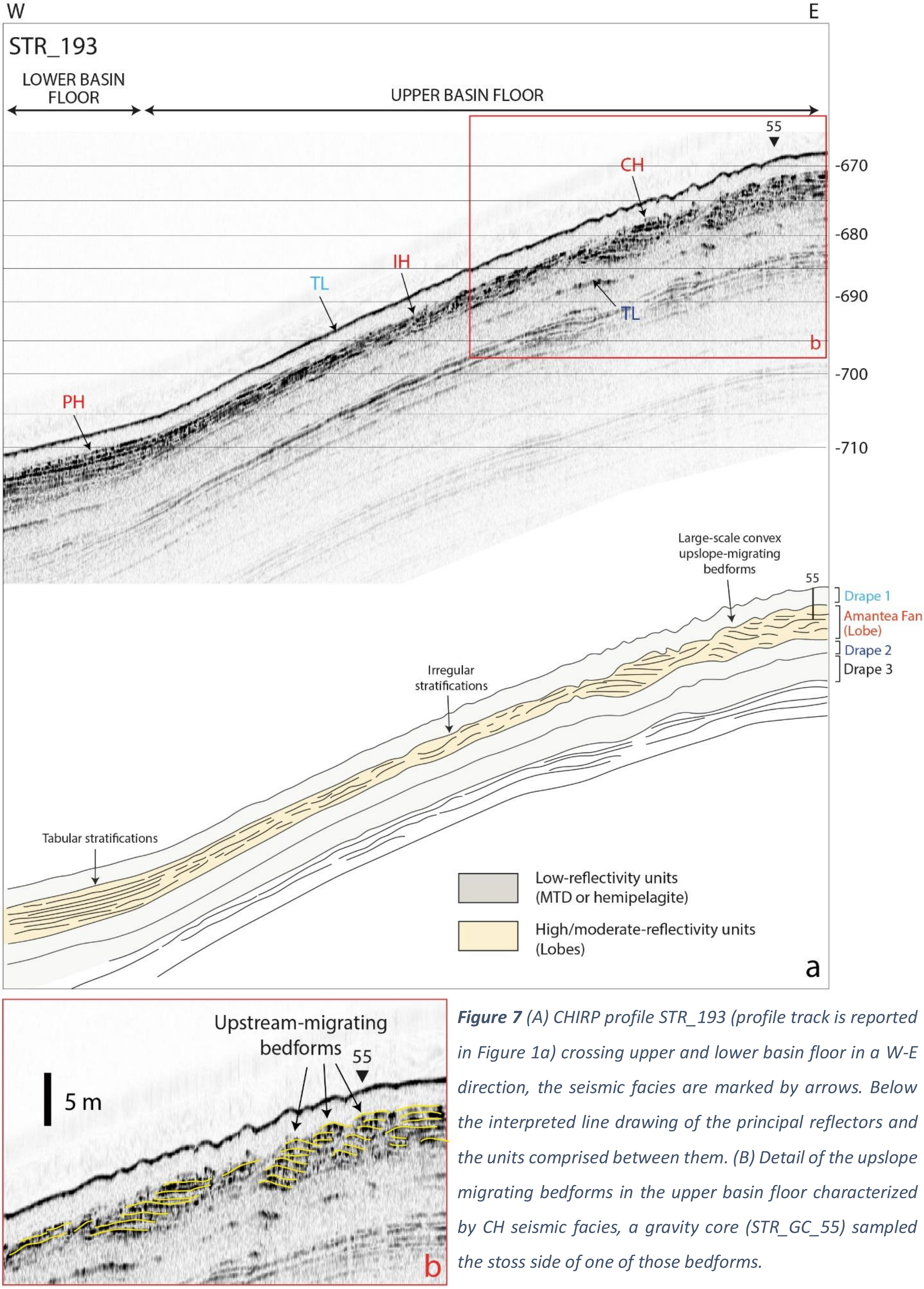

Figure 7 *(A) CHIRP profile STR_193 (profile track is reported in Figure 1a) crossing upper and lower basin floor in a W-E direction, the seismic facies are marked by arrows. Below the interpreted line drawing of the principal reflectors and the units comprised between them. (B) Detail of the upslope migrating bedforms in the upper basin floor characterized by CH seismic facies, a gravity core (STR_GC_55) sampled the stoss side of one of those bedforms.*

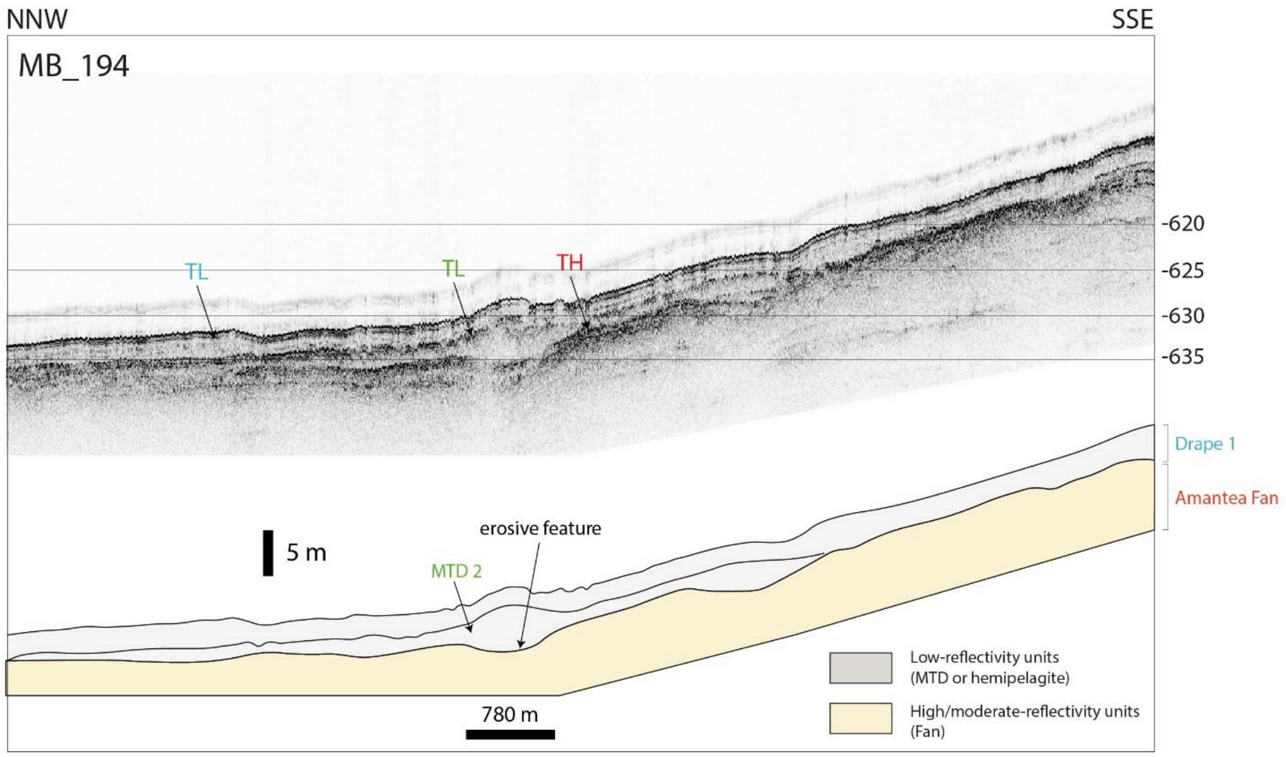

Figure 8 *(A) CHIRP profile MB_194 (profile track is reported in Figure 1a) crossing the upper basin floor in NNW-SSE direction, the seismic facies are marked by arrows. Below the interpreted line drawing of the principal reflectors and the units comprised between them. Note the depression, 780 m-wide and about 1.5 m deep, localized where the gradient of the slope decrease.*

Internally, this facies presents convex-shaped reflectors, but they are smaller and symmetrical respect to those that characterize CH facies (Figure 4c). The thickness of the fan increases in the lower basin floor where is seismically characterized by PH facies interpreted as tabular stratifications (Figures 5-7). The lobe reaches the maximum thickness (7.5 m) at the toe of the Paola ridge while, as previously said, it decreases in thickness until falls below the seismic resolution on its surface (Figure 5). Through the interpretation of the available seismic profile the extension of each unit in the study area has been mapped (Figure 9), except for the drape deposits since they are expanded all through the study area. The MTD 3 is extended in a W-E direction, it reaches -690 m of depth, its westward termination is uncertain. Above its surface, the lobe of the Amantea Fan expands for about 240 Km^2, pinching to the south and spreading to the north. Where the lobe presents convex-shaped reflections (CH and IH seismic facies) interpreted as bedforms, has been mapped and called as “Bedforms area” (Figure 9). The Bedforms area is 25 Km^2 and is stretched towards the west, in the direction of the corridor. The MTD 2 is at least 21 Km^2 and is elongated in a W-E direction (Figure 9).

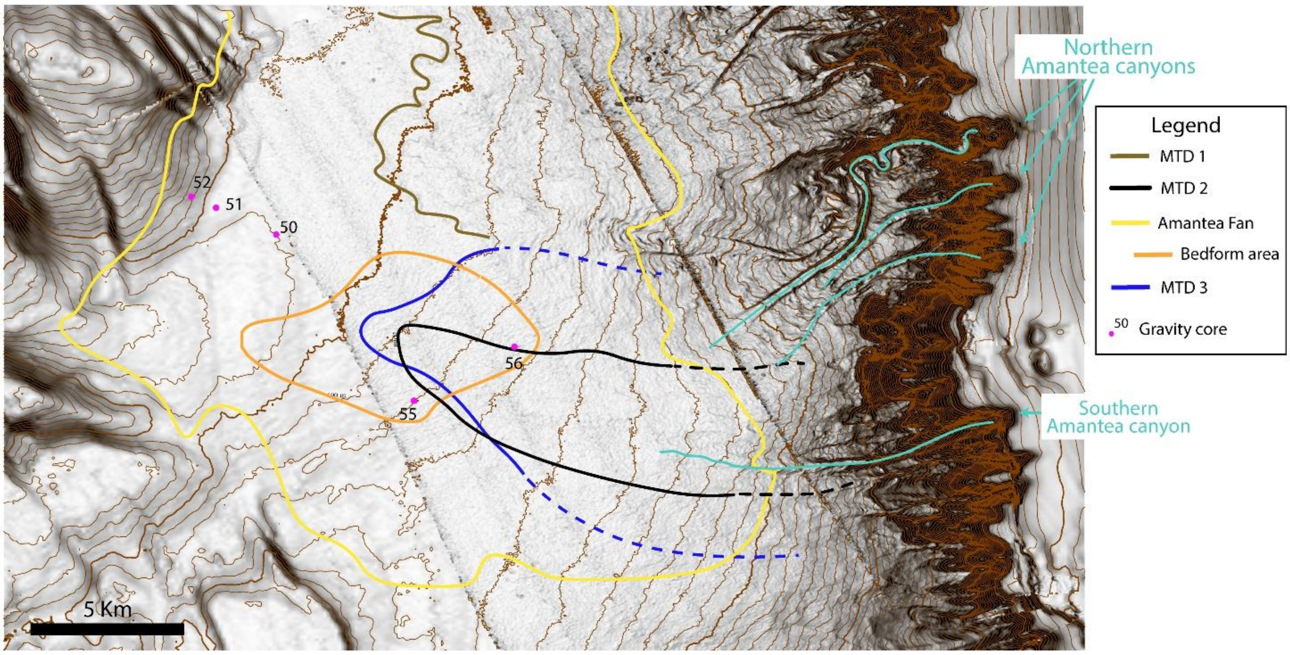

Figure 9 Map of the different units identified in the seismic profiles. Note the Amantea Fan (yellow) distribution that close on the southern margin of the basin and expand towards the north. Also the bedform area have been mapped (orange).

4.3 Cores sedimentological description

Five gravity cores sampled the Amantea Fan; two cores (STR_GC_56 and 55) are located in the Bedforms area in the upper basin floor, one core (STR_GC_50) is located in the lower basin floor and, finally, two cores (STR_GC_51 and 52) have been sampled on the Paola ridge. The cores in the upper basin floor create a transect 3.1 Km long directed SW-NE (Figure 10) whilst another transect 9.6 Km long cross the basin floor and the Paola Ridge in a NW-SE direction (Figure 11). All the cores recovered on average 2,4 m of muddy sediment corresponding to Drape 1 (Figure 10-11). The mud drape contains, typically at 30 cm of depth, the 7.9 A.D tephra layer of the Plinian eruption of Vesuvius (Trincardi et al., 1995). The 79 A.C tephra layer is a 2 cm thick bed composed by femic black tephra with a medium grain-size. Below the mud drape, the upper part of the lobe is sampled and contains turbidite beds. Another tephra bed (TB-2) occurs at about 3.7 m of depth in the basinal area, while it is shallower in the cores on the Paola ridge (2.3-3.2 m of depth). TB-2 is a key bed composed of very coarse to coarse sandstone in the northern cores (Figure 11) and a fine-grained sandstone in the southern STR_GC_55 core; its composition consists in femic tephra and pumice fragments (Figure 10). It is interpreted as a tephra layer and can be considered a key bed that facilitated and reinforced the cores-by-core correlation. The high-precision localization of the cores in the seismic profiles led to the connection of the facies associations to specific depositional elements (Table 1).

Table 1 *Location of the coring sites collected in the study area during the cruise STRADE 17, the recovery in meters of each core is reported as well as the type of depositional/erosional element sampled.*

Sample name	Recovery (m)	Depth (-m)	Latitude/ Longitude	Depositional/erosional element sampled	Sample location
STR17_GC_56	4.26	674	39°06’39.6074’’N/ 15°53’03.8396’’E	Scours	Fig.5
STR17_GC_55	3.67	680	39°05’41.9975’’N/ 15°51’16.9213’’E	Bedforms (Stoss side)	Fig.6
STR17_GC_50	4	710	39°08’38.9657’’N/ 15°48’50.4006’’E	Frontally-confined tabular beds	Fig.4
STR17_GC_51	5.2	703	39°09’07.1928’’N/ 15°47’46.2995’’E	Beds on Paola Ridge	Fig.4
STR17_GC_52	5.86	689	39°09’18.2524’’N/ 15°47’20.3993’’E	Beds on Paola ridge	Fig.4

STR_GC_56 (Scour)

The core is composed by an upper 2,75 m-thick interval of bioturbated mud where the TL facies have been recognized in seismic profiles (Figure 6b) and a lower 1.5 m thick interval corresponding to the TH facies (Figure 6b) composed of very coarse to medium-grained turbidite beds (Figure 10a). Those beds have a variable thickness ranging from very thin (2 cm) to thick-bedded (45 cm). Below the TB-2 layer, thin-bedded top-cut-out (*sensu* Postma et al., 2014) coarse-grained beds with traction carpets can be found (see Tb3 according to Postma & Cartigny, 2014 and F7pb according to Tinterri, 2022 in preparation, respectively facies schemes in Figure 10 in Chapter 1). They have a slightly erosive base. Conversely, the bed above the TB-2 layer, presents an erosive base testified by the deep scouring of the substrate, able to rework the underlying TB-2 (Figure 10b). Flame structures occurs at the base of this bed (Figure 10b). It is composed by massive basal sand (Ta, F8f in Figure 10b) and laminated top (Tb2, F8l in Figure 10b). The upper turbidite bed has an erosional base and is composed of very coarse-grained massive sand with mudclasts occurring at the base and near the top (Ta; F5d, Figure 10b). Aligned mud clasts mark the occurrence of an amalgamation surface, also highlighted by the overlying sediment with a coarser-grain size. All these beds are characterized by sharp tops with evident grain-size breaks (i.e., the fine-grained portion is absent). These beds have been sampled in the trough of a scour in the proximal lobe area (Figure 6b).

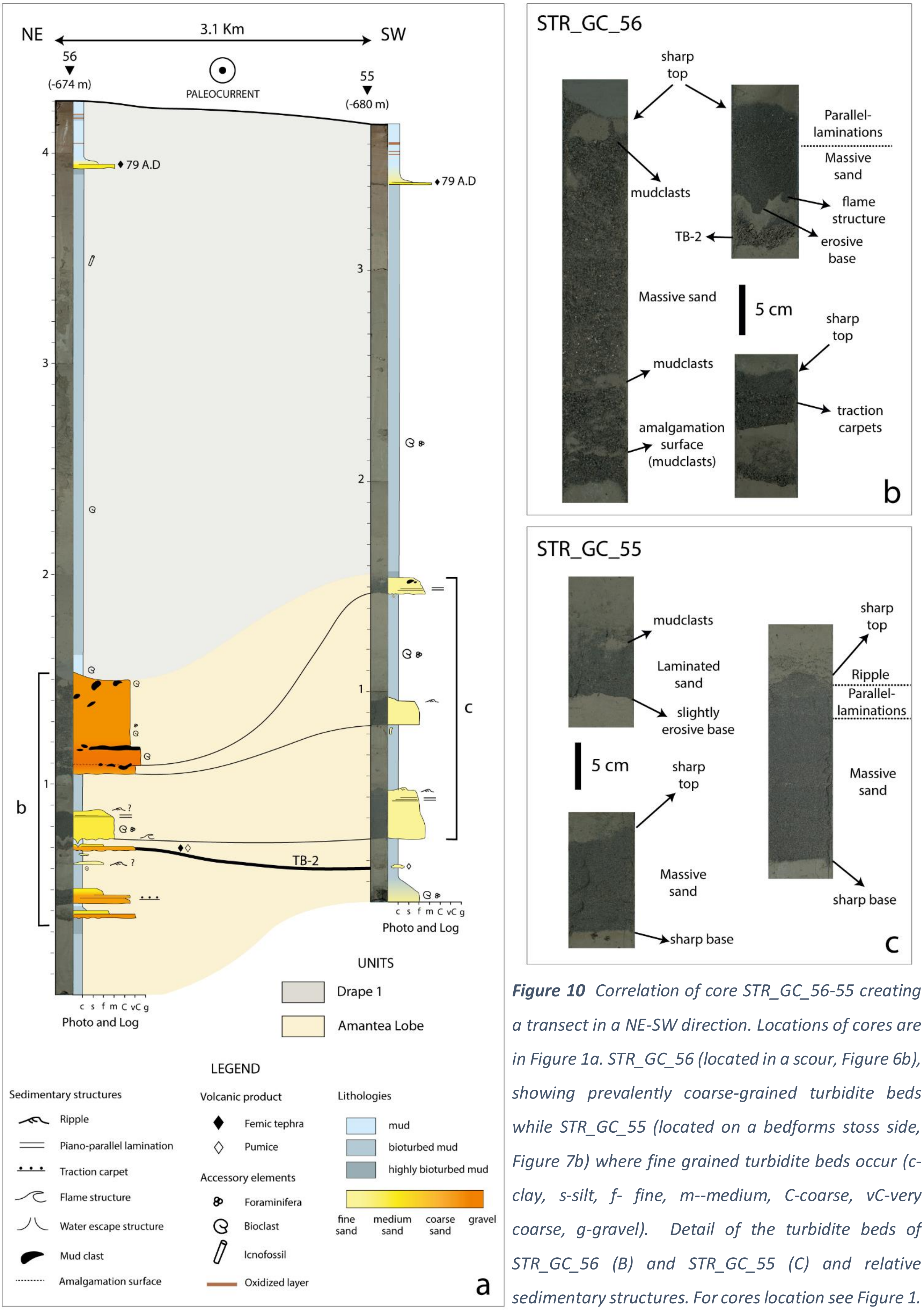

***Figure 10** Correlation of core STR_GC_56-55 creating a transect in a NE-SW direction. Locations of cores are in Figure 1a. STR_GC_56 (located in a scour, Figure 6b), showing prevalently coarse-grained turbidite beds while STR_GC_55 (located on a bedforms stoss side, Figure 7b) where fine grained turbidite beds occur (c-clay, s-silt, f- fine, m--medium, C-coarse, vC-very coarse, g-gravel). Detail of the turbidite beds of STR_GC_56 (B) and STR_GC_55 (C) and relative sedimentary structures. For cores location see Figure 1.*

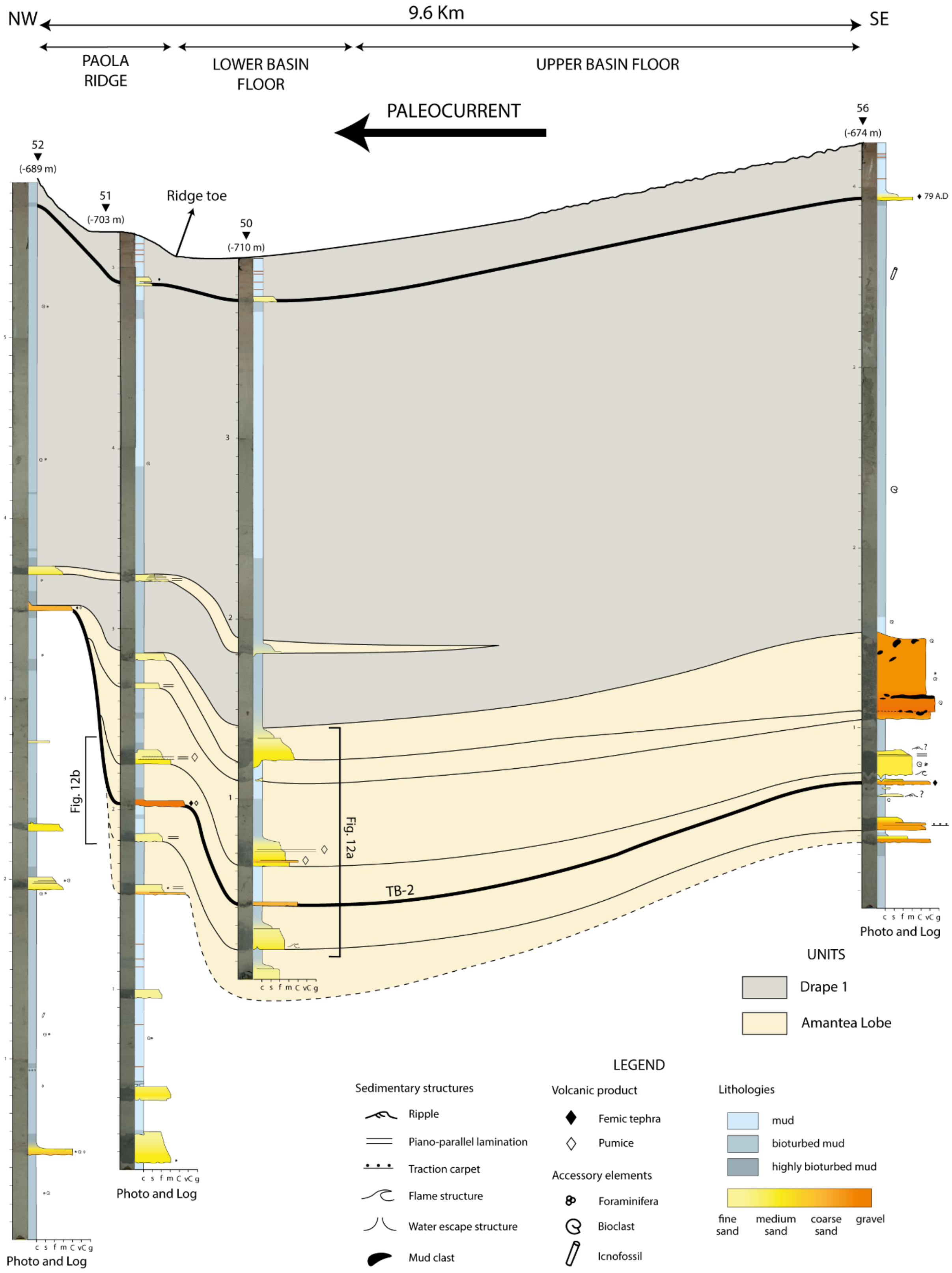

Figure 11 *Correlation of core STR_GC_56-50-51-52 creating a transect in a NW-SE direction. Locations of cores are in Figure 1a. The correlation highlight that most of the beds onlap on the surface of the Paola Ridge and are absent in STR_GC_52. STR_GC_50, that sampled the tabular beds in the lower basin floor (Figure 5b) where medium grained turbidite beds occur, while STR_GC_51 (located on the Paola Ridge) prevalently sampled thin bedded fine-grained turbidites (c-clay, s-silt, f- fine, m--medium, C-coarse, vC-very coarse, g-gravel).*

STR_GC_55 (Bedform stoss side)

The core is composed by an upper interval, 2,6 m thick, of bioturbated mud where the TL facies have been recognized in seismic profiles (Figure 7b) and a lower 1.6 m thick interval corresponding to the CH facies (Figure 7b) composed by fine-grained turbidite beds (Figure 10a). The thickness of the turbidite beds range from thin-bedded (8 cm) to thick bedded (37 cm). The base of those beds is sharp or slightly erosive and some trace fossils occur. These beds are composed by massive fine-grained basal sands (Tb4, F8m) in which laminations (Tb1) and ripples (Tc) can be found at the top, the silt fraction is absent and consequently the beds pass upward into a clay division through a sharp contact (top-cut out-bed, Figure 10c). Some mudclasts can occur at the top. These beds have been sampled in the proximal lobe area where train of upslope-migrating bedforms are identified (Figure 7a). The core has been sampled on the stoss side of one of those bedforms (Figure 7b).

STR_GC_50 (Frontally-confined tabular beds)

The core is composed by an upper interval (2,1 m) of bioturbated mud where the TL facies have been recognized in seismic profiles (Figure 5b) and a lower 1.4 m thick interval corresponding to the PH facies (Figure 5b) characterized by turbidite beds composed of medium-grained sand (Figure 11). They have an almost constant thickness of about 15 cm (medium-thick beds). The base of these beds is erosional or slightly erosional with small-size flames structures (Figure 12a). These beds are normally graded with massive bases made of medium-grained sand (Ta, F8f), sporadically pumice laminae are found; these basal divisions pass upward into fine-grained sands (Tb1) and silt (Td). The turbidite beds are sampled in the distal lobe area, in the lower basin floor, where tabular beds occur (Figure 5b).

STR_GC_51 and 52 (Beds on Paola Ridge)

Fine-grained beds are recognized in STR_GC_51 and 52. The core STR_GC_51 is composed by an upper interval (2,3 m) of bioturbated mud where the TL facies have been recognized in seismic profiles (Figure 5b) and a lower 2,9 m thick interval corresponding to the PH facies (Figure 5b) composed of thin-bedded fine-grained beds (Figure 11). They are principally normally graded beds characterized by plane-parallel laminations (Tb1-Td, F9) (Figure 12b). Also in this case pumice laminae can be found. These beds are prevalently located above the proximal part of the Paola Ridge.

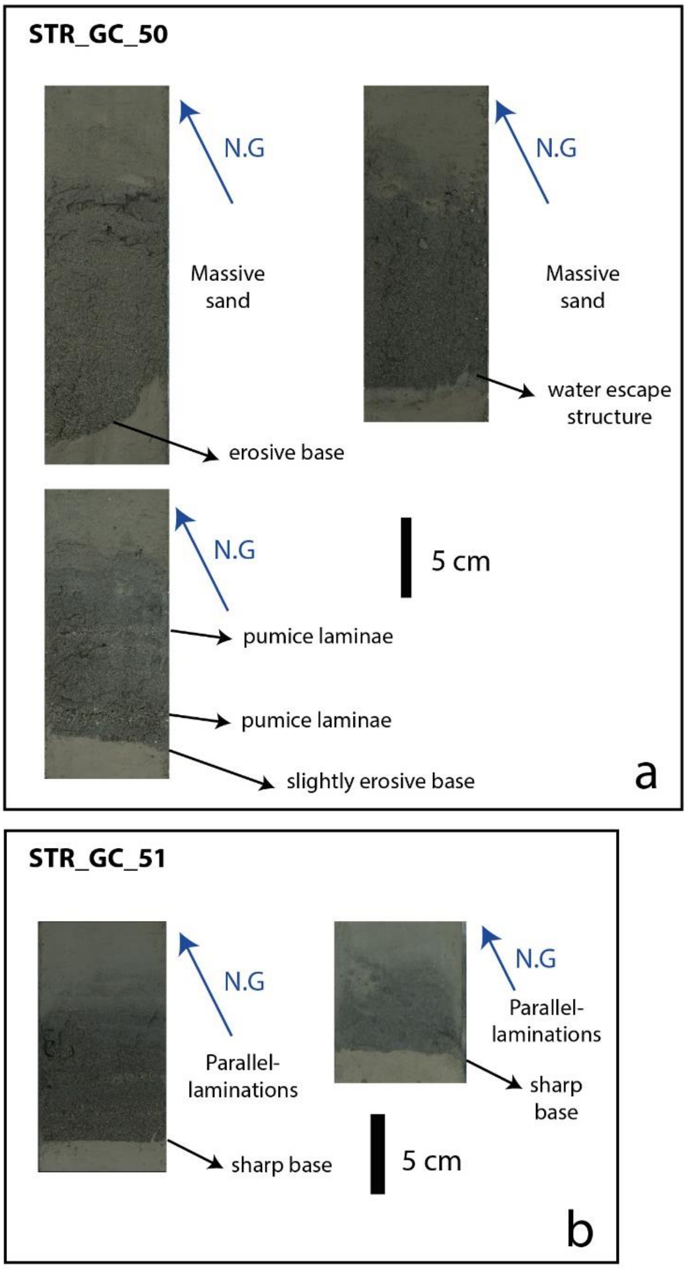

Figure 12 *Detail of the turbidite beds of STR_GC_50 (B) and STR_GC_51 (C) and relative sedimentary structures. The location of the core in Figure 1a and 5b.*

While the core STR_GC_52 is composed of an upper interval (2,3 m) of bioturbated mud where the TL facies have been recognized in seismic profiles (Figure 5b) and a lower interval corresponding to the PL facies (Figure 5b). The cores correlation (Figure 11) and the picking of the reflector in the seismic profile (Figure 5b) reveal that the TB-2 key bed is the only bed occurring also in the other cores to be sampled in this location.

The sedimentological analysis of the cores combined with the seismic facies interpretation allowed the calibration of the lithology for most of the seismic facies except the IH facies (Table 2).

***Table 2** Seismic facies recognized in the Acquarone Fan and their relative lithological interpretation calibrated with gravity cores. The units and the setting where the facies are recognized are reported.*

Seismic facies	Brief description	Gravity core	Lithological interpretation	Setting	Unit
TL	Transparent, faintly reflective	STR_GC_56-55-50-51-52	Relatively homogeneous and bioturbated mud	Expanded all throughout the study area	MTD 1-2-3 Drape 1-2-3
PL	Parallel, low-amplitude reflections	STR_GC_52	Well stratified fine-grained beds	Paola ridge	Drape 1
PH	Parallel, high-amplitude reflections	STR_GC_50-51	Well stratified medium to fine-grained beds	Lower basin floor	Amantea Fan
IH	Irregular and small-scale convex, high-amplitude reflection	na	Fine-grained beds with variable thickness	Upper basin floor	Amantea Fan
CH	Large-scale convex, high-amplitude reflections	STR_GC_55	Well stratified fine-grained beds with variable thickness	Upper basin floor	Amantea Fan
TH	Transparent, highly reflective	STR_GC_56	Very coarse to coarse-grained beds sporadically amalgamed	Upper basin floor	Amantea Fan

5. Discussion

5.1 Identification of the lobe source area

Understanding the location of the source area is not a simple process where continental margins are widely incised by canyons as the Paola Basin slope (Figure 3). In order to understand the orientation of the identified depositional and erosional elements respect to the main flow direction it is unavoidable the identification of the source area. To reach this goal, the distribution of the main depositional elements will be analysed in relation to the morphology of the basin. The basin floor dips towards NW (Figure 1a), for this reason the canyons located to the north of the study area are excluded as source areas since their southward expansion would be limited by the counter slope.

Mapping the Amantea Fan (Figure 9) the importance of confinement has been highlighted. The lobe extends towards the west, in this direction it is confined by the Paola ridge on whose surface most of the beds onlap and close (STR_GC_52, Figure 11), and to the north following the slope gradient. This configuration could be potentially created both by Northern and Southern Amantea canyons or by a combination of their sedimentary supply. The suspect pool is narrowed thanks to the interpretation of the seismic profiles. Perpendicularly to the slope direction, the lobe has a mounded shape and present high thickness value in front of the Southern Amantea canyon (Figure 6). Moreover, bedforms cross-sections, that are parallel to the flow direction, are imaged by STR_196 seismic profile directed WNW-ESE (N 300°, Figure 4). For this reason, the more probable source area has been identified in the Southern Amantea canyon (Figures 3 and 9). The axis of this canyon is directed W-E that, combined with a NW dipping slope, could perfectly fit with turbidity currents flowing from ESE to WNW. On the contrary, the northern canyons are principally directed in a SW-NE direction; turbidity currents flowing in this direction on the slope are not expected to have a clockwise turn of about 60° on such low dip slope values. Anyway, a combined sedimentary supply also from the Northern Amantea canyon cannot be completely ruled out during the formation of Amantea Fan. In conclusion, the Southern Amantea canyon is identified as the most probable source area for the lobe and relative depositional and erosional elements analysed.

5.2 The Amantea lobe-type

The lobe analysed in this work is prevalently depositional throughout the study area. Its deposition is clearly recognized from the base of the lower slope where coarse-grained sediments (TH facies) are found (Figure 4-8). Near to the channel mouth the Amantea lobe does not present large-scale erosional features like amalgamated scours or plunge pools. The only erosive element identified is a small depression that, according to its proximity to the channel mouth, it could more probably represent the downslope termination of the feeder channel (Figure 8). The absence of large erosive elements near the channel mouth highlights that the Amantea Fan does not present the channel-lobe transition zone (CLTZ). Generally, CLTZ are absent in low-efficiency systems that principally produce attached lobes (Mutti & Normark, 1987; Wynn et al., 2002). Considering the geological setting (intraslope basin), the distribution of the lobe in relation to the position of the channel mouth, and the absence of erosional features typical for CLTZ, the lobe here presented can be interpreted as a low-efficiency sand-rich attached lobe.

5.3 From the data to the flow dynamics

Recent experimental and field studies have identified that both sub- and supercritical turbidity currents have characteristic facies associations (e.g., Postma & Cartigny, 2014, Tinterri, 2022 in preparation). The most superficial turbidite beds of the lobe have been sampled in different depositional and erosional elements and relative facies have been assigned. The applied facies schemes are focused to understand the criticality of the flow through the interpretation of different facies associations (see Figures 8 and 10 in Chapter 1).

In the upper basin floor some erosional (scours) and depositional elements (upslope migrating bedforms) generally associated to the action of supercritical turbidity currents have been found (Figures from 4 to 7). In particular, the presence of scours is generally associated with the occurrence of hydraulic jumps, able to erode the substrate. In fact, the characteristic sedimentary signature of a hydraulic jump includes scours overlain by structureless, coarse-tail graded sediments associated with flame structures and other disrupted material (i.e mudclasts) (see Postma et al., 2009, 2014; Postma & Cartigny, 2014; Tinterri, 2022 in preparation). The two more superficial turbidite beds, sampled in the trough of a scour located parallel to the principal flow direction, present the sedimentological characteristics mentioned above (Figure 10b) and thus they are interpreted as hydraulic jumps deposits (Figure 13a). These beds are overlain by thin-bedded top-cut-out beds with traction carpets (Figure 10b). The occurrence of coarse-grained traction carpets is usually associated with rapid flows with relatively high-fall out rates, related to supercritical high-density turbidity currents (Postma et al., 2009; Tinterri, 2022 in preparation). The passage from supercritical flow conditions to hydraulic jump is typical of cyclic step dynamics; in particular, this transition occurs from the lee side of the cyclic step to the through (Figure 13a). The cyclic steps in this position are interpreted to be net-erosional due to the high-erosive power of the turbidity currents (i.e., scour and erosive bases).

Laterally to the principal flow direction, the core STR_GC_55 is sampled in the stoss side of a depositional bedform (Figure 7). The train of bedforms are internally characterized by upslope migrating reflectors. Generally, the upslope migration is associated with the action of supercritical turbidity currents and in particular with cyclic steps deposition (Cartigny et al., 2014; Postma et al., 2014; Slootman & Cartigny, 2020). On the stoss side of cyclic steps, the flow is subcritical and prone to deposition. Traction is the prevalent transport mechanism resulting in stratified beds with top-cut-out (Postma & Cartigny, 2014). In particular, sampled turbidite beds are sharp-based fine-grained with top-cut-out of the silt portion (Figure 10c). This facies sequence well fits with the deposition of low-density turbidity current in subcritical flow conditions on the stoss side of a cyclic step (Figure 13a). In particular, they have been interpreted as depositional cyclic steps since no erosional features occur.

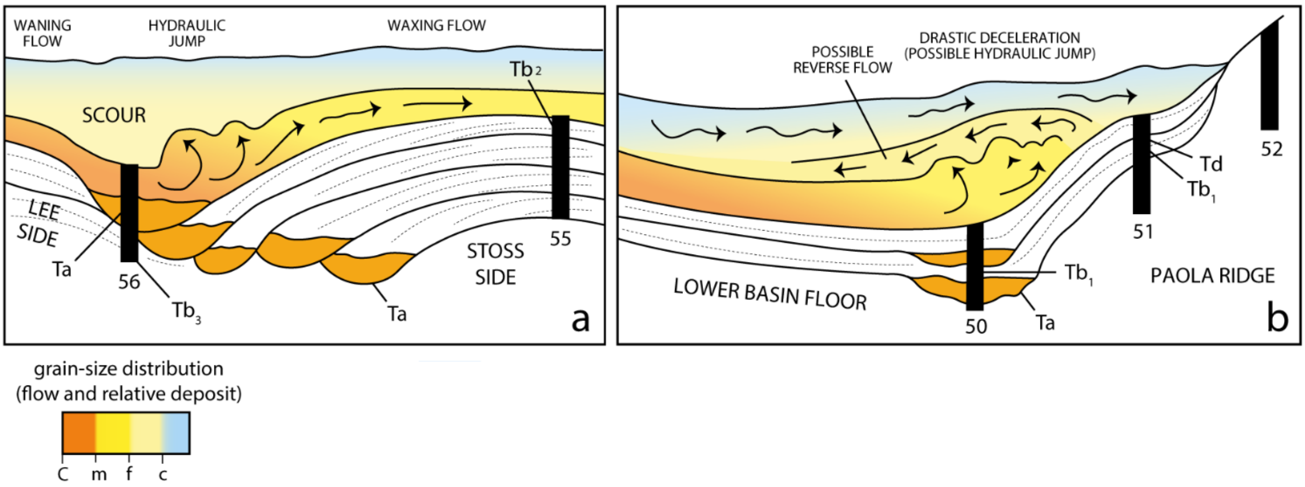

__Figure 13__ Interpretation of the flow dynamics according to the sedimentological facies (A) Cyclic step construction with supercritical flow on the lee side, resulting in traction carpets, hydraulic jump in the scour, equivalent to the massive facies, and subcritical flow on the stoss side where tractive structures occur. (B) Flow dynamic relative to the interaction between turbidity currents and frontal confinement possibly producing a hydraulic jump at the toe of the ridge (marked by massive facies with flames structures) and the production of a reverse flow.

Downslope respect to the depositional cyclic steps mostly irregular concave and convex reflections (IH facies, Figure 6) occur. An upslope migrating pattern is still recognizable, indicating that the flows were still supercritical crossing the basin floor, but a clear cross-sectional shape of the related bedforms cannot be identified.

Parallel to the flow direction, in the lower basin floor, turbidity currents impacted against the surface of the Paola Ridge. Numerical modelling (Howlett et al., 2019), tank experiments (Patacci et al. 2015; Soutter et al., 2021) and field studies (Tinterri et al. 2016, 2022) on frontally-confined basin show that turbidity currents arrived at the fold backlimb counter-slope, were decelerated from supercritical to subcritical and were abruptly inflated. In fact, the topographic constriction of the segment increased the flow thickness causing a reflected overflow bore of dilute suspension (Howlett et al., 2019; see also models deriving from field studies by Tinterri et al. 2022). The beds at the base of the ridge toes are prevalently massive with flames structures testifying the high fall-out rate of the basal dense part of the flow in this position (Figure 12). This facies is associated in these facies schemes to the possible occurrence of hydraulic jump at the toe of the ridge (Figure 13b).

They exhibit a normal grading trend recording the passage and/or the partial collapse of the upper turbulent low-density part of the flow (Figure 12). This facies can be related both to the deposition from a waning and depletive flow or to a reflected and ponded turbidity current (see Tinterri et al., 2016, 2022 for more details) (Figure 13b).

Turbidity currents impacting above a morphologic high result in the progressive onlap of the beds against the barrier (Figure 11). Fieldwork studies revealed that the topographic confinement promotes the decoupling of the upper turbulent flow able to ascend the morphologic high and the final collapse of fine-grained turbidite beds on its surface (Tinterri & Tagliaferri, 2015). In the same way, the core located on the surface of the Paola ridge presents fine-grained beds with low regime tractive structures. Those beds well fit with the deposits from low-density subcritical turbidity current (Postma & Cartigny, 2014; Tinterri et al., 2022 in preparation).

In conclusion in the upper basin floor (gradient of about 0.4°) high-density supercritical turbidity currents characterize the lobe axis region where erosive cyclic steps occur, while low-density supercritical turbidity currents flow through the off-axis region resulting in prevalent depositional upslope-migrating cyclic steps. In the lower basin floor (0.02°) the turbidity currents are interpreted to be high-density and supercritical while turning into subcritical passing through the hydraulic jump at the toe of the ridge. Whilst only low-density subcritical flows are able to overcome the frontal morphological high represented by the Paola ridge.

5.4 Influence of confined topography on the behaviour of turbidity currents

Topographically complex slopes occur when tectonic processes or deformation of the sea floor crate topographic lows or highs that can affect the path and behaviour of gravity-driven flows traveling downslope. In this case study, turbidity currents were completely frontally confined by the Paola ridge while laterally were slightly confined by the counterslope of the southern margin of the Paola basin. This physiography of the basin, principally dipping towards NW, led the turbidity currents to expand northward respect to the source area (Figure 9). Moreover, the basin floor in the study area has an articulate topography with an upper basin floor 0.4° steep and an almost flat lower basin floor. The lobe in upper basin floor area performs erosional and depositional cyclic steps while in the lower basin floor consists of tabular beds. Recent studies highlighted that cyclic steps appear to occur in certain ranges of slope gradients ranging from 0.26° to 1.24°(Zhang & Dong, 2020), the concentration of cyclic steps in the upper basin floor and their absence in the lower slope is coherent with this data and confirm the strict relation between slope gradient and supercritical flows.

In the steeper sector of the upper slope (0.5°, Figure 4), the thickness of the lobe decreases respect to the upslope and downslope area, indicating that supercritical turbidity currents partially bypassed this area. If a supercritical flow presents low aggradation rates the resulting deposit is characterized by approximately planar and thinner laminae and in a worse preservation of the bedform profile (Cartigny et al., 2014), a similar behaviour is interpreted to occur in this sector. It can be thus interpreted that even a small variation of slope degree can drastically change the relative deposit from supercritical turbidity currents and obscure the shape of the relative bedform and its internal stratifications.

Submarine lobe deposits are generally considered to thin and fine radially away from the channel mouth, resulting in the traditional radial distribution of grain-size characterizing unconfined lobe deposits (Bouma, 1962; Mutti & Ricci Lucchi, 1972; Talling et al., 2012). Anyway, modern tank experiments highlighted that confining topography drastically deforms the classical lobe-shaped geometry and the flow velocity pattern. In particular experiments on laterally confined flows observed a longitudinal expansion of the high-velocity high-density part of the flow respect to unconfined flows and a drastic wining of the flow perpendicularly to the flow direction (Soutter et al., 2021). This evidence is also supported by various field studies in tectonically controlled mini-basins showing how the basin morphology and lateral confinement can control the geometry and rate of expansion of the jet flows (Amy et al., 2004; Cunha et al., 2017; Mutti & Tinterri, 2004; Tinterri et al., 2016, 2017, 2022). In this case, the flows appear to have a slightly homogeneous transport capacity in the flow axis while it drastically decreases from the axis to the off-axis area. A similar grain-size distribution can be hypothesized for the turbidity currents building the lobe. In fact, the turbidite beds acquired perpendicularly to the flow direction, 3 Km apart one from the other, perform a drastic decrease in grain-size, from very-coarse in the lobe axis to fine in the lobe off-axis (Figure 14a-c). While parallel to the flow direction a minor difference in grain-size is observed, from very-coarse in the upper basin and medium in the lower basin, even if the cores are more than 9 Km apart (Figure 14a-b). The lobe is interpreted to have a narrow high-velocity and high-density flow in the lobe axis promoting erosion of the substrate (scours) while only the low-density part of the flow is able to ascend the counterslope of the southern margin. The slower, but still supercritical, velocity of the upper turbulent part of the flow increases the depositional rate away from the flow axis resulting in the deposition of upstream migrating bedforms.

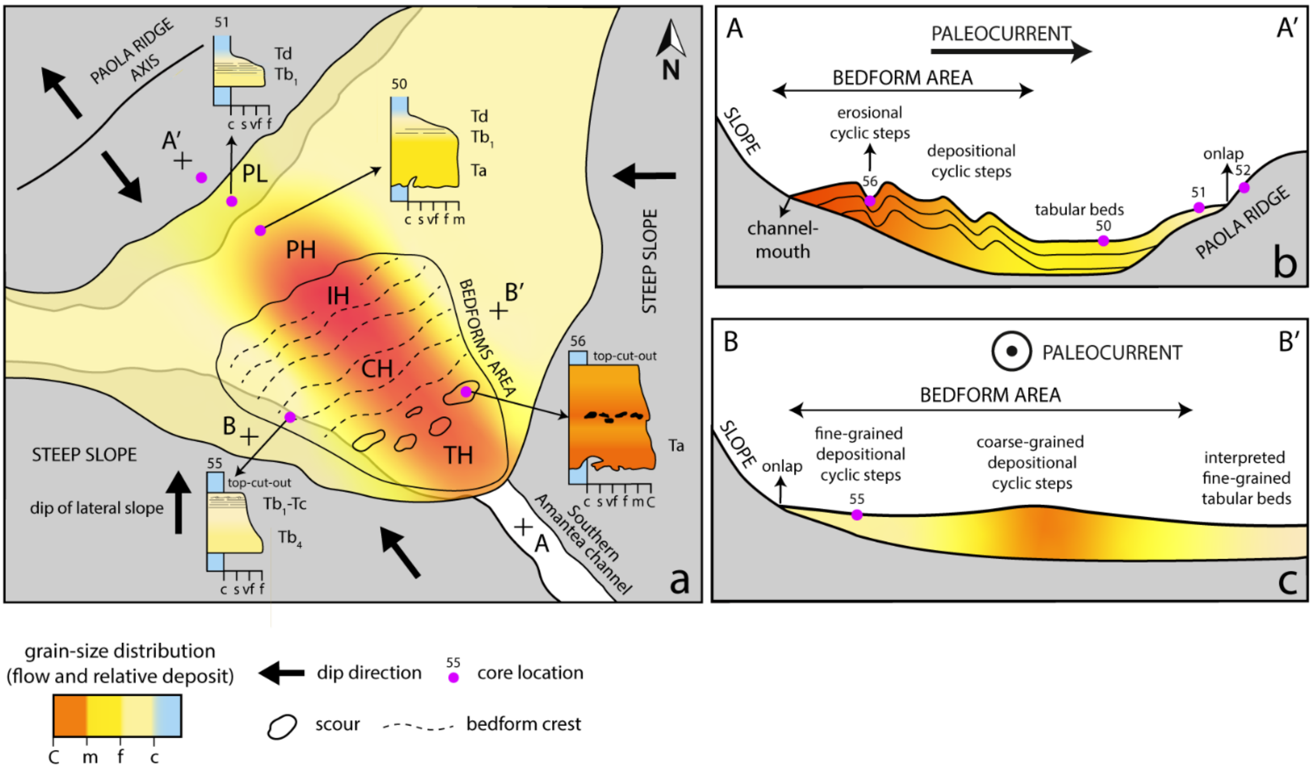

Figure 14 (A) Summary sketch of the different facies associations according to their different location in the lobe. The graded colours represent the interpreted grain-size distribution inside the flows. Profile parallel (B) and perpendicular (C) to the flow direction (localization in insert A) showing the variation of erosive and depositional elements and their relative grain-size.

The sudden deceleration with possibility to form a hydraulic jump at the toe of the ridge can form a thicker deposition of sediment upstream of the barrier. This type of hydraulic jump (defined as upstream hydraulic jumps by Soutter et al. 2021) is strongly controlled by the topography of the basin and depends on the Fr number of the incoming flow in relation to the degree of deceleration of the flow. The occurrence of this type of topographically-induced deceleration and possible hydraulic jump has been observed in tank experiments (Hamilton et al., 2017; Pohl et al., 2020; Soutter et al., 2021) and numerical modelling (Howlett et al., 2019) but the relative deposit of this process in sandy lobe or basin plain deposits have been rarely recognized in outcrops and in seismic studies. In tectonically controlled low efficiency systems, hydraulic jump facies related to high density turbidity currents against a lateral bounding slope have been recognised by Tinterri et al. (2016, 2017) and Cunha et al. (2017) in the Ranzano Sandstones (northern Apennines, Italy) and Annot Sandstones (western Alps, France). In more efficient turbidite systems characterized by efficient substrate erosion and mud incorporation, the toes of proximal morphologic highs are often characterized by hybrid beds marking instantaneous flow decelerations (Muzzi Magalhaes &

Tinterri, 2010; Tinterri & Tagliaferri, 2015). These field studies also show that with a decrease in flow efficiency and an increase in tectonic confinement there is a progressive disappearance of hybrid beds. Consequently, our study is not only one of the few that highlights these processes in seismic and core analysis studies but further confirms how in these low-efficiency systems the deceleration due to morphological obstacle tend to produce massive sand-rich beds rather than hybrid beds as in high-efficient turbidite systems.

6. Conclusions

The lobe of the Amantea Fan is an example of a frontally and laterally confined, channel-attached sandy lobe, whose deposition occurred during the last falling stage, in which seafloor topography plays an important role in controlling the style of deposition. Interpretation of the lobe geometry and its internal stratifications allowed the identification of the feeder system consisting in the Southern Amantea canyon. The interpretation of the seismic profiles and the analysis of the samples acquired on the surface of the lobe, parallelly and perpendicularly to the principal flow direction (300° N), led to the identification of different depositional styles. In the upper steep basin floor the lobe resulted to be composed by a bedform area (with erosional and depositional cyclic steps) that evolve downslope, in the flat floor, in tabular stratification and onlap of the surface of the Paola Ridge. For the first time, supercritical bedforms in a submarine lobe have been sampled in two distinct positions, in the scour of an erosional cyclic step and in the stoss side of a depositional cyclic step. Coarse to medium grained massive sand with flame structures, generally associated with the occurrence of hydraulic jumps, have been identified in the scour and at the toe of the ridge. The latter represents an example of topographically induced hydraulic jump driven by a frontal confinement, a phenomenon previously observed in tank experiments and numerical modelling and rarely in the field (see above). Fine sand with tractive structures and top-cut-out have been sampled on the stoss side of a cyclic step recording the passage, after the hydraulic jump, to the subcritical phase. The distance from the source area and the dip of the slope are here assumed to be the major factor controlling the observed fan-lobe depositional style. The lateral confinement is determined as the principal controlling factor for the grain-size distribution resulting in a narrow high-density turbidity current in the flow axis while the laterally confined area is reached by lower-density off-axis turbidity currents. On the whole, the present study broadens the understanding of the range of processes that are driven by the interaction between turbidity currents and seafloor topography. The recognition that the topography influences the density structure and the degree of criticality of the flow and consequently the morphodynamics and facies of the relative deposits may help to explain sediment distribution and improve depositional models of fan lobe in confined settings.

Chapter 4

“Small-scale facies change in relation to the articulate seafloor topography in two lobes of the Paretaio Turbidite System (Marnoso-arenacea Formation, Northern Apennines)”

1. Introduction

The Marnoso-arenacea Formation (MAF) is the most studied and one of the more famous turbiditic succession of the world. Its great exposure and poor post-depositional deformation made this formation the perfect case study for both the elaboration of regional-scale geological reconstruction of the foredeep basin morphology and detailed sedimentological analysis that give great insight into the turbiditic deposition dynamics (Ricci Lucchi & Valmori, 1980; Amy & Talling, 2006; Muzzi Magalhaes & Tinterri, 2010; Tagliaferri & Tinterri, 2016; Talling, Amy, et al., 2007; Tinterri & Muzzi Magalhaes, 2011; Tinterri & Tagliaferri, 2015). Most of these studies relate on the high-resolution stratal correlations over significant distances on the other hand, very few are the works whose main focus is related to short and small-scale sedimentological variation (Cattaneo, A. & Ricci Lucchi, 1995; Eggenhuisen et al., 2010; Fonnesu et al., 2015; Tinterri & Tagliaferri, 2015).

The Unit VI of the MAF (*sensu* Tinterri et al. 2016) was deposited during the upper Serravallian in an important tectonic phase that took to the transition from an inner and highly-efficient basin to an outer poorly-efficient basin (Mutti et al., 2002; Mutti & Ricci Lucchi, 1972; Ricci Lucchi, 1981, 1990). Thrust-related (M. Castellaccio thrust) fold grew within the foredeep leading to the creation of the outer basin where a large-scale mass-transport complex (MTC) and structurally controlled turbidites (Paretaio Turbidite System) deposited. The seafloor topography should thus be anything but flat at that time, with topographic highs and relative lows. Infact, thickness variations of the strata of Paretaio Turbidite System (PTS), observed in a direction parallel to the M. Castellaccio thrust, have been interpreted as two morphologic highs and a depocentre in the middle (Tinterri & Tagliaferri, 2015). In this depositional setting, the substrate topography can influence the dynamics of the sediment gravity flows, thereby forming a flow-substrate feedback mechanism.

The effect of seafloor topography on sediment gravity flows and their deposits have been studied through outcrop data (Amy et al., 2004; Muzzi Magalhaes & Tinterri, 2010; Puigdefabregas et al., 2004; Tinterri et al., 2016, 2017, 2022; Tinterri & Tagliaferri, 2015), subsurface data (Deptuck et al., 2008; Gamberi et al., 2014; Scacchia et al., 2022), numerical (Howlett et al., 2019) and physical models (Amy et al., 2004; Kneller, 1995; Kneller et al., 1991; Patacci et al., 2015; Soutter et al., 2021). Those studies revealed that the interaction between topographic changes and turbidity currents alterates the fairly uniform radial spreading and deceleration of flows, and development of elongate to lobate sedimentary bodies with predictable facies transitions.

Moreover, natural and experimental studies revealed that hydraulic jumps can occur when flows are forced to decelerate in relation to their orientation respect to an obstacle (Howlett et al., 2019; Soutter et al., 2021) created a by tectonic process (Tinterri et al., 2017; Tinterri & Tagliaferri, 2015) or by previous deposits relief (i.e lobe) (Hamilton et al., 2015, 2017; Hoyal & Sheets, 2009; Postma et al., 2016; Postma & Kleverlaan, 2018). Hydraulic jumps are most commonly associated with channelized flows (Hage et al., 2018; Zhong et al., 2015), flows over levees (Fildani et al., 2006; Scacchia et al., 2022), or slope breaks (Pohl et al., 2020). The prevalence and character of hydraulic jumps and their associated deposits are less well understood in topographically-complex settings.

Recognition of this feedback is very important because it provides a natural window on the flow processes controlled by a small-scale topography capable of affecting flow dynamics. In our case, the great lateral continuity of the outcrops of the study area permits high-resolution bed correlations that well highlight small facies changes occurring on a short distance. This paper aims to advance insight into processes within turbidity currents by studying variability of sedimentological characteristics and facies around the identified small-scale topography. In particular, the objectives of this work are: 1) to give a detailed characterization of two lobes of the PTS belonging to the MAF (Northern Apennines), deposited during the Upper Serravallian in a confined foredeep basin; 2) to strictly characterize the small-scale seafloor topography previously identified in the study area and 3) to understand the relationship between the topography and the turbiditic sedimentation through a detailed sedimentological facies description and granulometric analysis.

2. Geological setting

This work focuses on the Paretaio turbidite system, one of the units of the MAF (Unit VI introduced by Tinterri and Tagliaferri, 2015). This formation was deposited in the foredeep basin created by the flexure of the Adria plate in front of the growing Apennine orogenic wedge from the late Burdigalian to Tortonian age (Figure 1A). The MAF is more than 4000 m thick and consists principally of siliciclastic turbidites and sporadic mass-transport complexes (Figure 1B). The origin of the turbidites is linked to fluvio-deltaic systems located in the emergent Alps, in the Teritiary Alpine basins, that were able to produce turbidity currents flowing towards SE following the direction of the elongate, NW-SE-stretched foredeep basin (Figure 1A). The MAF foredeep basin had a very articulate shape, it was fragmented through a series of structural highs and depocentres related to the major thrust-faults (i.e Monte Nero, Monte Castellaccio, and Santa Sofia) running roughly parallel to the main NW-SE trend (Figure 1C). Ricci Lucchi (1986) divided the MAF stratigraphic succession into two different phases or basins related to a well-defined degree of confinement: (a) Inner stage (Langhian to upper Serravalian, Figure 1B) with highly efficient basinal turbidite systems (as meant by Mutti, 1992) and associated hemipelagic deposits that pass upward into (b) Outer stage (Tortonian to lower Messinian, Figure 1B) to characterized by “mixed” low efficiency (as meant by Mutti et al. 2003) sandstone-rich turbidites deposited in a narrowed foredeep. More recently, several works (Muzzi Magalhaes & Tinterri, 2010; Tinterri & Muzzi Magalhaes, 2011; Tinterri & Tagliaferri, 2015) stressed the importance of the “transitional phase” (Figure 1B), upper Serravallian in age, that records the progressive displacement of the main depocenter from the inner to the outer basin due to the growth of an important regional structure represented by the Monte Castellaccio thrust-related fold (CTRF) within the foredeep (Figure 1C). This stage differs from the older deposits of the inner stage (Unit I, II, III and IV in Muzzi Magalhaes & Tinterri, 2010; Tinterri & Muzzi Magalhaes, 2011) for the absence of key beds with hybrid and carbonate composition coming from the south due to the progressive closure of the foredeep and for the appearance of large-volume MTCs and thick accumulation of sandstone lobes in the thrust-related structural depressions. Recently the deposits of the transitional phase have been divided into two units by Tinterri & Tagliaferri 2015) : Unit V, known in literature as the Firenzuola turbidite system (Mutti et al., 2002; Tagliaferri & Tinterri, 2016; Tinterri & Tagliaferri, 2015) and the Unit VI, corresponding to the Paretaio turbidite system (PTS) (Mutti et al., 2002; Tinterri & Tagliaferri, 2015) (Figure 1C).

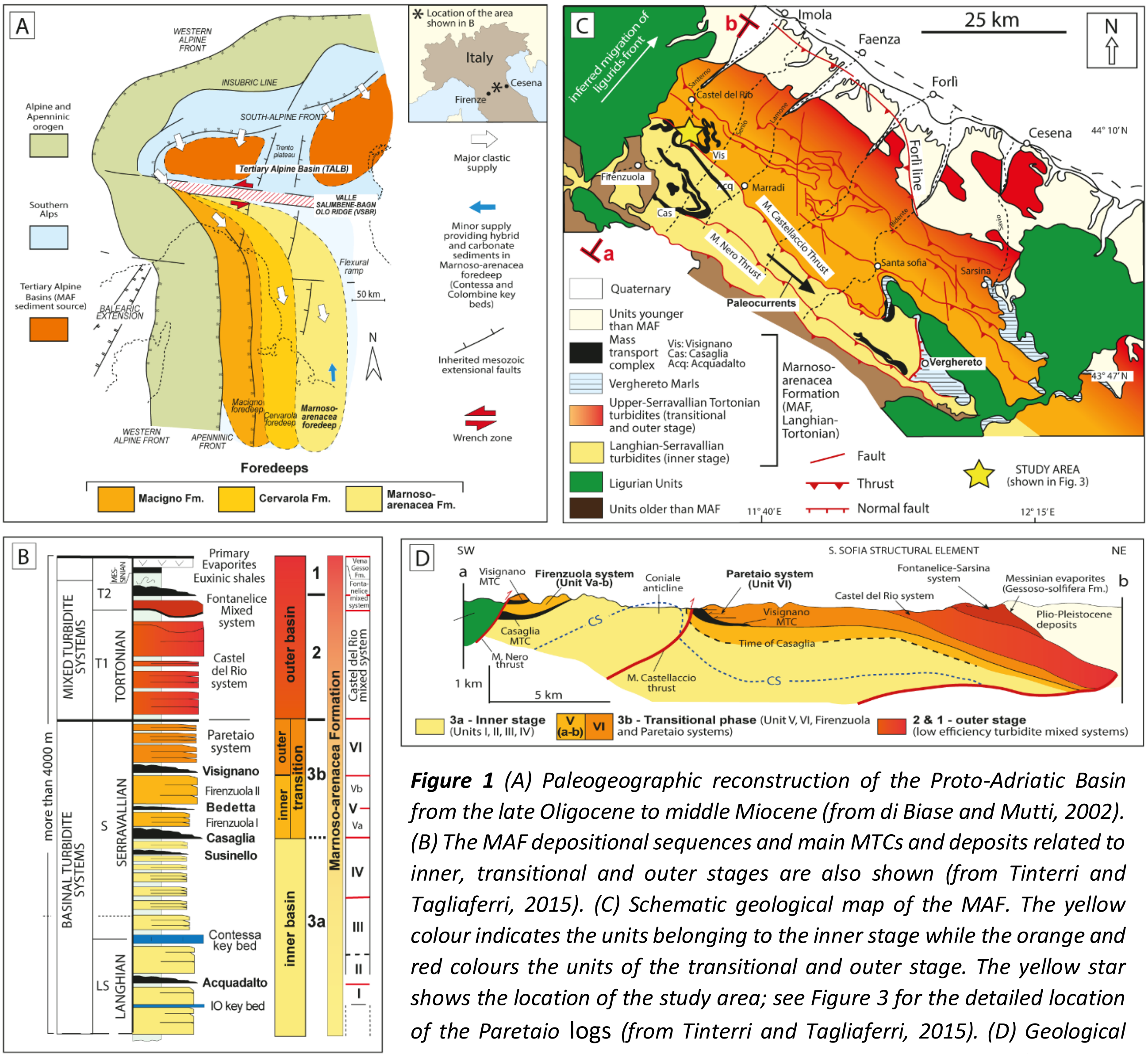

Figure 1 *(A) Paleogeographic reconstruction of the Proto-Adriatic Basin from the late Oligocene to middle Miocene (from di Biase and Mutti, 2002). (B) The MAF depositional sequences and main MTCs and deposits related to inner, transitional and outer stages are also shown (from Tinterri and Tagliaferri, 2015). (C) Schematic geological map of the MAF. The yellow colour indicates the units belonging to the inner stage while the orange and red colours the units of the transitional and outer stage. The yellow star shows the location of the study area; see Figure 3 for the detailed location of the Paretaio* logs *(from Tinterri and Tagliaferri, 2015). (D) Geological cross-section transverse to the basin axis showing the position of the major thrust faults: the M. Nero and the M. Castellaccio (from Tinterri and Tagliaferri, 2015).*

The deposition of the PTS took place from the upper Serravallian age during a strong phase of propagation of the CTRF that led to the closure of the inner basin with the consequent shifting of the main depocenter in the outer basin where the turbidites of this unit were deposited (Figure 1C). The first deposits of the outer basin are the mass-transport deposits of the Visignano MTC a heterogeneous chaotic body composed of extra- and intrabasinal sediments (Lucente, 2004, Figure 1A). The Visignano olistostrome has an irregular top surface and is sealed by decametric-thick fine-grained deposits which pinch drastically towards SW and are onlapped by the turbidites of the Paretaio system (Tinterri and Tagliaferri, 2015).

3. The Paretaio Turbidite System (PTS)

The PTS crops out extensively in the Santerno Valley near the Coniale village (Figure 1B). The PTS was previously studied by Cattaneo & Ricci Lucchi (1995) that interpreted the sandstone beds as basinal sheet lobes without evidences of positive features created by bed depositions. Later, Tinterri & Tagliaferri (2015) analyzed this succession through six stratigraphic logs covering the stratigraphic interval from the Visignano MTC to the Montecchio key bed, revealing a succession of six sandstone lobes and relative interlobes showing an evident cyclicity (Figure 2A). The occurrence of sole casts at the base of the indicates that the gravity flows were directed towards SE (N 130°) parallel to the CTRF alignment. The succession presents a single key bed, the Montecchio bed, located about 280 m above the top of the Visignano MTC (Figure 2A). It is a thick (about 5 m) massive to crudely-laminated bed made of very coarse to medium-grained sandstone that can be traced all through the study area (Figure 2C). The presence of aligned mudstone clasts near the base suggests that the Montecchio key bed is composed by the amalgamation of at least two events.

The stratigraphic succession of Unit VI has been subdivided into three main intervals by Tinterri & Tagliaferri (2015). These three intervals are characterized by a progressive change, not only in bed types, but also in bioturbation degree, sandstone/mudstone ratio and beds angle of dip (for further information see Tinterri & Tagliaferri, 2015). The basal interval “A” (around 80 m thick), included between the top of the Visignano MTC and bed 41, records the onlap of the PTS basal part on the Visignano MTC (Figure 2). The intermediate interval “B”, where the lobes 5 and 6 occur, includes the stratigraphic succession, about 200 m thick, between bed 41 and the Montecchio key bed in which well-developed depositional lobes can be observed (Figure 2). The upper interval “C” describes the uppermost part of Unit VI stratigraphic succession between the Montecchio key bed and the uppermost bed 179 that tries to document the vertical passage into the Castel del Rio mixed system by Mutti et al. 2002 (see Figure 4 of Tinterri & Tagliaferri, 2015).

Evident stratigraphic thickness variations in a direction parallel and perpendicular to the CTRF have been observed in the intermediate part of the stratigraphic succession. In particular, parallel to the CTRF alignment, there are two decreases in stratigraphic thickness in proximal and distal logs (Figure 2B). This variation have been interpreted to be related to differential thrust movements perpendicular to the CTRF that were able to produce subtle morphologic highs in the proximal and distal zones and a depocentre in the middle (Figure 2B). Furthermore, a stratigraphic pinching towards the CTRF together with the progressive upward decrease in the bed’s angle of dip testify

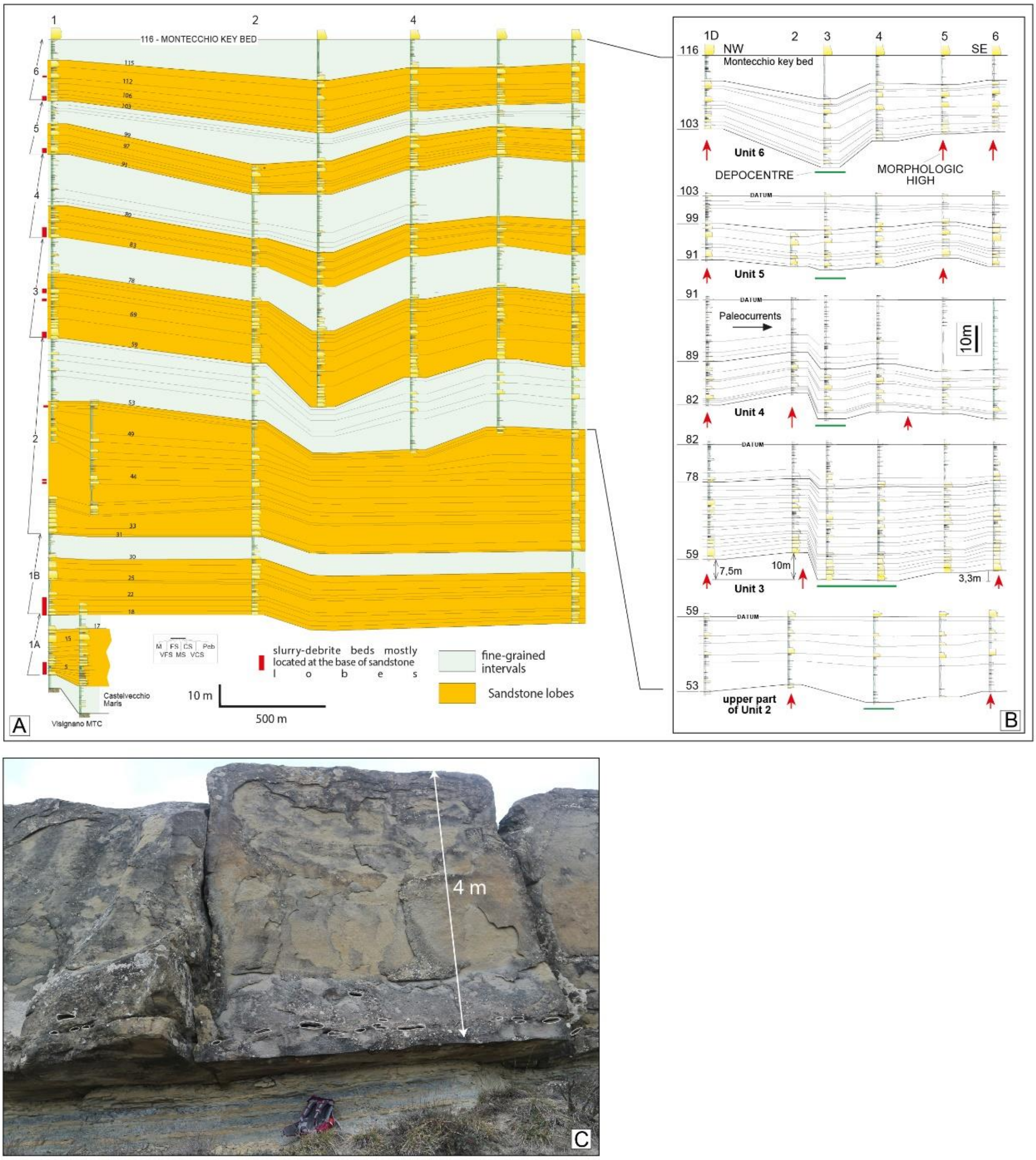

***Figure 2** (A) Detailed stratigraphic cross-section of Unit VI (PTS) included between the Visignano MTC and the Montecchio key bed (from Tinterri and Tagliaferri, 2015). The trace of the cross-section is parallel to the CTRF (see figure 1). The log's location is shown in Figure 3. Note the location of lobes 5 and 6 that are the object of this study. (B) Detail of the cross-section showing the progressive flattening of the intermediate part B of Unit VI where subtle morphologic highs and a depocentre can be observed. (C) Montecchio key bed (Cattaneo & Ricci Lucchi, 1995) note the aligned mudclasts near the base.*

that during the deposition of the PTS the growth of the CTRF was still ongoing. The tectonic uplift is highlighted also by the increase in percentage in the occurrence of Ophiomorpha-type trace fossils, which may suggest a decrease in the water depth (see Tinterri and Tagliaferri, 2015 for more details).

4. Methodology

This study was carried out by combining a classical fieldwork-based sedimentological approach and a laboratory-based approach performing granulometric analysis on a large number of samples (Tables 1 and 2). The way we have dealt with the two different approaches will be described in the following paragraphs.

4.1 The study area and sedimentological analysis

We focused our research in the upper part of the PTS including lobes 5 and 6 by Tinterri & Tagliaferri (2015), until the Montecchio key bed (Figure 2A).To appreciate the short-distance variations of the sandstone beds, the number of stratigraphic logs in the study area was increased performing twelve closely spaced stratigraphic logs (Log1_{a-b}-11, Figure 3). Logs 1a and 1b are located on the left side of the Santerno river and are spaced about 760 m from each other. The beds here have a strike of N 70°, a dip direction towards NNE and a dip angle of about 20°. Conversely, Logs 2 to 11 were traced on a cliff located on the right side of the Santerno river, with beds strike of about N 130-135° (parallel to the paleocurrents), a dip direction towards NNE and a dip angle of about 15°.

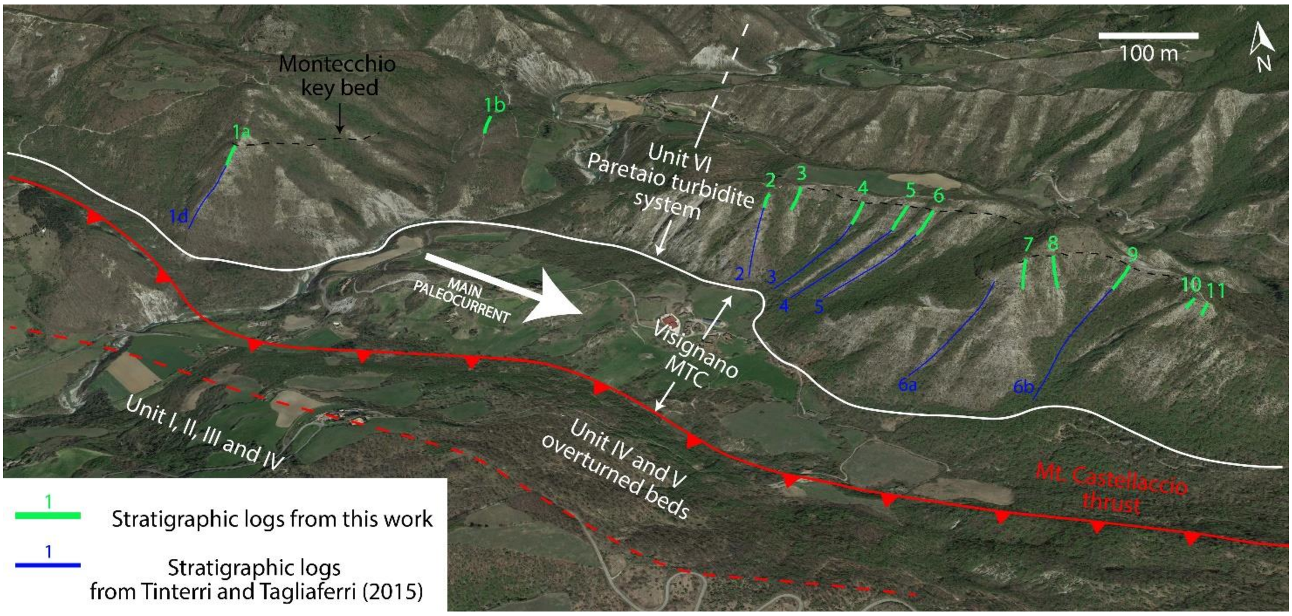

Figure 3 *Panoramic overview of the study area showing the location of the measured logs in this work (green) and those analysed by Tinterri & Tagliaferri (2015) (blue), the Visignano MTC and Mt. Castellaccio thrust. Note the increased number of logs limited to lobes 5 and 6 and their direction parallel to the main paleocurrents.*

The lateral extension of the PTS outcrops in this area offers a rare opportunity to trace individual beds for up to 2,5 kilometers and perform closely spaced logs whose distance is comprised from 350 to 40 m. Turbidite facies have been distinguished performing bed-by-bed measurements recording bed thickness, grain-size, sedimentary structures, paleocurrent, and trace fossils. The general referential facies scheme is that of Mutti et al., 2003, described in the first chapter.

4.2 Grain size analysis

In this work, we combined the classical sedimentological approach based on the facies analysis, with a detailed granulometric characterization of the facies carried out through a laser diffraction particle size analyzer. Specifically, the granulometric analysis were performed with a Malvern Mastersizer 3000 laser diffraction granulometer, designed for measuring particle sizes in the 0,02 µm (clay) to 2000 µm (granules) range (Storti & Balsamo, 2010). This technique is the most quick and reliable for mixed sand-silt-clay samples of varying distribution (Brooks et al., 2022), as in our case study. Each bed has been named with the first letter representing the type of bed (i.e "S" for hybrid beds and "T" for classic turbidite beds) and a progressive number (Figure 4). A total number of 124 samples of sandstone were acquired from hybrid beds (73, Annex Table 1) and turbidite beds (51, Table 2). A specific sampling procedure was operated for turbiditic and hybrid beds (Figure 4). Specifically, for turbidites, a sample was collected in each facies composing the facies sequence of the beds. Conversely, hybrid beds were sampled in each of the three units composing the strata (see Units "a", "b" and "c" in Figure 4), with particular attention to the slurry unit ("b" interval) where 3

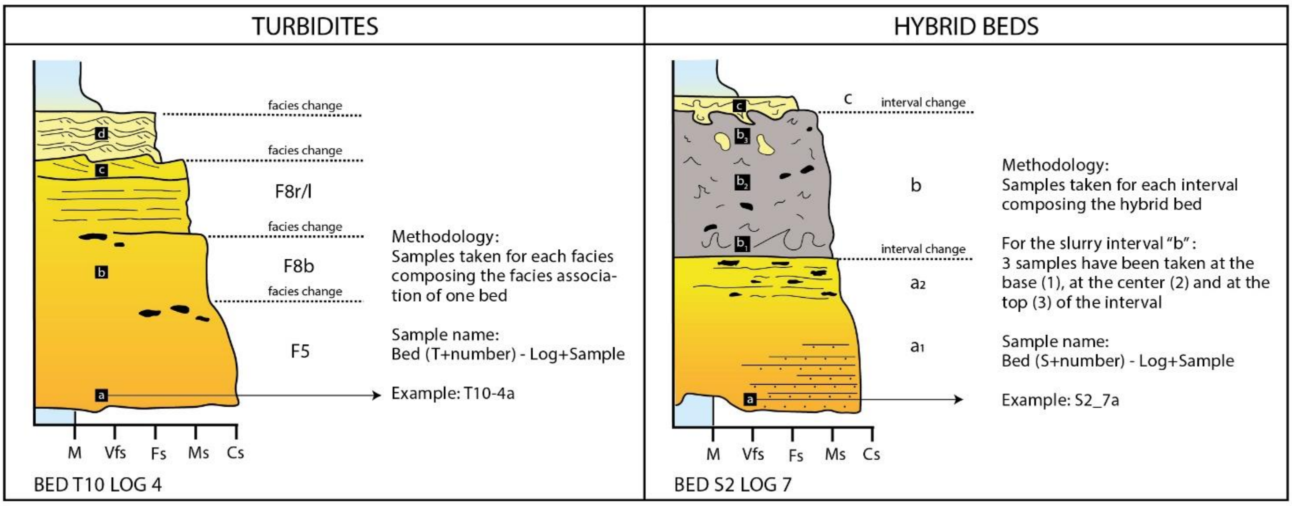

Methodology:
Samples taken for each facies composing the facies association of one bed

Sample name:
Bed (T+number) - Log+Sample

Example: T10-4a

Methodology:
Samples taken for each interval composing the hybrid bed

For the slurry interval "b":
3 samples have been taken at the base (1), at the center (2) and at the top (3) of the interval

Sample name:
Bed (S+number) - Log+Sample

Example: S2_7a

***Figure 4** Sampling procedure operated for turbiditic and hybrid beds. Specifically, for turbidites, a sample was collected in each facies composing the facies association of the beds. Conversely, hybrid beds were sampled in each of the three units composing the strata, with particular attention to the slurry unit ("b" interval) where 3 samples have been collected, at the base, in the middle and at the top of the unit.*

samples have been collected, at the base, in the middle and at the top of the unit. The naming convention is Bed name - Log+Sample. The collected samples were poorly cemented, and consequently, they could be sampled easily with a hammer, and vice versa for the finer samples rich in mud and more cemented, sampling was more difficult. Particle size distributions were measured from wet dispersions using a small subsample of 0,5 g considered more accurate with respect to the large ones (Brooks et al., 2022). The subsample was manually disaggregated in a bath of deionized water without difficulty. Since the amount of sample analysed is small, it can be directly introduced into the laser particle size analyser without the need for further subdivision. For consistency, we performed the same measurement procedure for all the sandstone samples consisting of 25 consecutive measurements run 20 seconds long with a pump speed of 2200 rpm. To prevent clay flocculation during measurements, an internal ultrasonic instrument was turned on. Granulometric analysis give a reliable measure of grain-sizes proportion inside a sample. This information is fundamental to understanding important sedimentological information such as the maximum grain-size and the degree of sorting of the deposit. The measure of the latter is given by the value of the span which is the measurement of the width of the distribution. The narrower the distribution, so better the sorting, and the smaller the span becomes.

5. Results

Data from the Paretaio turbiditic succession provide new insight into the dynamics of sediment gravity flows in relation to subtle topographic variations. The following sub-sections will be focused on: the lobe hierarchy (5.1), the facies scheme designed for lobes 5 and 6, and the interpretation of the related flow dynamics (5.2) and the beds/lobe thickness variation downcurrent (5.3).

5.1 Stratigraphic cross-section and lobe hierarchy

Our study is based on the detailed measurement of twelve stratigraphic logs that resulted in a high-resolution stratigraphic cross-section (Figure 5). The orientation of the stratigraphic cross-section is parallel to the paleocurrent direction corresponding to N130° (average of different paleocurrent directions deriving from the sole casts, Figure 5A) and to the direction of the CTRF (Figure 5A). Several studies have proposed that successions of sand-prone submarine lobes can be subdivided using a hierarchical approach. We applied the fourfold hierarchy of lobe deposits established by Prélat et al. (2009) where 1) a “bed” represents a single depositional event; 2) one or more beds form a “lobe element”; 3) one or more lobe elements form a “lobe”; 4) one or more genetically

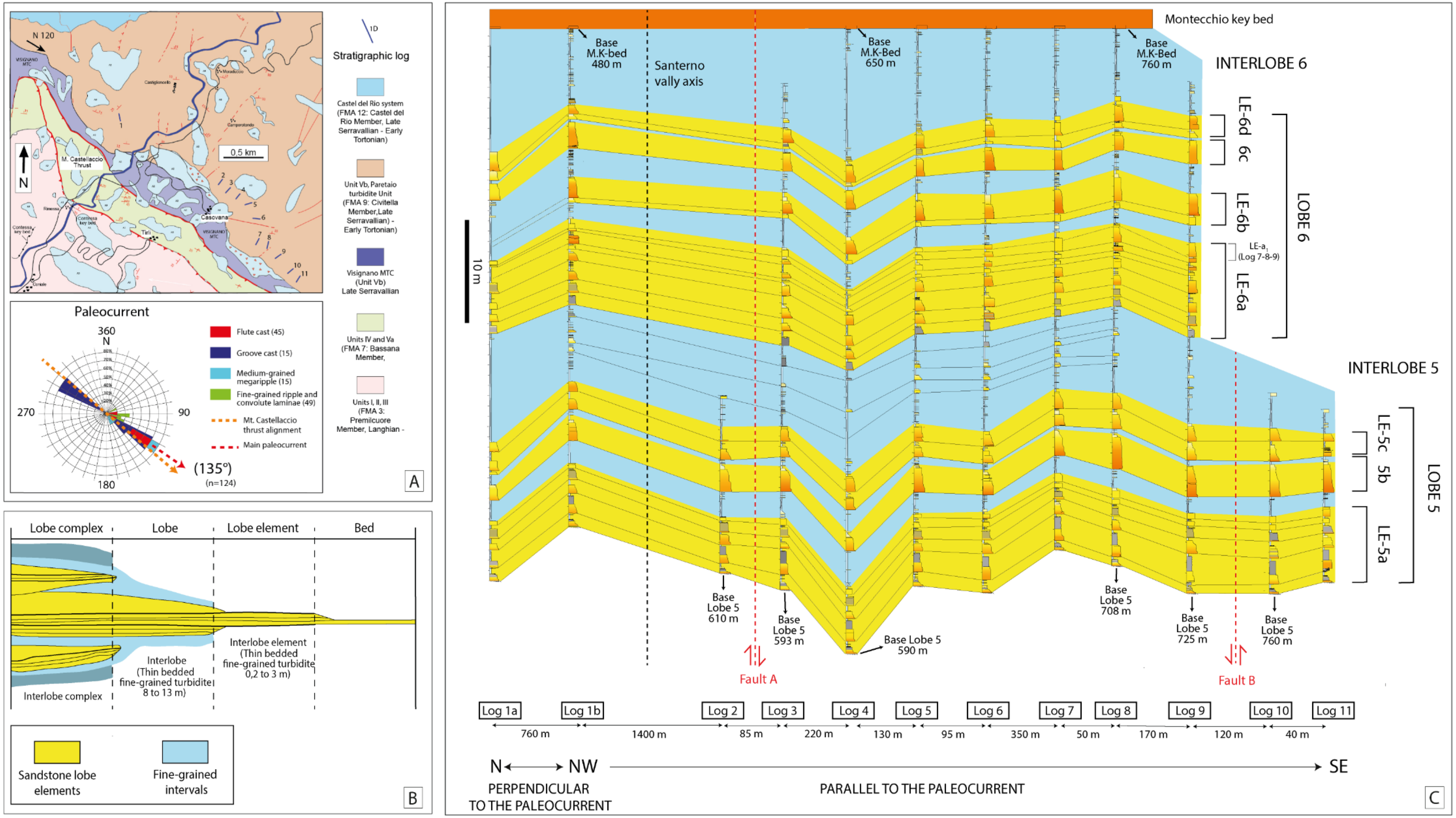
N 120
N
0,5 km
M. Castellaccio Thrust
Casovana
1D
Stratigraphic log
Castel del Rio system (FMA 12: Castel del Rio Member, Late Serravallian - Early Tortonian)
Unit Vb, Paretaio turbidite Unit (FMA 9: Civitella Member,Late Serravallian) - Early Tortonian)
Visignano MTC (Unit Vb) Late Serravallian
Units IV and Va (FMA 7: Bassana Member,
Units I, II, III (FMA 3: Premilcuore Member, Langhian -
Paleocurrent
360
N
270
90
180
(135°)
(n=124)
Flute cast (45)
Groove cast (15)
Medium-grained megaripple (15)
Fine-grained ripple and convolute laminae (49)
Mt. Castellaccio thrust alignment
Main paleocurrent
A
Lobe complex
Lobe
Lobe element
Bed
Interlobe complex
Interlobe (Thin bedded fine-grained turbidite 8 to 13 m)
Interlobe element (Thin bedded fine-grained turbidite 0,2 to 3 m)
Sandstone lobe elements
Fine-grained intervals
B
Montecchio key bed
Base M.K-bed 480 m
Santerno vally axis
Base M.K-Bed 650 m
Base M.K-Bed 760 m
INTERLOBE 6
LE-6d
6c
LE-6b
LE-a, (Log 7-8-9)
LE-6a
LOBE 6
INTERLOBE 5
LE-5c
5b
LE-5a
LOBE 5
10 m
Base Lobe 5 610 m
Base Lobe 5 593 m
Base Lobe 5 590 m
Base Lobe 5 708 m
Base Lobe 5 725 m
Base Lobe 5 760 m
Fault A
Fault B
Log 1a
Log 1b
Log 2
Log 3
Log 4
Log 5
Log 6
Log 7
Log 8
Log 9
Log 10
Log 11
760 m
1400 m
85 m
220 m
130 m
95 m
350 m
50 m
170 m
120 m
40 m
N
NW
SE
PERPENDICULAR TO THE PALEOCURRENT
PARALLEL TO THE PALEOCURRENT
C

Figure 5 *Simplified geologic map of the study area, where the location of measured logs is indicated. Below, a rose diagram showing the paleocurrents derived from flute casts (red), groove casts (blue) and medium-grained megaripples (light blue) directed towards SE i.e parallel to the CTRF, while the fine-grained ripple and vergent convoluted laminae (green) have a more dispersed pattern. (B) Hierarchical scheme applied to lobes 5 and 6. Four scales of elements: bed, lobe element, lobe and lobe complex are recognized. Modified from Prelat et al. (2009). (C) High-resolution correlation panel where sandstone lobes (yellow) are separated by relative interlobes (light blue). Faults are marked with red dotted lines.*

related lobes stack to form a "lobe complex" (Figure 5B). The two lobes analysed (Lobe 5 and 6) fit well with this type of classification because of the high degree of correlation at the bed-scale. Lobe 5 and Lobe 6 are respectively composed by three (LE 5a-b-c) and four lobe elements (LE 6a-b-c-d, Figure 5C). A lobe element is defined when a sandstone bed is clearly composed of two or more amalgamated beds. The amalgamations can be highlighted by bed correlations, aligned mudstone

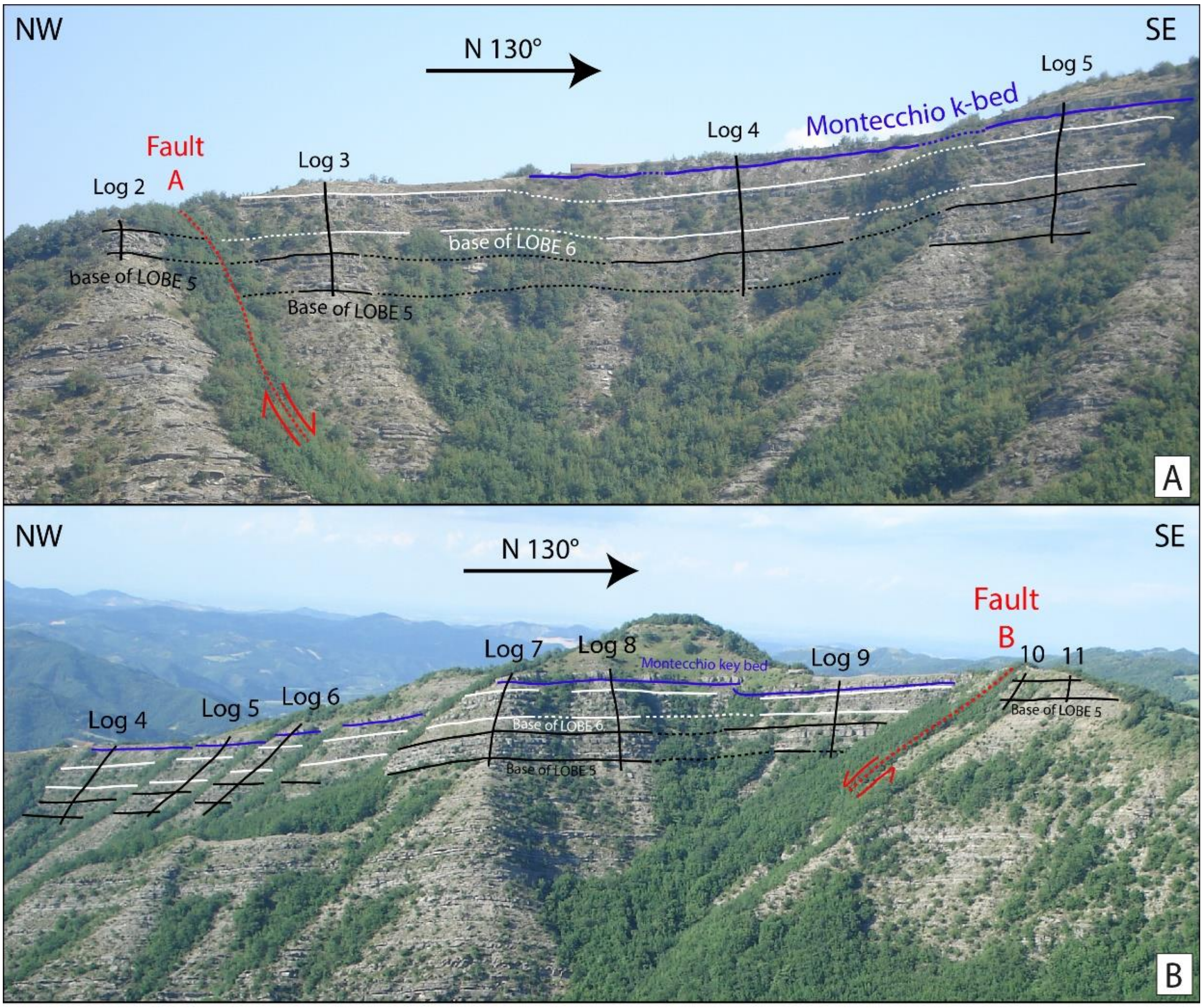

Figure 6 *Panoramic views of lobes 5 and 6. The base and top of the lobe 5 (black) and 6 (white) are marked as well as the Montecchio key bed (purple). The line drawing highlights the presence of two faults (red) that dislocate part of the succession, between logs 2 and 3 and logs 9 and 10 (see also Figure 5).*

clasts, scours, or sharp surfaces truncating trace fossils. The lobe elements have a thickness ranging from 2 to about 7 meters and are separated from each other by interlobe elements of 0.2 to 3 meters. The two lobes 5 and 6 are bounded by 8-13 m thick units of laterally persistent fine-grained deposits that can be interpreted as interlobes 5 and 6 (Figure 5C). These laterally persistent thin-bedded fine-grained packages mark a widespread decrease in sand supply (Prélat et al., 2009; Spychala et al., 2017a; Spychala et al., 2017b). The two lobes are part of a lobe complex, including also the underlying lobes (Figure 2A). The two lobes studied were easily recognized in each log with the exception of Logs 2, 10, and 11 due to lack of lobe 6 (Figure 5C). In fact, the presence of two faults in the study area dislocates part of the succession (see faults A and B in Figure 6). Although the faults are not well exposed and are covered by vegetation, the approximate estimation of the vertical throw (based on the stratigraphic cross section of figure 5C and the overviews of figure 6), is about 30 m for Fault A and 15 m for the Fault B.

5.2 Facies association of Lobe 5 and 6

The sedimentological characteristics of the PTS have been described first by Tinterri & Tagliaferri (2015) in a general facies scheme elaborated for the unit of the transitional phase (both Paretaio and Firenzuola turbidite system; see their figure 5). For this study a detailed facies scheme has been elaborated for the two lobes analyzed, representing an evolution of the previous facies scheme. We recognized seven main bed types (Type A, B, C, D, E, and F, Figure 7) that are composed by a specific facies sequence. The bed types are described both from the sedimentological and granulometric points of view and interpreted in term of depositional processes. Our reference facies scheme is that of Mutti et al. (2003) and Tinterri (2022, in preparation). Furthermore, particular attention has been given to type E beds since are composed by a new facies, the F8r/l presented for the first time in (Tinterri, 2022)(see also Tinterri et al., 2023, Figure 10 in chapter 1).

Hybrid beds (Type A)

- *Description*

Type A are thick (30 to 100 cm) to very thick (>100 cm) bipartite or tripartite beds characterized by a basal or intermediate slurry unit. The slurry unit consists of a poorly sorted mixture of sand, silt, and, in minor percentage, clay. Two bed types (A.1 and A.2, Figures 8 and 9) are distinguished according to the net-to-gross (N/G) ratio measured inside the slurry unit and their peculiar sedimentary characteristics.

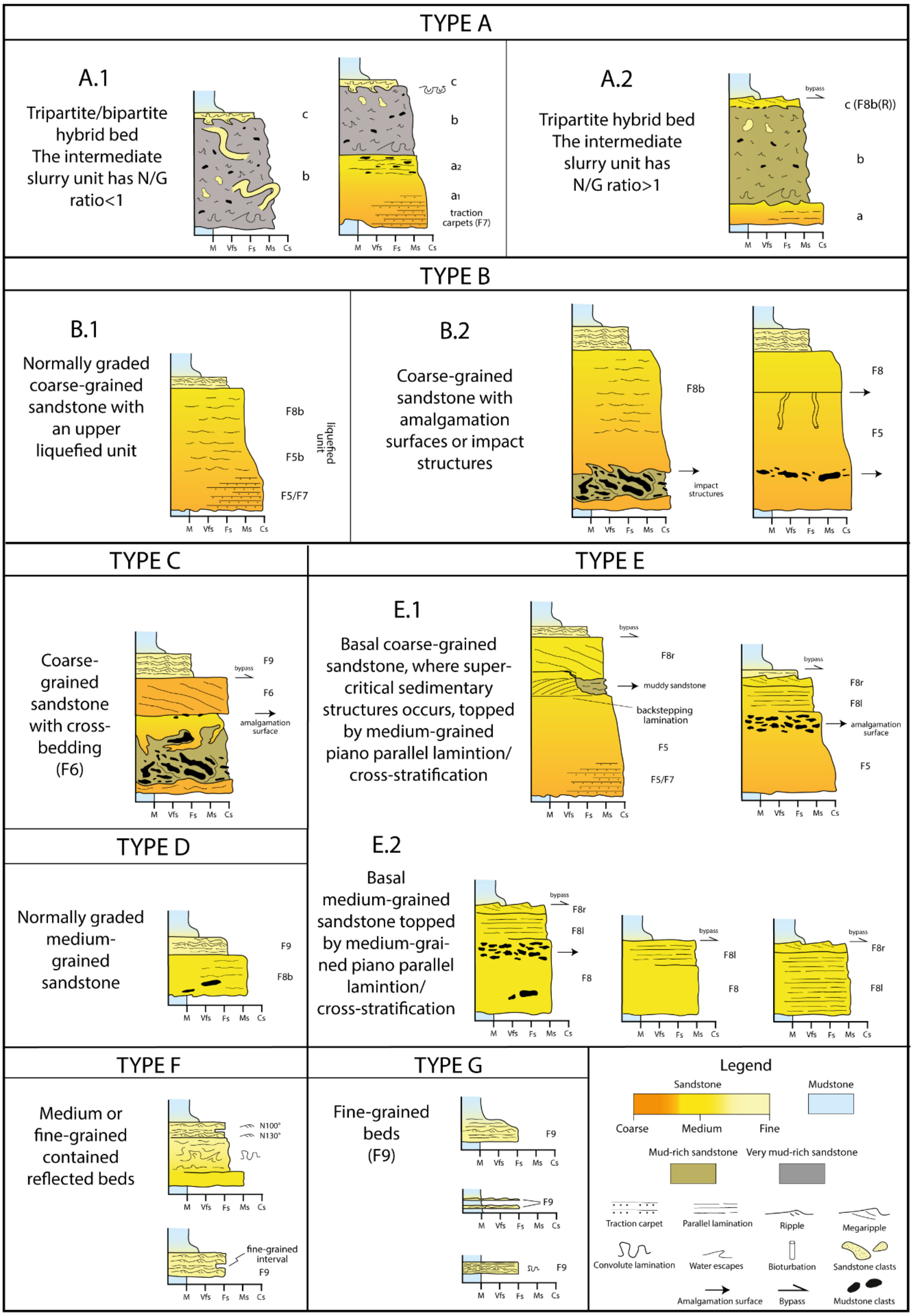

Figure 7 *The main bed types of the study area characterizing the lobes 5 and 6 of Unit VI and their general description, for the interpretation, the reader is referred to the text. This facies scheme represents the evolution of the one elaborated by Tinterri & Tagliaferri (2015); new facies have been recognized (Type A.2 and Type E) important to understand the different phases of evolution of the lobes.*

Type A.1 are tripartite beds with variable thickness (Figure 8). The three intervals that compose this beds are:

a) basal coarse to medium-grained massive to laminated sandstone. They have a highly erosional base, where delamination features (*sensu* Fonnesu et al., 2016) can be common. The basal interval “a” has a net-to-gross ratio > 1, and is generally poorly sorted and the grain size analyses indicate a fine/medium-grained sand with a high percentage of silt (Figure 8D, Table 1). The vertical passage from this unit “a” into the intermediate unit “b” can occur in different ways: it can be sharp (Figure 8A) or characterized by a unit of banded sandstone featured by alignments of mudstone clasts (a_2, Figure 8C).

b) an intermediate slurry unit with liquefaction structures, pseudonodules, mudstone clasts, folded fine-grained beds, and plant fragments (Figure 8A, 8B). This unit is characterized by a high content of mud and can be defined as a muddy sandstone (8D). The analyses in the “b” interval reveal that very few differences occur from the base to the top of the slurry unit that can be considered lithologically homogeneous (Table 1). For simplicity, we calculated the average curve of the three samples (b_1, b_2, and b_3) to compare the curve of this interval (b) in different beds and locations. The curves of the slurry unit present two modes composed of silt and very fine-grained sand (Figure 8D).

c) an upper thin- to very thin fine-grained unit characterized by ripple cross-stratification and convolute laminae or, in other cases, by load structures that can evolve into pseudonodules within the underlying “b” (Figure 8C).

Type A.2 are tripartite beds composed by:

a) basal coarse to medium-grained sandstone (Figure 9A); this interval is better sorted respect to its correspondent in type A.1, mainly composed of very fine- to fine-grained sand (Figure 9C).

b) an intermediate slurry unit with liquefaction structures and mudstone clasts (Figure 9A). The slurry unit of this type is composed of mud-rich sandstone but with a higher net-to-gross ratio and thus percentage of sand (Figure 9C, Table 1) in comparison with interval “b” of the bed type A.1. The granulometric curves of this slurry unit have the same trend of the curves of Type A.1 with two modes composed of silt and fine-grained sand (Figure 9C).

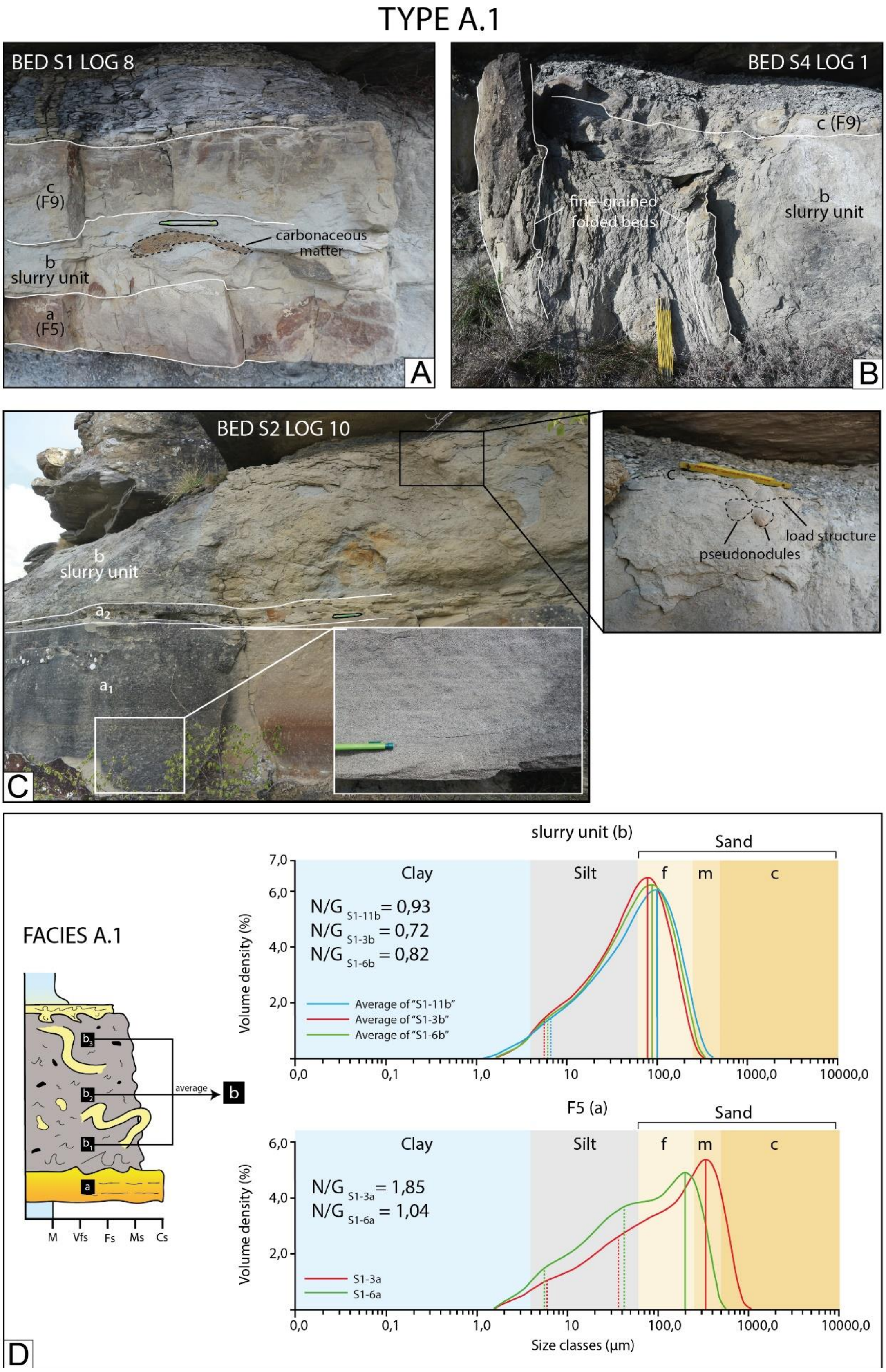

Figure 8 *Examples of Type A.1 beds characterized by intermediated slurry units (b) with a N/G proportion < 1 (insert D). The basal coarse-grained sandstone (insert D) unit is absent in the case of S4 bed (insert B). The upper interval (c) is composed by fine-grained sandstone (F9, insert A and B) that can present load structure or pseudonodules at the contact with the slurry unit.*

c) an upper unit composed of medium-grained sandstone with tractive structures such as parallel lamination and ripple/megaripple (F8r, Figure 9B). From the granulometric point of view, they are poorly sorted with a high content of silt and clay (Figure 9C).

-Interpretation

We interpreted these beds as hybrid sediment gravity flow deposits (sensu Haughton et al., 2009). The divisions of hybrid event beds have different transport mechanism: the basal clean sand division ("a") represent the result of a high-density turbidity current, the slurry interval ("b") is similar to a debrite emplaced by en-masse freezing of laminar or weakly turbulent cohesive flow and the upper unit ("c") is deposited by a dilute and turbulent flow (e.g., Talling et al., 2004; Haughton et al., 2009; Muzzi Magalhaes and Tinterri, 2010). Several studies have indicated that hybrid beds are more prevalent in the distal parts of submarine fan and lobe settings (Amy and Talling, 2006; Muzzi Magalhaes and Tinterri, 2010; Haughton et al., 2009; Spychala et al., 2017b, 2017a). Anyway in the fan fringe environment hybrid beds are thin to very thin bedded and the slurry interval is prevalently characterized by mudstone chips and carbonaceous sediment (Spychala et al., 2017). Where hybrid beds have been observed in more proximal settings enhanced erosion and deceleration have been recognized. In fact, they have been strictly connected to slope changes favor both mud erosion and decelerations (Fonnesu et al., 2016; Muzzi Magalhaes & Tinterri, 2010; Tinterri et al., 2016). Type A beds can have erosive bases and delamination features and contain folded sandstone beds and mudstone rafts. These characteristics are indicative of a strong erosion of the substrate. For all of this reason, Type A beds in the PTS have not been associated with a fan fringe environment. Instead, they have been interpreted as hybrid beds originating by substrate erosion and silt incorporation related to slope changes. According to the grain size distribution of the slurry unit, we have interpreted that Type A.1 beds to derive from a more evolute hybrid flow while the type A.2 have been interpreted as poorly evolved hybrid beds and can represent the up current equivalent of Type A.1 beds.

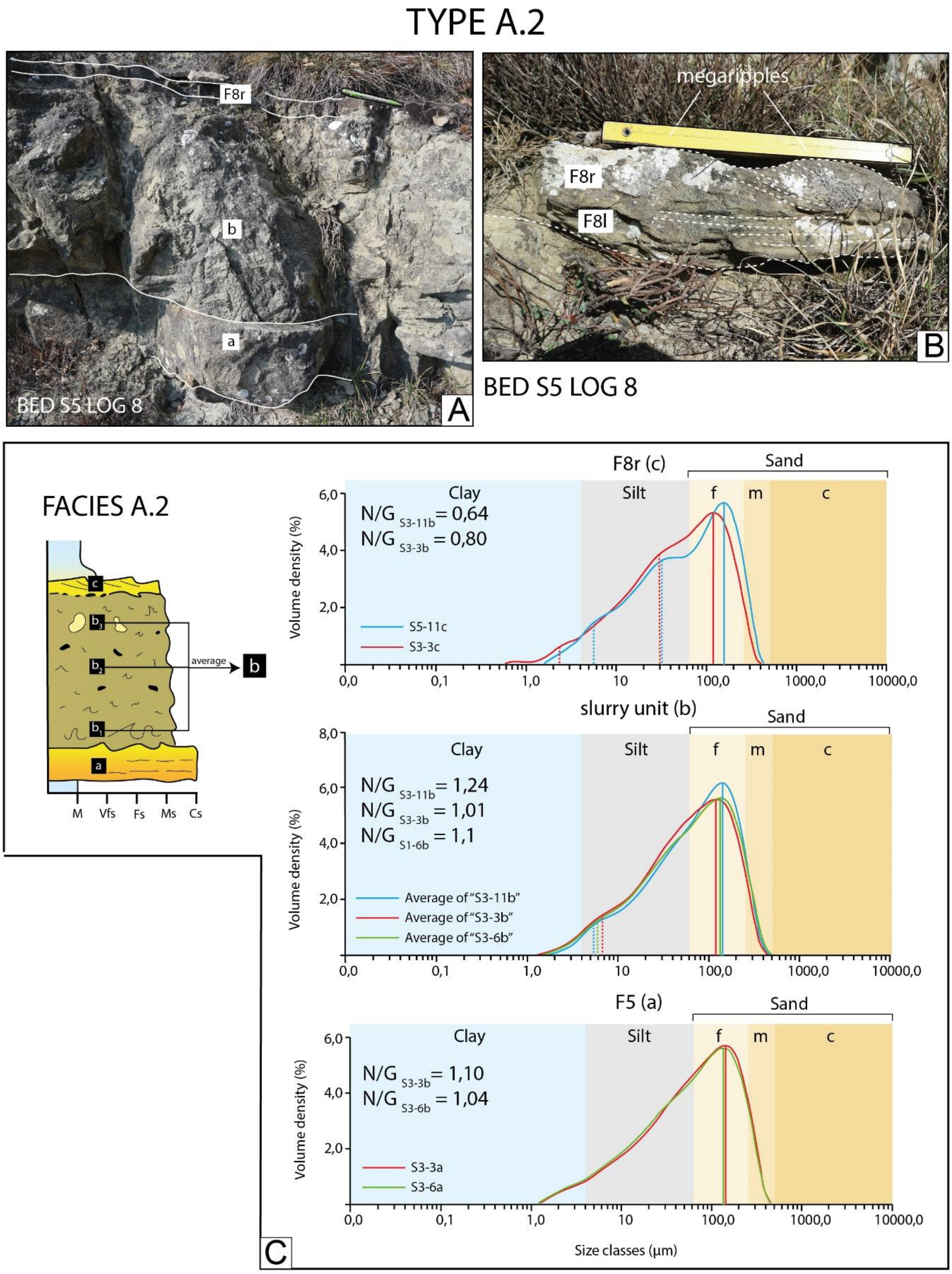

Figure 9 *Examples of Type A.2 beds characterized by intermediated slurry units (b) with a N/G proportion > 1 (insert D). The upper interval (c) is composed of medium-grained sandstone that can be composed by megaripples (F8r in insert A) and/or piano parallel laminations (F8l in insert B). Note that the grain-size spectrum of Type A.2 slurry unit (b) has a similar trend respect to the one obtained from the slurry unit of Type A.1 (Figure 8D).*

Liquefied and amalgamed coarse-grained sandstone beds (Type B)

- *Description*

The beds belonging to this category are thick to very thick beds made of coarse-grained sandstones (F5). These beds present a very thin upper grained division (F9) or in some cases is completely absent. They are divided in two categories:

Type B.1 are normally graded and are characterized, in their upper parts, by liquefied units with common water escape structures (Figure 10A).

Type B.2 beds have amalgamation surfaces highlighted by aligned mudstone clasts, sharp surfaces marked by grain-size breaks or interrupted trace fossils (Figure 10B, 10C). Sometimes they present basal "chaotic" unit characterized by impact structures characterized by sand injections, mud clasts in a muddy sandstone resembling hybrid event beds. These "chaotic" units evolve downcurrent into divisions characterized by aligned mudstone clasts.

Samples collected in the Type B beds have a net-to-gross ratio > 1 (Figure 10D, Table 2). In general, the lower part type B beds is composed by coarse-grained massive (F5) or crudely laminated sandstone (F5b); this intervals are poorly sorted as shown by the presence of two modes in the granulometric curve, one in fine-grained sand and the other one in silt. Conversely, the upper part of this bed type is composed of a crudely laminated medium-grained sandstone (F8b), is better sorted and presents a unimodal sediment distribution with a mode characterized by fine-grained sand.

- *Interpretation*

Type B beds are interpreted as deposited by bipartite high-density turbidity currents characterized by a basal dense flow and an overlying turbulent flow, which undergo sudden decelerations (Mutti et al. 2003; Tinterri & Muzzi Magalhaes, 2011). This process produces the sudden deposition of coarse-grained sandstone. In the case of Type B.1 the drastic deceleration is highlighted by the liquefied unit. While in Type B.2 this dynamics is reflected by impact structures and amalgamations related to substrate delamination (Fonnesu et al., 2016). The genesis of the impact structures can be related to irregularity of the seafloor induced by tectonics or by the deposition of very thick coarse-grained beds, able to create a local obstacle or may be also related to hydraulic jumps (Tinterri & Piazza, 2019).

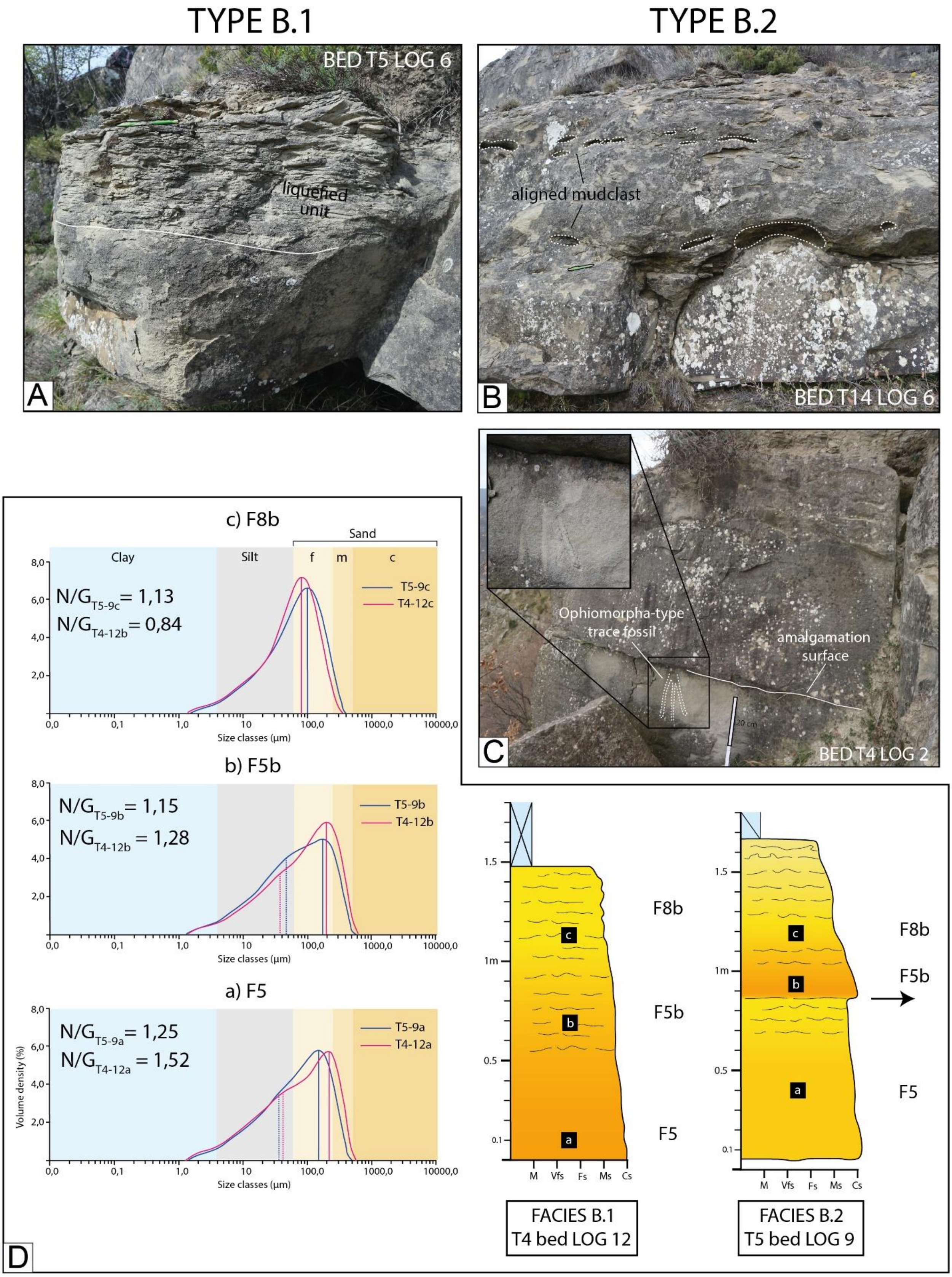

***Figure 10** Examples of Type B beds consisting of coarse-grained massive (F5) to crude laminated (F5b) sandstones (insert A) or amalgamed sandstones (insert B-C). Granulometric-analysis confirm that the higher grain-size is the coarse sand. Note that the N/G ratio is slightly higher respect to the slurry unit of Type A.2 (Figure 9D).*

Beds with bypass structures made of coarse-grained sandstones (Type C)

- *Description*

Only one bed of this type have been recognized in the succession. It presents an upper portion composed of a thick coarse-grained sandstone characterized by cross-bedding (Figure 11A, 11B), consisting in the facies F6 of Mutti et al. (2003). This facies, where the maximum grain-size is the coarse sand, is very poorly sorted and with a polymodal sediment distribution marked with a graph with a left skew (Figure 11C, Table 2). The coarser mode is in fine sand range (first peak in Figure 11C), while the finer mode is in the silt range (second and third peak in Figure 11C). The base of this interval is marked by mud clasts and trace fossils identified as *Ophiomorpha*. The F6 facies passes upward into a fine-grained division with ripples (F9). The facies F9 is better sorted, with unimodal sediment distribution with mode in the silt range (Figure 11C).

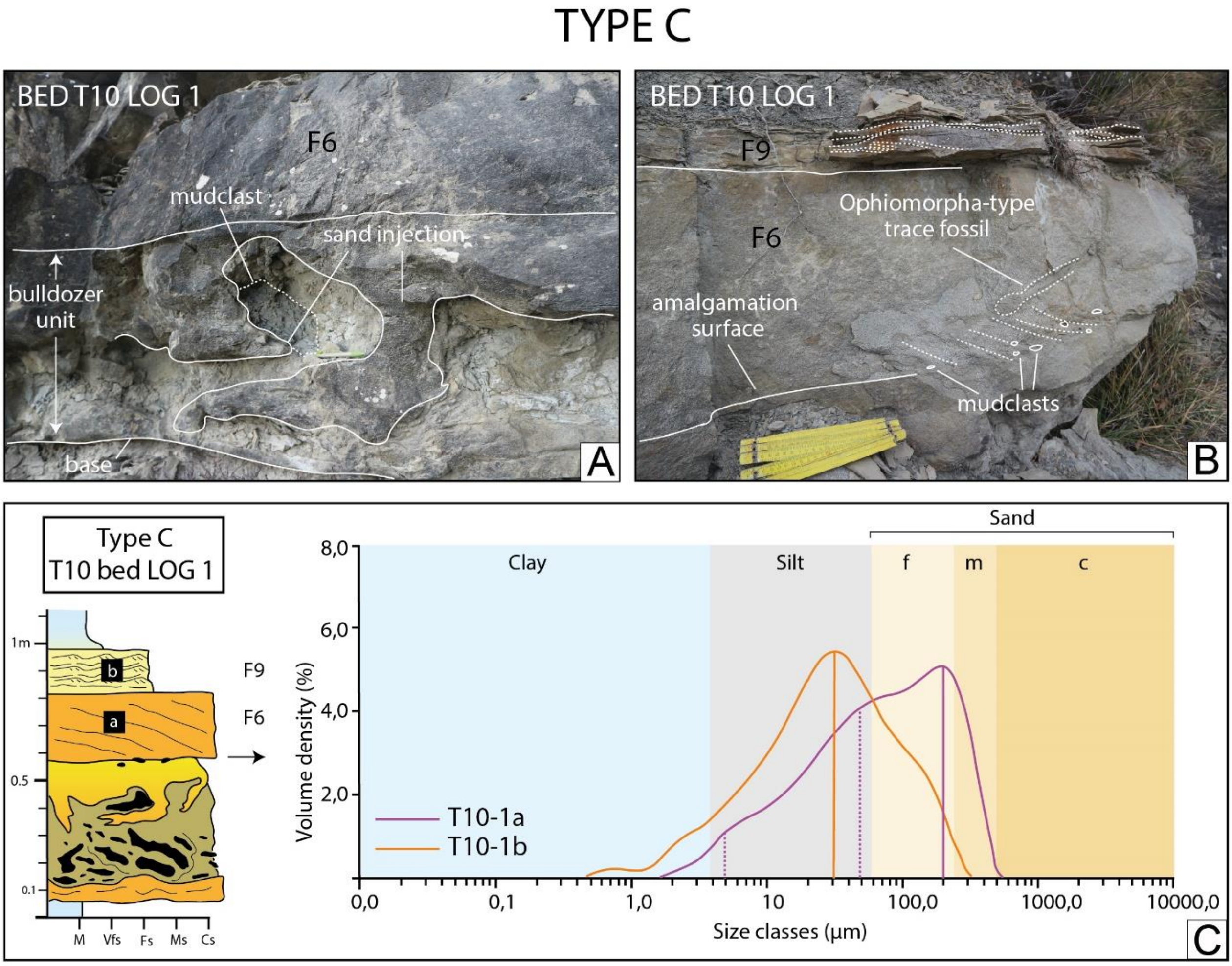

Figure 11 *Examples of Type C bed where a basal unit characterized by impact structures, mudclasts and sand injections (bulldozer unit, insert A) is overlayed by thick coarse-grained sandstone characterized by cross-bedding (F6, insert A-B). The grain-size analysis highlighted that F6 sample (T10-1a) is poorly sorted with polymodal (3 modes) sediment distribution while F9 sample (T10-1b) F9 is better sorted, with unimodal sediment distribution.*

- *Interpretation*

This facies association corresponds to homonymous Type C beds described by Tinterri & Tagliaferri (2015). These beds where interpreted as recording the drastic deceleration of a high-density flow and the bypass of more diluted turbulent flows, able to transport the medium grain size population further downcurrent. This bypass process produces the tractive structures represented by the cross-bedded coarse-grained sandstone (Mutti et al., 2003). In general, the presence of this facies (F6) indicates a high deceleration degree with the possibility to produce hydraulic jumps (Tinterri & Tagliaferri, 2015). Conversely, the deposition of the fine-grained facies (F9) is associated with traction-plus-fallout processes related to the tail of the turbulent flow.

Medium-grained sandstone beds (Type D)

- *Description*

Type D beds are generally medium-thick beds consisting of basal massive medium-grained sandstones often characterized by rip-up mudstone clasts that pass upward into thin fine-grained intervals consisting of slightly undulated laminae and ripples (Figure 12).

- *Interpretation*

These beds are consistent with Type D beds described by Tinterri & Tagliaferri (2015). This bed type records the deposition of the medium-grained sand and the bypass of the finer grain sizes. This bed type, therefore, is interpreted as deposited by decelerating sandy high-density turbidity currents,

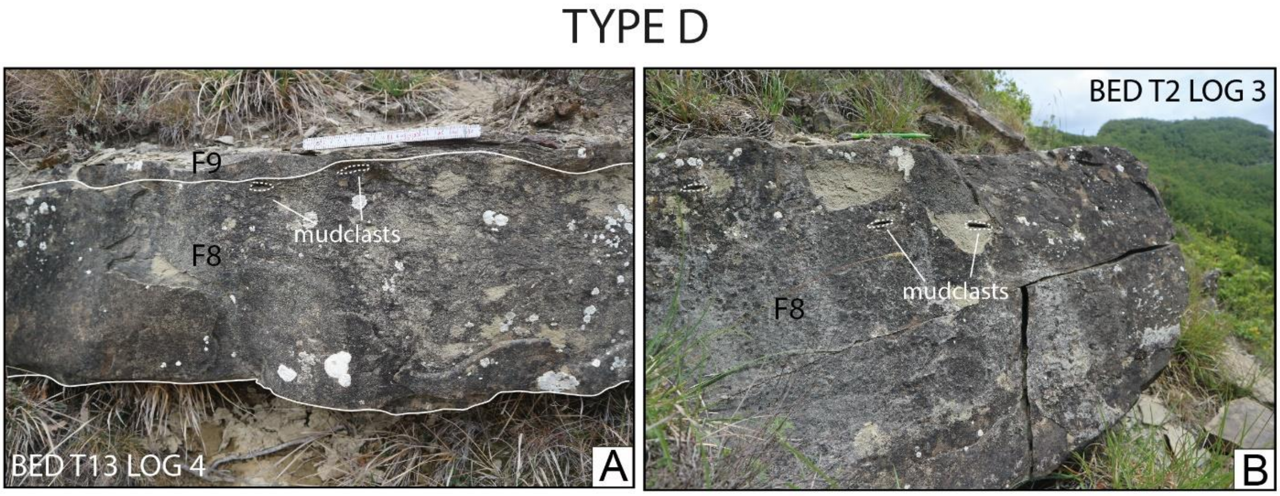

Figure 12 *Examples of Type D beds characterized by medium-grained massive sandstone (F8) with sporadic mudclasts and by a thin fine-grained interval (F9).*

where massive facies (F8) is deposited by high-fall out rates, whereas the thin fine-grained facies are transported further downslope.

Beds with bypass structures made of medium-grained sandstones (Type E)

- *Description*

There are two categories of Type E beds distinguished according to their maximum grain-size: *Type E.1* are coarse-grained massive thick (> 1.5 m) beds while *Type E.2* are medium-grained medium (> 1 m) beds (Figures 13 and 14). They are distinguished from Type B and Type D beds since Type E beds are characterized, in their upper parts, by medium-grained lenticular geometry/ripples (F8r, Figure 13C-E and 14A-B-D) and/or plane parallel laminae (F8l, Figure 13C-B-D). The base of this facies (F8l/r) is sharp and often aligned mudstone clasts mark this contact (Figure 14A-C-D). In some cases, the F8l/r facies is recognized above the interval of muddy sandstone with convolute thin-bedded laminations and water escape structures (Figure 13C). Type E beds are capped by thin-bedded fine-grained interval (F9) but in most of the cases, this interval is completely absent (see Figure 10 in chapter 1 for more details on the terminology, from Tinterri, 2022, in preparation).

All the samples analysed of the F8r/l facies (11 samples, Table 2) confirm the presence of the medium grain-size as the maximum grain-size recognized. With respect to the underlying facies (i.e facies F8 in Figure 14E), they have a higher difference in the proportion of grain-sizes and so appear less sorted; the curves present two or three component populations, with finer and coarser modes of silt and fine-grained sand (Figure 14E). The minor degree of sorting of this facies is confirmed by the higher span value performed by F8r/l facies respect to the underlying facies (Figure 14E, Table 2). The shape of the curve is similar to the one obtained from the coarse-grained analogous, i.e. F6 in Type C beds (Figure 11C). The granulometric analysis on this bed type unearths that often the facies F8r/l is composed of grain-sizes coarser than the underlying facies (Figure 14E).

In some cases, in the basal part of Type E.1 beds, backset laminae have been recognized in intervals of coarse to medium-grained sandstones (Figure 13B-D-F). Low-angle backset lamination is more common, but in one case high-angle backset lamination have been recognized.

- *Interpretation*

The facies F8r/l are interpreted as the downcurrent equivalent of the horizontally (F7) and cross-stratified megaripples-shaped beds (F6) according to the facies scheme of Mutti et al. (2003) but in the medium-grained sandstone range. This is confirmed by the correlation of T10 bed presenting F6 facies that evolve downslope in the F8r/l facies (Annex Figure 4). For this reason, similarly to Type C beds, we interpreted Type E beds to record the deceleration of a high-density turbulent flow, that

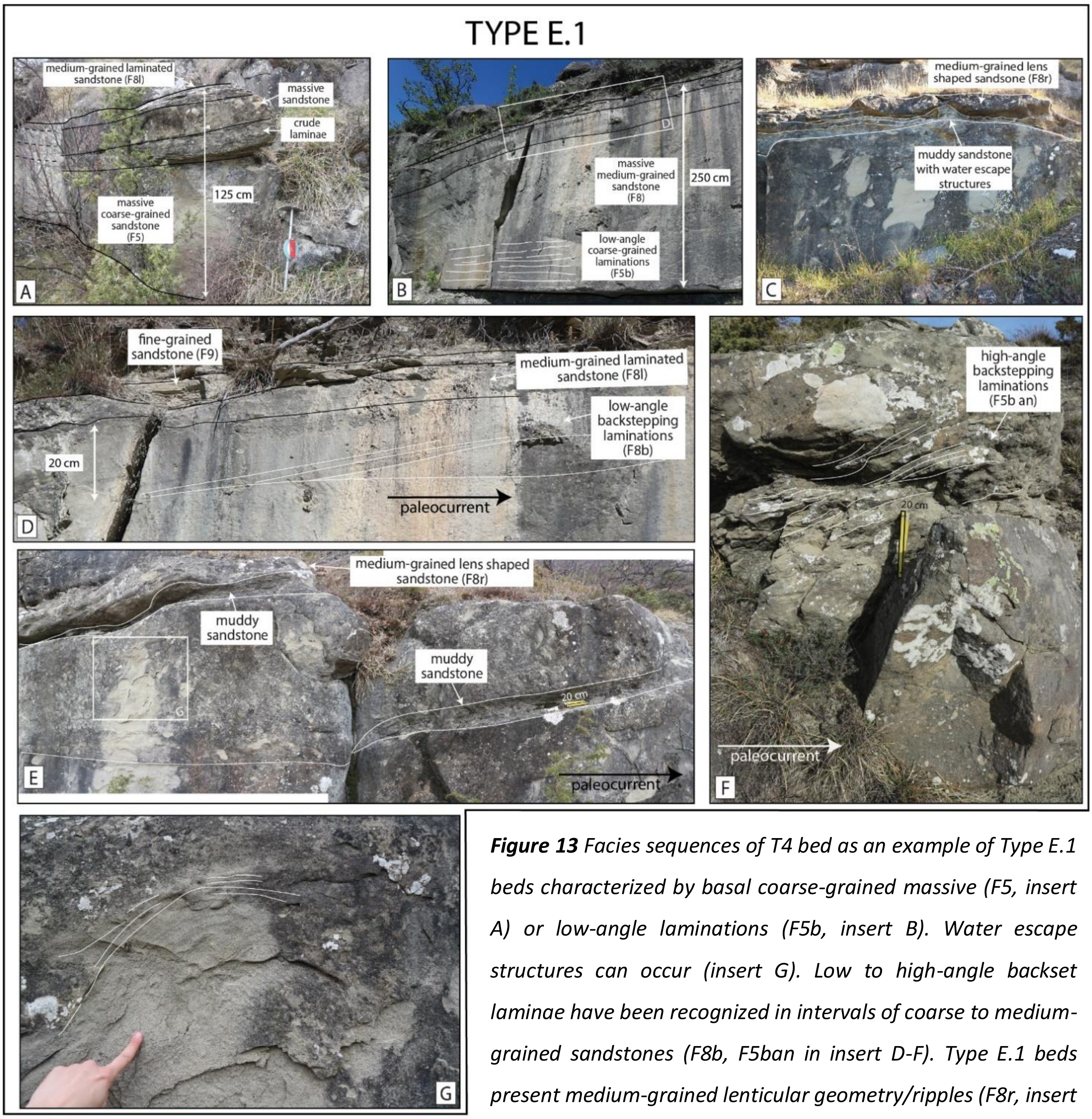

Figure 13 *Facies sequences of T4 bed as an example of Type E.1 beds characterized by basal coarse-grained massive (F5, insert A) or low-angle laminations (F5b, insert B). Water escape structures can occur (insert G). Low to high-angle backset laminae have been recognized in intervals of coarse to medium-grained sandstones (F8b, F5ban in insert D-F). Type E.1 beds present medium-grained lenticular geometry/ripples (F8r, insert C-E) and/or plane parallel laminae (F8l, insert A-D). In some cases F8r/l facies are located above muddy sandstone intervals with water escape structures (insert C-E).*

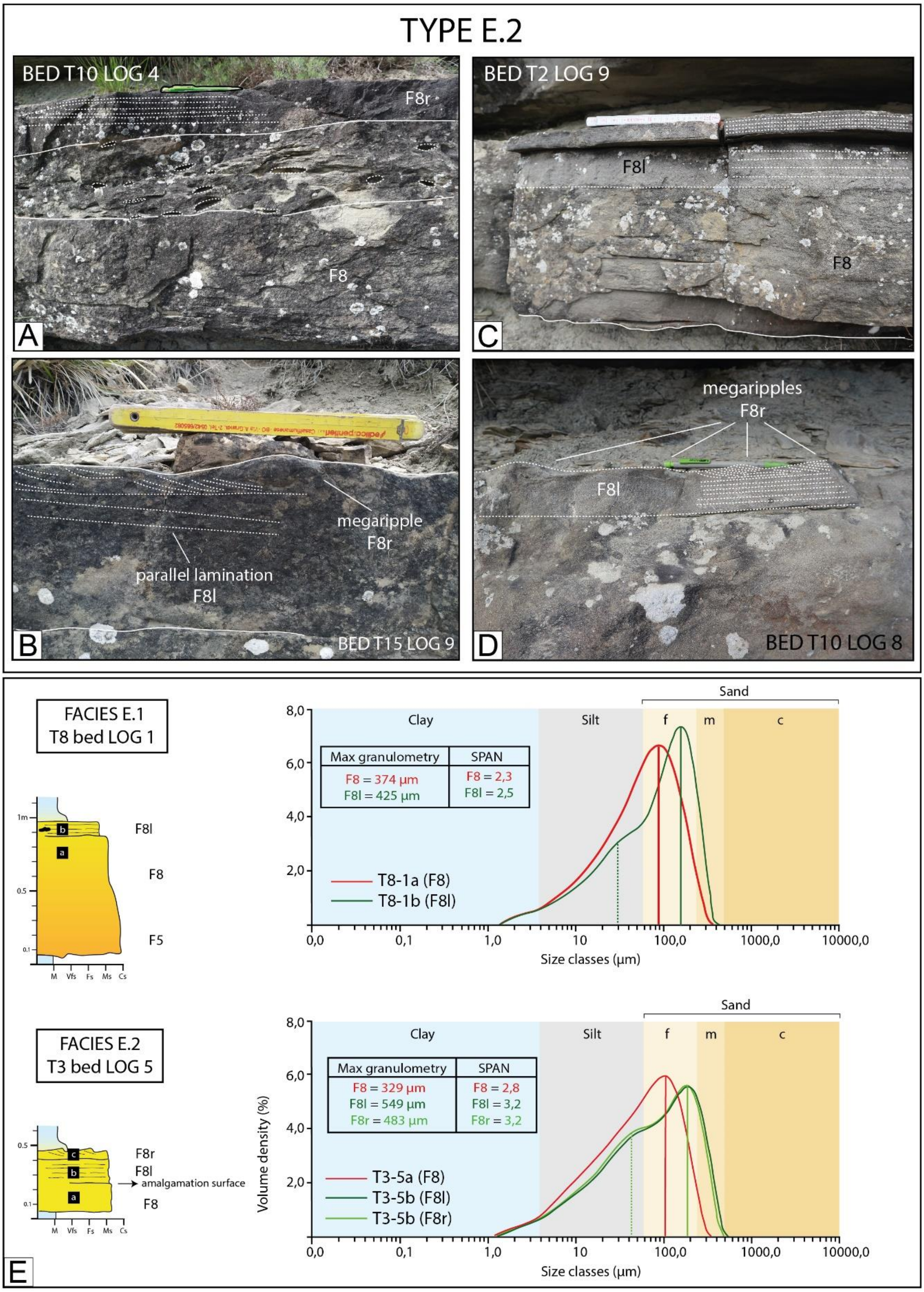

***Figure 14** Above some examples of Type E.2 beds characterized by basal medium-grained sandstones (F8, insert A-C) and upper medium-grained lenticular geometry/ripples (F8r, insert A-B-D) and/or plane parallel laminae (F8l, insert B-C-D). The granulometric analysis highlighted that F8r/l facies are poorly sorted (Span value increase in those facies, see also Table 2) with polymodal (2 modes) sediment distribution. Note that F8r/l spectrum has a similar trend respect to the one obtained from a sample of F6 (Figure 11C).*

matches with the deposition of basal massive coarse- to medium-grained sandstone (F5-F8), and the successive reacceleration of it causing the bypass of more diluted turbulent flows, able to transport fine-grained sand and mud further downcurrent. We interpreted that the bypassing turbidity currents are able to rework the top of the underlying bed in plane parallel lamination (F8l) or megaripples (F8r), according to the degree of deceleration absent (see Figure 10 in chapter 1 for more details, from Tinterri, 2022, in preparation; see also Tinterri et al. 2023). The presence of coarser grain-sizes in this facies compared to the underlying facies can be interpreted in two ways: a) this facies can mark the presence of an amalgamation surface or b) the reacceleration of the flow is able to re-elaborate the top of upslope and coarser grained beds and deposit the eroded sediment in a downslope location. According to our interpretation, the second hypothesis is here preferred. In conclusion type E beds are interpreted as the deposits of bipartite high-density turbidity current characterized by a deceleration and a successive reacceleration of the flow velocity, this behaviour may be associated with the occurrence of hydraulic jumps (Mutti et al., 2003; Tinterri & Tagliaferri, 2015, Tinterri 2022, in preparation). This interpretation is further sustained by the occurrence in type E beds of low- to high angle backset lamination, commonly associated with upstream-migrating bedforms, such as antidunes (Cartigny et al., 2014; Postma & Cartigny, 2014).

Contained-reflected beds (Type F)

- *Description*

These medium-thick beds are often characterized by a basal massive medium-grained sandstones (F8) and an upper fine-grained division composed of an alternation of undulated, convoluted laminae, biconvex ripples, and megaripples with different paleocurrent directions (F9). The fine-grained interval can be characterized by occurrence of a fine-grained laminaset in the intermediate part of the bed (Figure 15A-C-D). In the interlobe elements are also present thin hybrid beds composed of an alternation of well-developed basal undulated laminae and liquefied units (Figure 15B).

- *Interpretation*

The F8 and F9 facies in Type F beds are interpreted to derive from high and low-density turbidity currents, respectively. In particular, the presence of a very-thin, fine-grained laminaset is interpreted as recording a delay, due to rebound and decoupling processes, in the arrival of the

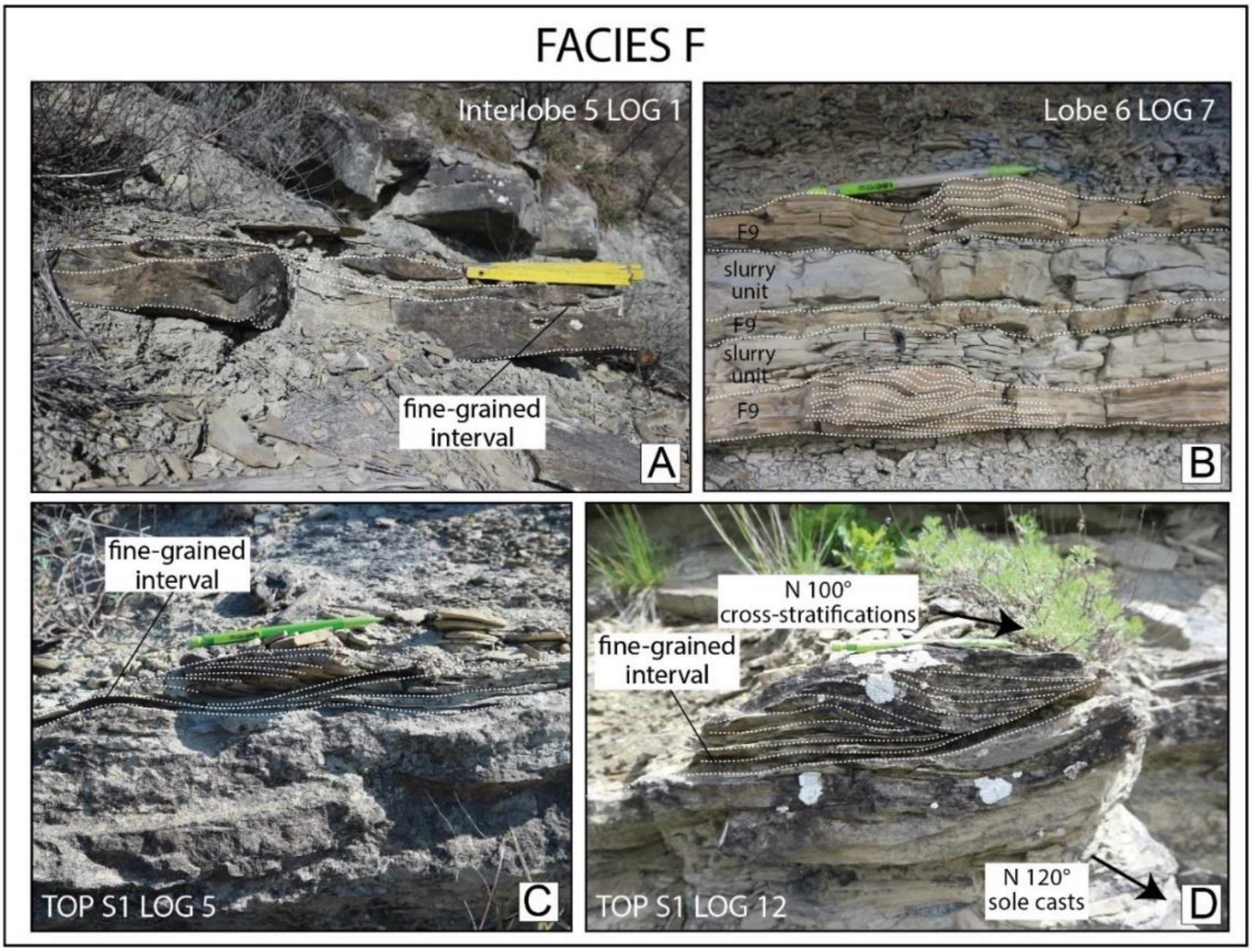

Figure 15 *Examples of Type F contained reflected beds. They consist of fine-grained sandstone (F9), generally characterized by an alternation of different types of sedimentary structures that can be interrupted by a fine-grained laminaset (insert A-C-D). Type F can consist also in bed presenting an alternation of well-developed basal undulated laminae and liquefied units (insert B).*

reflected bores responsible for the deposition of the upper laminasets (Tinterri & Muzzi Magalhaes, 2011, Tinterri, 2022 and in preparation,). The thin alternations of well-laminated divisions and liquefied units probably result from a similar process as already seen in Muzzi Magalhaes & Tinterri (2010). The alternating laminated and liquefied units could be related to the passage of decaying bores of different energy generated by successive reflections of turbidity currents against the surface of the CTRF. The reflection against the surface of the CTRF is partially recorded also by the measure of the ripples that diverge of about 20-30° from the direction measured from sole marks (Figure 5A, 15D).

Fine-grained beds (Type G)

- *Description*

This thin- to medium-thick beds are fine-grained sandstones often characterized by an alternation of undulated, convoluted laminae and biconvex ripples and megaripples (F9, Figure 16).

- *Interpretation*

The fine-grained sandstone interval (F9) represents the result of traction-plus-fallout processes related to waning turbulent flow. They can represent the deposit of a low-density turbidity current or of the residual tail of a high-density turbulent flow.

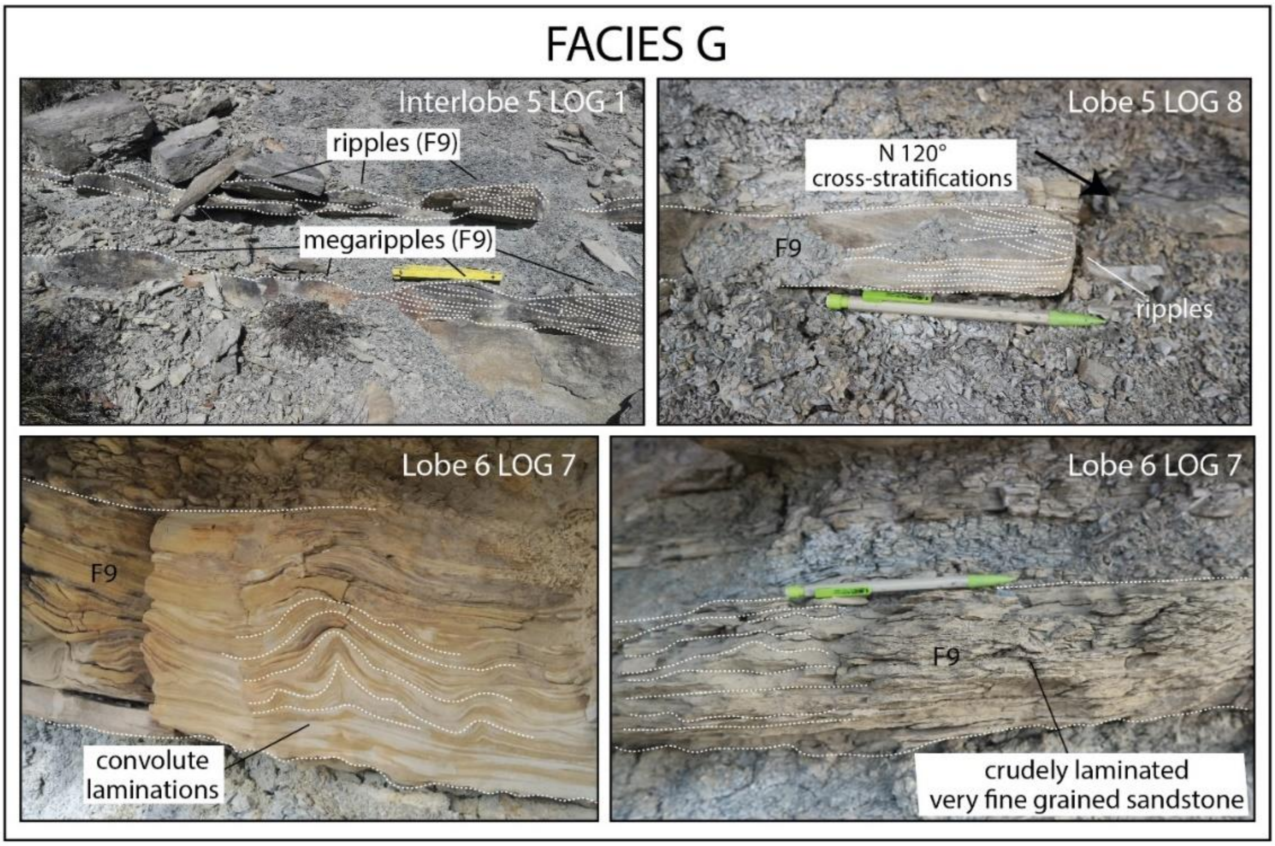

Figure 16 *Examples of Type G beds. They consist of fine-grained sandstone (F9), often characterized by an alternation of undulated, convoluted laminae (insert and biconvex ripples and megaripples.*

5.3 Thickness analysis

A progressive flattening approach can be used as a tool for the interpretation of paleo-topography of the seafloor (e.g., Muzzi Magalhaes and Tinterri, 2010; Tinterri and Tagliaferri, 2015). Generally, the maximum depositional relief is calculated by assuming that all the thickness change is attributable to sea bed topography (Prélat et al., 2009). The bed thickness analysis has been widely used also to understand the relationship between deposition, generally associated with lobe/lobe element sedimentation, and compensation phenomena, controlled by the drape of fine-grained sediment acting during an interlobe/interlobe element deposition. To help the assessment of paleo-topography of the seafloor, the thickness data were plotted for each bed from each stratigraphic log measured in the 2,5 Km long stratigraphic transect (figures 5C, 6). The yellow colour for the lobes and the dark blue colour for the interlobes mark the minimum measured thickness values, with different shades are represented the amount of difference between the value of the thickness in a given point and the minimum values. In the case of lobe elements composed of several but amalgamated beds, the thickness of the entire lobe element is considered. For the purpose of this study, the bed unit taken into account include only the sandstone division of a turbidite bed excluding the thickness of the overlying mudstone layer. Thickness of mudstone layers was not taken into account because, in most of the cases, it is covered or its quantification can be altered by the erosion operated by the successive sediment gravity flows (i.e., see erosional delamination features at the top of S1 bed in logs 9 and 11, figure 5c). However, when it can be identified, the thickness of the mud interval is always of little entity (less than 5% of the bed thickness) and their exclusion is not significant for the purpose of the analysis.

5.3.1 Downcurrent variation of the beds thickness

The thickness of the beds composing lobe 5 reveals two minimum values, the former, quite evident, is identified between logs 1b and 2, and the latter, milder, occurs between logs 10 and 11. The depocenters of the beds have different but sometimes systematic locations. The lower part of the lobe element 5a shows that from the log 3 towards SE there is an increase in bed thickness with the maximum values located persistently in log 9 (S2 and T1, Annex Figure 1). It's evident, after the deposition of T1, that the point of maximum deposition (marked by an asterisk in Annexes figures) is shifting towards NW (T1, S3, and T2, Annex Figure 1). Also the lobe element 5b and 5c show increasing thickness values towards SE reaching the maximum values at log 9 (Annex Figure 2). Regarding the lobe element 6a, the minimum values of bed thickness are located in log 1b with few exceptions such as in the cases of S4, T10, and T15 beds. The basal beds of lobe element 6a (S5 and T7, Annex Figure 3) present maximum thickness values near log 3 and became gradually thinner towards SE; while the upper part of the lobe element is composed of beds whose depocentre is shifting again towards NW (T8, T9, and T10, Annex Figure 4). The lobe element 6b, composed of two beds, shows maximum thickness value in the location of lobe 9 (T13) and then slightly shifted toward log 8 (T14). The lobe element 6c, made up by at least two beds, have two zones of maximum deposition, i.e. in logs 1b and 6 (Annex Figure 5). Finally, the lobe element 6d is composed by the amalgamation of two beds (T16 and T17) whose depocentre shifts from SE to NW. In conclusion, most of the beds (17/20) have low thickness values at logs 1b-2. In the case of the beds composing lobe 5 they present maximum thickness value in the log 9 (5/8), whereas the beds of lobe 6 have two different depocentres located in logs 3-4 (4/12) and logs 8-9 (4/12).

5.3.2 Lobes and interlobes downcurrent thickness variations

Figure 17 shows two flattenings, the former takes into account lobes 5 and 6 with relative interlobes whereas the latter considers the two lobes without the interlobes. For simplicity, we will identify as the "north-western sector" the area between log 1b and log 2, as "proximal central sector" the area between log 3 and log 6, as "distal central sector" the area between log 7 and 9 and as "south-eastern sector" the area between log 10 and 11. Lobe 5 has important thickness variations; the minimum thickness values, coherently with what observed in the single beds, are located in the logs of the north-western and south-eastern sectors. In the central sector lobe 5 is thicker, especially near the faults, where its thickness increases of about 2-3 m. In the same way, lobe 6 is thin in the north-western sector and its thickness increase towards SE. Specifically, also lobe 6 shows the

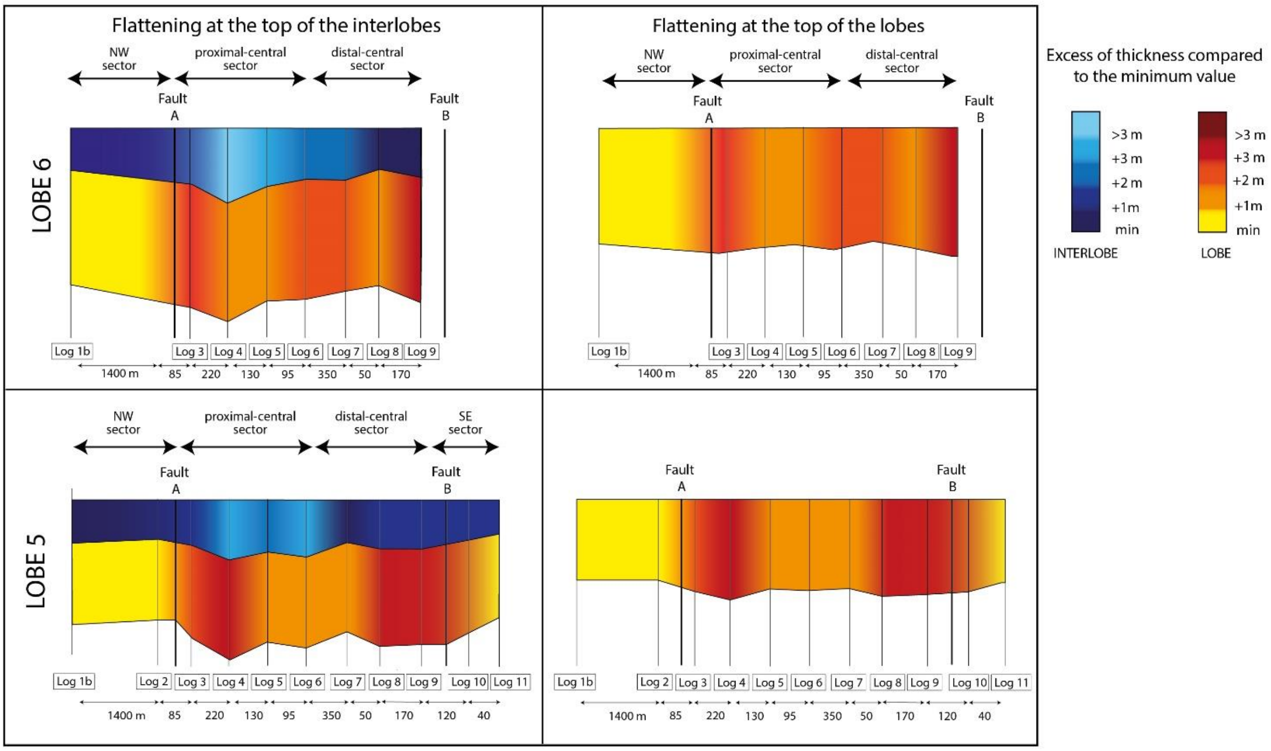

Figure 17 *Detail of the cross-section showing the progressive flattening at the top of the interlobes and at the top of the lobes. The different gradations highlight the measured difference in thickness (in meter) respect to the minimum thickness value. In the blue tone for the interlobes and in the yellow tone for the lobes. Note that near the faults A and B the thickness of the lobes increase.*

maximum thickness value near the faults (an increase of about 2-2,5 m). The interlobes 5 and 6 have similar behaviour, they show low thickness values in the north-western sector, reach the maximum thickness value in the proximal central sector and then gradually decrease towards SE (Figure 17).

6. Discussion

The data presented in the previous chapters provide new insights into the depositional dynamics of the PTS turbidites. The following subsections of this chapter discuss the interpreted paleo-topography of the seafloor at the time of deposition of lobe 5 and lobe 6 (6.1); the small-scale sedimentological response of hybrid beds and turbidites to the topographic variations (6.2) and finally the lobe depositional model elaborated for our specific study case (6.3).

6.1 Interpretation of the paleotopography

Generally, sediments tend to fill the lows of the topography so where the thickness of the deposits is high (depocentre) the presence of a depression of the seafloor is assumed, on the contrary a topographic high occurs where they are thin. During a lobe-building phase they tend to compensate the topography of the seafloor derived from a combination of structural setting, different compaction, and the relief of the underlying deposits. Analysing the relation between the downcurrent variation of the vertical thicknesses of lobes and interlobes, the paleo-topography of the seafloor at the time of deposition of lobes 5 and 6 can be extrapolated.

A previous study (Tinterri & Tagliaferri, 2015) identified, through the progressive flattening of the intermediate part B of unit VI two subtle morphologic highs and a depocentre associated with the M. Castellaccio thrust activity (see Figures 1A, B). In particular, the architecture of lobes 5 and 6 is characterized by two subtle morphologic highs in the proximal (see Log 1D in Figure 2B) and distal zone (see Logs 5 and 6 in Figure 2B) and a depocentre in the middle (Log 3 in Figure 2B). However, the detailed analysis of bed thickness gives the opportunity to better constrain the origin of those highs and depocentre.

The thickness analysis indicated that in the north-western sector, all the beds composing lobes 5 and 6 have low thickness values, as well as the thicknesses of the interlobes. According to this evidence, our analysis confirms the presence of a proximal morphologic high in the north-western sector.

In the proximal central sector, lobe 5 and overlying interlobe are highly depositional, showing the maximum thickness values near fault A. The permanence of a depocentre in the proximal central sector during the deposition of lobe 6 and its relative interlobe, points out that the interlobe 5 does not entirely compensate the topography. For this reason, the presence of a permanent depocentre is assumed in this sector.

In the distal central sector, the lobes maintain high thickness values, especially near fault B. However, the thickness of the interlobes decreases in this location. Our interpretation is that in this location the lobes form a positive topography that is able to influence the relative interlobes as highlighted by their subtle compensational stacking pattern.

Regarding the south-eastern sector, we can analyse only the lobe 5 since the lobe 6 does not crop out in this sector. The thickness of all beds slightly decreases, highlighting the presence of another distal morphologic high. The vertical expression of the latter is interpreted to be lower than that of the proximal morphologic high.

The lobes depocentre, identified in the proximal and distal central sector, is always located between faults A and B, suggesting a syndepositional nature of these faults. Consequently, a tectonic control

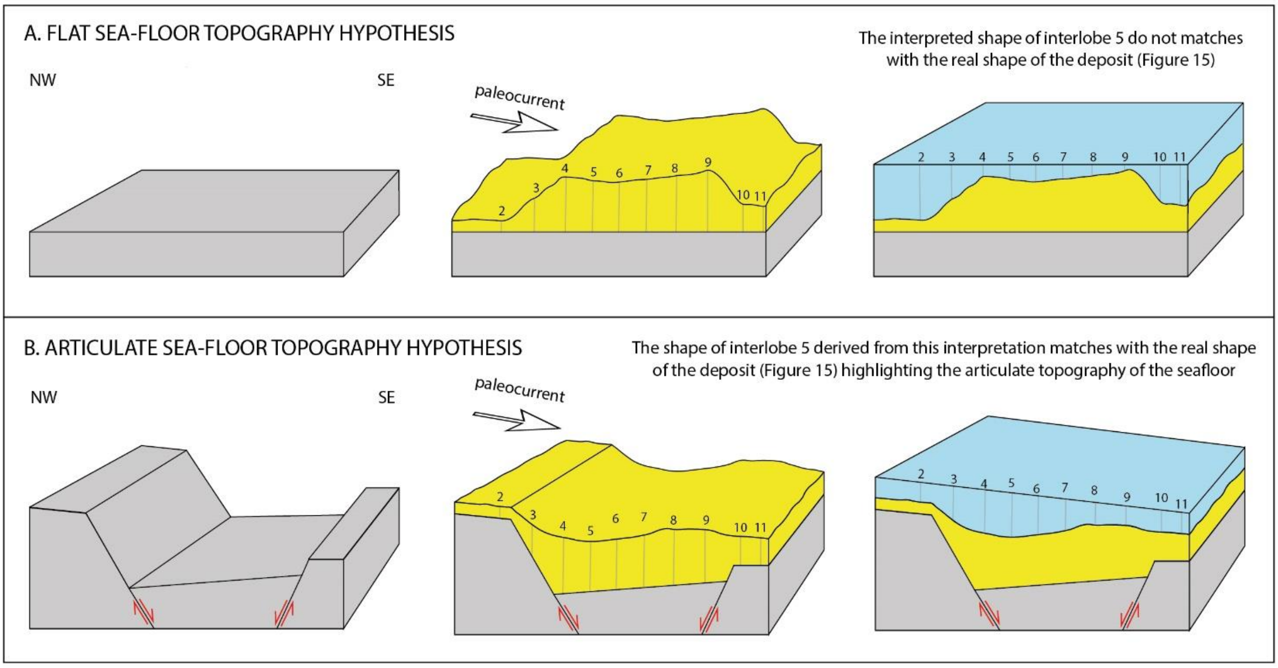

The interpreted shape of interlobe 5 do not matches with the real shape of the deposit (Figure 15)

The shape of interlobe 5 derived from this interpretation matches with the real shape of the deposit (Figure 15) highlighting the articulate topography of the seafloor

*this represent an interpretation, the thickness of the lobe 5 plotted here have been vertically exagerated in order to better appreciate their variation

Figure 18 *Plotting the thickness of lobe 5 on the hypothesis of a flat seafloor (A) and of an articulate shape of the seafloor (B). The resulting shape of interlobes have been compared with the real data. Note that the shape of interlobe resulting from an articulate seafloor is perfectly consistent with the real one that can be observed in the stratigraphic cross section in Figure 17.*

influenced the paleo-topography of the seafloor creating an about 1 Km long structural depression in the central sector, bounded by a proximal morphologic high (in the NW sector) and by another distal high located in the SE sector. According to this interpretation, these faults are assumed to be normal faults. This structural depression is interpreted to be deeper in the proximal central sector, where both lobes and interlobes thicknesses have the highest values. In particular, thanks to the thickness analysis, we have interpreted that the morphological step between the proximal high and the depocentre is about 3 m during the deposition of lobe 5 whereas became slightly lower (2- 2,5 m) during lobe 6. According to these data, we can suppose that the paleo-topography was less irregular at the time of deposition of the lobe 6.

This interpretation of the seafloor paleo-topography is further sustained by the shapes of the interlobes. Plotting the thickness of lobe 5 on a flat seafloor the shape of the resulting interlobe is not consistent with the reality, while on an articulate seafloor with proximal high-depocentre-distal high the resulting interlobe geometry is perfectly consistent with the real one that can be observed in the stratigraphic cross section (Figure 18).

6.2 Relationship between short-scale facies change and basin topography

A great part of the MAF stratigraphic studies are focused on high-resolution stratal correlations over significant distances (e.g., Amy & Talling, 2006; Muzzi Magalhaes & Tinterri, 2010; Ricci Lucchi & Valmori, 1980; Tagliaferri & Tinterri, 2016; Talling, Amy, et al., 2007; Tinterri & Muzzi Magalhaes, 2011) on the other hand, very few are the works whose main focus is related to short and small-scale sedimentological variation (e.g., Cattaneo, A. & Ricci Lucchi, 1995; Eggenhuisen et al., 2010; Fonnesu et al., 2015; Tinterri & Tagliaferri, 2015). In this depositional setting, the substrate topography can influence the dynamics of the sediment gravity flows, thereby forming a flow-substrate feedback mechanism. Recognition of this feedback is very important because it provides a natural window on the flow processes controlled by a small-scale topography capable of affecting flow dynamics. The great lateral continuity of the outcrops of the study area permits high-resolution bed correlations that can well highlight facies changes occurring on a short distance.

6.2.1 Relationship between hybrid bed deposition and basin topography

Hybrid event beds have different downslope evolution according to the degree of confinement of the basin, producing different longitudinal and lateral facies tracts. In an unconfined setting the slurry unit progressively thickens down-dip in the outer fan and fan fringe before finally pinching out; in this case, facies transitions occur over several kilometres (Haughton et al., 2003). In a confined setting, as the PTS characterized by lateral confinement, the slope forces the flow to decelerate, rapidly damping the turbulence and producing a transformation to cohesive flow which deposits close to the margin (Muzzi Magalhaes & Tinterri, 2010; Patacci et al., 2014; Tinterri et al., 2016; Tinterri & Muzzi Magalhaes, 2011). Also, local gradient changes can favor debris flow development and deposition (Talling et al., 2007) and important short-length facies variations (over meters to tens of meters) have been observed in hybrid event beds (Fonnesu et al., 2015, 2016; Tinterri & Tagliaferri, 2015). This variability is generally expressed by changes in the proportions of the basal sandstone and the overlying muddy slurry unit, as well as variations in the percentage of mudclasts and the occurrence of substrate delamination features. This short-scale facies variation has been related by the aforementioned author to the erosion and incorporation of the muddy substrate and progressive disaggregation of the eroded mud.

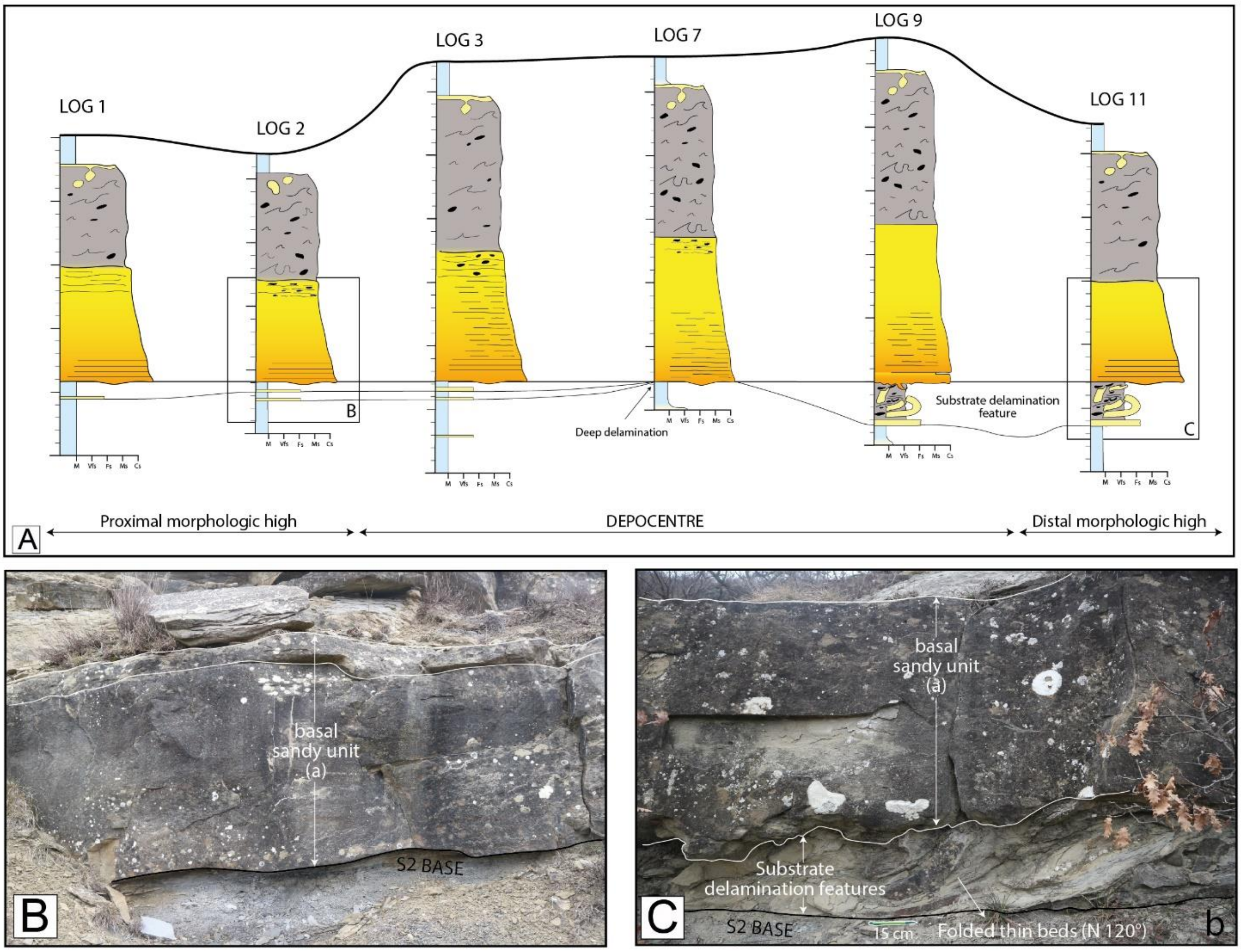

Figure 19 *(A) Lateral thickness and facies change in the hybrid bed S2. Note the minor thickness above the interpreted morphologic highs and the high thickness value in the depocentre. The hybrid bed has an irregular base in the proximal sector (insert B) while downslope the base became strongly erosive approaching the distal morphologic high, manifested through the erosion of the underlying fine-grained bed and substrate delamination feature (insert C) where the flow is interpreted to impact above the distal morphologic high.*

In particular, in many examples, the thickness variations of the basal sandy unit (“a”) are compensated by the slurry unit (“b”) highlighting their strict relationship and how the slurry units formation is a self-levelling process to maintain the overall bed thickness (see Fonnesu et al., 2015).

However our closely-spaced logs on hybrid beds highlighted that thickness changes occur on scale of few tens of meters, this is particularly evident in thicker-bedded hybrid beds. For example, S2 bed thickens of 80 cm in 85 m passing from the morphologic high into the depocentre area with a concomitant thickness increase of basal sandy and slurry units (Figure 19). In our case, it seems to prevail a compensation of the paleo-topography with respect to a self-levelling process performed in other settings as shown by Fonnesu et al. (2015). We thus conclude that the self-levelling behaviour probably prevail in flat seafloor setting, while in the case of an irregular seafloor topography, hybrid beds tend to fill the topographic lows where in general the deposition rate increases both for the basal unit “a” and for intermediate slurry unit “b”.

The detailed grain size analysis performed on hybrid beds highlighted another straightforward relationship between hybrid flow dynamics and seafloor paleo-topography. The hybrid beds belonging to lobe 5 (S1, S2, and S3 Figure 20A) have been sampled on the proximal morphologic high, in the depocentre and in the distal morphologic high. In the same way, the hybrid beds of lobe 6 (S4 and S5, Figure 20B) have been sampled in the proximal morphologic high and in the depocentre but not in the distal morphologic high where they do not crop out. As a substitute, they have been sampled in log 7, where the thickness of this beds is low, as in the morphologic highs. The granulometric curves highlight that the slurry units deposited in the depocentre (red curves in Figure 20) present a higher percentage of fine-grained fraction, corresponding to the amount of clay and silt fraction, respect to those collected on the morphologic highs (green and blue curves in Figure 20). The fine-grained fraction increase from 2 to 9% where the hybrid beds are more depositional (Table in Figure 20). Bed S4 is the only exception, the granulometric curves are similar and the fine-grained fraction is almost the same in all the samples. The increase in mud content is related to rapid deposition from the denser portion of the turbidity current (Mutti & Nilsen, 1981). Drastic sediment deposition can be triggered by small but abrupt decrease in seafloor gradient; one of the most striking example is the landslide in the Agadir basin described by Talling et al. (2007). Exiting a steep ramp, the deceleration of the turbidity current at the slope break reduced the turbulent mixing causing en-masse settling of structureless, mud-rich debrite sand where gradients are low (Muzzi Magalhaes & Tinterri, 2010; Tinterri & Piazza, 2019).

Figure 20A *Granulometric curves acquired in the slurry unit of the hybrid beds in lobe 5 (S1-S2-S3). The samples collected above the morphologic highs (blue and green curves in the graphs) present lower fine-grained fraction compared to the samples acquired in the depocentre (red curve), this data is highlighted in the table on the right where the percentage of the fine and coarse fraction are reported and the difference in fine fraction between the sample in the depocentre -proximal high and depocentre-distal high.*

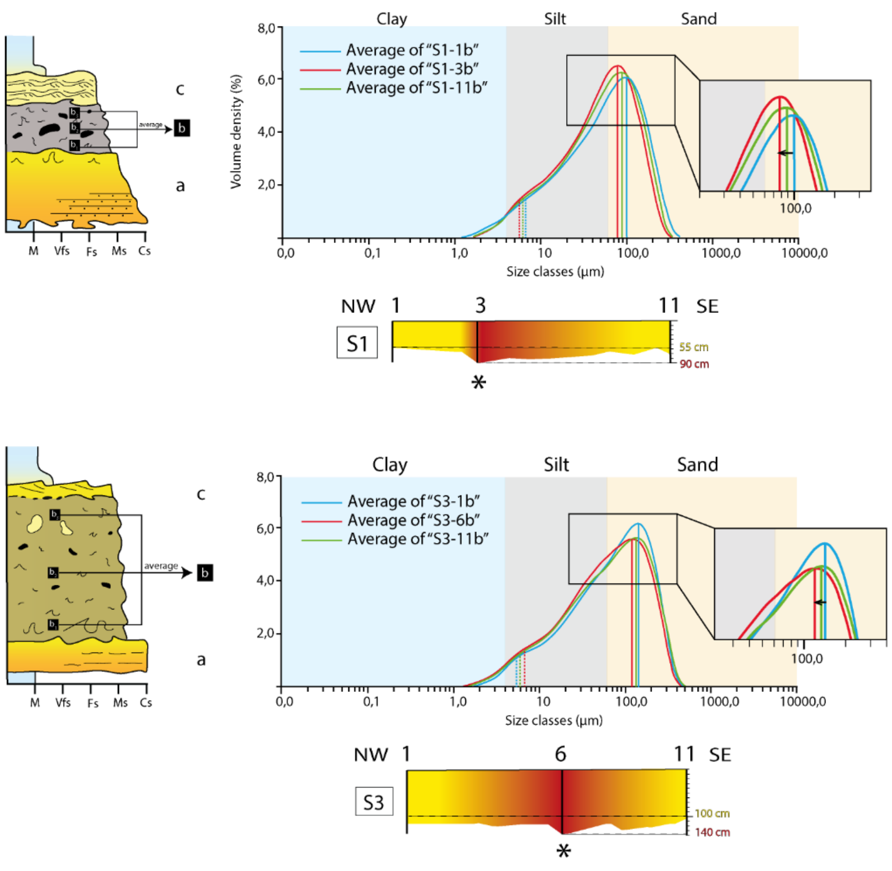

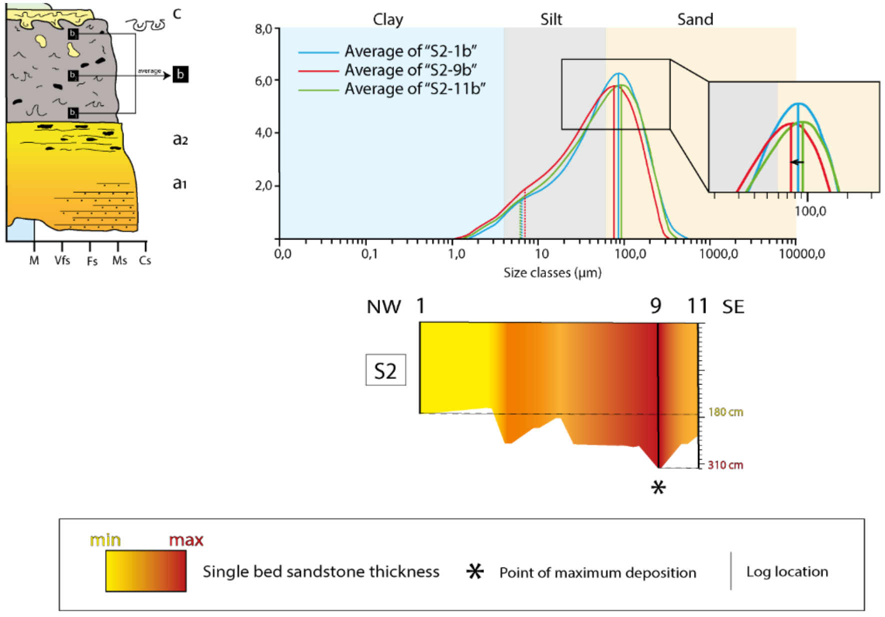

Bed	Log	Fine fraction (%)	Coarse fraction (%)	Δ Fine fraction
S1	1	52,18	47,81	3,1-5,7%
S1	3	57,93	42,07	
S1	11	54,8	45,2	
S2	1	52,03	47,69	4,5-7,3%
S2	9	59,33	40,66	
S2	11	54,85	45,13	
S3	1	44,54	55,45	2,1-5,2%
S3	6	49,78	50,21	
S3	11	47,7	52,28	

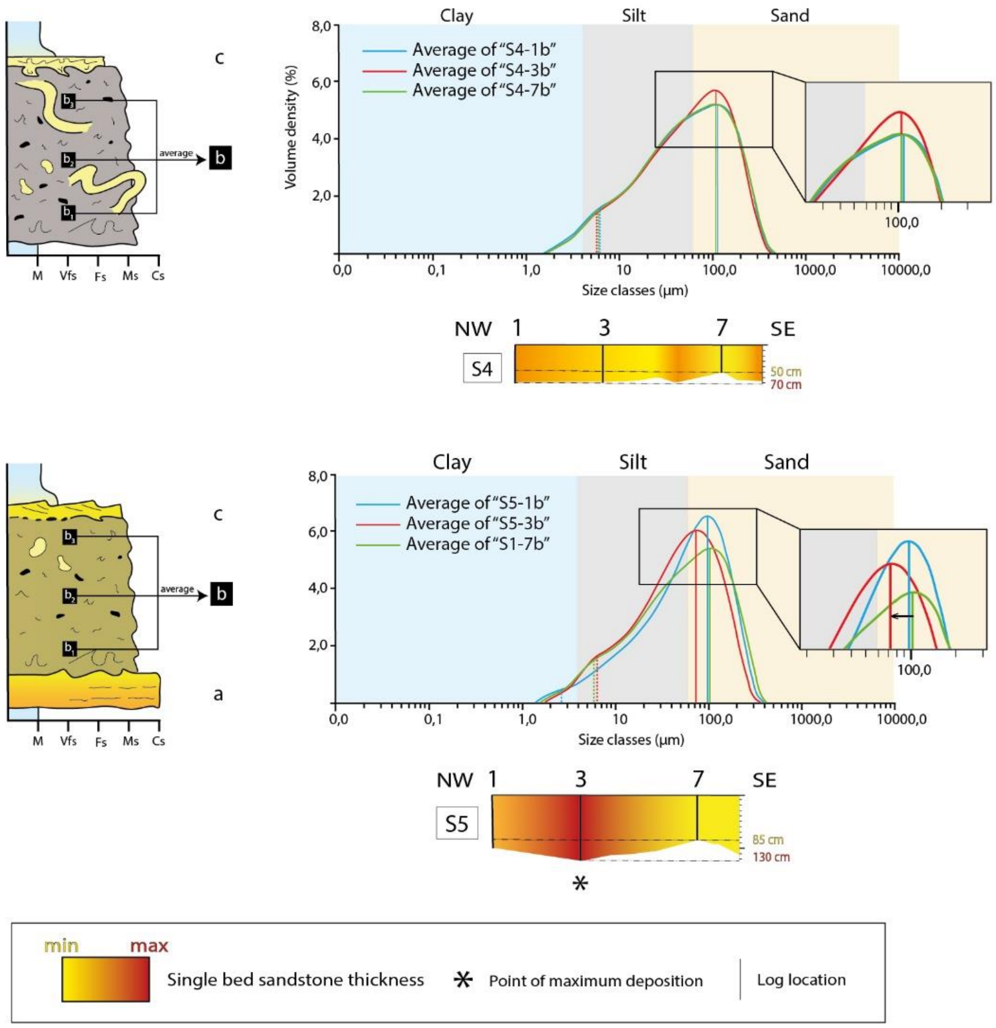

Figure 20B Granulometric curves acquired in the slurry unit of the hybrid beds in lobe 6 (S4-S5). The samples acquired in the morphologic highs (green and blue curves) and in the depocentre are homogeneous in the case of S4 bed. While the samples of S5 bed present lower fine-grained fraction in the sample acquired on the morphologic highs compared to the samples acquired in the depocentre. Note that the S4 samples show a negligible increase in the fine fraction on the morphologic highs, differently from all the other hybrid beds.

Bed	Log	Fine fraction (%)	Coarse fraction (%)	Δ Fine fraction
S4	1	53,12	46,87	1,3-2,5%
S4	3	51,76	48,24	
S4	7	54,28	45,71	
S5	1	49,17	50,83	5-9%
S5	3	58,43	41,57	
S5	7	53,53	46,47	

Differently, an increase of seafloor gradient stimulated the bypass of the fine-grained portion resulting in the deposition of prevalently sandy turbidites where the gradient is high. We interpreted that a similar mechanism occurred when the mud rich hybrid flows approached the slope break at the base of the proximal morphologic high. The deceleration of the flow at the foot of the slope can be connected to the occurrence of a hydraulic jump in the basal high-density part of the flow (Figure 21). Indeed, it is especially the basal high-density part of bipartite flows that may undergo a hydraulic jump (Dorrell et al., 2016; Soutter et al., 2021). This hypothesis is supported by the fact that all the hybrid beds showing an increase in the fine-grained fraction have a basal sandy interval (S1, S2, S3, and S5, Figure 20) while the S4 hybrid bed, that do not report an increase in the fine-

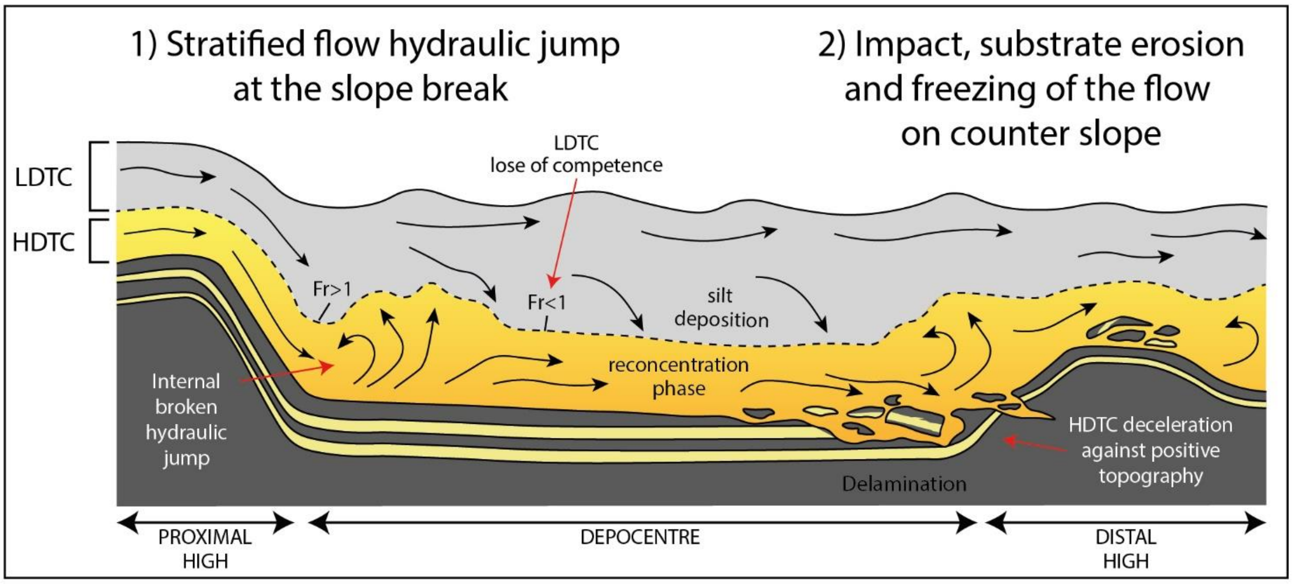

Figure 21 *Interpretation of the hybrid flow dynamics in relation to the articulate topography of the seafloor. The high-density part of the turbidity current (HDTC) pass through an internal hydraulic jump at the slope break of the proximal morphologic high. The drastic deceleration of the HDTC is associated to the increase in silt deposition in the depocentre due to the lose of competence of the upper low-density part of the flow (LDTC). The impact of HDTC on the surface of the distal morphologic high cause a strong erosion of the substrate with consequent transport and deposition of the eroded material on the surface of the distal morphologic high.*

grained percentage, have not a sandy basal portion (Figure 20B). In conclusion, we have interpreted that the deceleration of the flow in the depocentre is reached when the hybrid flow has a stratified structure with a basal high-density portion able to pass through the hydraulic jump.

The same beds show erosional features at bed base localized at the transition between depocentre and distal morphologic high. This feature consists of a 20-30 cm interval of laminated mudstone and folded thin-beds mostly oriented parallel to the paleocurrent (Figure 19C). The same thin-bedded turbidites are *in situ* beneath the bed along the other logs of the stratigraphic cross-section (Figure 19A). Therefore it can be interpreted as the result of substrate scouring, transport with consequent deformation and deposition, in literature these deposits are identified as substrate delamination features (*sensu* Fonnesu et al., 2016). The presence of irregular seafloor topography has assumed to be a prerequisite for the detachment of substrate beneath highly energetic turbulent flow (Fonnesu et al., 2016; Tinterri & Piazza, 2019). Other cases of substrate delamination features have been observed close to confining slopes, in particular near steep counter slope (Puigdefabregas et al., 2004; Tinterri et al., 2017). In our case, this feature is interpreted to result from the interaction between the dense part of the hybrid flow and the distal morphologic high (Figure 21). The load and tangential stress of the incoming dense flow resulted in the development of a sub horizontal intrastratal injection that delaminated the underlying soft deposits. According to the low degree of disruption of the eroded thin-beds it can be interpreted that they have been transported for a short distance. The rapid suppression of the shear velocity at the base, due to the impact with the morphologic high, caused the rapid freezing of the flow and the consequent deposition of this interval at the base of the morphologic high and at the top of it.

6.2.2 Relationship between high-density turbidity current deposition and basin topography

The lobe element 5b, composed of a single Type E.1 bed passing downcurrent into a Type B.2 bed, shows an important variation in thickness and facies association. The detailed correlation of the facies characterized by the same sedimentary structures and grain size populations (see Mutti et al., 2003 and Tinterri, 2022, in preparation) allowed us to obtain important insights between flow dynamics and seafloor topography.

In this bed, the depositional phases discussed in Tinterri (2022, in preparation; see Figure 10 in chapter 1) have been recognized. This bed, indeed, is characterized at the base by a crude lamination in coarse-grained sandstone, often dipping upcurrent (F5pb in Tinterri, 2022, in preparation). This facies has been widely associated with the supercritical regime of the basal dense layer of a bipartite flow (Cartigny et al., 2013; Talling et al., 2012). High basal sediment concentrations and flow stratification suppress the turbulence and expand the supercritical flow domain, increasing the stability field of the plane beds (Postma et al., 2009). This facies pass downcurrent, near the distal morphologic high, into high-angle backstepping laminations (F5an in Tinterri 2022, in preparation), upper flow regime structures related to supercritical bedforms such as antidune (Cartigny et al., 2014; Hage et al., 2018; Ono et al., 2021; Postma & Cartigny, 2014). This basal interval has been recognized in all the sedimentary logs. We have thus interpreted that the basal part of this bed results from the deposition of a supercritical gravelly high-density turbidity current able to form long wave antidune (SUPERCRITICAL PHASE - I, Figure 22).

This basal crudely laminated interval is overlain by massive liquefied coarse-grained sandstone, sometimes characterized by soft sediment deformation such as crude convolute structures (F5m in Tinterri, 2022 in preparation, Figure 13G-22). These structureless beds are associated to high fall-out rate related to rapid drop in flow velocity that may be associated with a hydraulic jump (Postma et al., 2009).

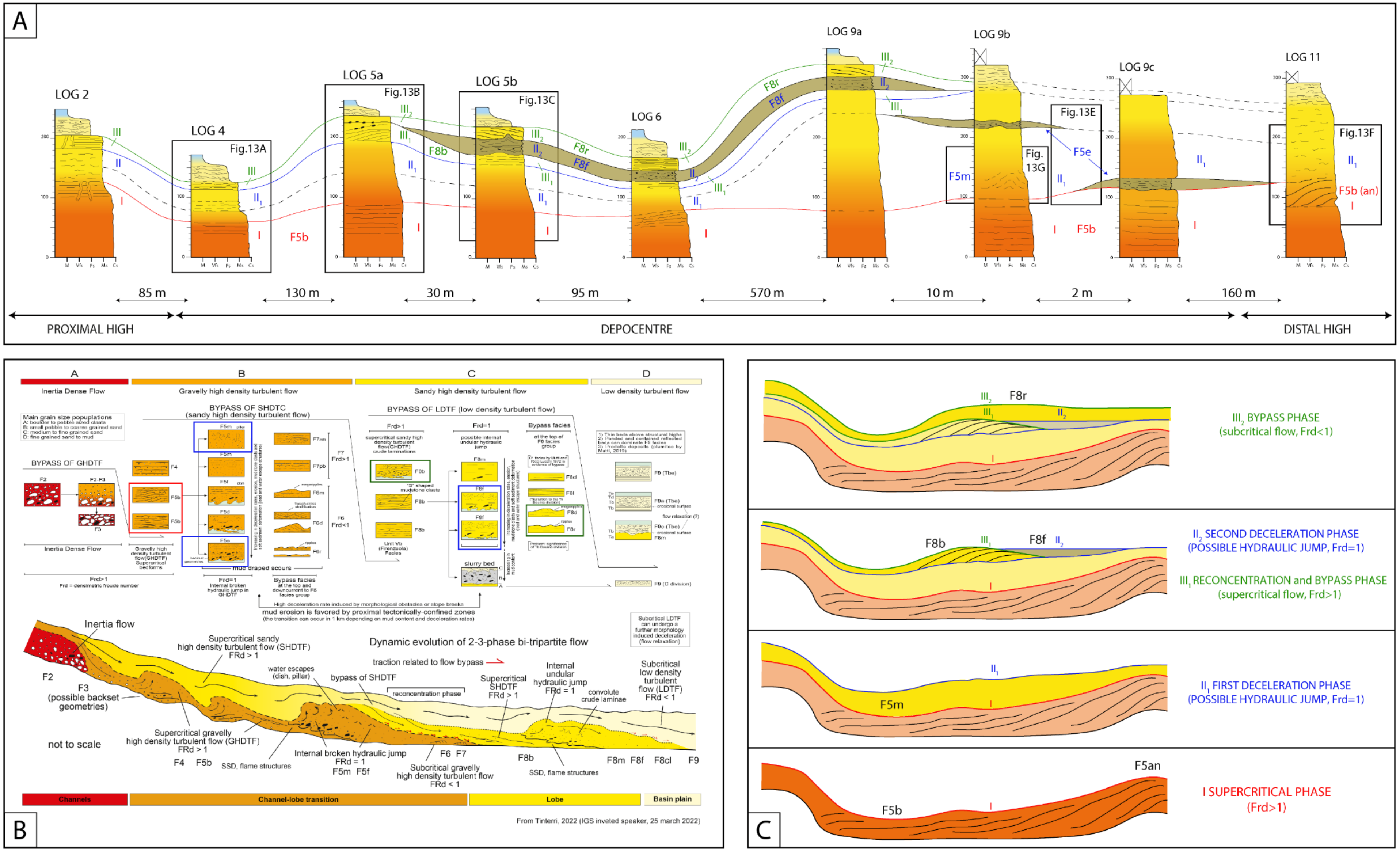

From Tinterri, 2022 (IGS inveted speaker, 25 march 2022)

Figure 22 *Interpretation of the turbiditic flow dynamics in relation to the articulate topography of the seafloor. (A) Lateral thickness and facies change in the turbidite bed T4. The correlation of the facies recognized (according to the reference facies scheme of Tinterri 2022; in preparation, insert B) highlights the presence of different flow phases. (C) Initially, the flow is supercritical (I) and deposits crudely laminated (F5b) and high-angle backstepping laminations (F5 an). Follows a deceleration phase (II1) characterized by massive facies (F5m) associated with a hydraulic jump. After the jump the flow undergoes a reconcentration and bypass phase (III1) with low-angle backstepping laminations (F8b), this phase is followed by a second deceleration phase (II2) marked by the deposition of a muddy sandstone interval (F8f). The last phase is associated to medium-grained tractive facies (F8r) indicative of the bypass (III2) of a fine-grained turbulent flow.*

In this interval, lens of crudely laminated muddy sandstone evolving into sharp surfaces are also present; they are recognized in the outcrop thanks to their erosional profile (Figure 13C-E). This interval, bounded by the blue line in Figure 22, recognized in all the sedimentary logs, changes in thickness. It presents minimum thickness values in Log 4 and gradually increases towards SE, reaching its maximum in Log 9. The sedimentary characteristics of this interval, which include structureless sandstones and a sort of mud-draped scours suggest the sudden decelerations of supercritical bipartite flows possibly related to the occurrence of a hydraulic jump (FIRST DECELERATION PHASE - II_1, Figure 22).

Between Log 5a and 6 a thin interval develops above the massive sandstone facies previously described. This interval is about 20 cm thick in Log 5a where it is composed by medium-grained sandstone characterized by low-angle backstepping laminations (F8b in Figure 13D). These sedimentary structures can be associated with supercritical flows leading to the formation of low aspect-ratio antidunes (*sensu* Cartigny et al., 2014) evolving downstream into a plane parallel lamination (see Log 5b and 6, Figure 22). We interpreted this interval as associated with a re-acceleration of the bypassing flow recording a sort of reconcentration after the flow expansion as stated in Tinterri (2020, 2022; see also Mutti 1992). The flow re-acceleration led to the bypass of the finer grain-sizes (RECONCENTRATION and BYPASS PHASE - III_1).

Another muddy sandstone interval, similar to the lens in interval II_1, occurs between Log 5b, 6, and 9a. The extension of this interval, in a downcurrent direction, is about 650 m; this is indicative that it has a higher order of magnitude in comparison with the more localized lens-shaped muddy sandstone of the interval II_1. It has an irregular base and is composed of an alternation between muddy sandstone and thin-bedded medium-grained sandstones; this facies passes upward into a lenticular cross-stratified medium-grained sandstone (F8r in Figure 13C). The thin-bedded layers show soft sediment deformations as water escape structures (Figure 13C) indicative of the drastic deceleration rates during the deposition of this interval. We have interpreted that this interval

records another deceleration of the flow with the possible occurrence of an internal hydraulic jump (II_2 SECOND DECELERATION PHASE, Figure 22). This interpretation is further supported by the presence of the medium-grained tractive facies (F8r) indicative of the bypass of a fine-grained turbulent flow (III_2 BYPASS PHASE, Figure 22).

This bed is interpreted to record the different phases of flow transformations from supercritical to subcritical with strong analogies with the models shown by Mutti (1992) and Postma (2011) with an internal hydraulic jump occurring in the gravelly high-density part of the flow and another one in the sandy high-density turbulent flow phase interspersed by a reconcentration phase with a consequent bypass of the uppermost component of the flow (Tinterri et al., 2020; see also Tinterri 2022, in preparation).

It is interesting to note that the bed has the minimum thickness in Log 4, at the slope break between the proximal morphologic high and the depocentre, before doubling its thickness 130 m to the south-east (Log 5a), i.e. a little further downstream of the slope break associated with fault A. This can produce a deceleration up to causing a series of hydraulic jumps able to deposit massive units in backstepping, each followed by a bypass phase. Stratified flows, indeed, are strongly influenced by changes in seafloor slope that can accelerate or decelerate the flow (Dorrell et al., 2016). Consequently, the formation of a hydraulic jump at the slope break can produce a higher erosion and bypass in the location of log 4, while downcurrent the slope break a combination of high depositional rate and available accommodation space make possible the preservation of all intervals related to the different phases linked to the flow transformations (i.e. supercritical, deceleration and bypass phases as suggested by the model proposed by Tinterri, 2022 in preparation; see also Postma et al. 2009).

6.3 Lobe depositional model

Lobes 5 and 6 show the same recurrence of bed type associations and lobe element stacking patterns. In literature many models of lobe formations have been discussed and proposed (e.g., Mutti and Ricci Lucchi, 1972; Mutti and Ghibaudo, 1972, Mutti, 1977; Walker, 1978; Mutti and Normark, 1987; Cornamusini, 2004; Prelat et al. 2009; Mulder and Etienne, 2010), nevertheless on the analyses carried out on these lobes we propose a depositional model including three stages of evolution characterized by specific bed types.

Stage I is characterized by hybrid beds (Type A) with an upward decrease in the degree of evolution (upward transition from Type A.1 to A.2, Annex Figures 1 and 3). The deposition of this bed type is thus limited to the first phase of lobe initiation. The origin of these hybrid beds is interpreted to be related to the action of strongly erosive flow able to incorporate a sufficient amount of mud up to suppress the turbulence and form a slurry facies (Baas et al., 2011; Haughton et al., 2009). The presence of hybrid beds has frequently been associated with high deceleration rates due to the proximity to morphological obstacles or slope breaks (Muzzi Magalhaes & Tinterri, 2010; Tinterri & Muzzi Magalhaes, 2011; Tinterri & Tagliaferri, 2015). The growth of the CTRF, still ongoing during the Upper Serravallian, produces a lateral confinement of the PTS turbidites as also testifies by the onlap of these deposits against the CTRF (Tinterri & Tagliaferri, 2015). In this geological setting, it is possible to advance the hypothesis that, in the first phase of lobe construction, upcurrent non-equilibrium slopes (able to promote significant flow incision and mud incorporation) can exist. The drastic deceleration of these mud-rich flows against the relief produced by the CTRF resulted in the deposition of tripartite hybrid beds. The transition from Type A.1 to A.2 beds can be associated with successive slightly less erosive flows able to form slurry intervals with a lower amount of mud.

Successively to the Stage I, Type B.1 beds begin to prevail characterizing the initial phase of lobe building (Stage II). The turbidity currents are still forced to decelerate due to the lateral confinement as highlighted by the presence of relatively liquefied units in these beds (Figure 10A). However, after this initial part characterized by Type B.1 beds, Stage II is principally composed of Type E beds; initially, there is a prevalence of medium-grained sandstone (i.e., Type E.1 beds), successively Type E.2/B.2 coarse-grained beds become the prevalent bed types. Both these bed types can be interpreted as associated with the deceleration of bipartite flows (see above). The deceleration induced by the lateral confinement leads to the deposition of basal massive facies (i.e., F8 in the case of Type E.1 beds and F5 in the case of Type E.2/B.2), and the bypass of turbulent flows leading to the deposition of traction facies at the top of the beds (F8r/l). The upward increase in Type E.2/B.2 can be interpreted as an increase in the rate of deceleration favoured, at least in part, by the morphology created by the lobe-building phase. This process is also testified by an increase in the erosive capacity of the flows marked by an increase in amalgamation surfaces and flow impact structures as well as supercritical structures passing upward into massive facies. Stage 2, therefore,

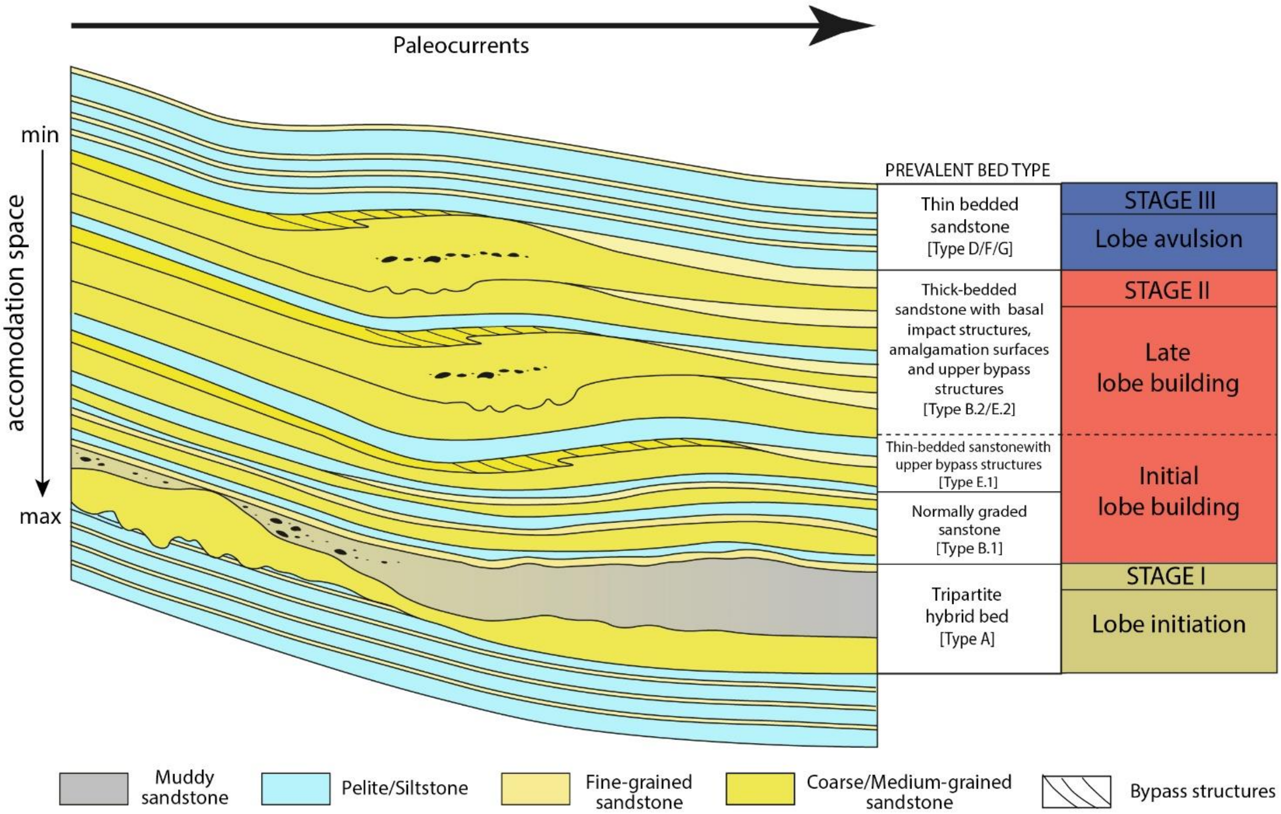

Figure 23 *Schematic illustration of the three-stage mode (i.e lobe initiation, building and avulsion) elaborated for the lobes 5 and 6. Each stage is composed of one or more bed types reported in the lateral column. See the text for more detail.*

tends to favor efficient decoupling processes highlighted also by efficient bypass processes of the fine-grained turbulent flows (see also discussion in Piazza & Tinterri, 2020).

Stage 3 is characterized principally by thin-bedded fine-grained turbidite beds (Type G) and in a minor portion by medium-grained normally graded beds (Type D) sometimes presenting evidence of rebound structures (Type F).

These dynamics shares similarities with the three stage model proposed by Hamilton et al. (2017) obtained from tank experiments and their comparison with various field studies such as those made by McDonald et al. (2011), Postma & Kleverlaan (2018) and Piazza & Tinterri (2020) and previously inspired by the experiment of Hoyal & Sheets (2009). These experiments found that each lobe-building cycle, which takes into account both lobe and relative feeder channel consists of four phases, namely: 1) channel formation and basinward extension in conjunction with sheet flow at the channel outlet to produce the lobe elements, 2) cessation of channel extension and lobe aggradation up to choked-flow condition, 3) hydraulic jump at the channel outlet and upstream retreat of the channel to lobe transition, and 4) channel relocation (avulsion).

Stage 1 well fit with the first phase recognized in those models corresponding to the lobe initiation, while the initial stage 2 records the lobe aggradation phase. Postma & Kleverlaan (2018) recognized an increase in the flow energy in the aggradation phase associated to the action of stratified supercritical turbidity currents. In the same way, Hamilton et al. (2017) associated to the continuous lobe aggradation, the progressive creation of frontal obstruction until the flow is forced to decelerate (choked flow condition). The turbiditic beds of the initial stage 2 manifest the increasing effect of the deceleration and consequent flow decoupling recorded by the passage from Type B to Type E.1 beds. The aggradation phase in the models terminates with the occurrence of a hydraulic jump that led to the passage to the channel backfill phase (see also the flow impact and bypass phase by Piazza & Tinterri, 2020). This stage is associated in Piazza & Tinterri (2020) to the deposition of massive coarse-to medium-grained sandstones (F5-F8) and tractive structures, such as traction carpets (F7) and megaripples (F6), rich in mudstone clasts. In our lobes, the amalgamed beds rich in mudstone clasts (Type B.2) that can present also upper bypass structures (Type E.2) that characterize the late stage 2, can be consistent with the “flow impact and bypass phase” identified by those authors and associated to the hydraulic jump phase of Hamilton et al. (2017) and Postma et al. (2018). This phase led to the progressive abandonment phase followed by the deposition of fine-grained interlobes. The last stage associated to the final avulsion of the system is represented in the models by the deposition of thinning and fining upward turbidite beds produced mainly by subcritical, low-density flow. Our stage 3, marked by muds interval deposition occurring in the interlobes, is analogous to the last phase of the models and is thus related to the channel avulsion and a lobe-switching phase. In conclusion, our three-stage model well fit with the previously elaborated models, further sustaining their validity and the incredible utility of facies association identification to discriminate the different depositional processes characterizing the lobe’s evolution.

7. Conclusions

This study presents a detailed physical stratigraphy and facies analysis of two depositional lobes of the intermediate part of the Paretaio Turbidite System, belonging to the Marnoso arenacea Fm., one of the most important foredeep systems of the northern Apennines (see Figure 5). In this stratigraphic succession, a four-fold hierarchy of the turbidite deposits has been recognized, namely: bed, lobe element, lobe and lobe complex. Thanks to the detailed facies analysis, a facies scheme specific for those lobes, similar to that presented by Tinterri & Tagliaferri (2015) for Units V and VI, has been proposed (Figure 7).

The two lobes have been characterized at large (lobe) scale and small (bed) scale, analysing the vertical and lateral variations of the facies in relation to the lateral basin confinement produced by the Mt. Castellaccio thrust, and to the small (meters scale) topographic seafloor variations associated with the normal faults A and B (Figures 17, 18). The latter created an about 1 Km long and about 2-3 m deep structural depression in the central sector of the study area bounded by two morphologic highs, one proximal and the other one distal (Figures 17, 18). This work, therefore, through a detailed physical stratigraphy, has been able to improve the knowledge of the geometry of this structural depression, revealing, through an analysis of facies and bed thicknesses, the synsedimentary nature of the two faults.

Closely-spaced stratigraphic logs led to the recognition of short and small-scale facies variations both in hybrid and turbidite beds in relation to the subtle topographic variations. Regarding the former bed types, the drastic deceleration of the basal high-density part of mud rich hybrid flows can produce, in the depocenter, slurry units with a higher fine fraction in comparison with those above the morphologic highs (Figure 21). Conversely, regarding the turbidite beds, the deceleration of high-density turbulent flows can produce facies sequences recording a hydraulic jump transformation, as suggested by the model proposed by Tinterri (2022) and Tinterri et al. (2023; in preparation, Figure 10 in chapter 1), (see also Postma, 2009). The phases recognized in the turbidite beds are: 1) initial supercritical flow condition (F5b-F5an); 2) first internal hydraulic jump occurring in the gravelly high-density part of the flow (F5m); 3) a first bypass phase of the sandy portion (F8b), in which a reconcentration process, restoring supercritical condition in the gravelly high-density turbulent flow, can occur; 4) a second hydraulic jump in the sandy high-density turbulent flow (F8f, muddy sandstone) and 5) a second phase of bypass of the uppermost part of the flow (F8r/l).

The cyclic recurring of the identified facies associations in the two lobes is the basis for a three-stages model of lobe development. The depositional model consists in: 1) a lobe initiation phase, mainly composed of hybrid beds (Type A beds) recording the deceleration of mud-rich flow due to the lateral confinement operated by Mt. Castellaccio thrust; 2) a lobe building phase characterized by the beds aggradation showing a progressive vertical increase in amalgamations and impact structures (transition from Type B.1 to B.2) and flow decoupling (i.e., bypass structures, Type E). This phase records flow decelerations and hydraulic jumps, induced by the morphology created by the underlying depositional lobe; 3) a final abandonment phase of the lobe with the deposition of fine-grained sediment deposited by very dilute turbulent flow characterizing the interlobe deposits.

In conclusion this work provide three important messages:

a) A detailed facies analysis linked to a thickness beds analysis (resulting from a progressive flattening approach applied at the scale of beds, lobe elements and lobes) is a quite valid method for the identification of subtle topographic variations of the seafloor (Figure 17 and 18).
b) subtle topographic variations (i.e., meters scale) are able to modify high-density gravity flows dynamics favouring the formation of supercritical bedforms, hydraulic jumps and hybrid beds (Figure 21) as well as to conditionate their preservation (i.e., erosion and bypass on the highs and deposition in the depocenter; see Figure 22)
c) our depositional model (which is also supported by various similar evolutive schemes in the literature deriving both from field works and experimental data - see above), interprets the formation of lobes and lobe elements as controlled primarily by autogenic processes. These processes are related to the seafloor basin morphology and to the depositional relief associated with the lobe building (Figures 22 and 23).

Chapter 5

General conclusions

This dissertation is based on a multidisciplinary approach for the study of two modern fans, the Acquarone Fan (located in the Gioia Basin, Southern Tyrrhenian Sea) and the Amantea Fan (located in the Paola Bains, Southeastern Tyrrhenian Sea) and two ancient lobes, belonging to the Paretaio turbidite system (Marnoso-arenacea Fm, Northern Apennines). Modern submarine fans have been investigated particularly from the morphologic point of view (feasible through the morphobathymetries) and according to their large-scale architecture (through seismic profiles) interpreting the spatial lithological variations through seismic facies analysis or core calibration. Conversely, ancient lobes were analysed from the lithological point of view, identifying and interpreting the meaning of sedimentological facies to extrapolate information about the paleotopography of the seafloor and the large-scale architectures of the lobes. The two approaches are thus complementary and provide a wide spectrum of information. Utilizing these data, the influence of topographic variations on the dynamics of supercritical flow and relative deposits currents was studied in three types of submarine fans located in basins with different degrees and types of confinement. General results of this dissertation include the influence of large-scale morphologic variation (structural highs) and small-scale morphologic variation (i.e metric order) on the stratigraphic architecture and flow dynamics in tectonically controlled basin. Specific conclusions and contributions of each of the studies are described below.

Chapter 2 - "The influence of channel planform and slope topography on turbidity current overbank processes: the example of the Acquarone Fan (Southeastern Tyrrhenian Sea)"

The Acquarone Fan is an example of transient fan laterally confined by an important structural high (Acquarone high) (Figure 1). Transient fans are generally characterized by erosive channels and overbank deposits are absent due to the large bypass of the fine-grained fraction. In fact, in passive margins, overbank wedges are generally composed of thin-bedded fine-grained beds whose trend transverse and parallel to the channel are thought to be simple and predictable. Our study highlighted that the confinement operated by the Acquarone high strongly conditioned erosive and depositional processes controlling the channel-levee architectural evolution. The lateral confinement led to the overspill of a large amount of sediment outside the bend and to the confinement of overbanking turbidity currents, inducing flow deflection. Mass-transport deposits derived from the collapse of the steep margin of the high on the overbank area lead to reverse channel asymmetry (higher left levee). Sediment wave formation was inhibited on the left overbank and enhanced on the right one by the combined effect of the lateral confinement of the proximal left overbank, flow reflection on the structural high, occurrence of mass-transport deposits on the distal left overbank and the rightward flow deflection by the Coriolis force. Three wave fields have been recognized on the right overbank and their location changed through time (Figure 10). We envisaged that interacting with gradient variations along the channel course, turbidity currents behave differently, depending on their vertical density profiles. In particular, high-density turbidity currents produced coarse-grained upslope migrating cyclic steps outside the bend unlike lower-density flows, confirming the predisposition of stratified flow in developing hydraulic jumps. Knick-points in the channel talweg, inferred by tectonic structures transverse to the channel course whose topography is not completely healed, led to the occurrence of hydraulic jumps. According to the amplitude of the jump, which can be connected to the density stratification of the flow, this process may or not have a depositional expression on the overbank area (Figure 14). In particular, hydraulic jumps occurring in high-density stratified flows lead to the formation of antidunes with low relief channels occurring in their through. We have highlighted that, according to the degree of stratification of the flow, even small-topographic variations can influence the architecture of a channel-levee system. In conclusion, we showed that, differently from passive margins, the sediment distribution on the overbank changes in time and is principally related to the interaction of different flow types with the complex morphology created by active tectonics.

Chapter 3 - "Supercritical bedforms and related downslope evolution in a confined lobe, Amantea Fan, Paola Basin (Southeastern Tyrrhenian Sea)"

The Amantea Fan is a ponded fan localized in the southern sector of the Paola Basin (Figure 1), and the principal object of investigation is one of its depositional lobes. The shape of the basin, principally structurally-controlled, consists in a steep slope and an articulate basin floor frontally bounded by the Paola ridge and limited to the south by a NW-dipping slope (Figure 3). The morphology of the basin strictly controlled the different geometries of the beds composing the lobe. The gradient of the slope (>0.1°) resulted to be crucial for the development of supercritical flow conditions in the upper basin floor where erosional and depositional cyclic steps are recognized. In literature, the presence of supercritical bedforms near the channel mouth is associated with the presence of a channel-lobe transition zone. Anyway, the low degree of efficiency of the system resulted in a channel-attached lobe prevalently depositional and devoid of a well-developed channel-lobe transition zone. The Amantea lobe thus highlighted that, differently to what was envisaged in the models in literature, supercritical bedforms develop even in lobe environment. Moreover, the higher preservation potential of erosive and depositional supercritical bedforms in this environment can be related to the ponded nature of the fan where the bypass of the fine-grained portions is hindered by the basin morphology. The frontal confinement related to the Paola ridge forces the deceleration of the lower high-density parts of the flows, leading the development of hydraulic jumps at the toe of the ridge, as observed in frontally confined flow created through tank experiments. The frontal impact of the flows possibly induced the rebound of the upper low-density turbulent flows or their drastic collapse. Despite the high fine-grained deposition, the low efficiency of the system prevents the massive incorporation of the substrate occurring in more efficient systems. This process results in the deposition of massive sand where the flow is forced to decelerate, differently from highly efficient system where hybrid beds are deposited near topographic highs. The lateral confinement is determined as the principal controlling factor for the grain-size distribution resulting in a narrow high-density turbidity current in the flow axis while the laterally confined area is reached by lower-density off-axis turbidity currents, challenging the notion that basin floor deposits fine radially. The stretching of axial concentration is coherent with experimental results on laterally confined lobe. In conclusion, the recognition that the topography can influence the density structure and criticality degree of the flow and consequently the type of facies, may help to explain sediment distribution and to improve depositional models of fan lobe in confined settings.

Chapter 4 - "Small-scale facies change in relation to the articulate seafloor topography in two lobes of the Paretaio Turbidite System (Marnoso-arenacea Formation, Northern Apennines)"

The lobes 5 and 6, belonging to the Paretaio turbidite system, were deposited in the Upper Serravallian in the outer foredeep basin of the northern Apennines, laterally confined by the Coniale anticline created by the Mt. Castellaccio thrust (Figure 1). The two lobes have been studied at the large-scale (lobe) and at small-scale (bed), analysing the vertical and lateral variations of the facies associations (Figure 7) in relation to the lateral basin confinement and to metric topographic variations of the seafloor related to two normal faults able to create a small structural depression (Figure 18B). In particular, the large-scale lateral confinement resulted in the deposition at the base of the lobe (lobe initiation phase) of hybrid beds. These beds tend to occur in structurally controlled high-efficient turbidite systems where intrabasinal topographic highs and depocentre with slope changes favour both mud erosion and decelerations. The hybrid and turbiditic beds are interpreted as syntectonic deposits in relation to the Mt. Castellaccio thrust and to its associated faults. In particular, hybrid beds thickness is always markedly higher in the structurally-controlled depocenter, highlighting how they are not governed by self-levelling process but tend to compensate the topography (Figure 19). Their response to small-topographic changes is also marked by the increase in mud content in the depocenter related to the hydraulic jumps occurring in the basal high-density part of the flow (Figure 21). Also turbiditic beds are characterized by higher thicknesses in the depocenter where the accommodation space is higher. The top of the lobes (lobe building phase) is composed by amalgamed beds rich in mudstone clasts with upper bypass structures associated to the occurrence of hydraulic jumps induced by the morphology created by the underlying depositional lobe. These beds record the different phases of flow transformations from supercritical to subcritical with an internal hydraulic jump characterizing both the gravelly and sandy high-density parts of the flow (Figure 22). In the depocentre a combination of high depositional rate and available accommodation space makes possible the preservation of all intervals related to the different phases linked to the flow transformations while on the morphologic highs, more efficient erosive and bypass processes prevent their complete preservation.

Finally, the cyclic recurring of the identified facies associations in the two lobes is the basis for a three-stages model of lobe development very similar to others present in the literature (Figure 23). The depositional model consists in: 1) a lobe initiation phase, mainly composed of hybrid beds; 2) a lobe building phase characterized by the beds aggradation showing a progressive vertical increase in amalgamations and impact structures and flow decoupling (i.e., bypass structures). This phase records flow decelerations and hydraulic jumps, induced by the morphology created by the underlying depositional lobe; 3) a final abandonment phase of the lobe with the deposition of fine-grained sediment deposited by very dilute turbulent flow characterizing the interlobe deposits. In conclusion this study pointed out that lobe architecture is influenced by the presence of allogenic structural highs and by the morphology created by lobe building reflecting autogenic processes. Also subtle topographic variations are able to modify high-density gravity flows dynamics and to conditionate the preservation of their deposits.

References

Abd El-Gawad, S., Cantelli, A., Pirmez, C., Minisini, D., Sylvester, Z., and Imran, J. (2012) Three-dimensional numerical simulation of turbidity currents in a submarine channel on the seafloor of the Niger Delta slope. J. Geophys. Res. 117, C05026. https://doi.org/10.1029/2011JC007538

Adeogba, A.A., McHargue, T.R., and Graham, S.A. (2005) Transient fan architecture and depositional controls from near-surface 3-D seismic data, Niger delta continental slope. AAPG Bulletin. 89:5, 627–643. https://doi.org/10.1306/11200404025

Alvarez, W., Cocozza, T., & Wezel, F. C. (1974). Fragmentation of the Alpine belt by microplate dispersal. Nature, 248, 309–314.

Amy, L. A., McCaffrey, W. D., & Kneller, B. C. (2004). The influence of a lateral basin-slope on the depositional patterns of natural and experimental turbidity currents. *Geological Society Special Publication*, *221*(January), 311–330. https://doi.org/10.1144/GSL.SP.2004.221.01.17

Amy, L. A., & Talling, P. J. (2006). Anatomy of turbidites and linked debrites based on long distance (120 × 30 km) bed correlation, Marnoso Arenacea Formation, Northern Apennines, Italy. *Sedimentology*, *53*(1), 161–212. https://doi.org/10.1111/j.1365-3091.2005.00756.x

Antonioli, F., Ferranti, L., Lambeck, K., Kershaw, S., Verrubbi, V., and Dai Pra, G. (2006) Late Pleistocene to Holocene record of changing uplift rates in southern Calabria and northeastern Sicily (southern Italy, Central Mediterranean Sea). Tectonophysics. 422, 23–40. http://dx.doi.org/10.1016/j.tecto.2006.05.003

Arnott, R.W.C. (2007). Effect of suspended sediment concentration on deposition from suspended sediment dispersions. AAPG Annual Convention and Exhibition. April 1-4 2007, Long Beach, CA.

Azpiroz-Zabala, M., Cartigny, M. J. B., Talling, P. J., Parsons, D. R., Sumner, E. J., Clare, M. A., Simmons, S. M., Cooper, C., & Pope, E. L. (2017). Newly recognized turbidity current structure can explain prolonged flushing of submarine canyons. *Science Advances*, *3*(10). https://doi.org/10.1126/sciadv.1700200

Baas, J. H., & Best, J. L. (2002). Turbulence modulation in clay-rich sediment-laden flows and some implications for sediment deposition. *Journal of Sedimentary Research*, *72*(3), 336–340.

https://doi.org/10.1306/120601720336

Baas, J. H., Best, J. L., & Peakall, J. (2011). Depositional processes, bedform development and hybrid bed formation in rapidly decelerated cohesive (mud-sand) sediment flows. Sedimentology, 58(7), 1953–1987. https://doi.org/10.1111/j.1365-3091.2011.01247.x

Baas, J. H., McCaffrey, W. D., Haughton, P. D. W., and Choux, C. (2005) Coupling between suspended sediment distribution and turbulence structure in a laboratory turbidity current. J. Geophys. Res. 110, C11015. https://doi.org/10.1029/2004JC002668

Baas, J. H., van Kesteren, W. and Postma, G. (2004) Deposits of depletive high-density turbidity currents: a flume analogue of bed geometry, structure and texture. Sedimentology. 51, 1053–1088. https://doi.org/10.1111/j.1365-3091.2004.00660.x

Bagnold, R.A. (1954). Experiments on a gravity free dispersion of large solid spheres in a Newtonian fluid under shear. Proceedings of the Royal Society of London, Series A, 225, 49–63.

Birman, V.K., Meiburg, E., and Kneller, B. (2009) The shape of submarine levees: exponential or power law? J. Fluid Mech. 619, 367–376. https://doi.org/10.1017/S0022112008004862

Bouma, A.H. (1962). Sedimentology of some Flysch deposits. A Graphic Approach to Facies Interpretation. Elsevier, Amsterdam (168 pp.).

Brooks, H. L., Steel, E., & Moore, M. (2022). Grain-Size Analysis of Ancient Deep-Marine Sediments Using Laser Diffraction. Frontiers in Earth Science, 10(April), 1–24. https://doi.org/10.3389/feart.2022.820866

Carter, L., Burnett, D., Drew, S., Marle, G., Hagadorn, L., Bartlett-McNeil, D., & Irvine, N. (2009). Submarine cables and the oceans – Connecting the world: United Nations Environment Programme. In *United Nations Environment Programme, World Conservation Monitoring Centre, Biodiversity Series*. https://doi.org/10.7312/clar91608-007

Cartigny, M.J.B. (2012). Morphodynamics of supercritical high-density turbidity currents. Ph.D. thesis, Utrecht Studies in Earth Sciences, 153 p.

Cartigny, M. J. B., Eggenhuisen, J. T., Hansen, E. W. M., & Postma, G. (2013). Concentration-dependent flow stratification in experimental high-density turbidity currents and their relevance to turbidite facies models. Journal of Sedimentary Research, 83(12), 1046–1064. https://doi.org/10.2110/jsr.2013.71

Cartigny, M. J. B., Postma, G., van den Berg, J. H., & Mastbergen, D. R. (2011). A comparative study of sediment waves and cyclic steps based on geometries, internal structures and numerical modeling. *Marine Geology*, *280*(1–4), 40–56. https://doi.org/10.1016/j.margeo.2010.11.006

Cartigny, M. J. B., Ventra, D., Postma, G., & van Den Berg, J. H. (2014). Morphodynamics and sedimentary structures of bedforms under supercritical-flow conditions: New insights from flume experiments. *Sedimentology*, *61*(3), 712–748. https://doi.org/10.1111/sed.12076

Casalbore, D., Bosman, A., Casas, D., Chiocci, F., Martorelli, E., and Ridente, D. (2019) Morphological Variability of Submarine Mass Movements in the Tectonically–Controlled Calabro–Tyrrhenian Continental Margin (Southern Italy). Geosciences. 9, 43. https://doi.org/10.3390/geosciences9010043

Casalbore, D., Chiocci, F. L., Mugnozza, G. S., Tommasi, P., & Sposato, A. (2011). Flash-flood hyperpycnal flows generating shallow-water landslides at Fiumara mouths in Western Messina Strait (Italy). Marine Geophysical Research, 32(1), 257–271. https://doi.org/10.1007/s11001-011-9128-y

Casas, D., Chiocci, F., Casalbore, D., Ercilla, G., and Ortiz de Urbina, J. (2016) Magnitude-frequency distribution of submarine landslides in the Gioia Basin (southern Tyrrhenian Sea). Geo-Marine Letters. 36, 405–414. https://doi.org/10.1007/s00367-016-0458-2

Catalano, S., and Di Stefano, A. (1997) Sollevamenti e tettogenesi pleistocenica lungo il margine tirrenico dei Monti Peloritani: integrazione dei dati geomorfologici, strutturali e biostratigrafici. Il Quaternario. 10:2, 337-342.

Cattaneo, A. & Ricci Lucchi, F. (1995). Long-distance correlation of sandy turbidites: a 2.5 km long cross- section of Marnoso--Arenacea, Santerno Valley, Northern Apennines. Pickering, K.T., Hiscott, R.N., Kenyon, N.H., Ricci Lucchi, F. (Eds.), Smith Atlas of Deep Water Environments: Architectural Style in Turbidite Systems., 303–306.

Clementucci, R., Lafosse, M., Casalbore, D., Ridente, D., d’Acremont, E., Rabaute, A., Chiocci, F. L., & Gorini, C. (2022). Common origin of coexisting sediment undulations and gullies? Insights from two modern Mediterranean prodeltas (southern Italy and northern Morocco).

Geomorphology, 402(January), 108133. https://doi.org/10.1016/j.geomorph.2022.108133

Cornard, P. H., & Pickering, K. T. (2019). Supercritical-flow deposits and their distribution in a submarine channel system, Middle Eocene, Ainsa Basin, Spanish Pyrenees. *Journal of Sedimentary Research*, *89*(6), 576–597. https://doi.org/10.2110/jsr.2019.34

Cornard, P. H., & Pickering, K. T. (2020). Submarine topographic control on distribution of supercritical-flow deposits in lobe and related environments, middle eocene, Jaca basin, Spanish pyrenees. *Journal of Sedimentary Research*, *90*(9), 1222–1243. https://doi.org/10.2110/JSR.2020.59

Corradino, M., Pepe, F., Bertotti, G., Picotti, V., Monaco, C., & Nicolich, R. (2020). 3-D Architecture and Plio-Quaternary Evolution of the Paola Basin: Insights Into the Forearc of the Tyrrhenian-Ionian Subduction System. Tectonics, 39(2). https://doi.org/10.1029/2019TC005898

Covault, J. A., Kostic, S., Paull, C. K., Sylvester, Z., & Fildani, A. (2017). Cyclic steps and related supercritical bedforms: Building blocks of deep-water depositional systems, western North America. *Marine Geology*, *393*, 4–20. https://doi.org/10.1016/j.margeo.2016.12.009

Cunha, R.S., Tinterri, R., Muzzi Magalhaes, P. (2017). Annot Sandstone in the Peıra Cava basin: an example of an asymmetric facies distribution in a confined turbidite system (SE France). Mar. Pet. Geol. 87, 69-70. https://doi.org/10.1016/j.marpetgeo.2017.04.013

Dalla Valle, G. and Gamberi, F. (2009) Erosional sculpting of the Caprera confined deep-sea fan as a result of distal basin-spilling processes (eastern Sardinian margin, Tyrrhenian Sea). Marine Geology. 268, 55–66. https://doi.org/10.1016/j.margeo.2009.10.012

de Leeuw, J., Eggenhuisen, J. T., & Cartigny, M. J. B. (2018). Linking submarine channel-levée facies and architecture to flow structure of turbidity currents; insights from flume tank experiments. *Sedimentology*, *65*, 931–951. https://doi.org/10.1111/ijlh.12426

Deptuck, M. E., Piper, D. J. W., Savoye, B., & Gervais, A. (2008). Dimensions and architecture of late Pleistocene submarine lobes off the northern margin of East Corsica. Sedimentology, 55(4), 869–898. https://doi.org/10.1111/j.1365-3091.2007.00926.x

Deptuck, M.E., Sylvester, Z., Pirmez, C., and O'Byrne, C. (2007) Migration-aggradation history and 3-D seismic geomorphology of submarine channels in the Pleistocene Benin-major Canyon, western Niger Delta slope: Marine and Petroleum Geology. 24, 406–433, https://doi.org/10.1016/ j.marpetgeo.2007.01.005.

Dorrell, R. M., Peakall, J., Sumner, E. J., Parsons, D. R., Darby, S. E., Wynn, R. B., Özsoy, E., & Tezcan, D. (2016). Flow dynamics and mixing processes in hydraulic jump arrays: Implications for channel-lobe transition zones. *Marine Geology*, *381*(January 2017), 181–193. https://doi.org/10.1016/j.margeo.2016.09.009

Eggenhuisen, J. T., McCaffrey, W. D., Haughton, P. D. W., & Butler, R. W. H. (2010). Small-scale spatial variability in turbidity-current flow controlled by roughness resulting from substrate erosion: Field evidence for a feedback mechanism. Journal of Sedimentary Research, 80(2), 129–136. https://doi.org/10.2110/jsr.2010.014

Fabbri, A., Ghisetti, F., and Vezzani, L. (1980) The Peloritani-Calabria range and the Gioia basin in the Calabrian arc (Southern Italy): relationships between land and marine data. Geologica Rom. 19, 131–150.

Fildani, A., Hubbard, S. M., Covault, J. A., Maier, K. L., Romans, B. W., Traer, M., & Rowland, J. C. (2013). Erosion at inception of deep-sea channels. *Marine and Petroleum Geology*, *41*(1), 48–61. https://doi.org/10.1016/j.marpetgeo.2012.03.006

Fildani, A., Normark, W. R., Kostic, S., & Parker, G. (2006). Channel formation by flow stripping: Large-scale scour features along the Monterey East Channel and their relation to sediment waves. *Sedimentology*, *53*(6), 1265–1287. https://doi.org/10.1111/j.1365-3091.2006.00812.x

Fonnesu, M., Haughton, P., Felletti, F., & McCaffrey, W. (2015). Short length-scale variability of hybrid event beds and its applied significance. *Marine and Petroleum Geology*, *67*, 583–603. https://doi.org/10.1016/j.marpetgeo.2015.03.028

Fonnesu, M., Patacci, M., Haughton, P. D. W., Felletti, F., & Mccaffrey, W. D. (2016). Hybrid event beds generated by local substrate delamination on a confined-basin floor. *Journal of Sedimentary Research*, *86*(8), 929–943. https://doi.org/10.2110/jsr.2016.58

Gallignani, P. (1982). Recent sedimentation processes on the Calabria continental shelf and slope (Tyrrhenian Sea, Italy). Deep Sea Research Part B. Oceanographic Literature Review, 30(6), 448. https://doi.org/10.1016/0198-0254(83)90098-5

Gamberi, F. (2020). Systems supplying sediment to canyon heads (SSSCHs) in the Tyrrhenian Sea: The past and the present as a key to understanding deep-sea stratigraphy. *Marine and*

Petroleum Geology, *119*(August 2019), 104470. https://doi.org/10.1016/j.marpetgeo.2020.104470

Gamberi, F. & Marani, M. (2006) Hinterland geology and continental margin growth: the case of the Gioia Basin (southeastern Tyrrhenian Sea). Geological Society, London, Special Publications. 262, 349–363. https://doi.org/10.1144/GSL.SP.2006.262.01.21

Gamberi, F. & Marani, M. (2008) Controls on Holocene deep-water sedimentation in the northern Gioia Basin, Tyrrhenian Sea. Sedimentology. 55, 1889–1903. https://doi.org/10.1111/j.1365-3091.2008.00971.x

Gamberi, F., & Rovere, M. (2010). Mud diapirs, mud volcanoes and fluid flow in the rear of the Calabrian Arc Orogenic Wedge (southeastern Tyrrhenian sea). Basin Research, 22(4), 452–464. https://doi.org/10.1111/j.1365-2117.2010.00473.x

Gamberi, F. & Rovere, M. (2011) Architecture of a modern transient slope fan (Villafranca fan, Gioia Basin–Southeastern Tyrrhenian Sea). Sedimentary Geology. 236, 211–225. https://doi.org/10.1016/j.sedgeo.2011.01.007

Gamberi, F., Rovere, M., Mercorella, A., & Leidi, E. (2014). The influence of a lateral slope on turbidite lobe development on a modern deep-sea slope fan (Villafranca deep-sea fan, Tyrrhenian sea). Journal of Sedimentary Research, 84(6), 475–486. https://doi.org/10.2110/jsr.2014.37

Gamberi, F., Della Valle, G., Marani, M., Mercorella, A., Distefano, S., and Di Stefano, A. (2019) Tectonic controls on sedimentary system along the continental slope of the central and southeastern Tyrrhenian Sea. Ital. J. Geosci., 138, 317-332. https://doi.org/10.3301/IJG.2019.08

Garcia, M. & Parker, G. (1989). Experiments on hydraulic jumps in turbidity currents near a canyon-fan transition. *Science*, *245*(4916), 393–396. https://doi.org/10.1126/science.245.4916.393

Gong, C., Chen, L., & West, L. (2017). Asymmetrical, inversely graded, upstream-migrating cyclic steps in marine settings: Late Miocene-early Pliocene Fish Creek-Vallecito Basin, southern California. Sedimentary Geology, 360(September 2018), 35–46. https://doi.org/10.1016/j.sedgeo.2017.09.002

Hage, S., Cartigny, M. J. B., Clare, M. A., Sumner, E. J., Vendettuoli, D., Clarke, J. E. H., Hubbard, S. M., Talling, P. J., Gwyn Lintern, D., Stacey, C. D., Englert, R. G., Vardy, M. E., Hunt, J. E., Yokokawa, M., Parsons, D. R., Hizzett, J. L., Azpiroz-Zabala, M., & Vellinga, A. J. (2018). How to recognize crescentic bedforms formed by supercritical turbidity currents in the geologic record: Insights from active submarine channels. *Geology*, *46*(6), 563–566. https://doi.org/10.1130/G40095.1

Hamilton, P., Gaillot, G., Strom, K., Fedele, J., & Hoyal, D. (2017). Linking hydraulic properties in supercritical submarine distributary channels to depositional-lobe geometry. *Journal of Sedimentary Research*, *87*(9), 935–950. https://doi.org/10.2110/jsr.2017.53

Hamilton, P., Strom, K. B., & Hoyal, D. C. J. D. (2015). Hydraulic and sediment transport properties of autogenic avulsion cycles on submarine fans with supercritical distributaries. *Journal of Geophysical Research: Earth Surface*, *120*(7), 1369–1389. https://doi.org/10.1002/2014JF003414

Hampton, M. A. (1972). The role of subaqueous debris flows in generating turbidity currents. *J. Sediment. Pet*, *42*(4), 775–793.

Hansen, L. A. S., Callow, R. H. T., Kane, I. A., Gamberi, F., Rovere, M., Cronin, B. T., & Kneller, B. C. (2015). Genesis and character of thin-bedded turbidites associated with submarine channels. *Marine and Petroleum Geology*, *67*(November 2015), 852–879. https://doi.org/10.1016/j.marpetgeo.2015.06.007

Haughton, P. (1994) Deposits of deflected and ponded turbidity currents, Sorbas Basin, Southeast Spain. J. Sediment. Res. 64, 233–246. https://doi.org/10.1306/D4267D6B-2B26-11D7-8648000102C1865D

Haughton, P. D. W., Barker, S. P., & McCaffrey, W. D. (2003). “Linked” debrites in sand-rich turbidite systems - Origin and significance. *Sedimentology*, *50*(3), 459–482. https://doi.org/10.1046/j.1365-3091.2003.00560.x

Haughton, P. D. W., Davis, C., McCaffrey, W., & Barker, S. (2009). Hybrid sediment gravity flow deposits - Classification, origin and significance. *Marine and Petroleum Geology*, *26*(10), 1900–1918. https://doi.org/10.1016/j.marpetgeo.2009.02.012

Heijnen, M. S., Clare, M. A., Cartigny, M. J. B., Talling, P. J., Hage, S., Lintern, D. G., Stacey, C., Parsons, D. R., Simmons, S. M., Chen, Y., Sumner, E. J., Dix, J. K., & Hughes Clarke, J. E. (2020). Rapidly-migrating and internally-generated knickpoints can control submarine channel evolution. *Nature Communications*, *11*(1), 1–15. https://doi.org/10.1038/s41467-020-16861-x

Heiniö, P., and Davies, R.J. (2007) Knickpoint migra¬tion in submarine channels in response to fold growth, western Niger Delta. Marine and Petroleum Geology. 24, 434–449. http://dx.doi.org/10.1016/j.marpetgeo.2006.09.002

Hiscott, R.N., Hall, F.R, and Primez, C. (1997) Turbidity current overspill from the Amazon channel: texture of the silt/sand load, paleoflow from anisotropy of magnetic susceptibility and implications for flow processes. Proceedings of the Ocean Drilling Program, Scientific Results. 155, 53-78. https://doi.org/10.2973/odp.proc.sr.155.202.1997

Howlett, D. M., Ge, Z., Nemec, W., Gawthorpe, R. L., Rotevatn, A., & Jackson, C. A. L. (2019). Response of unconfined turbidity current to deep-water fold and thrust belt topography: Orthogonal incidence on solitary and segmented folds. *Sedimentology*, *66*(6), 2425–2454. https://doi.org/10.1111/sed.12602

Hoyal, D., & Sheets, B. A. (2009). Hydraulic Jumps as Controls on the Evolution of Distributary Channel Networks on Experimental Submarine Fans. *In the 33rd International Association of Hydraulic Research Congress, Vancouver BC. Canada*, 5474–5481.

Howlett, D. M., Ge, Z., Nemec, W., Gawthorpe, R. L., Rotevatn, A., & Jackson, C. A. L. (2019). Response of unconfined turbidity current to deep-water fold and thrust belt topography: Orthogonal incidence on solitary and segmented folds. Sedimentology, 66(6), 2425–2454. https://doi.org/10.1111/sed.12602

Hughes Clarke, J. E. (2016). First wide-angle view of channelized turbidity currents links migrating cyclic steps to flow characteristics. *Nature Communications*, *7*(May). https://doi.org/10.1038/ncomms11896

Hughes Clarke, J. E., Shor, A., Piper, D. J. W., & Mayer, L. A. (1990). Large-scale current-induced erosion and deposition in the path of the 1929 Grand Banks turbidity current. *Sedimentology*, *37*(4), 613–629. https://doi.org/10.1111/j.1365-3091.1990.tb00625.x

Jobe, Z., Z. Sylvester, M. B. Pittaluga, A. Frascati, C. Pirmez, D. Minisini, N. Howes, and A. Cantelli

(2017), Facies architecture of submarine channel deposits on the western Niger Delta slope: Implications for grain-size and stratification in turbidity currents, J. Geophys. Res. Earth Surf., 122, 473–491, https://doi.org/10.1002/2016JF003903.

Kane, I., McCaffrey, W., Peakall, J., and Kneller, B. (2010) Submarine channel levee shape and sediment waves from physical experiments. Sediment. Geol. 223, 75-85. https://doi.org/10.1016/j.sedgeo.2009.11.001

Kane, I., Pontén, A., Vangdal, B., Eggenhuisen J., Hodgson, D. and Spychala, Y. (2016) The stratigraphic record and processes of turbidity current transformation across deep-marine lobes. Sedimentology, 64, 1236-1273. https://doi.org/10.1111/sed.12346

Kastens, K. A., & Mascle, J. (1990). The geological evolution of the Tyrrhenian Sea: an introduction to the scientific results of ODP Leg 107. Proc., Scientific Results, ODP, Leg 107, Tyrrhenian Sea, November 2015, 3–26. https://doi.org/10.2973/odp.proc.sr.107.187.1990

Kato, Y., Fujinaga, K., Nakamura, K., Takaya, Y., Kitamura, K., Ohta, J., Toda, R., Nakashima, T., & Iwamori, H. (2011). Deep-sea mud in the Pacific Ocean as a potential resource for rare-earth elements. *Nature Geoscience*, *4*(8), 535–539. https://doi.org/10.1038/ngeo1185

Kneller B., Edwards D., McCaffrey W., Moore R. (1991) Oblique reflection of turbidity currents. Geology, 19, 250-252. https://doi.org/10.1130/0091-7613(1991)019%3C0250:OROTC%3E2.3.CO;2

Kneller, B. (1995). Beyond the turbidite paradigm: Physical models for deposition of turbidites and their implications for reservoir prediction. *Geological Society Special Publication*, *94*(94), 31–49. https://doi.org/10.1144/GSL.SP.1995.094.01.04

Kneller, B., Edwards, D., McCaffrey, W., & Moore, R. (1991). Oblique reflection of turbidity currents. *Geology*, *19*(3), 250–252. https://doi.org/10.1130/0091-7613(1991)019<0250:OROTC>2.3.CO;2

Kneller, B.C., and McCaffrey, W.D. (1999) Depositional effects of flow non-uniformity and stratification within turbidity currents approaching a bounding slope: deflection, reflection, and facies variation. J. Sediment. Res. 69, 980–991. http://dx.doi.org/10.2110/jsr.69.980

Komar, P. D. (1971). *Hydraulic Jumps in Turbidity Currents*. *Geological Society of America Bulletin*. https://doi.org/10.1130/0016-7606(1971)82

Kostic, S. (2011). Modeling of submarine cyclic steps: Controls on their formation, migration, and architecture. Geosphere, 7(2), 294–304. https://doi.org/10.1130/GES00601.1

Kostic, S. (2014). Upper flow regime bedforms on levees and continental slopes: Turbidity current flow dynamics in response to fine-grained sediment waves. *Geosphere*, *10*(6), 1094–1103. https://doi.org/10.1130/GES01015.1

Kuenen, P.H. (1952). Estimated size of the Grand Banks turbidity current. American Journal of Science, 250, 874–884, https://doi.org/10.2475/ajs.250.12.874.

Kuenen, H.P., Migliorini, C.I. (1950). Turbidity currents as a cause of graded bedding. J. Geol. 58, 91-127.

Li, S., Li, W., Alves, T. M., Wang, J., Feng, Y., Sun, J., Li, J., & Wu, S. (2020). Large-scale scours formed by supercritical turbidity currents along the full length of a submarine canyon, northeast South China Sea. *Marine Geology*, *424*(August 2021), 106158. https://doi.org/10.1016/j.margeo.2020.106158

Longhitano, S.G., Chiarella, D., Gugliotta, M. and Ventra, D. (2021), Coarse-grained deltas approaching shallow-water canyon heads: A case study from the Lower Pleistocene Messina Strait, Southern Italy. Sedimentology. 68, 2523-2562. https://doi.org/10.1111/sed.12866

Lowe, D.R. (1982). Sediment gravity flows; II, Depositional models with special reference to the deposits of high-density turbidity currents. J. Sediment. Pet. 52, 279-297. https://doi.org/10.1306/212F7F31-2B24-11D7-8648000102C1865D

Lowe, D. R., & Guy, M. (2000). Slurry-flow deposits in the Britannia Formation (Lower Cretaceous), North Sea: A new perspective on the turbidity current and debris flow problem. *Sedimentology*, *47*(1), 31–70. https://doi.org/10.1046/j.1365-3091.2000.00276.x

Lucente, C. C. (2004). Topography and palaeogeographic evolution of a middle Miocene foredeep basin plain (Northern Apennines, Italy). Sedimentary Geology, 170(3–4), 107–134. https://doi.org/10.1016/j.sedgeo.2004.06.002

Malinverno, A., & Ryan, W. B. F. (1986). Extension in the Tyrrhenian Sea and shortening in the Apennines as result of arc migration driven by sinking of the lithosphere. Tectonics, 5(2), 227–245. https://doi.org/10.1029/TC005i002p00227

McArthur, A., Kane, I., Bozetti, G., Hansen, L., & Kneller, B. C. (2020). Supercritical flows overspilling from bypass-dominated submarine channels and the development of overbank bedforms. *Depositional Record*, *6*(1), 21–40. https://doi.org/10.1002/dep2.78

Middleton, G.V. (1965). Primary Sedimentary Structures and Their Hydrodynamic Interpretation, 12. SEPM Special Publications, 265 pp.

Migeon, S., Savoye, B., and Faugeres, J.C. (2000) Quaternary development of migrating sediment waves in the Var deep-sea fan: distribution, growth pattern, and implication for levee evolution. Sediment. Geol. 133, 265–293. http://dx.doi.org/10.1016/S0037-0738(00)00043-9

Mutti, E. (1992). Turbidite Sandstones. Agip-Istituto di Geologia, Universita` di Parma, San Donato Milanese (275 pp.).

Mutti, E., Bernoulli, D., Lucchi, F. R., & Tinterri, R. (2009). Turbidites and turbidity currents from alpine "flysch" to the exploration of continental margins. *Sedimentology*, *56*(1), 267–318. https://doi.org/10.1111/j.1365-3091.2008.01019.x

Mutti, E. & Nilsen, T. H. (1981). Significance of intraformational rip-up clasts in deep-sea fan deposits. International Association of Sedimentologists Abstracts; 2nd European Regional Meeting., December, 117–119.

Mutti, E. & Normark, W. R. (1987). *Comparing examples of modern and ancient turbidite systems: problems and concepts* (pp. 1–38). Marine Clastic Sedimentology:London, Graham and Trotman.

Mutti, E. & Normark, W.R. (1991) An integrated approach to the study of turbidite systems. Seismic Facies and Sedimentary Processes of Submarine Fans and Turbidite Systems. New York: Springer-Verlag. DOI: 10.1007/978-1-4684-8276-8_4

Mutti, E. & Ricci Lucchi, F. (1972). Le torbiditi dell'Appennino settentrionale: introduzione all'analisi di facies. Mem. Soc. Geol. Ital. 11, 161-199.

Mutti, E. & Ricci Lucchi, F. (1975). Turbidite facies and facies association. In: Mutti, E., Parea, G., Ricci Lucchi, F., Sagri, M., Zanzucchi, G., Ghibaudo, G., Laccarino, S. (Eds.), Example of Turbidite Facies Associations From Selected Formation of Northern Apennines, 1975. International Association of Sedimentologists Congress, Nice, pp. 21-36.

Mutti, E., Ricci Lucchi, F., & Roveri, M. (2002). Revisiting turbidites of the Marnoso-arenacea formation and their basin-margin equivalents: problems with classic models. Excursion Guidebook of the Turbidite Workshop, …, May, 27–30. http://scholar.google.com/scholar?hl=en&btnG=Search&q=intitle:Revisiting+turbidites+of+the+Marnoso-arenacea+Formation+and+their+basin-margin+equivalents+:+problems+with+classic+models+Excursion+Guidebook#0

Mutti, E., & Tinterri, R. (2004). Cross-Stratified Coarse-Grained Sandstone Beds: Evidence of Flow-Margin Deposition and Reworking in Confined Turbidity Currents. AAPG Annual Meeting: April 18-21, 2004; Dallas, Texas, 1–5.

Mutti, E., Tinterri, R., Remacha, E., Mavilla, N., Angella, S., Fava, L. (1999). An Introduction to the Analysis of Ancient Turbidite Basins From an Outcrop Perspective, 39. AAPG Continuing Education Course Notes Series (93 pp.).

Mutti, E., Tinterri, R., Benevelli, G., Biase, D. di, & Cavanna, G. (2003). Deltaic, mixed and turbidite sedimentation of ancient foreland basins. *Marine and Petroleum Geology*, *20*(6–8), 733–755. https://doi.org/10.1016/j.marpetgeo.2003.09.001

Muzzi Magalhaes, P., & Tinterri, R. (2010). Stratigraphy and depositional setting of slurry and contained (reflected) beds in the Marnosoarenacea Formation (LanghianSerravallian) Northern Apennines, Italy. *Sedimentology*, *57*(7), 1685–1720. https://doi.org/10.1111/j.1365-3091.2010.01160.x

Nakajima, T., Kneller, B. (2013) Quantitative analysis of the geometry of submarine external levees. Sedimentology 60, 877-910. http://dx.doi.org/10.1111/j.1365-3091.2012.01366.x

Normark, W. R. (1970). Growth patterns of deep- sea fans. *American Association of Petroleum Geologists Bulletin*, *54*(11), 2170–2195. https://doi.org/10.1306/5d25cc79-16c1-11d7-8645000102c1865d

Normark, W. R., Piper, D. J. W., Posamentier, H., Pirmez, C., & Migeon, S. (2002). Variability in form and growth of sediment waves on turbidite channel levees. In *Marine Geology* (Vol. 192, Issues 1–3). https://doi.org/10.1016/S0025-3227(02)00548-0

Ono, K., & Plink-björklund, P. (2018). Froude supercritical flow bedforms in deepwater slope channels? Field examples in conglomerates, sandstones and fine-grained deposits.

Sedimentology, 65(3), 639–669. https://doi.org/10.1111/sed.12396

Ono, K., Plink-Björklund, P., Eggenhuisen, J. T., & Cartigny, M. J. B. (2021). Froude supercritical flow processes and sedimentary structures: New insights from experiments with a wide range of grain sizes. *Sedimentology*, *68*(4), 1328–1357. https://doi.org/10.1111/sed.12682

Patacci, M., Haughton, P. D. W., & McCaffrey, W. D. (2014). Rheological complexity in sediment gravity flows forced to decelerate against a confining slope, Braux, SE France. *Journal of Sedimentary Research*, *84*(4), 270–277. https://doi.org/10.2110/jsr.2014.26

Patacci, M., Haughton, P. D. W., & McCaffrey, W. D. (2015). Flow behavior of ponded turbidity currents. *Journal of Sedimentary Research*, *85*(8), 903–936. https://doi.org/10.2110/jsr.2015.59

Peakall, J., McCaffrey, W. D., Kneller, B. C., Stelting, C. E., McHargue, T. R., and Schweller, W. J. (2000) A process model for the evolution of submarine fan channels: implications for sedimentary architecture. Fine-grained turbidite systems, AAPG Memoir 72 /SEPM Special Publication. 68, 73–88. https://doi.org/10.1306/M72703

Pettingill, H.S. (2004). Global Overview of Deepwater Exploration and Production. In: Weimer, P., Pettingill, H. S. & Nilsen, T. H. (eds) Petroleum Systems of Deepwater Settings. Society of Exploration Geophysicists and European Association of Geoscientists and Engineers, 1–40, https://doi.org/10.1190/1.9781560801955.ch2.

Piazza, A. & Tinterri, R. (2020) Cyclic stacking pattern, architecture and facies of the turbidite lobes in the Macigno Sandstones Formation (Chattian-Aquitanian, northern Apennines, Italy). Mar. Pet. Geol. 122, 104704. https://doi.org/10.1016/j.marpetgeo.2020.104704

Pickering, K.T., and Hiscott, R.N. (1985) Contained (reflected) turbidity from the Middle Ordovician Cloridorme Formation, Quebec, Canada: an alternative to the antidune hypothesis. Sedimentology. 32, 373–394. https://doi.org/10.1111/j.1365-3091.1985.tb00518.x

Piper, D. and Normark, W. (1983) Turbidite depositional patterns and flow characteristics, Navy submarine fan, California Borderland. Sedimentology. 30, 681-694. https://doi.org/10.1111/j.1365-3091.1983.tb00702.x

Pirmez, C., Hiscott, R.N., and Kronen, J.K. (1997) Sandy turbidite successions at the base of channel-levee systems of the Amazon Fan revealed by FMS logs and cores: Unraveling the facies architecture of large submarine fans. Proceedings of the Ocean Drilling Program, Scientific Results. 155, 7-33.

Pirmez, C. & Imran, J. (2003) Reconstruction of turbidity currents in Amazon Channel. Mar. Pet. Geol. 20, 823-849. https://doi.org/10.1016/j.marpetgeo.2003.03.005

Pohl, F., Eggenhuisen, J.T., Tilston, M. et al. (2019) New flow relaxation mechanism explains scour fields at the end of submarine channels. Nat Commun. 10, 4425. https://doi.org/10.1038/s41467-019-12389-x

Pohl, F., Eggenhuisen, J. T., Kane, I. A., & Clare, M. A. (2020). Transport and Burial of Microplastics in Deep-Marine Sediments by Turbidity Currents. *Environmental Science and Technology*, *54*(7), 4180–4189. https://doi.org/10.1021/acs.est.9b07527

Posameinter, H.V., and Kolla, V. (2003) Seismic geomorphology and stratigraphy of depositional elements in deep-water settings. J. Sediment. Res. 73, 367-388. https://doi.org/10.1306/111302730367

Postma, G. (2011). Sediment gravity flow. In: Singh, V.P., Singh, P., Haritashya, U.K. (Eds.), Encyclopedia of Snow, Ice and Glaciers. Springer, pp. 1005-1010. DOI: 10.1007/978-90-481-2642-2_476

Postma, G., & Cartigny, M. J. B. (2014). Supercritical and subcritical turbidity currents and their deposits - A synthesis. *Geology*, *42*(11), 987–990. https://doi.org/10.1130/G35957.1

Postma, G., Cartigny, M., & Kleverlaan, K. (2009). Structureless, coarse-tail graded Bouma Ta formed by internal hydraulic jump of the turbidity current? *Sedimentary Geology*, *219*(1–4), 1–6. https://doi.org/10.1016/j.sedgeo.2009.05.018

Postma, G., Hoyal, D. C., Abreu, V., Cartigny, M., Demko, T., Fedele, J., Kleverlaan, K., & Pederson, K. H. (2016). Morphodynamics of Supercritical Turbidity Currents in the Channel-Lobe Transition Zone. Submarine Mass Movements and Their Consequences, Advances in Natural and Technological Hazards Research, 41, 469–478. https://doi.org/10.1007/978-3-319-20979-1

Postma, G., & Kleverlaan, K. (2018). Supercritical flows and their control on the architecture and facies of small-radius sand-rich fan lobes. *Sedimentary Geology*, *364*(December), 53–70. https://doi.org/10.1016/j.sedgeo.2017.11.015

Postma, G., Kleverlaan, K., and Cartigny, M. (2014) Recognition of cyclic steps in sandy and gravelly turbidite sequences and consequences for the Bouma facies model. Sedimentology. 61, 2268–2290. http://dx.doi.org/10.1111/sed.12135

Postma, G., Lang, J., Hoyal, D. C., Fedele, J. J., Demko, T., Abreu, V., & Pederson, K. H. (2021). Reconstruction of bedform dynamics controlled by supercritical flow in the channel–lobe transition zone of a deep-water delta (Sant Llorenç del Munt, north-east Spain, Eocene). *Sedimentology*, *68*(4), 1674–1697. https://doi.org/10.1111/sed.12735

Prélat, A., Hodgson, D. M., & Flint, S. S. (2009). Evolution, architecture and hierarchy of distributary deep-water deposits: a high-resolution outcrop investigation from the Permian Karoo Basin, South Africa. *Sedimentology*, *56*(7), 2132–2154. https://doi.org/10.1111/j.1365-3091.2009.01073.x

Puigdefabregas, C., Gjelberg, J., & Vaksdal, M. (2004). The Gres d’Annot in the Annot syncline: outer basin-margin onlap and associated soft sediment deformation. Deep-Water Sedimentation in the Alpine Basin of SE France: New Perspectives on the Grbs d’Annot and Related Systems. Geological Society, London, Special Publications, 221, 367–388.

Ricci Lucchi, F. (1986). The Oligocene to Recent foreland basins of the northern Apennines. In Foreland basins.

Ricci Lucchi, F. (1990). Turbidites in foreland and on-thrust basins of the northern Apennines. Palaeogeography, Palaeoclimatology, Palaeoecology, 77(1), 51–66. https://doi.org/10.1016/0031-0182(90)90098-R

Ricci Lucchi, F. & Valmori, E. (1980). Basin-wide turbidites in a Miocene, over-supplied deep-sea plain: a geometrical analysis. Sedimentology, 27(3), 241–270. https://doi.org/10.1111/j.1365-3091.1980.tb01177.x

Regione Siciliana (2006) Area Territoriale tra Capo Peloro e il bacino del Torrente Saponara (001). Relazione 2006. Piano Stralcio di Bacino per l’Assetto Idrogeologico (P.A.I.), Regione Siciliana, Palermo.

Remacha, E., Fernández, L.P, and Maestro, E. (2005) The Transition Between Sheet-Like Lobe and Basin-Plain Turbidites in the Hecho Basin (South-Central Pyrenees, Spain). J. Sediment. Res. 75, 798-819. https://doi.org/10.2110/jsr.2005.064

Rohais, S., Bailleul, J., Brocheray, S., Schmitz, J., Paron, P., Kezirian, F., & Barrier, P. (2021). Depositional Model for Turbidite Lobes in Complex Slope Settings Along Transform Margins: The Motta San Giovanni Formation (Miocene—Calabria, Italy). Frontiers in Earth Science, 9(November), 1–23. https://doi.org/10.3389/feart.2021.766946

Rovere, M., Gamberi, F., Mercorella, A., and Leidi, E. (2014) Geomorphometry of a submarine mass-transport complex and relationships with active faults in a rapidly uplifting margin (Gioia Basin, NE Sicily margin). Mar. Geol. 356, 31–43. https://doi.org/10.1016/j.margeo.2013.06.003

Sabato, L., & Tropeano, M. (2004). Fiumara: A kind of high hazard river. Physics and Chemistry of the Earth, 29(10), 707–715. https://doi.org/10.1016/j.pce.2004.03.008

Sanders, J.E. (1965). Primary sedimentary structures formed by turbidity currents and related resedimentation mechanisms. In: Middleton, G.V. (Ed.), Primary Sedimentary Structures and Their Hydrodynamic Interpretation, 12. SEPM Special Publications, pp. 192-219. https://doi.org/10.2110/pec.65.08.0192

Sartori, R. (1970). L'arco Calabro-Peloritano: aspetti di geologia marina. Rendiconti Società Italiana Di Mineralogia e Petrologia, 38, 941–950.

Scacchia, E., Tinterri, R., & Gamberi, F. (2022). The Influence of Channel Planform and Slope Topography on Turbidity Current Overbank Processes: The Example of the Acquarone Fan (Southeastern Tyrrhenian Sea). *Frontiers in Earth Science*, *9*, 1–24. https://doi.org/10.3389/feart.2021.785164

Sequeiros, O. E. (2012). Estimating turbidity current conditions from channel morphology: A Froude number approach. *Journal of Geophysical Research: Oceans*, *117*(4), 1–19. https://doi.org/10.1029/2011JC007201

Shepard, F.P. (1981). Submarine canyons: multiple causes and long-time persistence. Am. Assoc. Pet. Geol. Bull. 65, 1062–1077

Slootman, A., & Cartigny, M. J. B. (2020). Cyclic steps: Review and aggradation-based classification. *Earth-Science Reviews*, *201*, 102949. https://doi.org/10.1016/j.earscirev.2019.102949

Soutter, E. L., Bell, D., Cumberpatch, Z. A., Ferguson, R. A., Spychala, Y. T., Kane, I. A., & Eggenhuisen, J. T. (2021). The Influence of Confining Topography Orientation on Experimental

Turbidity Currents and Geological Implications. *Frontiers in Earth Science*, *8*(January). https://doi.org/10.3389/feart.2020.540633

Spinewine, B., Sequeiros, O. E., Garcia, M. H., Beaubouef, R. T., Sun, T., Savoye, B., & Parker, G. (2009). Experiments on wedge-shaped deep sea sedimentary deposits in minibasins and/or on channel levees emplaced by turbidity currents. Part II. Morphodynamic evolution ofthe wedge and of the associated bedforms. *Journal of Sedimentary Research*, *79*(8), 608–628. https://doi.org/10.2110/jsr.2009.065

Spychala, Y. T., Hodgson, D. M., & Lee, D. R. (2017a). Autogenic controls on hybrid bed distribution in submarine lobe complexes. *Marine and Petroleum Geology*, *88*, 1078–1093. https://doi.org/10.1016/j.marpetgeo.2017.09.005

Spychala, Y. T., Hodgson, D. M., Prélat, A., Kane, I. A., Flint, S. S., & Mountney, N. P. (2017b). Frontal and lateral submarine lobe fringes: Comparing sedimentary facies, architecture and flow processes. Journal of Sedimentary Research, 87(1), 75–96. https://doi.org/10.2110/jsr.2017.2

Storti, F. & Balsamo, F. (2010). Particle size distributions by laser diffraction: Sensitivity of granular matter strength to analytical operating procedures. Solid Earth, 1(1), 25–48. https://doi.org/10.5194/se-1-25-2010

Straub, K. M. & Mohrig, D. (2008) Quantifying the morphology and growth of levees in aggrading submarine channels. J. Geophys. Res. 113, 20. https://doi.org/10.1029/2007JF000896

Sylvester, Z., and Covault, J.A. (2016) Developmentof cutoff-related knickpoints during early evolution of submarine channels. Geology, 44, 835–838, https://doi.org/10.1130/G38397.1.

Symons, W. O., Sumner, E. J., Talling, P. J., Cartigny, M. J. B., & Clare, M. A. (2016). Large-scale sediment waves and scours on the modern seafloor and their implications for the prevalence of supercritical flows. *Marine Geology*, *371*, 130–148. https://doi.org/10.1016/j.margeo.2015.11.009

Tagliaferri, A., & Tinterri, R. (2016). The tectonically confined Firenzuola turbidite system (Marnoso-arenacea Formation, northern Apennines, Italy). Italian Journal of Geosciences, 135(3), 425–443. https://doi.org/10.3301/IJG.2015.27

Talling, P.J. (2013) Hybrid submarine flows comprising turbidity current and cohesive debris flow:

1065 Deposits, theoretical and experimental analyses, and generalized models: Geosphere, 9, 1-28. https://doi.org/10.1130/GES00793.1

Talling, P. J., Allin, J., Armitage, A., Arnott, R. W. C., Cartigny, M., Clare, M. A., Felletti, F., & Covault, J. (2015). Key future directions for research on turbidity currents and their deposits. *Journal of Sedimentary Petrology*, *85*, 153–169. https://doi.org/10.1007/978-3-642-14197-3_18

Talling, P. J., Amy, L. A., Wynn, R. B., Blackbourn, G., & Gibson, O. (2007). Evolution of turbidity currents deduced from extensive thin turbidites: Marnoso Arenacea Formation (Miocene), Italian Apennines. Journal of Sedimentary Research, 77(3–4), 172–196. https://doi.org/10.2110/jsr.2007.018

Talling, P. J., Amy, L. A., Wynn, R. B., Peakall, J., & Robinson, M. (2004). Beds comprising debrite sandwiched within co-genetic turbidite: Origin and widespread occurrence in distal depositional environments. *Sedimentology*, *51*(1), 163–194. https://doi.org/10.1111/j.1365-3091.2004.00617.x

Talling, P. J., Malgesini, G., Sumner, E. J., Amy, L. A., Felletti, F., Blackbourn, G., Nutt, C., Wilcox, C., Harding, I. C., & Akbari, S. (2012). Planform geometry, stacking pattern, and extrabasinal origin of low strength and intermediate strength cohesive debris flow deposits in the Marnoso-arenacea Formation, Italy. *Geosphere*, *8*(6), 1207–1230. https://doi.org/10.1130/GES00734.1

Talling, P. J., Masson, D. G., Sumner, E. J., & Malgesini, G. (2012). Subaqueous sediment density flows: Depositional processes and deposit types. Sedimentology, 59(7), 1937–2003. https://doi.org/10.1111/j.1365-3091.2012.01353.x

Talling, P. J., Wynn, R. B., Masson, D. G., Frenz, M., Cronin, B. T., Schiebel, R., Akhmetzhanov, A. M., Dallmeier-Tiessen, S., Benetti, S., Weaver, P. P. E., Georgiopoulou, A., Zühlsdorff, C., & Amy, L. A. (2007). Onset of submarine debris flow deposition far from original giant landslide. *Nature*, *450*(7169), 541–544. https://doi.org/10.1038/nature06313

Tek, D.E., McArthur, A.D., Poyatos-Moré, M., Colombera, L., Allen, C., Patacci M. & McCaffrey, W.D. (2021) Controls on the architectural evolution of deep-water channel overbank sediment wave fields: insights from the Hikurangi Channel, offshore New Zealand. New Zealand Journal of Geology and Geophysics. https://doi.org/10.1080/00288306.2021.1978509

Tinterri, R. (2020). Turbidites and turbidity currents (N. Scarselli, J. Adam, D. Chiarella, D. G. Roberts, & A. W. Bally (eds.); Regional G).

Tinterri, R. (2022). Turbidites of the northern Apennines: relationship between facies and basin morphology. Geosed (Società Geologica Italiana) Seminars, Invited Presentation, Online Webinar 25 March 2022.

Tinterri, R. & Civa, A. (2021). Laterally accreted deposits in low efficiency turbidites associated with a structurally-induced topography (oligocene molare group, tertiary piedmont basin, nw italy). Journal of Sedimentary Research, 91(7), 751–772. https://doi.org/10.2110/jsr.2020.174

Tinterri, R., Drago, M., Consonni, A., Davoli, G., & Mutti, E. (2003). Modelling subaqueous bipartite sediment gravity flows on the basis of outcrop constraints: First results. *Marine and Petroleum Geology*, *20*(6–8), 911–933. https://doi.org/10.1016/j.marpetgeo.2003.03.003

Tinterri, R., Laporta, M., & Ogata, K. (2017). Asymmetrical cross-current turbidite facies tract in a structurally-confined mini-basin (Priabonian-Rupelian, Ranzano Sandstone, northern Apennines, Italy). *Sedimentary Geology*, *352*, 63–87. https://doi.org/10.1016/j.sedgeo.2016.12.005

Tinterri, R., Mazza, T., & Magalhaes, P. M. (2022). Contained-Reflected Megaturbidites of the Marnoso-arenacea Formation (Contessa Key Bed) and Helminthoid Flysches (Northern Apennines, Italy) and Hecho Group (South-Western Pyrenees). *Frontiers in Earth Science*, *10*(February), 1–31. https://doi.org/10.3389/feart.2022.817012

Tinterri, R., & Muzzi Magalhaes, P. (2011). Synsedimentary structural control on foredeep turbidites: An example from Miocene Marnoso-arenacea Formation, Northern Apennines, Italy. *Marine and Petroleum Geology*, *28*(3), 629–657. https://doi.org/10.1016/j.marpetgeo.2010.07.007

Tinterri, R., Muzzi Magalhaes, P., Tagliaferri, A., & Cunha, R. S. (2016). Convolute laminations and load structures in turbidites as indicators of flow reflections and decelerations against bounding slopes. Examples from the Marnoso-arenacea Formation (northern Italy) and Annot Sandstones (south eastern France). *Sedimentary Geology*, *344*, 382–407. https://doi.org/10.1016/j.sedgeo.2016.01.023

Tinterri, R., & Piazza, A. (2019). Turbidites facies response to the morphological confinement of a foredeep (Cervarola Sandstones Formation , Miocene , northern Apennines , Italy). *Sedimentology*, *66*, 636–674. https://doi.org/10.1111/sed.12501

Tinterri, R., Pizzati, V., & Scacchia, E. (2023). Turbidite facies tracts as related to flow criticality and efficiency in tectonically confined basins: an outcrop perspective. *1st In-Person Bouma Deep Water Geoscience Conference - Utrecht, Netherlands, 17-21 April 2023, Abstract Book*.

Tinterri, R., & Tagliaferri, A. (2015). The syntectonic evolution of foredeep turbidites related to basin segmentation: Facies response to the increase in tectonic confinement (Marnoso-arenacea Formation, Miocene, Northern Apennines, Italy). *Marine and Petroleum Geology*, *67*, 81–110. https://doi.org/10.1016/j.marpetgeo.2015.04.006

Trincardi, F., Correggiari, A., Field, M. E., & Normark, W. R. (1995). Turbidite deposition from multiple sources: Quaternary Paola Basin (eastern Tyrrhenian Sea). Journal of Sedimentary Research B: Stratigraphy & Global Studies, B65(4), 469–483. https://doi.org/10.1306/d4268289-2b26-11d7-8648000102c1865d

Walker, R.G. (1967). Turbidite sedimentary structures and their relationship to proximal and distal depositional environments. J. Sediment. Pet. 37, 25-37. https://doi.org/10.1306/74D71645-2B21-11D7-8648000102C1865D

Wells, M., and Cossu, R. (2013) The possible role of Coriolis forces in structuring large-scale sinuous patterns of submarine channel–levee systems. Philos. Trans. A Math. Phys. Eng. Sci. 371, 19. https://doi.org/10.1098/rsta.2012.0366

Wynn, R. B., Kenyon, N. H., Masson, D. G., Stow, D. A. V, & Weaver, P. P. E. (2002). Channel-Lobe Transition Zones. *AAPG Bulletin*, *8*(8), 1441–1462.

Wynn, R. B., Masson, D. G., Stow, D. A. V., & Weaver, P. P. E. (2000). Turbidity current sediment waves on the submarine slopes of the western Canary Islands. *Marine Geology*, *163*(1–4), 185–198. https://doi.org/10.1016/S0025-3227(99)00101-2

Wynn, R. B., & Stow, D. A. V. (2002). Classification and characterisation of deep-water sediment waves. *Marine Geology*, *192*(1–3), 7–22. https://doi.org/10.1016/S0025-3227(02)00547-9

Zhang, L. F., & Dong, D. Z. (2020). Thickening-upward cycles in deep-marine and deep-lacustrine turbidite lobes: examples from the Clare Basin and the Ordos Basin. Journal of Palaeogeography, 9(1). https://doi.org/10.1186/s42501-020-00059-9

Zhong, G., Cartigny, M. J. B., Kuang, Z., & Wang, L. (2015). Cyclic steps along the South Taiwan Shoal and West Penghu submarine canyons on the northeastern continental slope of the South China Sea. *Bulletin of the Geological Society of America*, *127*(5–6), 804–824. https://doi.org/10.1130/B31003.1

Zhong, G., & Peng, X. (2021). Transport and accumulation of plastic litter in submarine canyons—The role of gravity flows. *Geology*, *49*(5), 581–586. https://doi.org/10.1130/G48536.1

Annex Figures

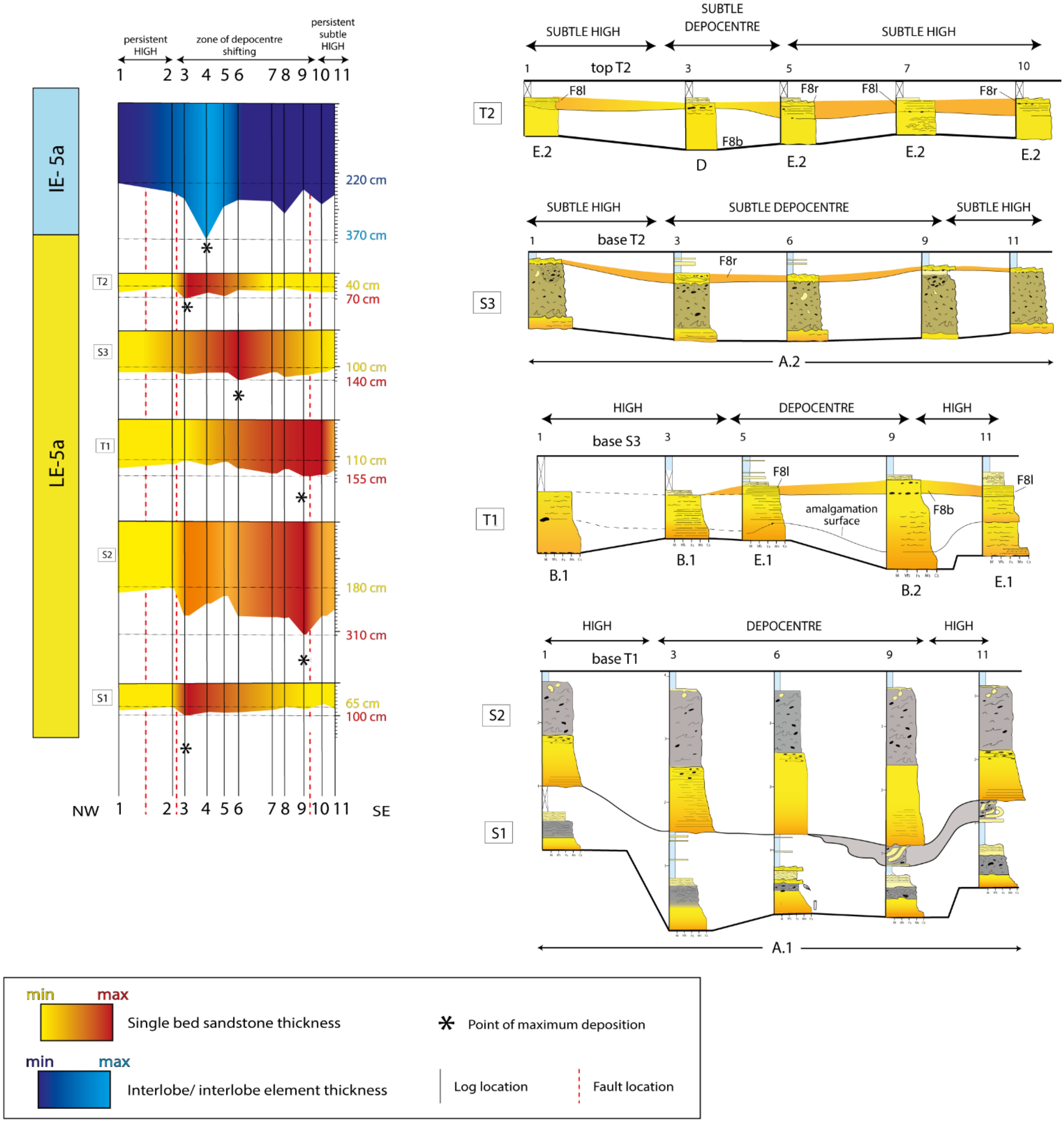

Annex Figure 1 *On the right the progressive flattening at the top of each bed. In the blue tone are reported the interlobes and in the yellow tone the beds/lobe elements. The different gradations highlight where the thickness value is low (yellow/dark blue) or high (red/light blue). On the left the downcurrent facies change of the beds of lobe element 5a.*

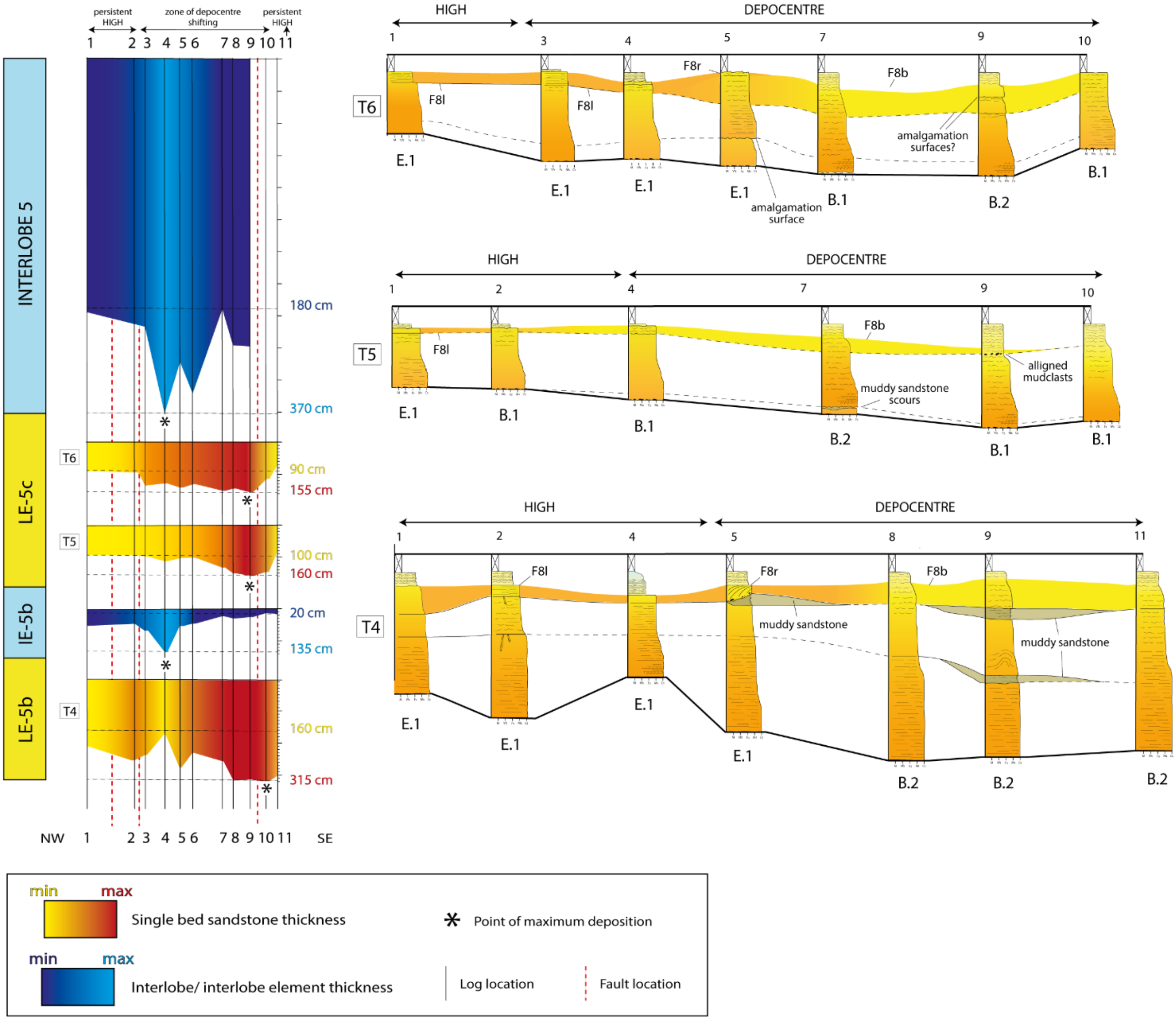

Annex Figure 2 *On the right the progressive flattening at the top of each bed. In the blue tone are reported the interlobes and in the yellow tone the beds/lobe elements. The different gradations highlight where the thickness value is low (yellow/dark blue) or high (red/light blue). On the left the downcurrent facies change of the beds of lobe elements 5b and 5c.*

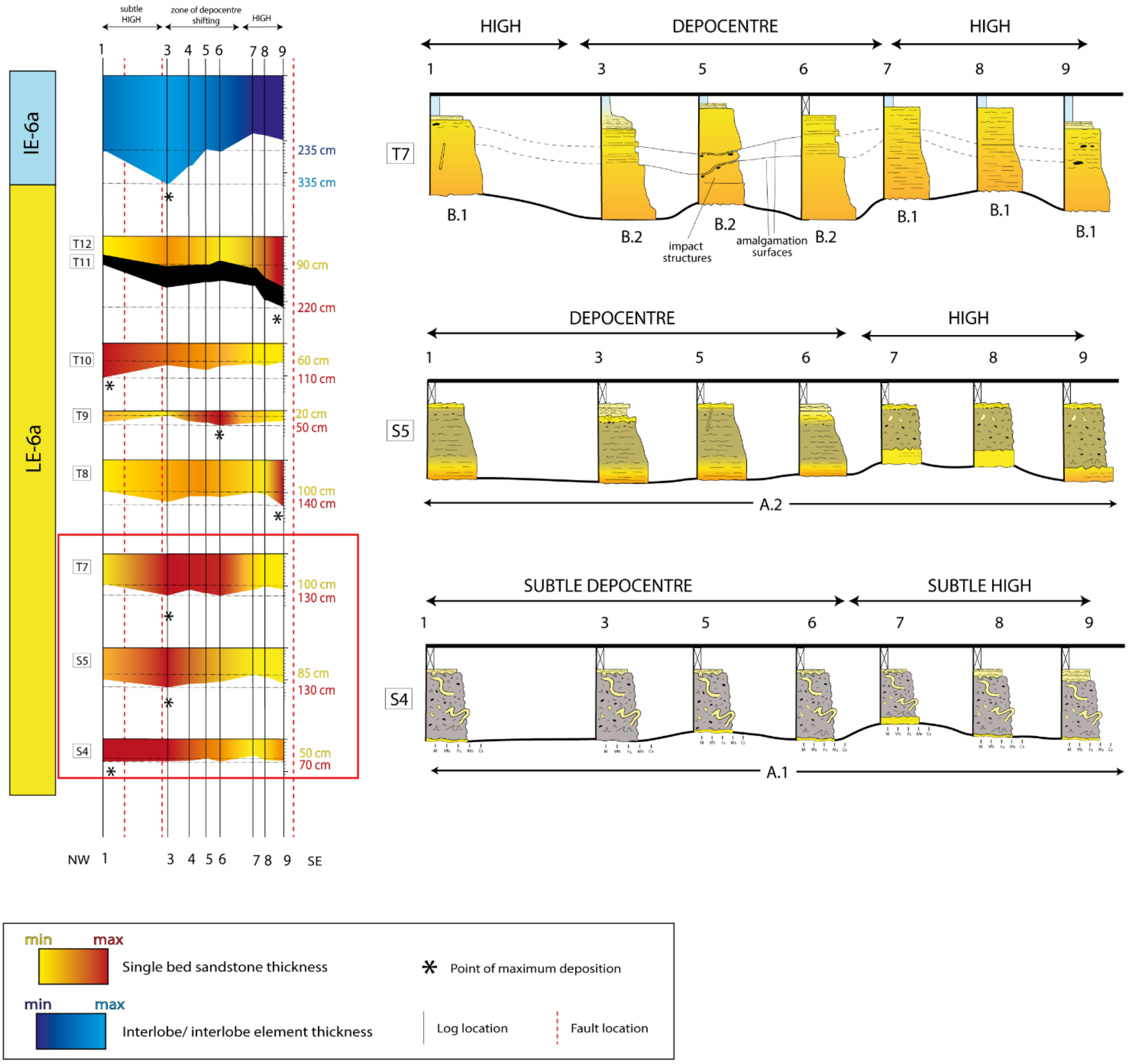

Annex Figure 3 *On the right the progressive flattening at the top of each bed. In the blue tone are reported the interlobes and in the yellow tone the beds/lobe elements. The different gradations highlight where the thickness value is low (yellow/dark blue) or high (red/light blue). On the left the downcurrent facies change of the beds of lobe element 6a.*

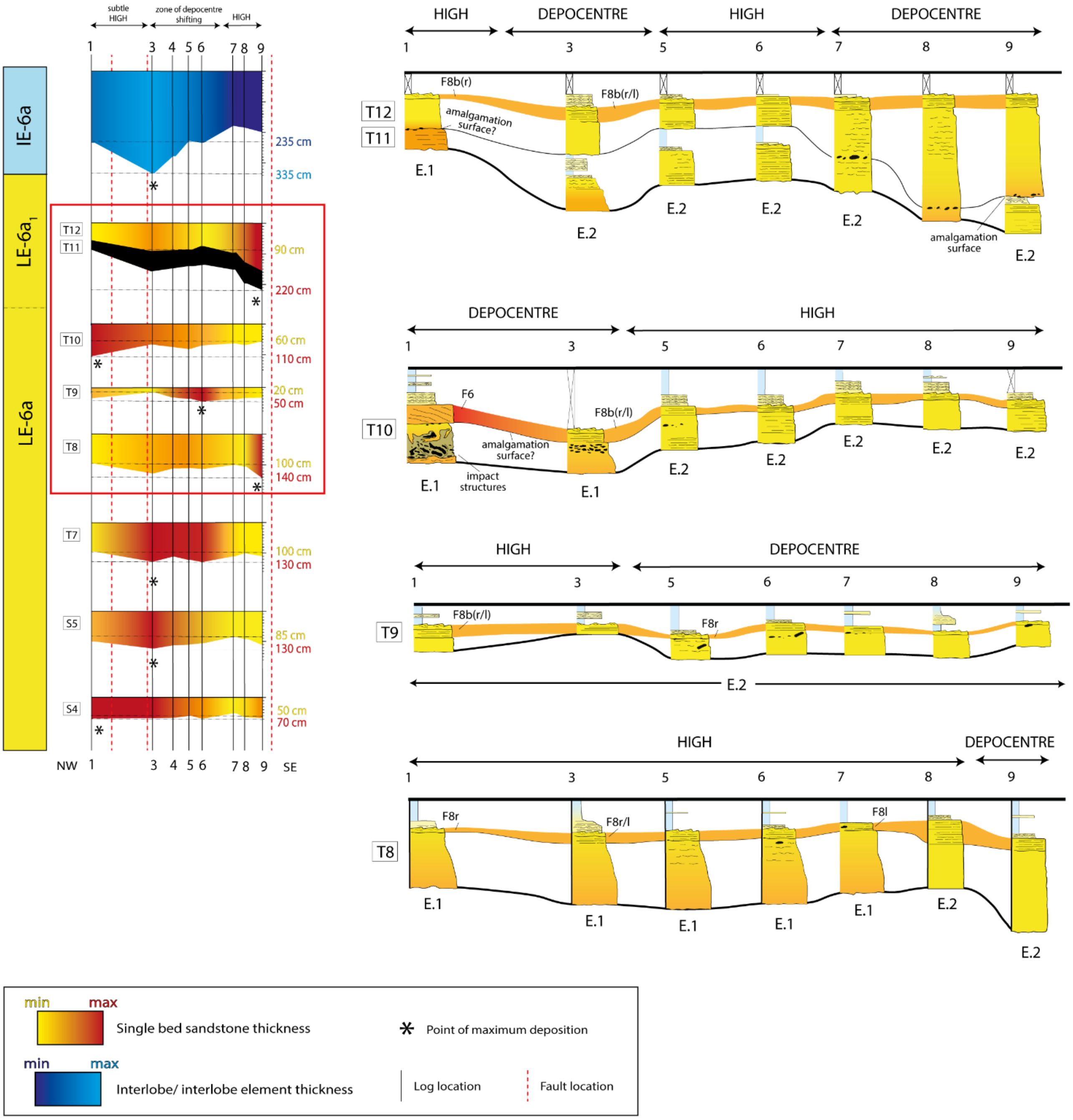

Annex Figure 4 *On the right the progressive flattening at the top of each bed. In the blue tone are reported the interlobes and in the yellow tone the beds/lobe elements. The different gradations highlight where the thickness value is low (yellow/dark blue) or high (red/light blue). On the left the downcurrent facies change of the beds of lobe element 6a.*

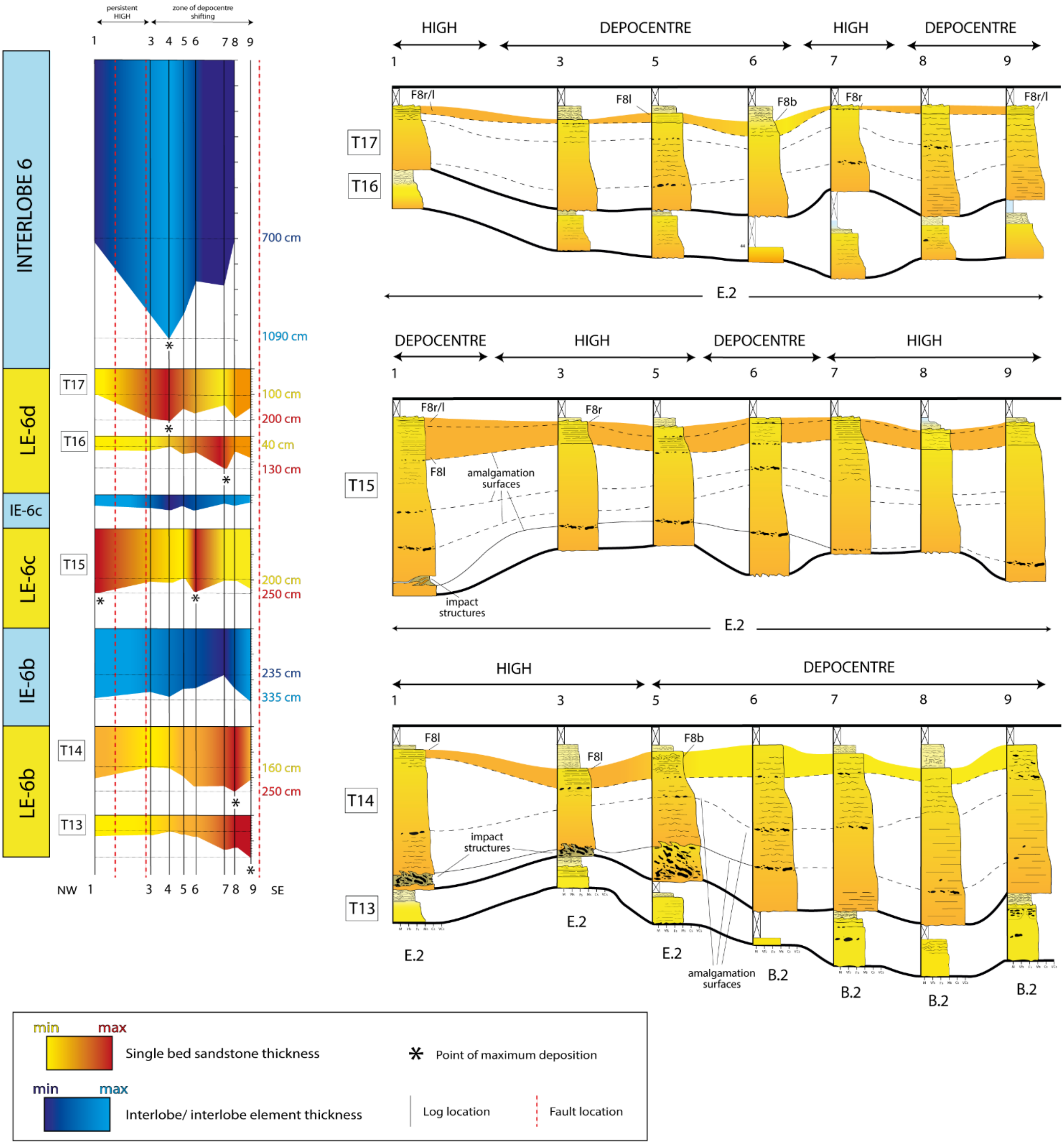

Annex Figure 5 *On the right the progressive flattening at the top of each bed. In the blue tone are reported the interlobes and in the yellow tone the beds/lobe elements. The different gradations highlight where the thickness value is low (yellow/dark blue) or high (red/light blue). On the left the downcurrent facies change of the beds of lobe elements 6b, 6c and 6d.*

Annex Tables

Table 1 – Granulometric analysis results on hybrid beds

Bed	Sample	Log	Morphology	Bed type	Facies	Clay	Silt	Very-fine	Fine	Medium	Coarse	Very coarse	Granules	Fine fraction	Coarse fraction	N/G	Higher grain-size
S1	S1-1b	1	High	A1	b	2,88	44,05	26,81	21,66	4,23	0,38			46,93	53,07	1,13	Coarse
S1	S1-1b2	1	High	A1	b	3,44	48,93	26,49	18,98	2,31				52,37	47,63	0,91	Medium
S1	S1-1b3	1	High	A1	b	2,05	55,2	25,92	15,56	1,27				57,25	42,75	0,75	Medium
S1	S1_3a	3	Depocentre	A1	a	2,04	33,1	14,99	18,7	23,2	7,93	0,04		35,14	64,86	1,85	Very corarse
S1	S1-3b1	3	Depocentre	A1	b	1,97	57,21	28,19	11,99	0,65				59,18	40,83	0,69	Fine
S1	S1-3b2	3	Depocentre	A1	b	2,12	55,63	28,27	13,76	0,23				57,75	42,26	0,73	Fine
S1	S1-3b3	3	Depocentre	A1	b	1,98	54,9	27,35	14,97	0,8				56,88	43,12	0,76	Fine
S1	S1_11a	11	High	A1	a	2,79	46,18	17,83	21,34	11,79	0,07			48,97	51,03	1,04	Coarse
S1	S1-11b1	11	High	A1	b	6,24	48,14	27,98	16,18	1,46				54,38	45,62	0,84	Medium
S1	S1-11b2	11	High	A1	b	2,27	53,48	27,18	15,95	1,13				55,75	44,26	0,79	Medium
S1	S1-11b3	11	High	A1	b	1,73	52,55	27,73	16,43	1,56				54,28	45,72	0,84	Medium
S2	S2-1a	1	High	A1	a	1,91	42,57	20,99	24,55	9,96	0,02			44,48	55,5	1,25	Coarse
S2	S2-1b1	1	High	A1	b	2,47	47,24	26,71	18,01	4,88	0,34	0,33	0,03	49,71	49,6	1,00	Granules
S2	S2-1b2	1	High	A1	b	2,39	49,83	27,42	17,41	2,82	0,12	0,02		52,22	47,65	0,91	Very corarse
S2	S2-1b3	1	High	A1	b	2,17	52,01	27,6	16,95	1,28				54,18	45,83	0,85	Medium
S2	S2-3b1	3	Depocentre	A1	b	5,79	53	24,9	15,55	0,76				58,79	41,21	0,70	Medium
S2	S2-3b2	3	Depocentre	A1	b	3,01	53,14	26,74	16,47	0,63				56,15	43,84	0,78	Medium
S2	S2-3b3	3	Depocentre	A1	b	2,76	60,29	24,96	11,64	0,33				63,05	36,93	0,59	Medium
S2	S2-1b1	1	High	A1	b	2,9	49,29	25,1	19,5	3,2				52,19	47,81	0,92	Medium

S2	S2-1b2	1	High	A1	b	2,83	49,79	26,26	19,53	1,59				52,62	47,38	0,90	Medium
S2	S2-1b3	1	High	A1	b	2,86	51,65	25,74	17,84	1,91				54,51	45,49	0,83	Medium
S2	S2-11a	11	High	A1	a	3,7	47,7	20,97	22,01	5,63				51,4	48,61	0,95	Medium
S2	S2-11b1	11	High	A1	b	4,58	52,31	24,76	16,67	1,67				56,89	43,1	0,76	Medium
S2	S2-11b2	11	High	A1	b	2,73	51,47	25,12	17,82	2,85				54,2	45,79	0,84	Medium
S2	S2-11b3	11	High	A1	b	2,7	50,78	26,55	18,19	1,78				53,48	46,52	0,87	Medium
S2	S2-11df	11	High	A1	delamination feature	4,38	58,05	26,43	11,1	0,04				62,43	37,57	0,60	
S3	S3-1b1	1	High	A2	b	1,39	44,49	23,93	25,7	4,5				45,88	54,13	1,18	Medium
S3	S3-1b2	1	High	A2	b	1,39	43	24,29	24,98	6,33				44,39	55,6	1,25	Medium
S3	S3-1b3	1	High	A2	b	1,36	42,01	24,62	24,64	7,36				43,37	56,62	1,31	Medium
S3	S3-1c	1	High	A2	c (F8r)	5,11	55,77	22,36	15,13	1,62				60,88	39,11	0,64	Medium
S3	S3-3a	3	Depocentre	A2	a	3,05	44,46	23,04	23,4	6,05				47,51	52,49	1,10	Medium
S3	S3-3b1	3	Depocentre	A2	b	3,37	48,4	23,65	21,46	3,11				51,77	48,22	0,93	Medium
S3	S3-3b2	3	Depocentre	A2	b	1,61	47,7	23,69	22,14	4,86				49,31	50,69	1,03	Medium
S3	S3-3b3	3	Depocentre	A2	b	1,68	46,6	24,11	21,7	5,91				48,28	51,72	1,07	Medium
S3	S3-3R	3	Depocentre	A2	c (F8r)	4,45	50,98	22,42	19,41	2,74				55,43	44,57	0,80	Medium
S3	S3-11a	11	High	A2	a	3,39	45,52	22,69	22,65	5,76				48,91	51,1	1,04	Medium
S3	S3-11b1	11	High	A2	b	2,71	45,3	22,53	23,3	6,15	0,02			48,01	51,98	1,08	Coarse
S3	S3-11b2	11	High	A2	b	1,83	45,15	23,56	22,4	7,04				46,98	53	1,13	Medium
S3	S3-11b3	11	High	A2	b	2,02	46,11	23,29	22,94	5,65				48,13	51,88	1,08	Medium
S3	S3-11c	11	High	A2	c (F8r)	2,62	45,79	27,46	20,6	0,33	0,03			48,41	51,22	1,06	Coarse
S4	S4-1b1	1	High	A1	b	2,66	52,28	22,5	18,48	4,07				54,94	45,05	0,82	Medium
S5	S4-1b2	1	High	A1	b	2,7	48,11	22,97	21,3	4,91				50,81	49,19	0,97	Medium
S4	S4-1b3	1	High	A1	b	2,39	51,24	23,19	20,02	3,16				53,63	46,37	0,86	Medium
S4	S4-3b1	3	Depocentre	A1	b	1,93	48,04	24,16	21,24	4,63				49,97	50,03	1,00	Medium

S4	S4-3b2	3	Depocentre	A1	b	2,33	49,19	24,04	20,73	3,71				51,52	48,48	0,94	Medium
S4	S4-3b3	3	Depocentre	A1	b	1,83	51,96	25,11	19,16	2,74				53,79	46,21	0,86	Medium
S4	S4-7a	7	High	A1	a	2,31	47,09	20,87	21,23	8,46	0,02			49,4	50,56	1,02	Coarse
S4	S4-7b1	7	High	A1	b	1,99	51,81	24,61	19,08	2,51				53,8	46,2	0,86	Medium
S4	S4-7b2	7	High	A1	b	2,26	51,25	22,14	19,04	5,31				53,51	46,49	0,87	Medium
S4	S4-7b3	7	High	A1	b	2,43	53,12	21,36	18,67	4,4				55,55	44,45	0,80	Medium
S4	S4-7c	7	High	A1	c (F9)	3,06	66,34	21,65	8,61	0,33				69,4	30,6	0,44	Fine
S4	S4-5b1	9	Depocentre	A1	b	2,93	53,76	23,07	17,5	2,75				56,69	43,32	0,76	Medium
S4	S4-5c	9	Depocentre	A1	Sand nodules	2	48,11	23,19	20,82	5,2	0,02			50,11	49,21	0,98	Medium
S5	S5-1b1	1	High	A2	b	2,52	46,6	28,57	20,57	1,74				49,12	50,88	1,04	Medium
S5	S5-1b2	1	High	A2	b	2,78	46,42	27,86	20,69	2,25				49,2	50,8	1,03	Medium
S5	S5-1b3	1	High	A2	b	2,42	46,78	29,26	19,49	2,07				49,2	50,82	1,03	Medium
S5	S5-1c	1	High	A2	C (F8r)	2,69	47,58	20,27	23,69	5,77				50,27	49,73	0,99	Medium
S5	S5-3a	3	Depocentre	A2	a	2,91	46,34	21,67	21,31	7,75	0,02			49,25	50,73	1,03	Coarse
S5	S5-3b1	3	Depocentre	A2	b	2,3	57,04	25,29	13,95	1,42				59,34	40,66	0,69	Medium
S5	S5-3b2	3	Depocentre	A2	b	2,11	56,83	25,68	14,23	1,15				58,94	41,06	0,70	Medium
S5	S5-3b3	3	Depocentre	A2	b	1,8	55,22	26,3	15,65	1,04				57,02	42,99	0,75	Medium
S5	S5-7b1	7	High	A2	b	1,85	47,85	24,18	21,67	4,46				49,7	50,31	1,01	Medium
S5	S5-7b2	7	High	A2	b	2,6	52,38	23,05	18,92	3,04				54,98	45,01	0,82	Medium
S5	S5-7b3	7	High	A2	b	2,63	53,28	23,64	17,61	2,84				55,91	44,09	0,79	Medium

Table 2 – Granulometric analysis results on turbidite beds

Bed	Sample	Log	Morphology	Bed Type	Facies	Clay	Silt	Very fine	Fine	Medium	Coarse	Fine fraction	Coarse fraction	N/G	Higher grain-size	Average span
T1	T1-1a	1	High	B.1	F5	1,52	43,24	22,69	24,59	7,96		44,76	55,24	1,23	Medium	2,95
T1	T1-1b	1	High	B.1	F8b	1,72	46,73	24,09	22,23	5,22		48,45	51,55	1,06	Medium	2,98
T1	T1-3a	3	Depocentre	B.1	F5/F7	2,35	47,14	22,89	21,36	6,28		49,49	50,51	1,02	Medium	3,20
T1	T1-3b	3	Depocentre	B.1	F8b	2,37	47,4	27,4	20,82	2,01		49,77	50,23	1,01	Medium	2,62
T1	T1-11a	11	High	E.1	F5/F7	2,49	39,76	21,24	24,91	11,45	0.15	42,25	57,75	1,37	Coarse	3,05
T1	T1-11b	11	High	E.1	F8b	2,81	43,18	23,56	23,37	7,08		45,99	54,01	1,17	Medium	3,00
T1	T1-11c	11	High	E.1	F8b	3,09	47,69	24,74	20,58	3,9		50,78	49,22	0,97	Medium	2,98
T1	T1-11d	11	High	E.1	F8b	3,03	41,75	22,8	23,64	8,71		44,78	55,22	1,23	Medium	3,05
T1	T1-11e	11	High	E.1	F8b	3,15	45,4	24,94	24,23	2,28		48,55	51,45	1,06	Medium	2,69
T2	T2-1a	1	High	E.2	F8	1,57	46,78	25,48	23,64	2,53		48,35	51,65	1,07	Medium	2,67
T2	T2-4a	4	Depocentre	E.2	F8	3,88	37,25	25,02	27,53	6,3		41,13	58,85	1,43	Medium	2,54
T2	T2-4b	4	Depocentre	E.2	F8b	4,29	39,79	27,33	23,6	5		44,08	55,93	1,27	Medium	2,62
T2	T2-4c	4	Depocentre	E.2	F8r	6,24	48,59	24,82	18,27	2,07		54,83	45,16	0,82	Medium	3,04
T2	T2-7a	7	High	E.2	F8r	6,1	46,68	25,29	19,99	1,94		52,78	47,22	0,89	Medium	2,90
T2	T2-9a	9	High	E.2	F8/F7	5,51	39,06	27,48	25,77	2,19		44,57	55,44	1,24	Medium	2,41
T2	T2-9b	9	High	E.2	F8r	4,75	42,01	24,89	25,07	3,27		46,76	53,23	1,14	Medium	2,68
T3	T3-5a	5	High	E.2	F8/F7	2,68	51,83	25,91	18,31	1,27		54,51	45,49	0,83	Medium	3,03
T3	T3-5b	5	High	E.2	F8l	2,4	41,32	19,58	24,41	12,25		43,72	56,24	1,29	Medium	3,23
T3	T3-5c	5	High	E.2	F8r	2,6	43,16	19,68	24,47	10,08		45,76	54,23	1,19	Medium	3,26
T4	T4-12b	12	Perpendicular	E.2	F5	2,11	37,59	20,26	25,7	14,21	0,14	39,7	60,3	1,52	Coarse	3,35
T4	T4-12a	12	Perpendicular	E.2	F5b	2,85	40,95	18,65	23,92	13,55	0,08	43,8	56,2	1,28	Coarse	2,97
T4	T4-12c	12	Perpendicular	E.2	F8b	2,2	48,48	31,19	16,92	1,2		50,68	49,32	0,97	Medium	2,36
T4	T4-12d	12	Perpendicular	E.2	F8r	2,72	51,57	29,48	15,36	0,86		54,29	45,71	0,84	Medium	2,49
T4	T4-7a	7	High	B.2	F5	2,55	38,9	18,82	24,86	14,77	0,11	41,45	58,55	1,41	Coarse	3,16
T4	T4-7b	7	High	B.2	F8b	2,6	44,87	26,77	22,92	2,84		47,47	52,53	1,11	Medium	2,60
T5	T5-9a	9	High	B.1	F5	2,54	42,5	22,56	24,46	7,93		45,04	54,95	1,22	Medium	2,99

T5	T5-9b	9	High	B.1	F5b	2,73	43,75	20,66	22,23	10,59	0,04	46,48	53,48	1,15	Medium	3,45
T5	T5-9c	9	High	B.1	F8b	2,08	44,95	28,46	21,39	3,12		47,03	52,97	1,13	Medium	2,55
T6	T6-9a	9	High	B.2	F5/F7	2,93	41,52	20,78	25,57	9,21		44,45	55,56	1,25	Medium	3,03
T6	T6-9b	9	High	B.2	F5b	2,59	42,15	27,25	25,25	2,76		44,74	55,26	1,24	Medium	2,45
T8	T8-1a	1	High	E.1	F8	2,17	37,68	23,3	30,49	6,37		39,85	60,15	1,51	Medium	2,38
T8	T8-1b	1	High	E.1	F8b	1,64	35,21	23,91	28,8	10,42		36,85	63,15	1,71	Medium	2,52
T8	T8-1c	1	High	E.1	F8br	2,39	49,39	28,87	17,85	1,51		51,78	48,22	0,93	Medium	2,53
T8	T8-9a	9	High	E.2	F8br	1,67	43,85	22,48	26,27	5,74		45,52	54,48	1,20	Medium	2,80
T9	T9-1a	1	High	E.2	F8	2,67	46,28	25,42	22,75	2,89		48,95	51,05	1,04	Medium	2,74
T9	T9-1b	1	High	E.2	F8br	3,23	49,1	22,1	21,7	3,87		52,33	47,67	0,91	Medium	3,22
T10	T10-1a	1	High	E.1	F6	1,88	44,22	19,74	22,18	11,92	0,06	46,1	53,9	1,17	Coarse	3,54
T10	T10-1b	1	High	E.1	F9	7,39	67,79	15,32	8,9	0,59		75,18	24,82	0,33	Fine	4,01
T10	T10-7a	7	High	E.2	F8br	1,56	49,25	28,26	20,13	0,79		50,81	49,19	0,97	Medium	2,50
T10	T10-8a	8	High	E.2	F8	3,98	53,27	28,46	14,9	0,38		57,25	42,75	0,75	Medium	2,66
T10	T10-8b	8	High	E.2	F8bl	3,66	52,39	24,12	18,85	0,99		56,05	43,95	0,78	Medium	3,01
T11	T11-7a	7	High	E.2	F8/F7	2,9	42,72	25,77	25,33	3,27		45,62	54,38	1,19	Medium	2,57
T12	T12-7a	7	High	E.2	F8b	2,23	41,75	24,12	25,9	5,99		43,98	56,02	1,27	Medium	2,70
T12	T12-7b	7	High	E.2	F8br	2,42	42,14	23,38	26,46	5,59		44,56	55,44	1,24	Medium	2,72
T14	T14-1a	1	High	E.2	F5b	3,82	33,19	22,45	25,99	14,27	0,28	37,01	62,99	1,70	Coarse	2,88
T14	T14-1b	1	High	E.2	F9	8,96	66,95	18,7	5,08	0,31		75,91	24,09	0,32	Medium	2,86
T15	T15-1a	1	High	E.2	F8	5,68	41,65	21,61	23,62	7,44		47,33	52,67	1,11	Medium	3,19
T15	T15-1b	1	High	E.2	F8b	4,79	40,86	20,75	23,82	9,77		45,65	54,34	1,19	Medium	3,25
T15	T15-1c	1	High	E.2	F8b	2,78	34,39	26,21	31,54	5,09		37,17	62,84	1,69	Medium	2,18
T15	T15-12a	12	Perpendicular	E.2	F8	2,97	46,87	27,91	20,36	1,88		49,84	50,16	1,01	Medium	2,59
T15	T15-12b	12	Perpendicular	E.2	F9	3,93	53,46	28,04	14,55	0,02		57,39	42,61	0,74	Fine	2,62